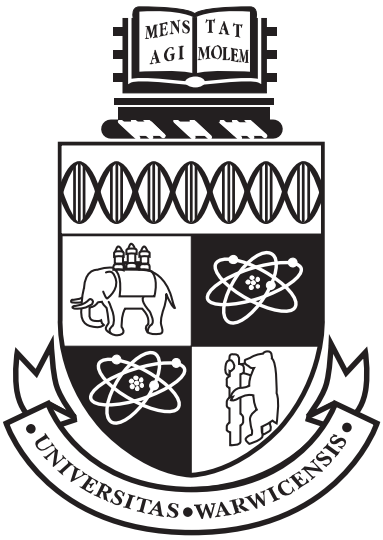

Electronic Transport in Single-Walled Carbon Nanotubes, and their Application as Scanning Probe Microscopy tips

by

Neil Richard Wilson

Thesis

Submitted to the University of Warwick

for the degree of

Doctor of Philosophy

Physics

April 2004

THE UNIVERSITY OF
WARWICK

Contents

List of Tables

List of Figures

Acknowledgments

Firstly I would like to thank the many people who have given me guidance over the last few years, not least of whom are my supervisors Dr David Cobden (Physics Department, University of Washington), and Dr Boris Mouzykantskii (Physics Department, University of Warwick). I especially thank Dr Julie Macpherson (Chemistry Department, University of Warwick) who has been positively involved in my work on a daily basis over the last couple of years. One of the primary pleasures I take from my research is the enjoyment of working with talented and interesting people. So I also thank Dr Jesper Nygård (Physics Department, Niels Bohr Institute), Dr David Smith (Physics Department, University of Southampton), Prof. John Weaver and Dr Phil Dobson (Electronics and Electrical Engineering, University of Glasgow), Prof. Robert Young (Materials Science Department, UMIST), Dr Mark Newton (Physics Department, University of Warwick), and the University of Warwick Electrochemistry Group.

This work would not have been possible without the excellent support of the technical staff at Warwick. In particular I thank Steve York (Physics Department) for his continual help and sense of humour, Frank Courtney (Engineering Department) for help and advice on lithography and device fabrication, and the Mechanical and Electrical Workshops of the Physics Department for their expertise

and patience. I have benefitted from the support of Veeco, and Dr Mike Conroy in particular, both through the loan of equipment and many useful discussions. I also thank the EPSRC for funding, and the Physics Department for providing additional funding for the last few months.

Finally, I thank all those who have reminded me that there is more to life than Physics, in particular of course Clare. My family have been a constant source of comfort, particularly when progress was difficult. I am especially grateful to my parents for their caring and unquestioning support. I would like to thank both my grandfathers, who unfortunately will not get to read this. Their desire to learn and understand, and interest in life in general, inspired me. Lastly, thanks to my friends who still talk to the Physicist at parties!

Declarations

Except where otherwise explicitly indicated, this thesis contains an account of my own independent research at the University of Warwick, and the University of Washington between October 2000 and April 2004 under the supervision of Dr B. Mouzykantskii, and Dr D. H. Cobden. I have also collaborated on a daily basis with Dr J. V. Macpherson of the Department of Chemistry, University of Warwick, in particular on carbon nanotube growth, and carbon nanotube atomic force microscopy tips. Steve York has helped considerably with electron microscopy. The research reported here has not been submitted, either wholly or in part, in this or any other academic institution for admission to a higher degree.

Some of this work has appeared in the scientific literature in the following joint publications:

Publications

1. Neil R. Wilson, David H. Cobden and Julie V. Macpherson, *Single-Wall Carbon Nanotube Conducting Probe Tips*; J. Phys. Chem. B.; **(Communication); 2002;** *106*(51);13102-13105

2. Neil R. Wilson and Julie V. Macpherson, *Single-walled Carbon Nanotubes as Templates for Nanowire Conducting Probes*; Nano Lett.; **(Communication); 2003;***3*(10);1365-1369

3. Neil R. Wilson and Julie V. Macpherson, *Enhanced Resolution Electric Force*

Microscopy with single wall carbon nanotube tips; submitted to Appl. Phys. Lett. (2004)

Oral Presentations

1. Neil R. Wilson and Julie V. Macpherson; *Enhanced Resolution Electric Force Microscopy with Single Wall Nanotube Probes*, UK CMMP meeting, University of Warwick (2004)

2. Neil R. Wilson, David H. Cobden, and Julie V. Macpherson; *Single Wall Nanotubes as Conducting Probe Tips*, Pittsburgh conference, Orlando (2003)

3. Neil R. Wilson, David H. Cobden and Julie V. Macpherson; *Single-wall carbon nanotubes dipped in mercury*, APS March Meeting, Austin (2003)

Patents

1. Neil R. Wilson and Julie V. Macpherson; *Fabrication of nanotube and conducting nanowire probes*; application lodged 13.08.2003, application number GB0318987.5

Abstract

Single-walled carbon nanotubes (SWNTs) are remarkable molecules composed of a graphite sheet rolled into a seamless cylinder. With nanometer diameter, and micrometer length, their physical properties are due to a mixture of quantum and classical effects. This work investigates the electrical transport properties of these molecules, and demonstrates their application as Atomic Force Microscopy (AFM) tips.

SWNTs were grown by catalysed chemical vapour deposition (cCVD), and characterized using AFM, electron microscopy and Raman spectroscopy. Electronic devices were fabricated from SWNTs grown by cCVD on SiO_2. Electronic transport through the SWNT devices was studied using electric force microscopy (EFM) and scanned gate microscopy (SGM). SGM was used to study the effects of defects on transport through the devices. A novel form of SGM, based on the modulation of the tip-gating potential by the oscillating tip in dynamic mode AFM, was demonstrated and shown to massively enhance the signal to noise ratio. Using EFM we directly demonstrated the transition from ballistic transport in metallic SWNT at low source-drain voltages, to diffusive transport at high-source drain voltages. EFM was also used to image the charge injection induced around a SWNT at high gate voltages, and correlate it with the observed hysteresis in the transconductance of SWNT devices. Both of these results are of fundamental importance to the future applications of SWNT electronic devices. The high bias behaviour of metallic SWNT is crucial to their proposed use as interconnects in nanoscale devices. Hysteresis in the transconductance of semiconducting SWNT devices is limiting their application as chemical and biological sensors, where environmental effects are monitored by the change in conductance of the devices.

SWNTs were mounted at the apex of AFM tips, and used as high resolution scanning probe tips. Electrical transport through the SWNT-AFM tips was investigated using both liquid (Hg) and solid contacts. An efficient technique for fabricating nanowire AFM tips, using SWNT-AFM tips as templates, was also invented. The resultant nanowire tips were shown to be robust, high aspect ratio, electrical probes. Using calibration samples fabricated from SWNTs, SWNT-AFM tips were quantitatively demonstrated to increase the resolution of EFM. Under optimal conditions identical features could be distinguished down to separations as low as 15 nm, comparable to the topographic resolution.

Abbreviations

AFM	Atomic Force Microscopy
c-AFM	conducting Atomic Force Microscopy
cCVD	catalysed Chemical Vapour Deposition
CFM	Chemical Force Microscopy
DWNT	Double-walled carbon nanotube
EFM	Electric Force Microscopy
EFGM	Electric Force Gradient Microscopy
FESEM	Field Emission Scanning Electron Microscopy
fm-EFM	frequency modulation Electric Force Microscopy
KSP	Kelvin Surface Potential
LFM	Lateral Force Microscopy
MFM	Magnetic Force Microscopy
mSWNT	metallic Single-Walled carbon nanotube
MWNT	Multi-Walled carbon nanotube

nt tip	Atomic Force Microscopy tip composed of a bundle of single-walled carbon nanotubes
PCB	Printed Circuit Board
SCM	Scanning Conductance Microscopy (also used to refer to Scanning Capacitance Microscopy but not in this thesis)
SEM	Scanning Electron Microscopy
SGM	Scanning Gate Microscopy
SIM	Scanning Impedance Microscopy
SPM	Scanning Probe Microscopy
SSPM	Scanning Surface Potential Microscopy
sSWNT	semi-conducting Single-Walled carbon nanotube
STM	Scanning Tunnelling Microscopy
STS	Scanning Tunnelling Spectroscopy
SWNT	Single-Walled carbon nanotube
TEM	Transmission Electron Microscopy
TM	Tapping mode Atomic Force Microscopy
TR mode	Torsional Resonance mode Atomic Force Microscopy

Chapter 1

Introduction

"But I would like not to underestimate the value of the world view which is the result of scientific effort. The same thrill, the same awe and mystery, comes again and again when we look at any question deeply enough. With more knowledge comes a deeper, more wonderful mystery, luring one on to penetrate deeper still. Never concerned that the answers may prove disappointing, with pleasure and confidence we turn over each new stone to find unimagined strangeness leading on to more wonderful questions and mysteries - certainly a grand adventure." - Richard Feynman

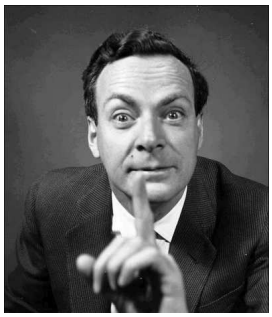

Richard Feynman, copyright of Caltech

In December 1959 the Nobel Prize winner, and inspirational physicist, Richard Feynman gave a revolutionary lecture entitled *'There's Plenty of Room at the Bottom- An Invitation to Enter a New Field of Physics'*. In it he envisaged a new field of physics based on the novel behaviour of objects at the small scale and '*..furthermore, a point that is most important is that it would have an enormous number of technical applications.*' Forty years later and 'nanoscience' and 'nanotechnology' have arrived. In his lecture Feynman predicted that a key role in the progress of the new field would be increased resolution electron microscopy. This has indeed been the case, however, a big impact has also been made by the discovery and development of scanning probe microscopy. It is this technique which forms the basis of the work presented here, and an introduction to it is given in Section 1.2.

A second factor of great importance to the sudden explosion of nanoscience and nanotechnology has been the development of new materials with nanoscopic dimensions, novel properties, and yet robust enough to endure the procedures necessary to address them with macroscopic experimental equipment. Of particular note are nanowires and carbon nanotubes, the subject of this thesis, which both have cross sections in the nanometre scale but lengths in the micrometre scale. Their small cross section results in novel quantum mechanical effects, whilst their long lengths facilitates their study by techniques developed for work at the micrometre scale, and incorporation into macroscopic structures.

The description 'carbon nanotubes' is applied to a wide variety of cylindrical carbon fibre like materials ranging in diameter from 4 Å to 100's of nm, and in length from a few nm to a few cm. These materials are formed from closed, seamless, cylinders of graphite and can be split into two groups: multi-walled carbon nanotubes (MWNTs), which consist of concentric cylinders in a Russian Doll fashion, and range in diameter from a few to 100's of nm; and single-walled carbon nanotubes (SWNTs), which consist of only one cylinder of graphite, and range

in diameter from 4 Å to a few nm. Section 1.1 gives a brief introduction to the remarkable properties of SWNTs, focussing on those relevant to this work.

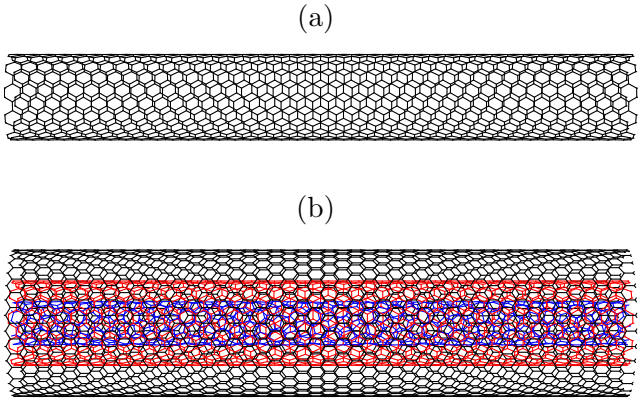

Figure 1.1: Representation of (a) a SWNT and (b) a MWNT

1.1 Introduction to Single-Walled Carbon Nanotubes

Since Iijima's famous paper in 1991 documenting his observation of '*Helical microtubules of graphitic carbon*' [Iij91] carbon nanotubes have intrigued scientists. The remarkable physical properties of these molecules make them a playground for physicists and chemists, whilst also inspiring economists with hopes of a nanotechnology revolution to revitalise flagging economies. The resultant increase in funding for carbon nanotube research has produced an exponential growth in the number of papers published on the subject, Figure 1.2. As a result of the sheer size of the literature this introduction to SWNTs will consider only topics of interest, or relevance to this thesis. In particular we will focus on electrical properties of SWNTs, so neglecting the large amounts of research done on their field emission and materials properties.

The remainder of this section will introduce the physical properties of SWNTs, focussing on those relevant to the research presented in this thesis. Each subsequent experimental Chapter contains an introduction to the specific aspect of SWNT research presented in it.

There are many excellent review articles on SWNT [Dai02a, BZd02, MFP02, Mor01]. At a basic level the June 2000 special edition of Physics World [McE00, SF00, de 00, Dai00] provides much good background, in addition Accounts of Chemical Research Number 12 (2002) [Dai02b, Avo02, RG02, DDJ$^+$02b, KBM02, SFLH02, OHL02, NHH$^+$03] gives a more detailed and up to date view of SWNT research. Much of the following introduction is based upon '*Physical Properties of Carbon Nanotubes*' by Saito et al. [SDD98]. Unfortunately, with the rapidly developing nature of the field a review article is quickly out of date. With that in mind, the following is a brief introduction to the fundamental properties of SWNT.

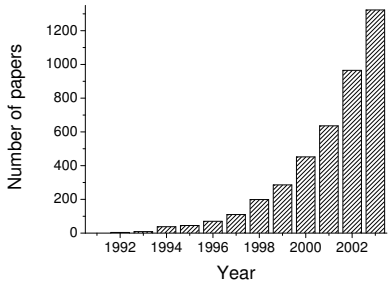

Figure 1.2: Number of papers with 'nanotube' in their title or abstract from a Web of Science search.

History

The timeline shown in Figure 1.3 denotes a selection of the more important pieces of work relevant to this thesis. An important point to note is that the synthesis of small quantities of C_{60} or carbon nanotubes is a fairly simple process, their observation and identification once formed was the limiting step to their discovery and use. Hence, rapid progress has been made since high resolution electron microscopy and scanned probe microscopy have enabled routine imaging of nanometre diameter objects.

1959	Richard Feynman's talk *'There's plenty of room at the bottom'* to the American Physical Society at Caltech
1981	Invention of the Scanning Tunnelling Microscope (STM) by Binnig et al. see e.g. [BR87]
1985	Discovery of C_{60} by Curl, Kroto and Smalley [KHO$^+$85]
1986	Invention of the Atomic Force Microscope (AFM) by Binnig et al. [BQG86] Nobel Prize for Physics awarded to Binnig and Rohrer
1991	Sumio Iijima observed MWNT in the soot generated by arc discharge [Iij91]
1993	Synthesis of SWNT independently by Iijima and Ichihashi [II93], and Bethune et al. [BKD$^+$93]
1996	Nobel Prize for Chemistry awarded to R. Curl, H. Kroto and R. Smalley Electrical transport experiments on ropes of SWNTs by Thess et al. [TLN$^+$96] MWNT used as AFM tips by Dai et al. [DHR$^+$96] Large scale (1-10 g) synthesis of, and electrical transport measurements on, high quality SWNTs by Thess et al. [TLN$^+$96],
1997	First electrical transport measurements on individual (metallic) carbon nanotubes [BCL$^+$97, TDD$^+$97]
1998	Field effect transistor fabricated from a single semi-conducting SWNT by Tans et al. [TVD98] Chemical vapour deposition synthesis of SWNTs by Hongjie Dai's group at Stamford University [KSC$^+$98, KCD98]
2000	HiPCO process for the formation of bulk quantities of high purity SWNT started.
2001	Logic circuits constructed from individual SWNTs [BHND01]
2002	Wafer scale synthesis of SWNT devices for logic circuits [JWY$^+$02] 'Vectorial growth' of SWNTs [JL02]
2003	Separation of SWNT according to electrical properties independently by [KHvK03, SDU$^+$03, ZJS$^+$03] Electrically induced photoemission from SWNTs [MMA$^+$03] Assembling SWNT devices from solution by DNA [KBB$^+$03] and surface modification [RHSH03]

Figure 1.3: Timeline

Structure and mechanical properties

Carbon nanotubes can be considered as seamless cylinders obtained by rolling up a graphite sheet. Typically they are ~ 1 nm in diameter but several micrometers in length. As a result end effects can be neglected and they can be considered to be of infinite length. The seamless cylindrical shape results in no 'dangling bonds', unlike at the edges of graphite sheets. This is the key to the formation of nanotubes, and will be discussed in more detail in Chapter 2. It is also key to the inert nature of SWNTs, they do not oxidise easily, are stable in most environments, and are resistant to most processing procedures making them easy to work with. In essence a SWNT has no edges, there are no 'bulk' and 'surface' properties of individual SWNTs as they are composed solely of surface atoms.

A single sheet of graphite is composed of a hexagonal, honeycomb like, lattice. Three dimensional graphite consists of layers of these sheets. The interaction between adjacent layers is relatively weak. The interlayer separation is 3.35 Å, substantially more than the inter atom separation within the layer, $a_{c-c} = 1.42$ Å. The hexagonal lattice is composed of a trigonal lattice with a two atom basis. Figure 1.4 shows the two inequivalent atoms, and the lattice vectors $\mathbf{a}_1$, green, and $\mathbf{a}_2$, red. We also define $a = |\mathbf{a}_1| = |\mathbf{a}_2| = \sqrt{3}a_{c-c} = 2.46$ Å, the lattice constant of graphite.

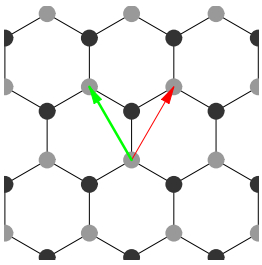

Figure 1.4: Lattice structure of graphite sheet

The graphite sheet can be rolled up in an infinite number of ways, forming an infinite number of different nanotubes. Each nanotube can be uniquely defined by its roll-up vector, $\mathbf{C}_h$. The roll-up vector connects two atoms on the graphite sheet which, once rolled up to form a nanotube, are mapped onto each other. Any atom

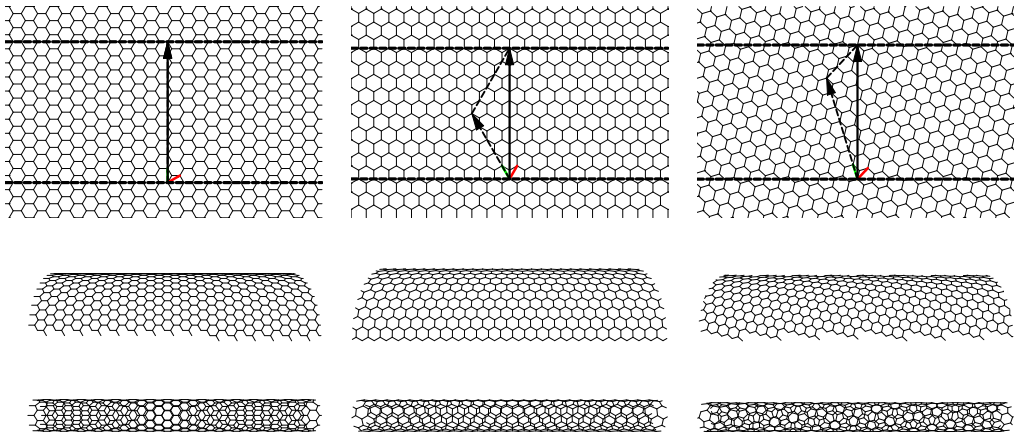

(a) (10,0) (b) (5,5) (c) (7,3)

Figure 1.5: Schematic of the formation of SWNTs by rolling a sheet of graphite

on the graphite sheet can be mapped onto another equivalent atom by an integral number of lattice vectors, so we can write

$$\mathbf{C}_h = n\mathbf{a}_1 + m\mathbf{a}_2 \tag{1.1}$$

for integer n, m. Thus every nanotube can be specified uniquely by the indices (n, m). Figure 1.5 shows the formation of nanotubes with indices (10,0), (5,5) and (7,3).

A nanotube is said to be chiral if its mirror image is different from itself. From Figure 1.5 it is clear that both (10,0) and (5,5) are achiral, whilst (7,3) is chiral. In general there are only two classes of nanotube which are achiral: 'armchair' nanotubes of the form (n,n), and 'zigzag' nanotubes of the form (n,0). They are named after the shape of their cross sectional rings. The chiral angle of a nanotube is defined as the angle between $\mathbf{C}_h$ and $\mathbf{a}_1$, and ranges between 0 for zigzag nanotubes to $\pi/6$ for armchair nanotubes. For a given nanotube of indices (n, m) the chiral angle θ is determined by

$$\cos\theta = \frac{\mathbf{C}_h.\mathbf{a}_1}{|\mathbf{C}_h||\mathbf{a}_1|} = \frac{2n+m}{2\sqrt{n^2+m^2+nm}} \tag{1.2}$$

The indices are also sufficient to specify the diameter of the nanotube, since they

determine the length of the wrapping vector which is the circumference of the nanotube. The diameter of the nanotube is given by

$$d_{nt} = \frac{a}{\pi}\sqrt{n^2 + m^2 + nm} \tag{1.3}$$

where, to first approximation, it is sufficient to use the carbon-carbon bond separation from graphite, i.e. as before $a = 2.46$ Å.

(n, m)	diameter (nm)	chiral angle
(10,10)	1.36	$\pi/6$
(15,5)	1.41	0.24
(18,0)	1.41	0
(18,2)	1.49	0.02
(11,11)	1.49	$\pi/6$

Table 1.1: Dependence of chiral angle and diameter on (n, m) indices

The in-plane strength of graphite is well known, and is based on the strength of the delocalised π bonds. Seamless cylinders of graphite are thus very stiff. The Youngs modulus of SWNT has been measured to be $Y_{nt} \approx 1$ TPa [KDE$^+$98], similar to that of a graphite sheet. For comparison, the Young's modulus of steel is about 200 GPa. SWNTs also reversibly buckle rather than break, e.g. [WSL97, FCT$^+$97], when subjected to axial compression, or large lateral forces. These properties make SWNTs very mechanically robust.

The high aspect ratio and small diameter of the SWNT also results in large Van der Waals attractions, both inter-SWNTs, and between a SWNT and a surface. The strength of the Van der Waals attraction increases with diameter [HWA98]. A 1 nm SWNT experiences a binding energy of about 2 eV/nm length on a Si surface. This is a large force and has two corollaries, (i) once adhered to a surface they are difficult to remove, (ii) they will remain in the shape in which they adhere to the substrate. i.e. the adhesion is too strong to allow them to relax to their natural (straight) shape.

The inter-SWNT attraction is similar in magnitude [GHL00] to the SWNT

to surface attraction. The binding energy between two (10,10) SWNTs is about 1 eV/nm. Hence, when SWNT touch each other they tend to 'zip' together maximising their length in contact. In general, SWNT grown away from surfaces tend to stick together forming 'bundles'. Once a bundle exceeds a certain number of SWNTs (~ 1000) it is often referred to as a 'rope', these are usually in effect composed of several bundles. The SWNTs tend to form a hexagonal close packed arrangement, with separations between SWNTs of about 3.2 Å, similar to the interlayer separation of 3.4 Å in graphite [GHL00]. The binding energy per (10,10) SWNT inside a large bundle, or rope, is about 3 eV/nm [GHL00]. As a result it is difficult to separate individual SWNTs from the bundles once they are formed.

Electronic properties of SWNT

We start by considering the band structure of graphite [SDD98]. The carbon atoms in graphite are sp^2 bonded, with the $2p_z$ orbitals forming π bonds delocalised throughout the entire sheet. Electronic conduction properties are determined by the nature of the electronic states near the Fermi energy and so are dominated by the properties of the π bonds.

The hexagonal structure of the graphite lattice results in a hexagonal reciprocal lattice. If the real space lattice vectors are given by

$$\mathbf{a}_1 = a\left(\sqrt{3}/2, 1/2\right), \quad \mathbf{a}_2 = a\left(\sqrt{3}/2, -1/2\right) \tag{1.4}$$

Then the reciprocal lattice vectors are given by

$$\mathbf{b}_1 = \left(\frac{2\pi}{\sqrt{3}a}, \frac{2\pi}{a}\right), \quad \mathbf{b}_2 = \left(\frac{2\pi}{\sqrt{3}a}, -\frac{2\pi}{a}\right) \tag{1.5}$$

and the corners of the hexagonal Brillouin zone

$$\mathbf{K}_i = \frac{4\pi}{3\,a}\left(\sin(i\frac{\pi}{3}), \cos(i\frac{\pi}{3})\right) \qquad \text{for } i = 1 \rightarrow 6 \tag{1.6}$$

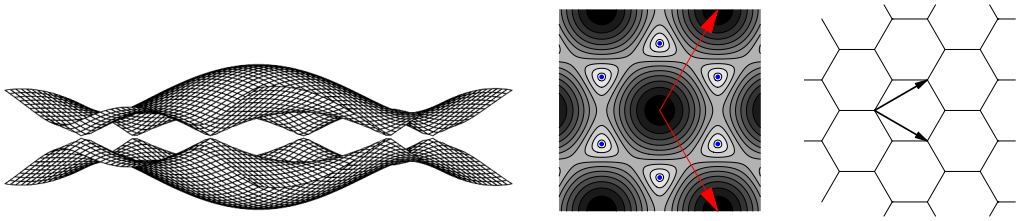

(a) (b) (c)

Figure 1.6: (a) Graphite band structure calculated by the tight binding method. (b) Contour plot of the conduction band and the first Brillouin zone of graphite. The blue circles mark the corners of the Brillouin zone, the '**K**' points. (c) corresponding orientation of the real space lattice.

As in the real space lattice, only two sites are inequivalent, $\mathbf{K}_i$ and $\mathbf{K}_{i+1}$, the others are related to them by reciprocal lattice vectors. A simple tight-binding calculation results in the following dispersion relation for graphite [SDD98]

$$E_{graph}(k_x, k_y) = \pm t \left[1 + 4\cos\left(\frac{\sqrt{3}k_x a}{2}\right)\cos\left(\frac{k_y a}{2}\right) + 4\cos^2\left(\frac{k_y a}{2}\right)\right]^2 \qquad (1.7)$$

where t is the overlap integral. t is often denoted instead by γ_0. Scanning Tunnelling Microscopy (STM) and Scanning Tunnelling Spectroscopy (STS) studies have found $\gamma_0 = 2.5 - 2.7$ eV, e.g. [HL02] and references therein, in comparison with 2.5 eV for graphite. Optical measurements infer a value of $\gamma_0 \approx 2.9$ eV, e.g. [JHaMH$^+$01].

A 3D plot of the band structure is given in Figure 1.6. The bonding (valence) π band and antibonding (conduction) π^* band meet at the corners of the Brillouin zone. Figure 1.6 (b) shows a contour plot of the conduction band on the k_x, k_y plane, and clearly demonstrates that the bands meet at the corners of the Brillouin zone, K_i marked by blue disks. This demonstrates the well known 'semi-metallic' conduction properties of graphite. In most lattice directions graphite acts as a semiconductor, however along the directions of the corners of the Brillouin zone it is metallic with a finite, though small, density of states at the Fermi level.

The band structure of SWNT can be calculated at first approximation, ignoring the effect of curvature, from the graphite band structure. The periodic boundary

conditions enforced by rolling graphite into a cylinder results in a new quantisation condition; there must be an integral number of wavelengths around the nanotube. This condition can be written as

$$\mathbf{C}_h \,.\, \mathbf{k} = 2\pi q \qquad \textit{for integer } q \tag{1.8}$$

The band structure of each nanotube consists of the line-sections of the graphite band structure which obey this condition. Assuming the nanotube to be of infinite length there are no quantization conditions on the wave vector parallel to the direction of the nanotube, k.

To demonstrate this procedure we first consider the simple case of an armchair nanotube, (n, n). Eq. 1.8 gives the quantisation condition $n\sqrt{3}k_x a = 2\pi q$, since k_x is in the circumferential direction for an armchair SWNT. Substituting this back into the graphite band structure, Eq. 1.7, we find the band structure for an armchair SWNT

$$E_{arm}(k) = \pm t \left[1 + 4\cos\left(\frac{\pi q}{n}\right)\cos\left(\frac{ka}{2}\right) + 4\cos^2\left(\frac{ka}{2}\right)\right]^2 \tag{1.9}$$

Similarly, we calculate the bandstructure for a zigzag SWNT, $(n, 0)$, from the relevant quantisation condition, $nk_y a = 2\pi q$.

$$E_{zig}(k) = \pm t \left[1 + 4\cos\left(\frac{\sqrt{3}ka}{2}\right)\cos\left(\frac{q\pi}{n}\right) + 4\cos^2\left(\frac{q\pi}{n}\right)\right]^2 \tag{1.10}$$

The results of this procedure are shown in Figure 1.7 for an armchair and three zigzag nanotubes. Both the armchair and the (9,0) zigzag nanotubes have bands that meet, i.e. a quantised line-section (marked in red on the figure) passes through a corner of the Brillouin zone (marked in blue). For these there is a finite density of states at the Fermi level, and hence they are metallic (mSWNT). The (10,0) and the (8,0) zizag SWNTs have no density of states at the Fermi level, no quantised line-section passes through the corners of the Brillouin zone. There is

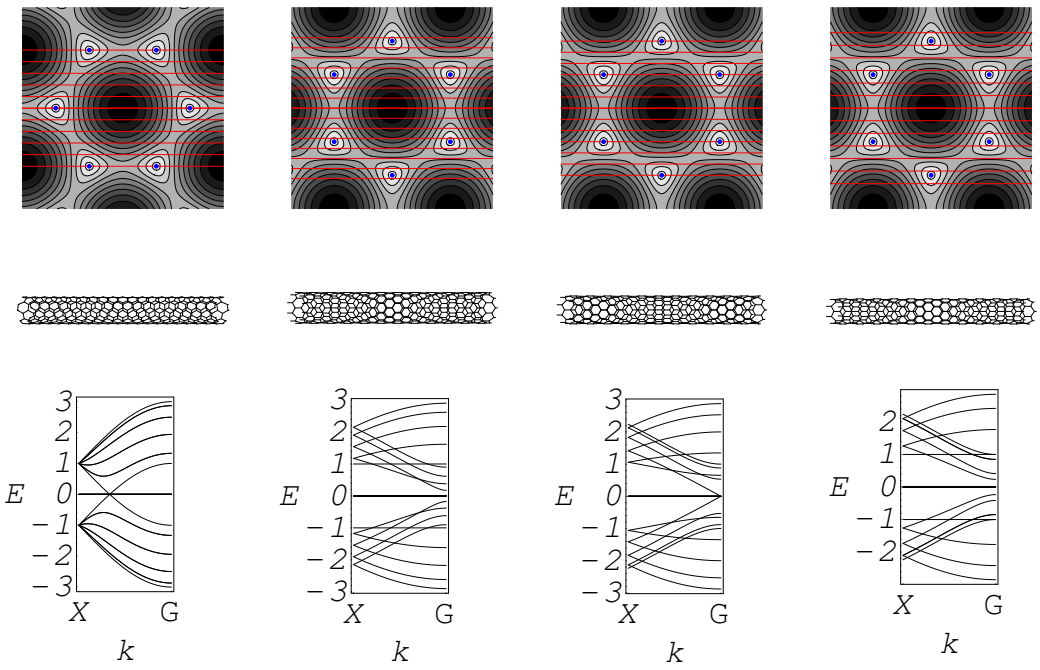

(a) (5,5) (b) (10,0) (c) (9,0) (d) (8,0)

Figure 1.7: *Upper row:* Contour plot of the conduction band of graphite with the **K** points marked in blue. The lines correspond to the relevant quantisation conditions for the SWNTs show schematically in the *middle row*. *Lower row:* the band structure of the SWNTs, k is along the axis and E is in units of γ_0.

an energy gap between the occupied and unoccupied states, hence these are semiconducting (sSWNT).

For a SWNT to be metallic a quantised line-section must pass through a corner of the Brillouin zone. Using Eq.'s 1.1, 1.4 and 1.6, we find

$$\mathbf{C}_h \,.\, \mathbf{K}_0 = \frac{2\pi}{3}(n-m) \qquad \mathbf{C}_h \,.\, \mathbf{K}_1 = \frac{2\pi}{3}(2n+m) \tag{1.11}$$

For the line section to pass through the corner of the Brillouin zone $\mathbf{K}_i$ must be an allowed vector by the quantisation condition Eq. 1.8, hence

$$\frac{(n-m)}{3} = \text{integer} \qquad \text{or} \qquad \frac{(2n+m)}{3} = \text{integer} \tag{1.12}$$

In fact these conditions are equivalent, if a linesection passes through one set of corners of the Brillouin zone, a line-section will also pass through the others. Defining

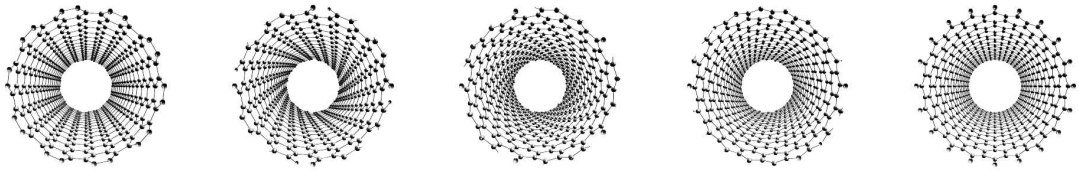

(a) (10,10) (b) (12,8) (c) (15,5) (d) (18,2) (e) (20,0)

(n,m)	type	diameter (nm)	chiral angle	band gap (eV)
(10,10)	mSWNT	1.36	30°	NA
(12,8)	sSWNT	1.37	23°	0.49
(15,5)	sSWNT	1.41	14°	0.47
(18,2)	mSWNT	1.49	5.2°	NA
(20,0)	sSWNT	1.57	0°	0.42

Figure 1.8: (a)-(e) End on schematics of a selection of SWNTs with diameters around 1.4 nm. The table shows the corresponding electrical properties, diameters, chiral angles and band gaps of the SWNTs depicted in (a)-(e). $\gamma_0 = 2.7$ eV was used to calculate the band gap.

$p = mod_3(n-m)$, (i.e $p = -1, 0, 1$), we see that $p = 0$ corresponds to a mSWNT, whilst $p = \pm 1$ are sSWNT. The conduction properties of SWNT are not a simple function of their diameter or chiral angle. Referring back to Table 1.1, the diameter of an (18,0) zigzag mSWNT is 1.41 nm, the sSWNT (15,5) has the same diameter to < 1 %. In this tight-binding model the size of the gap in the density of states for sSWNT is given by [SDD98]

$$E_g = \frac{|t| a_{c-c}}{d_t} \tag{1.13}$$

which is independent of the chirality and only depends on (n,m) through the diameter of the nanotube. More advanced calculations show a small dependence on p, and the response of $p = +1$ sSWNT to, for example, pressure is different to those with $p = -1$, e.g. [LY04].

Figure 1.8 shows a selection of SWNT, specifying their diameter, chiral angle, conduction properties, and for the sSWNT their band gaps calculated from Eq. 1.13. There are no obvious symmetries in their physical structure to differentiate between

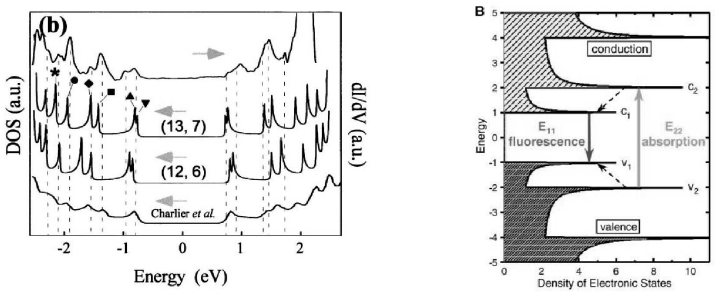

Figure 1.9: left: *Comparison of the DOS obtained from experiment (upper curve) and a π-only tight-binding calculation for the (13, 7) SWNT (second curve from top). The broken vertical lines indicate the positions of VHS in the tunneling spectra after consideration of thermal broadening convolution. The symbols correspond to the VHS shown in (a). The calculated DOS for a (12, 6) tube and an independent calculation for a (13, 7) tube are included for comparison.* Taken from [KOHL99]. right: *Schematic density of electronic states for a single nanotube structure. Solid arrows depict the optical excitation and emission transitions of interest; dashed arrows denote nonradiative relaxation of the electron (in the conduction band) and hole (in the valence band) before emission.* Taken from [BSK$^+$02]

the mSWNTs and sSWNTs. [1]

The accuracy of these tight binding calculations, and in particular the observed dependence of electronic properties on (n, m), was first probed using STM, and STS [WVR$^+$98, OHKL98]. STM and STS probe the density of electronic states (DOS). STM was used to image individual SWNT at atomic resolution, and hence assign (n, m) values to the SWNT. STS was then used to find the DOS as a function of energy. They were able to directly test the accuracy of the tight binding model, and verify that $p = 0$ SWNT were metallic with a finite DOS at the fermi level whilst $p = \pm 1$ were semiconductors with an energy gap consistent with Eq. 1.13. The DOS also matched well to the predictions from the tightbinding calculations.

A generic feature of the DOS in 1D systems is the presence of 'Van Hove Singularities'[2] , see e.g. [AM76], divergences in the DOS at band edges. These

[1] except the armchair nanotube where the symmetry between the two atoms forming the basis of the graphite sheet imply that it will be metallic.

[2] There is a simple explanation for their occurrence: for a free electron gas $E \propto k^2$, quantisation implies that the total number of states is $N \propto k^d \propto E^{d/2}$, and thus the density of states is $dN/dE \propto E^{d/2-1}$. Hence in 1D, i.e. $d = 1$, the density of states diverges at $E = 0$ which

are predicted by the tight bonding model and were observed by various authors in STS measurements, e.g. [WVR+98, KOHL99, OHCL01]. The large localised increase in DOS gives rise to many remarkable optical properties including enhanced flourescence [OBH+02], band-gap photoluminescence [LHF03], and resonant Raman scattering (discussed in more detail in Chapter 2). Optical experiments have also proved an effective way of probing the electronic properties of SWNT. A simple prediction of the tightbinding model is that for large diameter SWNT, where the curvature effects become unimportant, the ratio of the spacings between the first and second Van Hove singularities should be 2. Optical experiments suggest instead a ratio of 1.75. Theoretical work has shown that this 'ratio problem' can be explained by the inclusion of electron interaction effects, and used as a way of probing the strength of electron-electron interactions in SWNTs [KM03].

The effect of curvature on the band structure of SWNT can be included analytically within the tightbinding model, e.g. [KM97, KE01, DDC02]. For chiral mSWNT the curvature breaks the symmetry of the $\mathbf{K}_i$ points introducing a 'minigap', ~ 40 meV for 1 nm diameter mSWNT, to the DOS. Detailed STM and STS experiments confirmed the presence of a minigap in chiral mSWNT, but found none, as predicted, in armchair mSWNT where the symmetry is not broken [OHCL01]. However, a local strain on a mSWNT also breaks the symmetry and causes an additional energy gap, e.g. [YH00, MSA02, CBC02, FYMK03, GZB03]. In particular, a torsional strain breaks the symmetry of an armchair SWNT creating a minigap. The effect on the band gap of sSWNT is similar, and depends on p. For $p = +1$ a uniaxial tension increases the band gap, whilst for $p = -1$ the band gap is decreased.

As previously commented, a large Van der Waals attraction is felt between SWNTs in bundles, as well as by individual SWNT lying on a substrate. As a result a SWNT lying on a surface is unable to relax to its native (straight) configuration,

corresponds to the band edge.

and will instead experience a series of different local curvatures along its length which locally perturb the band structure. In addition, local charges on the surface also perturb the electronic states of the SWNT, as do adsorbed gas molecules. These local perturbations act as weak scatterers, which would be expected to cause electronic transport through even mSWNT to be diffusive in nature as the electrons repeatedly scatter from the local scattering sites, or 'defects'. However, experimentally it is found that mSWNT conduct ballistically over micrometre length scales even at room temperature [dPGNM$^+$02, PRY$^+$04, JGP$^+$04][3]. This is a direct result of the one dimensional (1D) nature of the electron dispersion within the SWNT. In 2D or 3D conduction electrons (at the Fermi energy, E_F) can be weakly scattered with small changes in momentum and direction. However, in a SWNT the electrons have a well defined momentum along the SWNT axis, and a quantised momentum circumferentially around the diameter of the SWNT. A scattering event requires a large change in momentum, hence they are resistive to back scattering. In addition, since the wavefunction is extended around the full circumference of the SWNT, localised disorder on length scales less than the diameter of the SWNT will be correspondingly suppressed. Finally, for metallic SWNT the orthogonality between the bonding and anti-bonding states which meet at the Fermi level reduces the allowed scattering events even further [MBC$^+$99]. In sSWNT the band gap removes the orthogonality of the states, resulting in increased sensitivity to disorder.

Numerous electrical transport studies have been made on bundles of SWNT, and individual SWNTs, by attaching macroscopic electrodes directly to them. An introduction to these is given in Chapter 2, where the practical issues involved in making and measuring SWNT devices are also discussed along with results from SWNT devices fabricated as part of this thesis. Preempting these results we can summarise the generic electrical transport behaviour of individual SWNT. Devices

[3]This will also be demonstrated by the results presented in Chapters 3 and 4

fabricated from individual SWNT can be loosely split into three groups: (i) field effect transistors which turn from a low conduction to high conduction regime as they are electrostatically doped, these are the most common; (ii) devices whose (high) conductivity shows only a weak dependence on electrostatic doping; (iii) devices with (high) conductivity independent of electrostatic doping, these are very rare. In light of the discussions above we can tentatively ascribe this behaviour to the presence of (i) sSWNTs, (ii) small gap mSWNTs, (iii) armchair SWNTs.

Why study SWNT devices: the Physics and the Funding

There has been considerable interest in the practical applications of SWNT devices. Single molecule field effect transistors with hole mobilities of > 75000 cm^2/Vs have been formed, orders of magnitude higher than the best Si devices (e.g. [DGCF04] and references therein). Their combination to form logic devices has been demonstrated, e.g. [JSD02]. In addition, by changing the doping levels along the length of a sSWNT, n-type and p-type regions have been formed in the same nanotube enabling the fabrication of an intermolecular complementary NOR gate, e.g. [KCDA02]. mSWNT are capable of carrying current densities in excess of 10^9 A cm^{-2} [YKD00], and do not fail over time, prompting proposals for their use as interconnects in ultra-small electronic devices. Perhaps more realistically in the short term are possible sensor applications, e.g. [KFZ$^+$00, LLY$^+$03, BLW$^+$03, QVG$^+$03, CMGR03, LLTR04]. The high sensitivity of sSWNT to their environment, combined with their small diameter (roughly the same as a single strand of DNA), has enabled sensor applications as diverse as nerve agent detection [NSH$^+$03], alcohol vapour sensors [SSK$^+$03], and specific protein sensors [SGBG03, BBSG04, CCB$^+$04] to be demonstrated. Recently, their electrical and optical properties have been capitalised upon in the demonstration of electrically induced light emission from a sSWNT device [MMA$^+$03]. The light emitted is due to recombination of holes from the conduction

band and electrons from the valence band and so has a frequency inversely proportional to the SWNT diameter, Eq. 1.13. In addition, their electromechanical properties have led to proposed applications from actuators to strain gauges, e.g. [GG03, FYMK03].

The fundamental stumbling block to the realisation of these applications has been the inability to selectively produce sSWNTs (or mSWNTs) with predetermined positions and orientations. Recently substantial progress has been made towards these goals. Procedures for separating sSWNT from mSWNT once suspended in aqueous solution have been developed separately by three different groups in the last year [KHvK03, SDU$^+$03, ZJS$^+$03]. Selective placement of SWNT from the liquid phase has also been demonstrated using surface chemical modification [RHSH03], and DNA templating [KBB$^+$03]. In addition, growth from predefined catalyst sites has been demonstrated previously, e.g. [FLC$^+$01], whilst recently direction of growth from those sites has been controlled using electric fields [ZCC$^+$01, JL02]. Recently, it has also been shown that plasma enhanced growth results in a high (90%) proportion of sSWNT, suggesting that selective growth of mSWNT or sSWNT may be possible [LMR$^+$04]. An additional breakthrough has been the growth of individual SWNTs several hundred micrometres long [KCL$^+$02, DGCF04, HCL03], which would facilitate large numbers of devices to be fabricated from the same SWNT, and hence with the same properties.

The interest in SWNT devices for the study of 1D physics has also been substantial, in particular with mSWNT devices. There have been numerous studies on Coulomb blockade in mSWNT devices, e.g. [CBM$^+$98, CN02, LBP02]. Due to the 1D nature of conduction in SWNT the level spacing (Δ) caused by finite length effects is relatively large and inversely proportional to the length of the SWNT quantum dot, $\Delta \approx 850$ meV nm$^-$1. This is comparable to the charging energy (U) in standard device geometries, for example in [LBP02] $U/\Delta = 0.26$. The relative

contributions of the level spacings and charging energy are in marked contrast to 2D quantum dots where for example in [PCS+98] a quantum dot of area 0.2 μm^2 was used, with a resultant energy level spacing of $\Delta = 18$ μeV, and charging energy $U = 760$ μeV, i.e. $U/\Delta = 0.02$. As a result the effect of level spacing variations, and exchange interactions, are more easily studied in mSWNT devices. Improvements in the electrical contacts to mSWNT resulted first in the observation of the Kondo effect, where a novel high magnetic field effect was observed [NCL00], and then to novel interference patterns in the transport behaviour due to resonant transport through the devices [LBB+01]. Finally, there has been much interest in probing the elusive Luttinger liquid behaviour of the 1D electron gas in SWNT, e.g. [BCL+99, IKS+03].

Despite all this progress, there are still active debates over fundamental issues concerning transport properties of SWNT devices. Some of these will be addressed in Chapters 2 and 3.

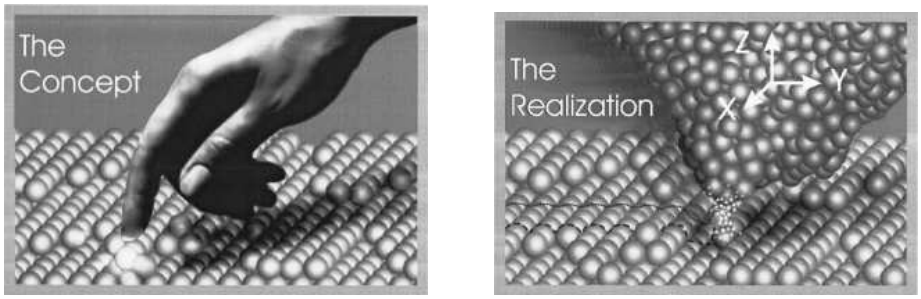

Figure 1.10: *Principle of a local probe: The gentle touch of a nanofinger. If the interaction between tip and sample decays sufficiently rapidly on the atomic scale, only the two atoms that are closest to each other are able to feel each other.* Taken from [BR99].

1.2 Introduction to Atomic Force Microscopy

The invention of the STM by Binnig and Rohrer heralded the start of a new field of microscopy, now called scanning probe microscopy (SPM). The techniques encompassed by this broad title share a common measurement theme; a fast decaying local signal (such as the tunneling current in STM) is experienced by a sharp tip as it is scanned across a surface. This is schematically represented in Figure 1.10. The initial discovery of STM[4] was followed shortly after by the invention of the atomic force microscope (AFM), by Binnig et al. [BQG86], in which the local signal is no longer a tunnelling current, but instead a force between tip and sample. This enabled investigation of insulators as well as conductors. Initially the focus was on achieving atomic resolution, requiring careful sample preparation and either UHV or liquid environments.

Currently thousands of AFMs are in use in university and industrial research laboratories, the majority are used for imaging samples where the length scales of interest are from 1 nm - 100 μm, and little or no surface preparation is required. Surface properties are also studied, complementarily to the surface topography. Tech-

[4] an excellent review of the discovery and principles of STM is given in Binnig and Rohrer's Nobel Prize speech [BR87]

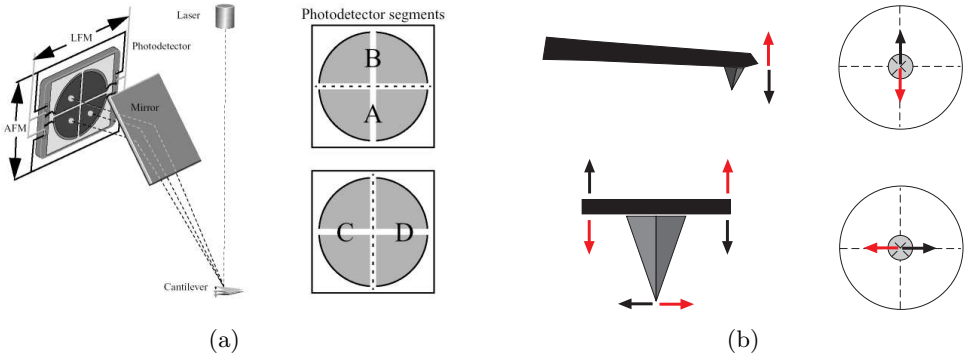

Figure 1.11: (a) Schematic of the optical detection of cantilever deflection. Taken from [Vee]. (b) Schematic of the effect of vertical and torsional deflections of the cantilever on the position of the laser spot on the photodetector.

niques such as lateral force microscopy (LFM), which gives a measure of surface adhesion, and magnetic force microscopy (MFM), which probes the local magnetic properties of a surface, are routinely used. The work presented here focuses on atomic force microscopy, and in particular the variants based on electrostatic forces which generically come under the name electric force microscopy, or EFM. The remainder of this introduction will concentrate on the basics of topographic imaging, and EFM.

Fundamental to the design and use of AFMs is the transduction of the force felt by the tip into a measurable quantity. The technique employed by the AFMs used for this work is very simple. The sharp probe is mounted at the end of a soft cantilever, hence any forces experienced by the tip result in a deflection of the cantilever from its equilibrium position. A laser beam is shone onto the back of the cantilever, and its reflection is directed onto a photodetector, as illustrated schematically in Figure 1.11 (a). When the cantilever is deflected the laser beam reflects at a different angle, hence striking the photodetector at a different position. The photodetector is split into quarters, as shown in Figure 1.11 (a). If the cantilever deflects up, the laser spot moves vertically on the photodetector, causing a difference

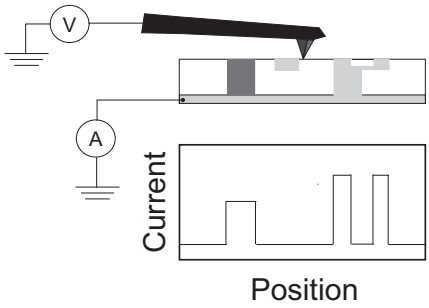

Figure 1.12: Schematic of c-AFM. White corresponds to insulating regions, light grey to high conduction, and dark grey to low conduction regions. A current is only recorded if there is a path through to the drain electrode, here shown on the back of the sample.

in light intensity between the top half, labelled A in Figure 1.11, and the lower half, labelled B. Twists in the cantilever result in a horizontal displacement of the laser spot, and similarly a difference between the intensity on C and D. Using this technique changes in the vertical, z, position of the tip can be measured with sub Å precision.

The simplest manifestation of AFM involves the tip being raster scanned over a sample surface whilst a feedback loop maintains a constant cantilever deflection, and hence a constant tip-sample force. This is called contact mode imaging. Simultaneous measurement of the torsional deflection of the cantilever gives a measure of the lateral force on the tip, called lateral force microscopy or LFM. The lateral force is related to the frictional force on the tip and depends not only on sample topography, but also on surface properties such as inhomogeneous adhesive forces.

The use of an electrically conductive tip enables simultaneous probing of the sample's electrical properties. As schematically illustrated in Figure 1.12, a potential difference is applied between the tip and surface and the current flow through the sample is recorded[5]. The recorded current will depend on the local conductivity, and whether there is a conduction path to the drain electrode. This technique is

[5]using electrodes placed on the sample surface lateral transport can be probed instead

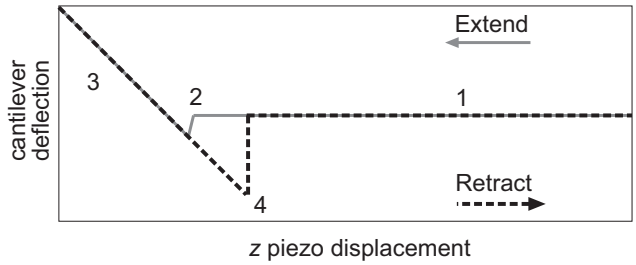

Figure 1.13: Schematic of a force curve in contact mode.

known as conducting AFM, or c-AFM.

The force as a function of vertical displacement can also be measured, commonly referred to as a force curve. This is achieved by turning off the feedback loop and ramping the z displacement in a linear fashion, so the tip approaches the sample at a constant rate, and then retracts away. Figure 1.13 illustrates the generic regimes in the force curve. In the absence of long range forces, such as electrostatic or magnetic forces, the cantilever deflection will be constant at its equilibrium value as the tip approaches the surface, 1. At a small distance away from the surface the Van der Waals attraction will overcome the stiffness of the cantilever and the tip will snap into contact with the surface, 2. Once in contact with the surface the deflection of the cantilever will linearly increase as the tip is pushed against the surface[6], 3. As the cantilever is retracted away from the surface the cantilever deflection decreases linearly, and continues to do so past the point of jump to contact on the approach. Eventually the adhesive force between the tip and sample is overcome by the deflection of the cantilever, which now corresponds to the cantilever pulling the tip off the surface, 4. Once removed from the surface the cantilever returns to its equilibrium position, 1. The linear relation during 3 between the deflection of the cantilever and the z displacement can be used to calibrate the sensitivity of the photodetector to deflection of the cantilever. For example, if an increase in z displacement of 100 nm resulted in a change in photodetector signal of 2 V, then the deflection sensitivity

[6]assuming the surface is much stiffer than the cantilever

would be 50 nm V^{-1}. As in the imaging mode, it is also possible to record the current flowing, enabling the acquisition of simultaneous force-distance ($f-d$) and current-distance ($i-d$) plots.

A significant drawback of contact mode AFM is the large tip-sample contact force which tends to deform soft samples. It also results in large lateral forces on the sample and tip. To overcome these problems dynamic or 'tapping' mode AFM is used. [7]

Dynamic or 'Tapping' mode AFM

In tapping mode AFM an oscillating cantilever is brought towards a surface until the tip starts to come into intermittent contact with the surface. This damps the oscillation from the free value, A_0, to a lower amplitude, A, as illustrated in Figure 1.14. The oscillation of the cantilever produces an oscillatory signal from the photodetector which is used to monitor the amplitude of oscillation. The tip is scanned across the sample whilst a feedback loop maintains a constant amplitude of oscillation, $A < A_0$, known as the 'setpoint' amplitude. Since the tip is only in intermittent contact with the surface the lateral forces are greatly reduced, as is the average tip sample force. Typical amplitudes of oscillation range from $10-50$ nm depending on the type of cantilever used, as discussed later. In almost all the work presented here 'light' tapping was employed, typically $A/A_0 \gtrsim 0.9$.

Since this technique is the predominant imaging mode used here, we discuss the idealised mechanics of cantilever oscillation in more detail.

In air most of the damping on the cantilever is due to viscous drag. This is a damping force linear in velocity, hence the equation of motion describing the motion

[7] noncontact AFM also involves much reduced forces compared to contact mode, however it was not used for any of the work presented in this thesis and so will not be discussed. Tip-sample forces in contact mode can be reduced by imaging under solution, however this technique was also not used and so is not discussed. All experiments presented in this thesis were performed under ambient conditions.

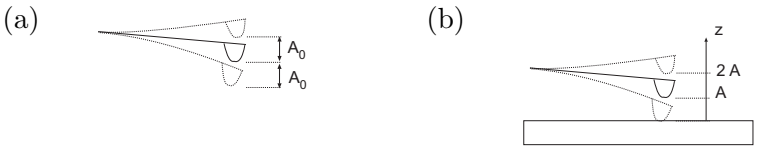

Figure 1.14: Schematic of (a) free oscillation, and (b) intermittent contact

of the cantilever is that of a generic sinusoidally driven, linearly damped, harmonic oscillator

$$\ddot{z} + 2\gamma\dot{z} + \sqrt{\frac{k}{m}}x^2 = A_{drive}e^{i\omega t} \tag{1.14}$$

where ω is the driving frequency, and the natural frequency of the cantilever is given by

$$\omega_0 = \sqrt{\frac{k}{m}} \tag{1.15}$$

The 'decay constant' γ is related to the viscous drag coefficient b and 'quality factor', Q, of the cantilever by

$$\gamma = \frac{b}{2m^*} = \frac{\omega_0}{2Q} \tag{1.16}$$

where m^* is the effective mass of the cantilever. The general solution to equation 1.14 is

$$z(t) = \alpha\ e^{-\gamma t}\ e^{i(\omega' t+\theta)} + A_{cant}e^{i(\omega t+\psi)} \tag{1.17}$$

where α and θ are constants of integration determined by the initial conditions of the oscillator, and $\omega' = \sqrt{{\omega_0}^2 - \gamma^2}$. The first term is the transient behavior. For a cantilever with resonance frequency of order 100 kHz, and Q factor of order 100, the transient will decay with a time constant of $\tau \sim 1$ ms, inversely proportional to Q. The response of the cantilever oscillation (excluding hard surface effects) is temporally limited by this effect, so that reasonable scanning rates are ~ 1 Hz. The change in resonance frequency is much quicker, ω' and ψ in the second term of Eqn. 1.17 will adjust over a few cycles, i.e. with a time constant independent of Q. The

second term in Eqn. 1.17 is the steady state solution. For large t

$$\begin{aligned} z(t) &= A_{cant} e^{i(\omega t+\psi)} \\ A_{cant}(\omega) &= \frac{A_{drive}}{\sqrt{(1-(\omega/\omega_0)^2)^2+\omega^2/(\omega_0 Q)^2}} \\ \psi &= \arctan\left(\frac{\omega}{Q\omega_0(1-\omega^2/\omega_0^2)}\right) \end{aligned} \tag{1.18}$$

For a cantilever with a large Q there is a distinct peak in the amplitude response, in fact there is a peak if $Q \geq 1/\sqrt{2}$. The frequency at which this peak occurs is

$$\omega_{peak} = \omega_0\sqrt{1-1/2Q^2} \tag{1.19}$$

for a cantilever with $Q \sim 200$ this corresponds to a fractional decrease in resonance frequency of 10^{-5}. Usually when discussing the resonance frequency we are implicitly using the resonance frequency in air, although this shows that the difference between the undamped, 'true', natural resonance and the damped resonance is small. The peak amplitude on resonance is

$$A_{cant}(\omega_{peak}) = A_{drive}\frac{Q}{\sqrt{1-1/4Q^2}} \tag{1.20}$$

Clearly for a reasonable value of Q this implies that $A_{cant}(\omega_{peak}) = A_{drive}Q$, so that the higher the Q the lower the driving force required. The phase lag between the cantilever response and the driving force is $\pi/2$ when driven at resonance. Far below resonance the phase lag $\psi = 0$, and far above $\psi = \pi$. The transition between the two becomes more rapid as Q is increased. Considering small frequency shifts $\Delta\omega$ about the resonance frequency, we define $\phi = \psi - \pi/2$ such that

$$\phi(\Delta\omega) = \arctan\left(\frac{Q\omega_0(1-(\omega_0+\Delta\omega)^2/\omega_0^2)}{\omega_0+\Delta\omega}\right)$$

Expanding to first order in $\Delta\omega/\omega_0$, and using the expansion $\arctan x = x - x^3/3 + ...$, we find

$$\begin{aligned} \phi(\Delta\omega) &= \arctan\left(-2Q\Delta\omega/\omega_0\right) \\ &= -2Q\Delta\omega/\omega_0 \qquad \text{to first order} \end{aligned} \tag{1.21}$$

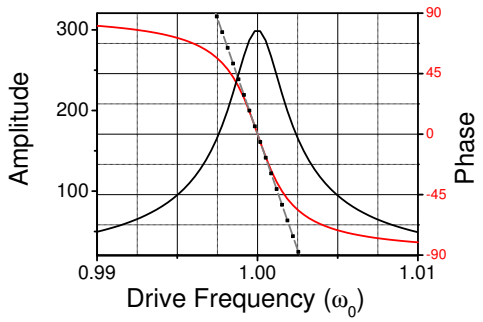

Figure 1.15: Theoretical cantilever amplitude (black) and phase (red) response as a function of driving frequency at constant driving amplitude, plotted from Eqn. 1.18. The straight black line corresponds to the linear approximation to the phase response given by Eqn. 1.21

which will be valid for small ϕ.

In amplitude modulation AFM, the conventional tapping mode procedure, the driving frequency is fixed. The physical property varying during scanning is thus not ω but ω_0, so we can rewrite Eqn. 1.21

$$\Delta\phi(\Delta\omega_0) = 2Q\Delta\omega_0/\omega_0 \tag{1.22}$$

assuming that $\Delta\omega_0 \ll \omega_0$.

Figure 1.15 shows the cantilever amplitude and phase response as the driving frequency is varied, at constant drive amplitude, according to Eqn. 1.18. Note that the phase response here is not the phase lag (ψ) between the cantilever oscillation and driving force directly, but $\phi = \psi - \pi/2$. The straight line also plotted is the linear approximation given by Eqn. 1.21. The approximation is good for $|\phi| \lesssim 40°$. Figure 1.16 shows a typical experimental cantilever response. The experimental amplitude response, the black line, was fitted to Eqn. 1.18, giving $Q \approx 500$ and $\nu_0 \approx 296$ kHz, the red line. These values were then used to generate the phase response, the red line, which correlates well with the experimental data, the black line. Also shown is the straight line approximation predicted by Eqn. 1.21. The

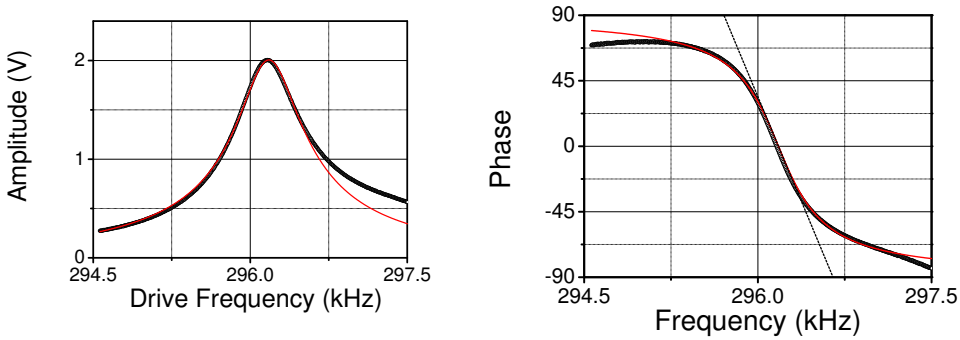

Figure 1.16: Experimental tuning curves (black circles) of *left* amplitude, and *right* phase, response of a TESP tip. The red lines show the *left* theoretical fit to the amplitude response, and *right* resultant predicted phase response, also plotted is the straight line approximation to the phase response.

small discrepancies between the predicted and experimental curves are due to non-linearities and imperfect physical contact between the piezo driving the cantilever to oscillate and the cantilever. The experimental cantilever response was taken far from the sample surface. As the tip approaches the surface the response will change due to damping effects. The driving frequency is conventionally set so the amplitude is 5% below the peak value (lower frequency) to compensate for this effect and to ensure the cantilever is driven slightly off resonance where the amplitude response is more sensitive.

The dependence of the resonance frequency on applied forces will be discussed in more detail in Chapter 5. At this point we will merely quote the relation derived there that the change in resonance frequency is proportional to the force gradient, or explicitly

$$\Delta\omega = -\frac{\omega}{2k}\frac{\partial f_{ts}}{\partial z} \tag{1.23}$$

where f_{ts} is the force between the tip and the sample. In general the force will decay away from the surface, hence negative changes in phase correspond to negative changes in resonance frequency, positive force gradients, and so attractive forces.

It should be noted at this point that the discussion so far has concentrated

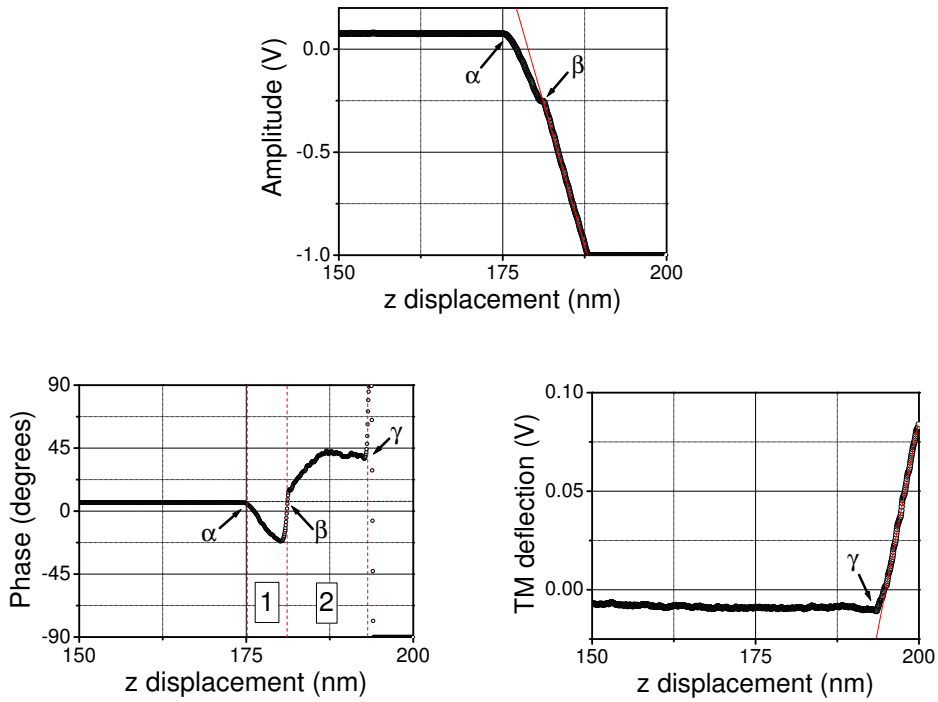

Figure 1.17: Force curves recorded against a solid surface in tapping mode demonstrating typical amplitude, phase, and TM deflection response. The straight line fit on the amplitude response demonstrates an amplitude sensitivity of 12.6 nmV^{-1}, the free oscillation amplitude was $A_0 = 1.62$ V.

on long range forces acting over the amplitude of oscillation which, except for in the initial consideration of damping effects, are conservative forces. Whilst imaging in tapping mode the tip comes into intermittent contact with the surface, this creates a spatially localised dissipative force that will generally dominate the response of the cantilever. In particular, the phase changes observed during imaging can be related to the viscoelasticity of the substrate rather than long range magnetic or electrostatic forces. In order to investigate the longer range forces this topographic contribution must be removed.

Force curves can also be recorded in tapping mode. Figure 1.17 shows a force curve taken against a gold surface. As the oscillating tip is brought down to the surface the amplitude starts to be damped at point α. From the phase response we

see that this corresponds to a net attractive force, the tip surface force is attractive and the tip is not yet striking the surface. At point β the tip starts striking the surface, this is revealed by a discontinuity in the slope of the amplitude, but more strikingly by the phase response which flips from being negative, i.e. an attractive force, to positive, i.e. a repulsive force. In this repulsive regime lowering the tip down, i.e. decreasing z, results in a linearly decreasing amplitude, marked by the red straight line. As with the deflection sensitivity in the contact mode force curve, the slope of this line can be used to calibrate the amplitude sensitivity of the cantilever. In this case we find an amplitude sensitivity of 12.6 nm V^{-1}. The free oscillation amplitude is 1.62 V, which using the amplitude sensitivity can be converted to 20.4 nm. As the tip is lowered further the amplitude is decreased, until at point γ the tip is no longer oscillating. Lowering the tip further still deflects the cantilever, as in the contact mode force curves. Conventionally, imaging in tapping mode is done in the repulsive regime, corresponding to intermittent contact with the sample.

Dynamic lateral force mode or 'Torsional Resonance' mode

Recently another mode of imaging has become widely available, dynamical lateral force microscopy or 'Torsional Resonance' microscopy (TR mode). In TR mode the cantilever is driven into a torsional oscillation so that the end of the tip oscillates parallel to the surface of the sample. The torsional motion of the cantilever produces an oscillatory lateral movement of the laser spot on the photodetector, and a resultant oscillatory output. The amplitude of the oscillation can be used as the feedback signal for topographical imaging of the surface, as in tapping mode. The amplitude of oscillation is in the nanometre range, although it is not entirely clear yet how far the tip is from the surface, i.e. whether it is operating in a contact or non-contact mode. The lateral forces on the tip are, however, much less than in contact mode. In addition, it provides information on forces and force gradients in

plane with the sample, complementary to the information obtainable from tapping mode. The resonance frequencies involved in the torsional resonance are far higher, typically $\sim$ MHz, than in tapping mode whilst the Q factors are only slightly higher. As a result it is capable of imaging at much higher scan rates.

Figure 1.18 shows a set of images of the same sample, although in different areas, taken using tapping mode, contact mode and torsional mode imaging. The sample is pressure densified polycrystalline alumina, thermally etched in air at 1100 °C for 2 hours. It is an extremely hard material ($>$ 20 GPa), and so is not deformed by imaging in contact mode. The different imaging modes give similar height images, although the tapping and TR modes give a 'sharper' image than the contact mode image since the tips are sharper (discussed later). The second image in each series (deflection for contact mode, and amplitude for tapping and TR modes) correspond to the signal going into the feedback loop for the tip height control. These correspond roughly to a derivative of the height image, as long as the tip is tracking the surface well. Although they do not contain quantitative information about relative heights, it is often easier to distinguish features on rough samples in the amplitude/deflection signals.

In the final images of both tapping mode and contact mode there are two clearly different responses on the surface. The sample had become contaminated, which clearly shows up as lighter areas in the tapping mode phase response, and the contact mode lateral response. The TR mode image was taken prior to contamination. The difference in response in the tapping mode phase image is due to the contamination layer being softer than the alumina, and so the energy dissipation being different. In the lateral force the contrast is due to differences in frictional properties between the alumina and contaminant.

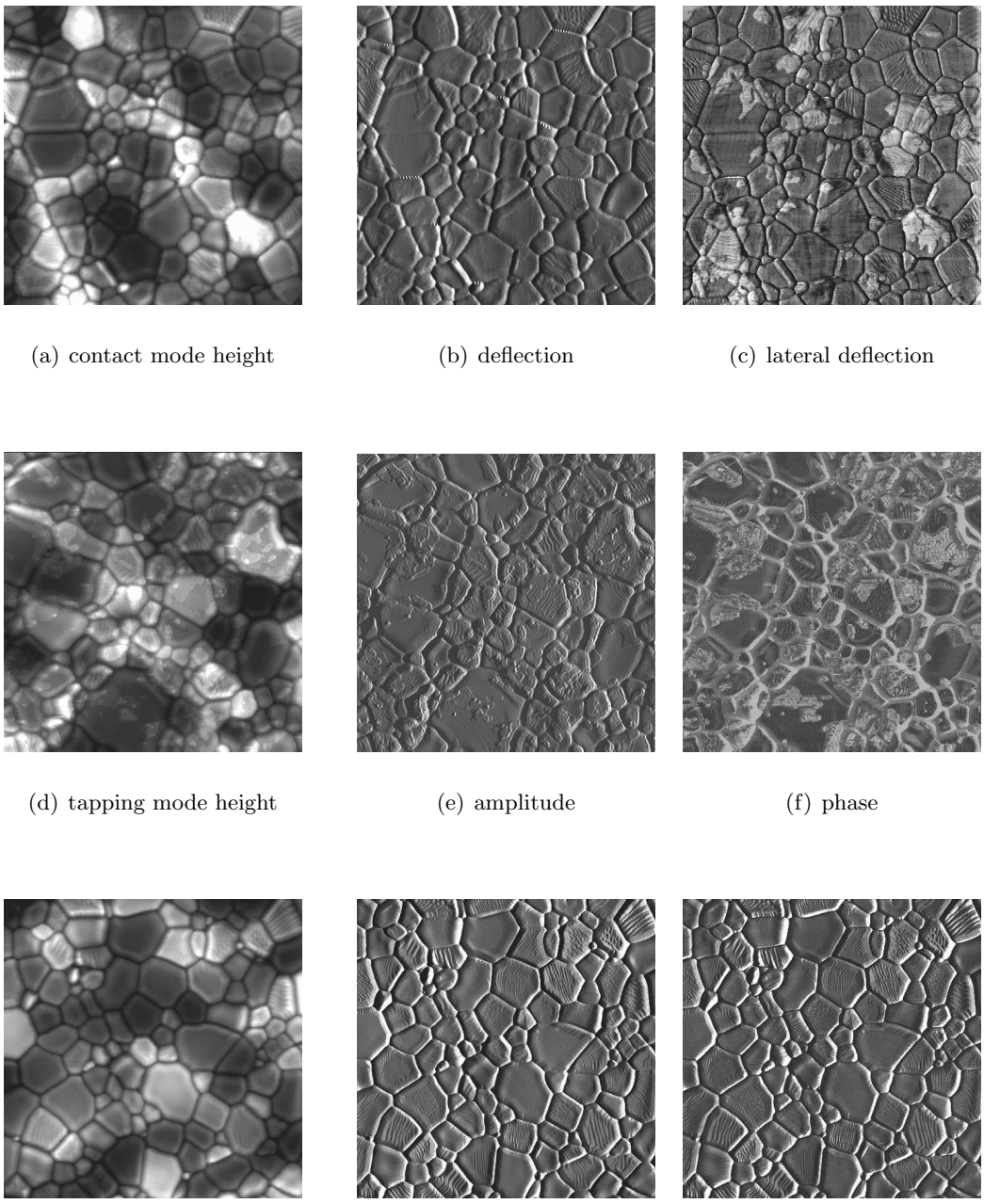

(a) contact mode height (b) deflection (c) lateral deflection

(d) tapping mode height (e) amplitude (f) phase

(g) TR mode height (h) amplitude (i) phase

Figure 1.18: 5 μm scans of pressure densified polycrystalline alumina, thermally etched in air at 1100 °C for 2 hours. 50 nm height scale. Sample courtesy of Geoff West, University of Loughborough.

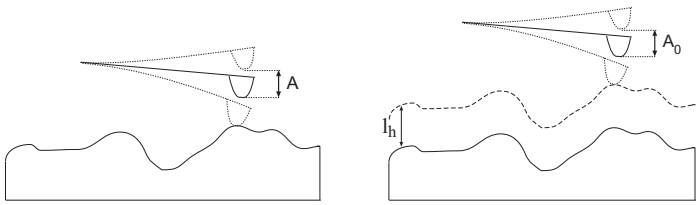

(a) topography linescan (b) 'lift mode'

Figure 1.19: Schematic of a tip operating in lift mode.

Electric Force Microscopy

Electric Force Microscopy, or EFM, is the generic name given to any imaging mode where the dominant force is electric in nature. As was mentioned previously, the dominant forces when imaging in intermittent contact with the surface are generally due to the hard surface repulsion. In order to remove the repulsive contact forces and keep the tip a constant distance away from the surface, i.e. removing topographic effects, 'lift mode' is used, as illustrated in Figure 1.19. First, a topography linescan is taken at constant amplitude $A < A_0$, Figure 1.19 (a). Then, the oscillating tip retraces the same line a constant distance l_h, the lift height, above the surface, Figure 1.19 (b). Thus the topography and EFM linescans are interleaved with one another. There are two important points to note. (i) If the tip did not track the topography well in the topography linescan, then it will not be a constant distance above the surface on the lift scan, producing artefacts in the image. (ii) The actual height of the tip above the surface on the lift scan is not l_h. It is necessary to correct for the oscillation of the tip. If imaging with $A_0 = 50$ nm, $A/A_0 = 0.9$, i.e. $A = 45$ nm[8], and $l_h = 20$ nm, the centre of oscillation of the tip is 65 nm above the surface and the closest point of approach of the tip to the surface is 15 nm.

The energy stored in a capacitor is given by $U = CV^2/2$, where C is the capacitance and V the potential difference. Considering the tip and surface as a

[8]Here using the amplitude appropriate for describing the tip position by $A\cos(\omega t)$

capacitor with capacitance $C_{ts}(z)$ we can write the electrostatic force

$$F_{ts}(z) = -\frac{1}{2}V^2\frac{\partial C_{ts}(z)}{\partial z} = -\frac{1}{2}V^2 C'_{ts}(z) \tag{1.24}$$

where we have assumed that $V \neq V(z)$. The force gradient, $f'_{ts}(z)$ is trivially given by

$$f'_{ts}(z) = -\frac{1}{2}V^2 C''_{ts}(z) \tag{1.25}$$

In dc-EFM the tip is operated in lift mode to remove the short range contact forces, and topographical contributions. A potential difference between the tip and sample results in a force gradient given by Eqn. 1.25, and hence, from Eqn.'s 1.23 and 1.22, a change in phase ($\Delta\phi$). The variation in $\Delta\phi$ is proportional to $C''_{ts}(z)$ as well as V^2.[9] In general V is composed of applied voltages, $V_{dc}^{appl.}$, and contact potential differences[10] (Ψ_{cpd}) between the tip and sample beneath the tip.

$$V_{dc} = V_{dc}^{appl.} + \Psi_{cpd}$$

If an additional ac potential, $V_{ac}(\omega)$, is applied either to the sample, or to the tip, then the total potential difference is given by

$$V = V_{dc} + V_{ac}(\omega) = V_{dc}^{appl.} + \Psi_{cpd} + V_{ac}\cos(\omega t) \tag{1.26}$$

giving a total force, from Eqn. 1.24, of

$$\begin{aligned} F_{ts}(z) =& -\frac{1}{2}V^2 C'_{ts}(z) \\ =& -\frac{1}{2}C'_{ts}(z)\left((V_{dc}^{appl.} + \Psi_{cpd})^2 + \frac{1}{2}V_{ac}^2\right) && (1.27) \\ & -\frac{1}{2}C'_{ts}(z)\left(V_{dc}^{appl.} + \Psi_{cpd}\right)V_{ac}\cos(\omega t) && (1.28) \\ & -\frac{1}{4}C'_{ts}(z)V_{ac}^2\cos(2\omega t) && (1.29) \end{aligned}$$

[9] The phase response is used rather than the amplitude response because it is more sensitive, and reacts faster as discussed earlier.

[10] these are dominated by work function differences, but are also effected by surface contamination layers, see e.g. [CFM+03]

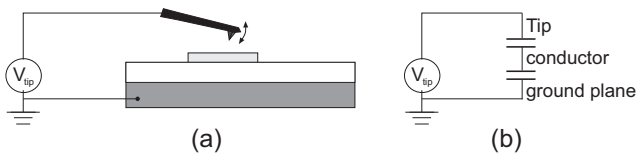

Figure 1.20: Schematic of Scanned Conductance Microscopy.

In Scanning Surface Potential Microscopy (SSPM) the tip is operated in lift mode, with no driving force on the piezo during the lift-scan. Instead $V_{ac}(\omega)$ is applied, with ω at the resonance frequency of the cantilever. This results in a force at the resonance frequency given by (1.28), and hence an oscillation of the cantilever. The dc (1.27) and 2ω (1.29) contributions will have negligible effect, since they will not excite the cantilever to oscillate. SSPM works on the Kelvin principle of nulling the force by using a feedback loop on $V_{dc}^{appl.}$ to minimise the oscillation amplitude. The dc voltage applied to the tip (V_{dc}^{tip}) which minimises the oscillation amplitude will, from Eqn. 1.29, be equal to the local potential on the sample. Hence, by recording V_{dc}^{tip} a map of the local potential on the sample can be formed. In SSPM the oscillation of the cantilever is used as a sensitive force transducer, as compared to dc-EFM which transduces the force gradient.

Scanning Conductance Microscopy, SCM, is a variant based on dc-EFM which detects the presence of conducting objects on an insulating (dielectric) surface, above a conducting ground plane [BMS+02]. A schematic of the setup is given in Figure 1.20. Again SCM operates in lift mode like dc-EFM, with the conducting plane grounded and a voltage applied to the tip, V_{tip}. If the capacitance between the tip and conducting object is C_{tc}, and C_{cg} is the capacitance between the object and ground, then the potential difference between the tip and conductor is given by

$$V_{tc} = V_{tip}\frac{C_{cg}}{C_{cg} + C_{tc}} \tag{1.30}$$

This results in a phase difference as in dc-EFM. In particular this technique is used in Chapter 2 to image SWNT lying on a highly doped Si substrate with oxide layer

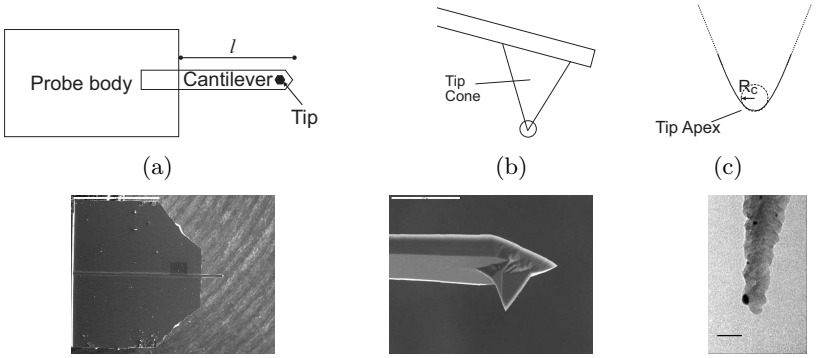

Figure 1.21: Schematics and (a), (b) SEM images, and (c) TEM image of the probe body, cantilever, tip cone, and tip apex. The scale bars are (a) 1 mm, (b) 20 μm, and (c) 25 nm. SEM images courtesy of Steve York, University of Warwick.

as dielectric. It is sensitive to both mSWNT and sSWNT, provided their lengths are $\gtrsim 0.5$ μm[11].

Tips and Cantilevers

The active component in any AFM is the tip. Figure 1.21 shows schematic representations and SEM images of a typical microfabricated Si tip. The probe body, cantilever, tip cone and tip apex are defined in the figure, and will be referred to later. Confusingly the word 'tip' is also used to refer to the whole structure, as well as the tip cone and tip apex combined, and sometimes as the part which actually comes into contact with the surface.

As demonstrated in Figure 1.21 (c), the tip is not atomically sharp but tends to come to a rounded end, which is conventionally characterised by its radius of curvature, R_c. The observed topography is a convolution of the real topography with the tip shape, and the lateral resolution is thus determined by the tip used. Typical microfabricated Si tips have $R_c \approx 15$ nm, as new, with a full cone angle of $\gtrsim 30°$.

[11] the minimum observable length is set by the ratio of capacitances and so can be reduced by decreasing the thickness of the oxide layer, and hence increasing C_{cg}

[12] Si_3N_4 tips are often used for contact mode imaging, however they were not used here.

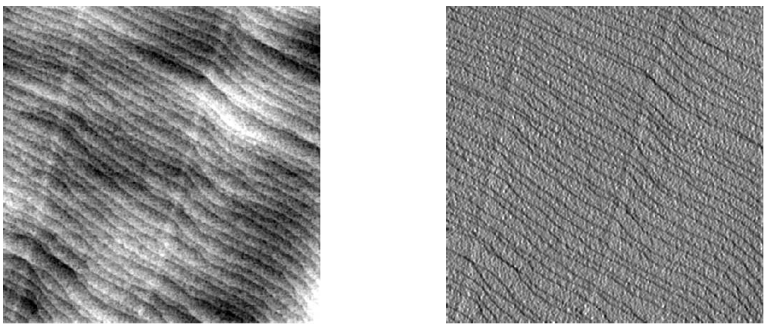

(a) height, full scale 1 nm (b) amplitude, 7.5 mV

Figure 1.22: 2 μm scans of 30% Al on AlInSb. Sample courtesy of Dr Chris McConville, University of Warwick.

The tip apex shown in Figure 1.21 (c) is of a sharp, new, tapping tip. The tip apex has a radius of curvature of $R_c \approx 12$ nm, although in this case there is an asperity with radius of curvature ≈ 6 nm. The tips are rapidly blunted further, especially in contact mode or on hard samples. The z resolution is, however, independent of the tip. Figure 1.22 is a tapping mode (a) height and (b) amplitude image. The full grey scale of the height image is 1 nm. Atomic steps are clearly visible, with heights of ~ 2.5 Å, demonstrating that atomic resolution in the z direction is easily attainable.

In this thesis three main types of tips were used, all microfabricated from highly n-doped Si. Table 1.2, shows typical properties of these tips. The spring constants are the quoted values from the manufacturer, and are not always accurate.

tip	'TESP'	'FESP'/ 'Force Modulation'	'Contact'
ν_0 (kHz)	260 - 410	60 - 100	10-17
Q	~ 500	~ 300	~ 60
k (N m^{-1})	21 - 78	1.2 - 5.5	0.07 - 0.4
cantilever length (μm)	125	225	450
ampl. sens. (nm V^{-1})	$\sim$ 10 - 15	$\sim$ 15 - 20	NA
defl. sens. (nm V^{-1})	NA	$\sim 60 - 70$	$\sim$ 120 - 150
use	tapping	tapping/contact	contact [12]

Table 1.2: Typical properties of tips used

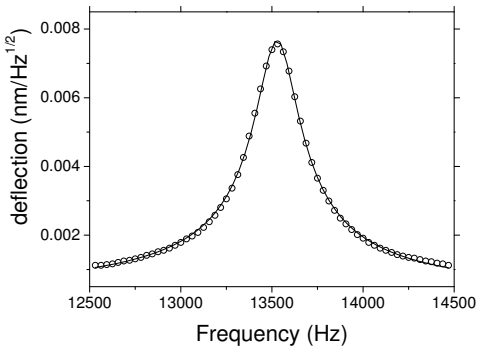

Figure 1.23: Thermal tune spectrum, ∘, and fit to a thermal resonance, solid line, for a Si contact tip. The fitted values are $Q = 56.9$, $A_{th} = 1.3 \times 10^{-4}$ nm Hz$^{-1/2}$, and $\nu_0 = 13.5$ kHz, giving a spring constant of $k = 0.2$ Nm^{-1}.

If k is required to within an order of magnitude then it must be measured for each tip. There are various methods for calibrating the spring constant of a tip, see for example [BCH$^+$03] and references therein. The method used in this thesis was the thermal noise method which is simple, non-destructive, quick and elegant, see for example [HB93]. At its most basic, it is an application of the equipartition theory. In thermal equilibrium with its surroundings at temperature T, the average energy in each mode of oscillation of the cantilever is $k_B T/2$. The energy in the oscillation of the cantilever is given by $k\langle x^2\rangle/2$, where x is the displacement of the cantilever from its equilibrium position. Thus

$$k = \frac{k_B T}{\langle x^2 \rangle} \tag{1.31}$$

In practise the presence of other noise in the output of the photodiode, as well as multiple modes of oscillation of the cantilever, make just measuring $\langle x^2\rangle$ inaccurate. Thermal noise acts as a white noise driving oscillation at each frequency equally. The resultant frequency spectrum of the cantilever oscillation will thus have a resonance at the cantilever's fundamental given by Eqn. 1.18. By measuring the spectrum of the noise and fitting it to Eqn. 1.18 Q, ν_0 and A_{th} (the thermal drive amplitude) can be obtained. An experimentally recorded thermal resonance is shown in Figure 1.23,

it was recorded using a Stanford Research Systems SR760 FFT Spectrum Analyzer. Integration of Eqn. 1.18 yields

$$\langle x^2 \rangle = \frac{\pi}{2} Q A^2 \nu_0 \tag{1.32}$$

The spring constant can now be related to the measured quantities

$$k = \frac{2 k_B T}{\pi Q A_{th}^2 \nu_0} \tag{1.33}$$

The largest uncertainty lies in the determination of the deflection sensitivity required to convert the photodiode output into a real deflection of the cantilever. This technique is only an approximation [SBL$^+$97, LM02, BCH$^+$03], and can only be used for cantilever's with $\nu_0 \lesssim 100$ kHz. However it is known to be accurate to ~ 20 %, sufficient for the purposes required here.

Multimode and Dimension AFM's

Two different AFM's have been used for this work, both produced by Digital Instruments (now Veeco). A Dimension 3100 with Nanoscope IV controller (in the Physics Department, University of Washington, Seattle), and a Multimode with Nanoscope IIIa controller (in the Physics Department, University of Warwick). In addition various modules have been added to the Nansocope IIIa controller through the course of this work. Both AFM's have similar optical detectors so that the deflection and amplitude sensitivities quoted above are equally valid for both instruments.

However, in the Multimode the sample is moved in the x-y direction, whilst in the Dimension the sample is stationary and the tip is scanned. Making electrical measurements on the Dimension is thus easier, as discussed in Chapter 3. Both AFM's were mounted on pneumatic vibration isolation tables, hence both had noise levels in the z direction of well below 1 nm (Figure 1.22 was in fact taken with the Multimode). They were both also situated inside Faraday cages to reduce electrical

noise for the electrical transport experiments. Both are equipped with a 'Signal Access Module' which allows access to the control signals going to the AFM from its controller, and the data signals going from the AFM to its controller. It also allows additional signals to be inputted into the controller and recorded alongside height/amplitude/phase etc. data.

The amplitude recorded by both controllers is an rms amplitude. In general the amplitudes of oscillation quoted in this thesis will also be rms, except where comparison with theory is required. In the Nanoscope IIIa controller this is measured using an rms converter on the output of the photodiode. The Nansoscope IV controller uses a lock-in to measure the amplitude of oscillation at the drive frequency, reducing the noise levels and allowing more stable imaging.[13] A second lock-in allows it to simultaneously measure the phase lag ϕ, as defined earlier. The Extender module works in series with the Nanoscope IIIa controller to measure the phase between the cantilever oscillation and the driving force. However the 'Bocek' phase it measures, ϕ_{Bocek}, is not the phase ϕ as defined before, but $\phi_{Bocek} \simeq \phi$ for small ϕ ($\sim \pm 15°$)[14]. Recently a Quadrex module was obtained on loan from Veeco, this replaces the Extender module and contains two lock-in amplifiers which upgrade the Nanoscope IIIa controller to measure amplitude and ϕ as in the Nanoscope IV. The TR mode module was also lent by Veeco, and was used with the Multimode, although it is available for use with the Dimension as well.

The $x-y$ position of the Multimode is inferred by the piezo voltages applied, and is calibrated periodically using known structures. However, it is subject to drifting as the piezo relaxes, as well as hysteresis effects that change over time, and

[13]However, it only allows the response to be measured at the driving frequency. In SSPM it can be instructive to apply the driving potential at half the resonant frequency to look only at the capacitive force given by the second harmonic (1.29). This is possible with the Nanoscope IIIa but currently not with the Nanoscope IV.

[14]for more information see the discussion in the Veeco SPM user group at http://spm.di.com/query.asp

thermal expansion effects. The Dimension contained a 'closed loop' scanner which measured rather than inferred the position, reducing these effects. A 'Picoforce' module was acquired for the Multimode which confers closed loop control in the 'z' direction, although it does not account for thermal expansion of the sample. The type of AFM used, and the specific configuration, will be stated for each experiment.

1.3 Outline of thesis

The enabling techniques for this work were growth of SWNTs, and fabrication of SWNT devices. Chapter 2 gives a brief introduction to these techniques, and presents our results and conclusions. The properties of the SWNT devices are investigated in Chapter 3 using a combination of EFM, manipulation, and Scanned Gate Microscopy (SGM).

One of the earliest realised applications of carbon nanotubes was as AFM tips, [DHR$^+$96]. Fabrication of, and imaging with, SWNT-AFM tips is discussed in Chapter 4. In addition, electrical transport through electrically connected SWNT-AFM tips is investigated. A novel technique for the formation of robust, conducting, nanowire AFM probes is also described.

The need for higher resolution EFM and SGM, highlighted by the work presented in Chapter 3, is addressed in Chapter 5. SWNT-AFM tips are quantitatively shown to increase the resolution of EFM, enabling similar features to be distinguished at separations ~ 15 nm, comparable to the topographic resolution. A novel version of SGM is also presented, which massively increases the signal to noise ratio, as well as increasing the spatial resolution of the technique.

A summary of the conclusions which can be drawn from this work, and the proposed direction of further studies, is given in Chapter 6.

Chapter 2

SWNT growth and devices

2.1 SWNT growth

The initial discovery of SWNTs in 1993 by Iijima and Ichihashi [II93] and Bethune et al. [BKD+93] was from the soot generated by arc-discharge from a carbon anode with a metal catalyst. The 'quality' of the SWNT were poor, with low yields, high defect densities and large amounts of amorphous carbon and catalyst material. It wasn't until 1996 that 'large' (1 - 10 g) quantities of high quality SWNT were produced using a laser ablation technique by Smalley and co-workers [TLN+96]. These became commercially available as a powder through the company Tubes@Rice, and were the basis for most of the original work on SWNT. The powder contained ropes and bundles of SWNT, as well as catalyst material.

In 1998 Professor Hongjie Dai's group at Stanford used catalysed chemical vapour deposition (cCVD) to grow SWNT in situ on substrates [KSC+98, KCD98], removing the need for postprocessing of the SWNT material, and allowing the study of pristine, high quality individual SWNT. The simplicity of the approach, as well as the low cost of the required equipment, allowed research laboratories around the world to grow their own SWNT, and has sparked the growth in the study of SWNT

devices in recent years. Currently, high quality SWNT are commercially available from Carbon Nanotechnologies Inc., the successor company from Tubes@Rice, for $500/gram. These are now grown by the 'HiPCO' technique which utilises high pressure carbon monoxide with iron carbonyl catalyst precursor at 1000 °C, [CS02]. Since this is an all gas phase reaction, it is easily scalable to mass production. SWNT produced by this technique are returning to favour for device applications after the recent discovery of techniques for dispersing individual SWNT from the powder form into aqueous solution e.g. [BSK+02], the subsequent separation of mSWNT from sSWNT [KHvK03, SDU+03, ZJS+03], and the selective positioning of SWNT from solution [RHSH03, KBB+03].

cCVD provides, a simple, quick, cheap, and efficient method for the growth of SWNT on substrates, and was the basis for all the work in this thesis. Iron, nickel or cobalt nanoparticles are usually used to catalyse SWNT growth in the cCVD process, see for example [NCK+03]. These transition metals were chosen due to the well known solubility of carbon in these materials at high temperatures [Dai02a]. Initially the nanoparticles were formed on an alumina support [KSC+98], however it was found that the support was not necessary and the SWNT could be grown directly on a silicon oxide substrate, e.g. [HCOL01]. By patterning the catalyst on a substrate the position of growth can be controlled, even at the wafer scale [FLC+01]. The control of subsequent direction of growth has been demonstrated using structured surfaces e.g. [FD00], and more recently electric fields [ZCC+01, JL02]. The polarisability of both mSWNT and sSWNT encourages them to align with electric fields, either applied externally or induced by the local substrate morphology [RHC04]. This allows 'vectorial growth' where both the start position and the direction are specified. Recently the growth of SWNT over 1 mm long (i.e. with an aspect ratio of $\sim 10^6$) has been demonstrated e.g. [KCL+02, DGCF04, HCL03]. Since active devices only require ~ 1 μm of SWNT, these long SWNT open up

the possibilities of 1000's of devices fabricated from the same molecule. In addition, long SWNT tend to align with the gas flow through the CVD oven [HCDL03], allowing control over the direction of growth. Another breakthrough has been the integration of patterned cCVD growth of SWNT with standard silicon MOS technology, [TXJ+04], and the fabrication of hybrid SWNT-semiconductor heterostructure devices [JHN+04].

Control over the diameter and type of SWNT, as well as their position, is highly desirable for their future use in electronic devices. Control over their diameter has been achieved, to a limited degree, by controlling the size of the catalytic nanoparticles used, e.g. [LKZ+01, CKPL02, AOML02, CKW+03]. Control of the diameter to a sufficient degree to grow only one type of SWNT is, however, unlikely to ever be achievable using this technique. Recent studies on the electronic properties of SWNT have shown that although cCVD grown SWNT seem to be randomly distributed in diameter, giving a one third to two thirds ratio of mSWNT to sSWNT as expected, the use of plasma enhanced cCVD increases this ratio to ~ 90 % sSWNT [LMR+04]. This suggests the possibility of selective growth of either mSWNT or sSWNT by application of suitable electric fields.

2.1.1 Experimental setup and results

The experimental setup used for SWNT growth is shown in Figures 2.1 (a) and (b), and schematically in (c). 1/4" stainless steel Swagelok tubing is used to connect the gas cylinders (1), via mass flow controllers (2) (MKS Type 1179A Mass-Flo® Controllers, linked to MKS Type 247D 4 channel power-supply and display) to a 1" diameter quartz tube. The quartz tube is connected with an O-ring fitting, sufficient for this ambient pressure application, and is placed in a Lindberg Blue 1" tube furnace (3). We found that over a period of a few months the growth yield dramatically decreased, this was remedied by periodically dismantling the system,

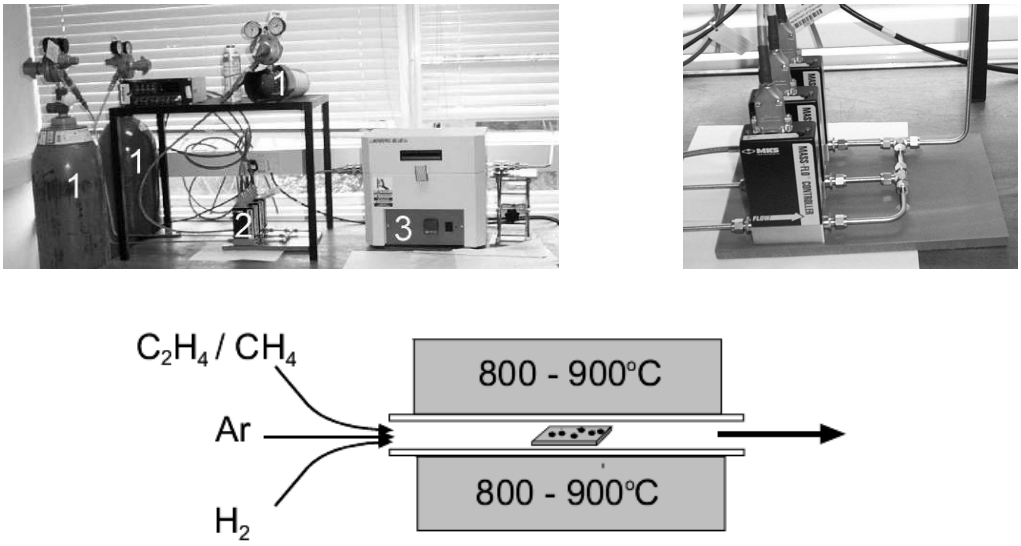

Figure 2.1: *Upper* Photographs, and *lower* schematic of the cCVD setup.

cleaning the joints and replacing the tubing. Essentially though, this CVD system is cheap and easy to construct.

Initially, efforts focused on reproducing the SWNT growth procedure described in [HCOL01]: '*Nanotubes were grown on oxidised silicon substrates by CVD using an iron catalyst. Briefly, a 150 $\mu g/mL$ solution of ferric nitrate nonahydrate in 2-propanol was prepared and stirred for 2 min. Silicon substrates were dipped in this solution for 10s, rinsed in hexane, and dried. These substrates were then placed in a tube furnace and annealed at 700 $^\circ C$ for 15 min under a flow of 600 standard cubic centimetres (sccm) argon and 400 sccm hydrogen. Ethylene was then added at 0.5 sccm for 6 min, and finally, the furnace was cooled under argon.*' Through a process of trial and error we found SWNT growth to occur, in our system, at growth temperatures (T_G) between 800 °C $\leq T_G \leq$ 850 °C, with ethylene (C_2H_4) flow rates between 1.5 and 3.0 sccm. An annealling step, involving maintaining the temperature at T_G for $\sim$ 10 min before adding C_2H_4, was found to occasionally increase the yield of SWNT. However, the results were very inconsistent, and the

observed optimal conditions tended to change over time.

Typically, the catalyst used was ferric nitrate nonahydrate ($Fe(NO_3)_3.9H_2O$), 99.99+% pure from Aldrich chemicals, dissolved in isopropanol (IPA). Ferric nitrate is extremely hygroscopic, as a result it was not feasible to weigh the small amounts required since it absorbed a significant proportion by mass of moisture during the time required to weigh it accurately. Instead, the concentration was adjusted according to the colour of the solution; a light straw colour. The ferric nitrate is also light sensitive, and, although it was kept in a dark place and exposed to the atmosphere as infrequently as possible, its catalytic ability was found to decrease over time. A new bottle of ferric nitrate crystals was required every few months.

The catalyst was prepared by transferring a small crystal of iron nitrate to IPA, agitating until dissolved, and then reducing the concentration by addition of IPA until the colour was correct. The substrate was then dipped into the resultant solution (for < 10 s), removed and rinsed with IPA, and then hexane[1], and immediately dried in a stream of dry nitrogen. This process resulted in the formation of small particles of a variety of sizes, though typically < 10 nm in diameter, on the surface of the oxidised silicon substrate. The process by which these particles form is not clear, though it could be due to the low solubility of ferric nitrate in IPA, and the low attraction between IPA and SiO_2 (IPA does not 'wet' SiO_2). It was found that sonication of the resultant solution for 1-2 min prior to dipping the substrate in it improved the dispersion of catalyst on the substrate, resulting in fewer large (> 5 nm diameter) particles.

Each individual catalyst solution was found to retain catalytic activity for less than 24 hours, possibly due to oxidisation. Hence a new catalyst solution was prepared for each growth attempt, this was possible due to the simplicity and speed

[1] it was not possible to grow carbon nanotubes of any kind without the final rinse in hexane prior to growth.

with which the catalyst solution could be made.

The substrate was cleaned prior to deposition of catalyst by rinsing with acetone, followed by sonication in acetone for ~ 5 min. After sonication the substrate was again rinsed in acetone, then IPA, and immediately dried in a flow of dry nitrogen.

After catalyst deposition the substrate was placed on a quartz support in the quartz tube in the middle of the tube furnace. Typical growth conditions would then be:

time (min)	Temperature (°C)	Gases
0 - 10	25 - 700	H_2 and Ar
10 - 20	700 - 850	H_2 and Ar
20 - 30	850	H_2 and Ar
30 - 40	850	H_2, Ar and C_2H_4
40 - ...	850 - 25	H_2 and Ar

Table 2.1: Typical growth conditions, with flow rates of Ar = 600 sccm, H_2 = 400 sccm, and C_2H_4 = 2 sccm.

An AFM image of a sample grown via these conditions is shown in Figure 2.2 (a). Opening the lid of the tube furnace reduced the time taken to return to room temperature, enabling the entire growth process, including catalyst preparation, to be finished within two hours.

Other catalysts were also used for SWNT growth, in particular an iron/molybdenum, supported on alumina, catalyst as in the original work [KSC$^+$98, KCD98]. Attempts were also made to produce more uniform catalyst particle diameters using iron pentacarbonyl decomposition [CKPL02] and artificial ferritin [LKZ$^+$01][2]. Optimal growth conditions were found to be similar for all the catalysts used. The alumina support based catalyst was found to reproducibly produce the highest concentration of SWNTs, but the large size of the support particles (some $\sim$ 100 nm) was

[2]This was done with Patrick Nicholson and Tom Day respectively as part of their MSc projects in the Warwick University Chemistry Department

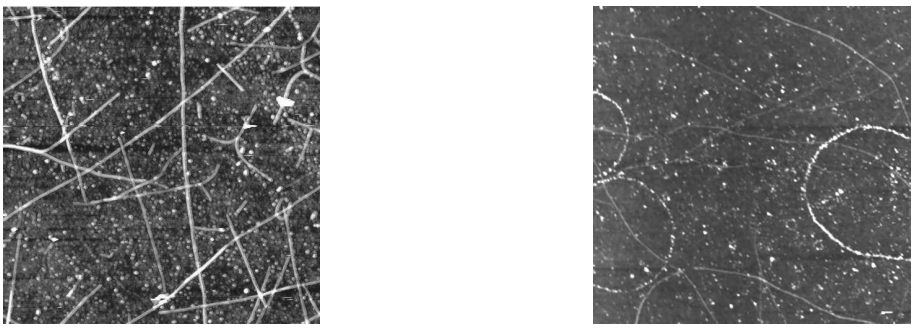

(a) (b)

Figure 2.2: Height image of SWNT grown with (a) C_2H_4, 3 μm scan, and (b) CH_4, 5 μm scan.

prohibitive for the further study of the SWNTs formed. The ferric nitrate catalyst was found to be the easiest to make and use, and so was adopted for the majority of the work.

The use of methane (CH_4) as the carbon feedstock gas in substitution for, or in combination with (based on [KCL$^+$02]) ethylene was also investigated. Figure 2.2 (b) shows a sample grown using methane as the feedstock[3]. However, growth with ethylene was found to be more reliable with our system, and the 'quality' of the SWNT produced was found to be high, as shall be shown later. Hence, the majority of the subsequent work presented is based on SWNT grown using ethylene as the carbon feedstock, and ferric nitrate as the catalyst.

Different substrates were also tried. SiO_2 is an ideal substrate for SWNT growth for the purpose of device fabrication due to its low surface roughness, high dielectric constant, and the presence of the underlying highly doped Si, which can act as a 'back gate'. However, AFM tips are fabricated from highly doped Si with only a native oxide layer, so growth on highly n-doped Si substrates was also investigated.

[3]the SiO_2 substrate was heated from 25 - 900 °C in 25 min under a flow of Ar and H_2. Then CH_4 was added for 20 min at 900 °C. The substrate was then cooled to room temperature under a flow of Ar. Flow rates were Ar = 800 sccm, H_2 = 1000 sccm, and CH_4 = 1500 sccm.

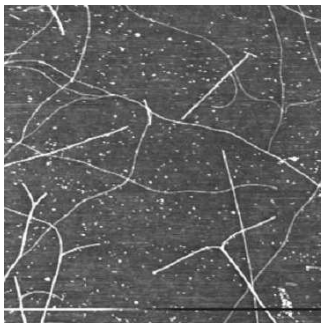

(a) SiO_2 height image, 5 nm full scale

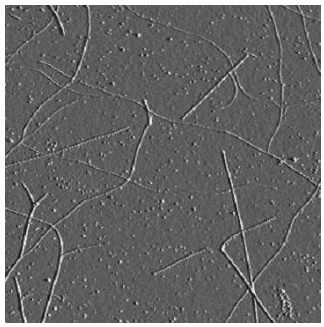

(b) amplitude

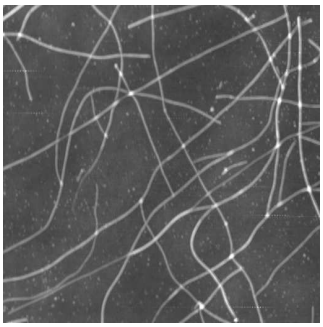

(c) Si height image, 15 nm full scale

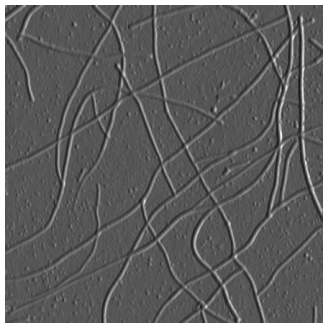

(d) amplitude

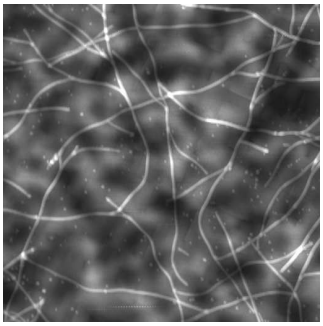

(e) Si on sapphire height image, 20 nm full scale

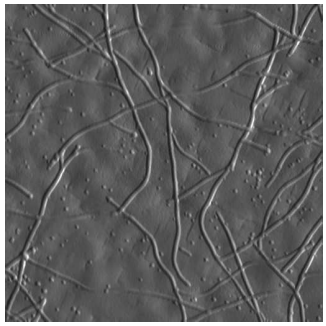

(f) amplitude

Figure 2.3: 3 μm square images of nanotube growth on SiO_2, Si, and Si on sapphire substrates.

As Figure 2.3 shows, growth on Si produced longer nanotubes with larger diameters ($\sim$ 3 - 5 nm), hence possibly double wall nanotubes (DWNT) or small MWNT rather than SWNT. Growth on Si on sapphire (a transparent substrate) was also demonstrated, and produced similar results.

Although the growth process was too unrepeatable to allow a systematic study of the effect of the different variables[4] within the time available, some general conclusions can be made. These are included in the following proposed growth model, based on our observations and [HKO$^+$03, FBP$^+$03, CKPL02]. It is based on the Vapour-Liquid-Solid (VLS) mechanism originally used to explain the formation of carbon fibre whiskers in the 1960's [WE64].

1. The growth process starts with the catalysed decomposition of the carbon feedstock gas on the solid catalyst particles releasing H_2, with the carbon being absorbed into the solid iron nanoparticles.

2. Absorption of carbon lowers the melting point of the nanoparticles, an effect enhanced by the large surface area to volume ratio of the small nanoparticles. This causes the nanoparticles to melt, facilitating diffusion of carbon through the nanoparticle.

3. Further absorption of carbon increases the concentration beyond the eutectic point of Fe-C, resulting in the precipitation of carbon.

4. Carbon precipitates, forming a 'cap', which either closes around the nanoparticle to form a fullerene, ending the growth process, or extends to form a SWNT.

5. Growth of the SWNT proceeds through the decomposition of the carbon feedstock vapour on the liquid catalyst particle, which then rapidly diffuses across

[4] such as T_G, flow rates of the gases, choice of carbon feedstock gas, growth times, anneal times and temperatures etc.

the catalyst particle, crystallising out and extending the SWNT.

6. Growth ends either by the completion of the fullerene cap around the nanoparticle, or by poisoning of the catalyst particle by contaminants, surface effects, or solidification.

The lower bound on T_G is thus due to steps 1 and 2. The finite size of the nanoparticles substantially reduces the melting point of the iron nanoparticles, from 1535 °C for bulk Fe in Ar, to 900 °C for 30 nm diameter particles [HKO$^+$03]. This effect is increased the smaller the nanoparticles become. The melting point decreases even further in the presence of carbon, from 1535 °C to 1148 °C for bulk Fe at the eutectic point of the Fe-C system [HKO$^+$03]. These effects explains why only SWNT with diameters in the range $\sim$ 0.7 - 3.0 nm are grown even though nanoparticles of larger diameters are present. Increasing T_G beyond 850 °C resulted in a higher proportion of larger diameter SWNT, as did increasing the ethylene flow rate beyond 3.0 sccm. Both of these effects would enable the melting of larger iron nanoparticles, facilitating the growth of larger diameter SWNT.

Increasing T_G beyond 850 °C also increases the amount of amorphous carbon present. The pyrolysis of ethylene is inhibited by the large partial pressure of hydrogen, and by the low partial pressure of ethylene. However, at temperatures greater than 850 °C ethylene starts to break down, resulting in a lower yield of SWNT and larger amounts of amorphous carbon. The presence of large amounts of amorphous carbon on the SWNT can be detected by AFM. However, the presence of small amounts can only be detected by TEM, and is vitally important for applications.

Steps 4 and 5 in the growth process rely on the high energy cost involved in 'dangling' bonds in graphite. The total energy of 60 carbon atoms formed into (a) a flat flake of graphite perpendicular to a metal surface is 45.9 eV, (b) a hemispherical cap on a metal surface is 16.8 eV, (c) a capped (5,5) tube on metal is 17.3 eV, and

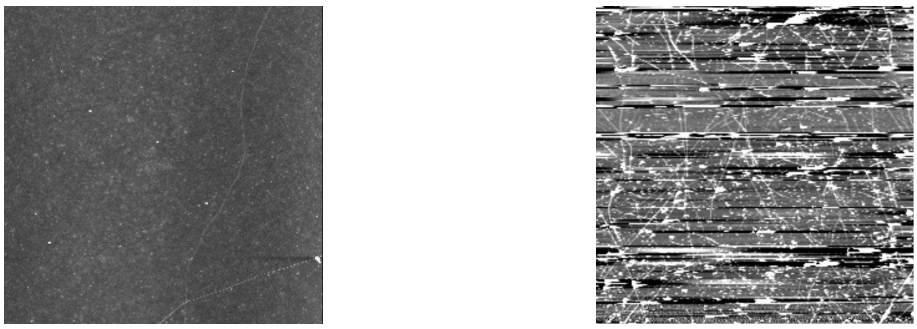

(a) (b)

Figure 2.4: 10 μm square height images of a low, (a), and high, (b), density cCVD growth of SWNT on SiO_2.

(d) a C_{60} is 24.0 eV [FBP$^+$03]. This reveals the energetic pathway to the formation of SWNT. The formation of graphite is clearly unfavourable, hence a cap is formed instead. The energetics dictate that the larger diameter cap is more favourable, i.e. (c) is a higher energy state than (b), hence the cap will increase in diameter until it is the same size as the catalyst particle. At this point it is more favourable to form a SWNT than to close to form a fullerene, i.e. (c) is more energetically favourable than (d). This also explains the observation that when catalyst particles are observed to be still attached to the SWNT they formed, they tend to have the same diameter as the SWNT. The diameter of the catalyst particle defines the diameter of the SWNT. However, since the difference between (d) and (e) is small the diameter of the catalyst particle could not be used to determine with certainty the chirality of the SWNT formed, especially at the high growth temperatures used.

SWNT growth from iron catalyst on alumina support particles has been demonstrated to be via a base growth mechanism [LKZ$^+$01], i.e. the catalyst particle remains in contact with the substrate. However, this has not been confirmed for growth from isolated catalyst particles as used here, and may be dependent on the substrate used. The substrate interaction in the growth process is not well understood, and can be inferred to be strong, see Appendix A.

SWNT growth focused on the production of two types of samples as illustrated in Figure 2.4: (a) low density samples, consisting of a low density of SWNTs and catalyst, for SWNT device fabrication; and (b) high density samples, consisting of a high density of short ($\sim$ 1 - 2 μm) SWNTs, for the fabrication of SWNT-AFM tips, as discussed in Chapter 4. The variation in density was mainly achieved by varying the catalyst concentration, whilst keeping the growth conditions at those giving the optimal yield. The SWNT produced were characterised by AFM, electron microscopy, micro-Raman spectroscopy, and by SWNT device fabrication and room temperature electrical transport studies.

2.1.2 Characterisation

AFM and SCM

The primary characterisation technique used for the substrates produced by the cCVD growth process was AFM. Topographical AFM imaging enables non-destructive measurement of lengths, diameters, and concentrations of the SWNTs on the substrate after growth. In addition, it enables analysis of the size and concentration of catalyst particles present.

Imaging must be performed in tapping mode, the lateral tip surface forces involved with contact mode imaging 'pushes' the SWNT around on the surface. Figure 2.5 shows a histogram of the diameters of SWNT in Figure 2.2 (a). The diameter of the SWNT is measured not from the apparent widths of the SWNT in the image, which are dominated by tip convolution effects, but from their apparent heights, which

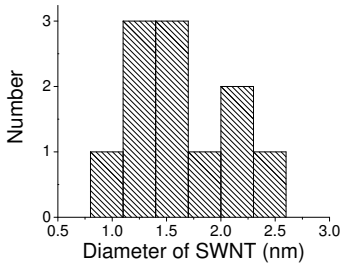

Figure 2.5: Histogram of SWNT diameters from Figure 2.2 (a)

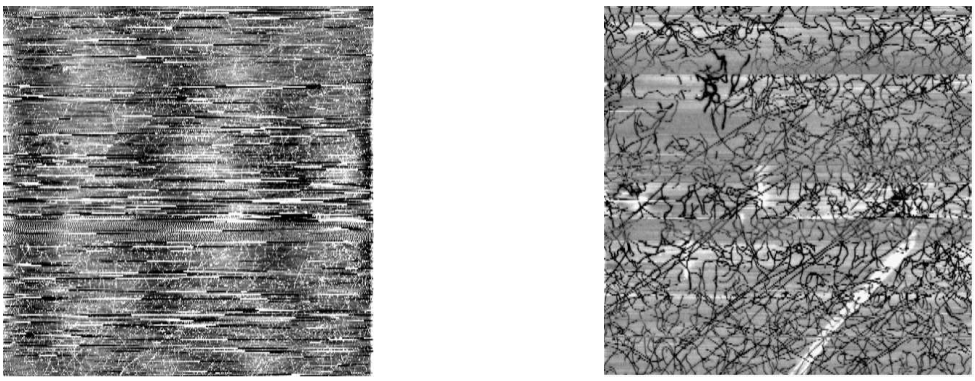

(a) (b)

Figure 2.6: 100 μm square (a) topography, and (b) SCM image of a SWNT growth sample. Sample courtesy of Tom Day.

are less prone to artefacts. In general, SWNT diameters in the range 0.8 - 3 nm were observed, with the peak of the distribution around 1 - 1.5 nm.

There is no other technique which can give the topographic information described above in situ on the SiO_2 substrate. However, AFM images cannot be used to distinguish between double wall nanotubes (DWNTs), large diameter SWNTs and small bundles of SWNTs. Nor is it capable of detecting small amounts of amorphous carbon, which is indistinguishable from the natural surface roughness of the oxide surface. In addition, scans of $\lesssim 10$ μm must be used in order to resolve the individual SWNTs, and each scan takes $\gtrsim 5$ min. This precludes the possibility of analysing large areas of the substrate. The distribution of SWNT growth on the substrate is far from uniform, and lengths of individual SWNT can exceed 100 μm. Clearly there are advantages to being able to analyse larger areas. This was achieved using SCM.

Figure 2.6 shows a 100 μm square (a) topography, and (b) SCM image of a SWNT growth sample. The SWNT are clearly visible in the SCM image even though they are almost indistinguishable in the topographic image. Although the SCM image has no information about diameters of the SWNT or catalyst concentration,

it can be used in conjunction with smaller scan topographic AFM imaging to study homogeneity of SWNT growth. Indeed, it is clear from Figure 2.6 that a 10 μm scan in the top left corner of the image would indicate a much lower yield than a 10 μm scan in the lower right of the image. Straight, individual SWNTs with lengths $>$ 100 μm running parallel to each other from the bottom left corner of the image to the top right are also clearly evident. These SWNTs are presumably aligned with the gas flow within the cCVD system, but their presence cannot not be distinguished on the small scans required for topographic AFM analysis. SCM is a complementary technique to topographic AFM for the study of SWNT growth, although it has not been used as such in the SWNT growth literature.

Electron Microscopy

An alternate technique for analysing growth on large length scales (10 μm - 1 mm) is field emission scanning electron microscopy (FESEM). As Figure 2.7 demonstrates, this technique is capable of clearly imaging SWNTs over large length scales. The contrast in the image stems from local potential differences between the conducting nanotube and insulating substrate, caused by charging due to the electron beam [BCD$^+$02]. The SWNTs themselves are not 'resolved', they are observed since they charge much more slowly than the surrounding substrate by distributing the charge along their length. The optimal imaging conditions for maximal contrast are thus, counter-intuitively, low beam current, low magnification, low accelerating voltages and high scan speeds. In addition SWNT connecting to each other, or to metal electrodes if present, to form conducting networks will give higher contrast. The disadvantages of this technique are its inability to give information about the diameter of the SWNTs formed, and its insensitivity to the presence of catalyst particles, amorphous carbon or surface contamination. In addition, care must be taken not to contaminate the surface whilst imaging, or damage the SWNT with high beam

currents. Use of FESEM was limited by lack of availability.

In the middle figure of Figure 2.7 the presence of long (> 100 μm) straight, parallel SWNTs is again evident, as is the inhomogeneity of the growth distribution. The lower figure shows a tilted image of the edge of the substrate. The oxide layer on top of the underlying Si substrate is clearly visible, as is the fact that SWNT grew both on the SiO_2 and the Si.

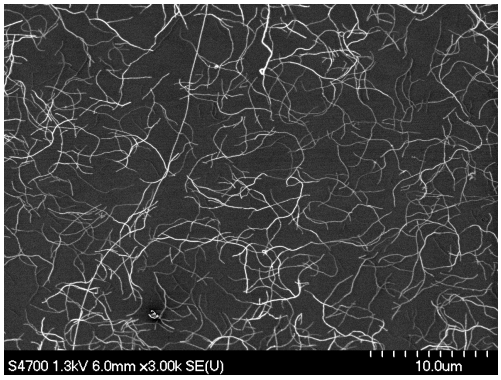

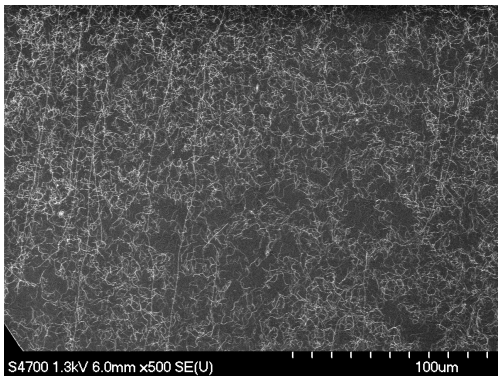

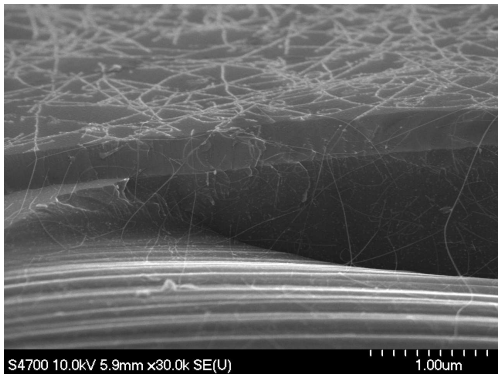

Figure 2.7: FESEM images of a Si substrate, with 300 nm SiO_2 layer, after cCVD growth of SWNT. Images taken with Dr Phil Dobson, University of Glasgow.

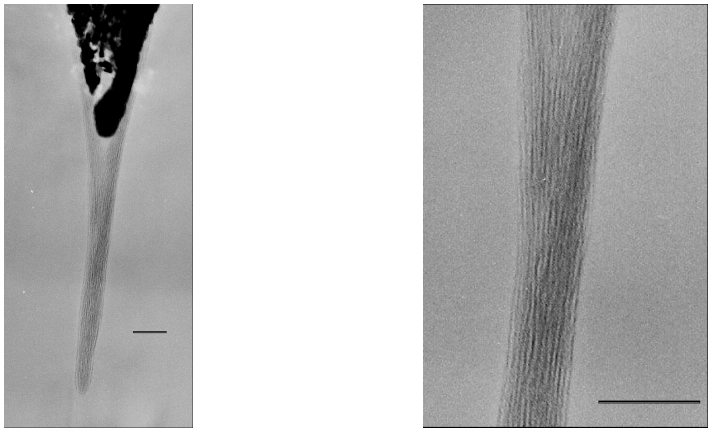

Figure 2.8: TEM images of a bundle of SWNT around the apex of an AFM tip. The scale bars are 50 nm.

Transmission electron microscopy (TEM) also proved to be a valuable technique for characterisation of SWNTs. TEM of SiO_2 substrates in situ after cCVD growth of SWNT has been reported in the literature using SiO_2 films on TEM grids e.g. [CKW$^+$03]. However, work with Tom Day showed that the growth conditions required for SWNT growth on these substrates in our system was different to that on the conventional substrates, making it an unsatisfactory method for characterising our SWNT cCVD growth. The 'pick-up' technique used for making SWNT-AFM tips, as discussed in Chapter 4, involves the removal of SWNTs from the growth substrates, and their positioning at the apex of AFM tips. This enabled subsequent TEM imaging of the SWNTs.

SWNT were found to be highly sensitive to damage by the focussed electron beam in the TEM, hence low beam currents were required. Care also had to be taken not to contaminate the SWNT-AFM tip. An example of a large bundle of SWNT on a metal coated AFM tip is given in Figure 2.8. Individual SWNT within the bundle are visible, although their diameters cannot be accurately resolved, and it is not possible to discount the presence of DWNT. The observed diameters are roughly consistent with those measured by AFM. Importantly, there is no evidence

of amorphous carbon.

TEM images were taken using a JEOL2000FX at 200 kV and a tilt angle of 60° in the Physics Department, at the University of Warwick.

micro-Raman spectroscopy

Raman microscopy is a well known technique for the characterisation of carbon based materials in general, and carbon nanotubes in particular. As such there is a wealth of literature on the subject. However, this is not a focus of the work presented here, and as such we refer to the discussions in [SDD98, EHJ95] concerning the Raman active modes in SWNT, and to the review articles [JPF$^+$03, DDJ$^+$02b, DDJ$^+$02a] concerning Raman spectroscopy of isolated individual SWNT, and the references therein.

Raman scattering involves the inelastic scattering of light from a molecule. It is a two stage process, involving first the absorption of a photon, exciting the molecule, and then the emission of a photon at a different wavelength from the incident, returning the molecule to a different energy state (typically due to the excitation of a phonon in the molecule). Since it is a two stage process, and hence second order, the signal is usually weak and large sample volumes and high laser intensities are required. However, if the laser energy is equal to the separation of the Van Hove singularities of the SWNT, discussed in Chapter 1, it can excite electrons from the sharp peak in the density of occupied states of the valence band edge to the sharp peak in the density of unoccupied states of the conduction band edge. This resonance enables the Raman spectra of individual SWNT, a single molecule, to be measured with relative ease [JHaMH$^+$01].

The spectra shown in Figure 2.9 were taken with a Renishaw 1000 Raman microprobe at the Materials Department, University of Manchester Institute of Science and Technology with Professor Robert Young. The laser spot size was ~ 1 μm.

Figures 2.9 (a) and (b) were taken with a HeNe laser (632 nm), whilst (c) and (d) were taken with a near-IR laser (780 nm).

The highest intensity peak in the spectra from SWNT is usually the 'G band' peak at $\sim$ 1590 cm^{-1}, which is also present in MWNT and graphite. Figure 2.9 (a) and (b) show a comparison between the spectra for SWNT powder purchased from Tubes@Rice, (a), and a spectra from SWNTs grown at Warwick University by cCVD on SiO_2, (b). The spectra from the powder corresponds to many SWNTs, whilst (b) corresponds to only one, or a few, SWNTs. The other dominant feature in spectra from SWNT is the Radial Breathing Mode (RBM), which gives a peak at lower inverse wavenumber (120 - 250 cm^{-1}), and whose position is inversely proportional to the diameter of the SWNT. This is not observed in graphite, and rarely in MWNT and so is a strong confirmation of the presence of SWNT. In addition, since its position can be related to the diameter of the SWNT it enables analysis of the diameters of the SWNT present[5]. Figure 2.9 (c) shows the Raman spectra of the bare SiO_2/Si substrate, and (d) shows the RBM due to an individual SWNT of diameter $\sim$ 1 nm. The diameters observed using this technique were consistent with those from AFM analysis.

[5]It is important to note however, that only those SWNT in resonance with the laser will give an appreciable signal, hence it artificially selects a diameter range to probe anyway.

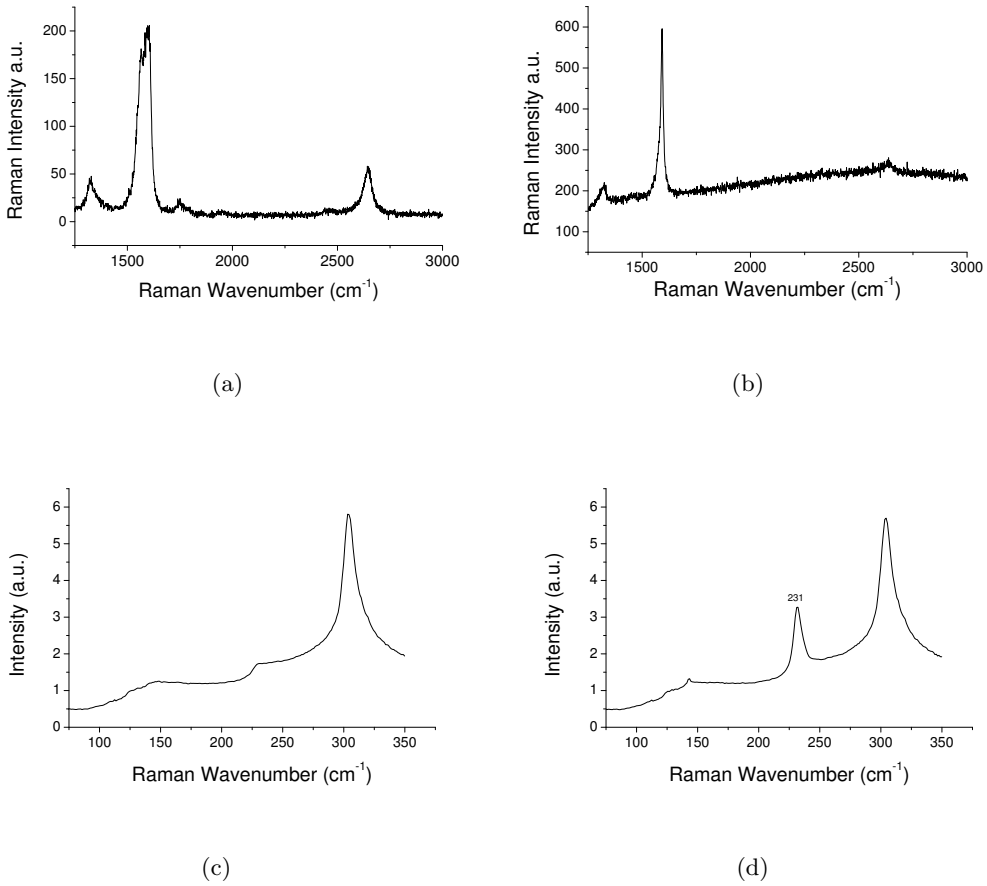

Figure 2.9: micro-Raman spectra of SWNTs taken with a Renishaw 1000 Raman microprobe. (a) and (b) using a HeNe laser (632 nm). (c) and (d) were taken with a near-IR laser (780 nm). (a) G band of untreated nanotube powder purchased from tubes@Rice, for comparison with (b) G band of a SWNT grown by cCVD. (c) Spectrum of bare SiO_2 substrate. (d) Radial Breathing Mode of a SWNT from the same sample used for (a). The position of the RBM identifies it as having a diameter of ≈ 1 nm. The spectra were taken at UMIST by Professor Robert Young.

2.2 SWNT devices

As outlined in Chapter 1 there has been a wealth of interest in the study of SWNT electronic devices, both for application based research and to study their fundamental properties. SWNT devices have been made in many different ways, and the techniques and materials have evolved as understanding has increased.

The connection of a molecule $\sim 10^{-9}$ m in diameter to macroscopic electrical leads $\sim 10^{-3}$ m in diameter is a considerable practical challenge. The basic techniques used are similar to those developed for semiconductor devices, and as such [Sze85] can be used as a basic reference text.

Initial experiments were dominated by poor contacts and damaged SWNTs, and failed to probe the inherent properties of the SWNTs. Most devices were made by laying SWNTs on top of metal electrodes, e.g. [TVD98, BCL$^+$97]. Instead, better electrical contact is made by placing the electrodes on top of the SWNTs allowing the formation of almost ideal contacts, e.g. [MJK$^+$03, JGW$^+$03]. The advent of cCVD grown SWNT has also dramatically affected SWNT device research. Initial experiments were dominated by tunnelling through defects in the SWNT, presumed to be caused by the processing procedures, which resulted in diffusive transport, e.g. [BCL$^+$97, TD00]. Recent experiments on cCVD grown SWNT have demonstrated ballistic transport in doped sSWNT [JGW$^+$03], and mean free paths of up to $l_{mfp} \approx 1.6$ μm in mSWNT at room temperature [PRY$^+$04].

SWNT device fabrication from cCVD grown SWNT is typically achieved in three different ways. Using lithographically defined catalyst islands, the positions of the SWNT on the substrate can be predetermined and electrodes positioned accordingly, e.g. [MYS$^+$03, JWY$^+$02]. Alternatively a random distribution of SWNT are grown on the substrate, alignment marks are then placed on the substrate and the position of the SWNTs relative to the marks are determined by AFM or FE-

SEM, and appropriate electrode patterns defined, e.g. [BLB+01, DGCF04] . Finally, SWNT can be grown randomly on the substrate, and then electrode patterns positioned on top without prior knowledge of the whereabouts of the SWNT. This final technique has a very low yield, however it is the least lithographically demanding. As a result, it was the technique chosen for the work presented here.

Lithography

Standard lithography techniques involve either the use of an adapted SEM, or a specialised system, for electron beam lithography (EBL), or the use of a 'mask-aligner' for photo-lithography. Unfortunately neither of these were available at Warwick University. Following a suggestion by Dr David Smith of the Physics Department, University of Southampton, a laser scanning confocal microscope (LSM) was used instead. Since this is not a standard lithographic pocedure[6], the capabilities and drawbacks of this technique are outlined below.

An LSM works in a similar way to an SEM, the laser light is focussed to a spot which is raster scanned in a plane perpendicular to the light beam. This is a very different technique to standard optical microscopy, where all the sample is continuously exposed to the light source. Analogously, unlike standard optical lithography using a mask aligner which involves simultaneous exposure of all areas of the sample to the UV source, LSM lithography works on a similar principle to EBL whereby the electron (or laser) beam is raster scanned over the sample, sequentially exposing areas of the substrate. The pattern which the laser spot traces is controlled by the software, and the beam can be quickly and effectively switched on and off using the optics inside the LSM. These are the requirements for use as a 'direct-write' lithography tool. 'Direct-write' implies that the lithographically defined pattern is not based on a solid unchangeable substrate, such as a mask for a mask aligner, but

[6] I have not seen the use of an LSM for lithography reported elsewhere.

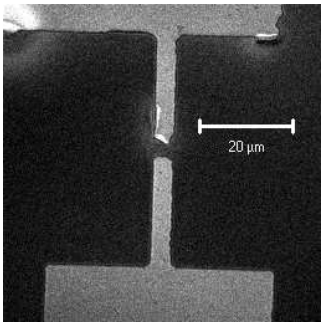

Figure 2.10: Metal electrodes under resist in the LSM.

is software defined. This allows different patterns to be designed and used as and when required.

The principle of lithography is that a material, or 'resist', is chemically modified by exposure to light of a certain frequency, or electron radiation. The modified positive (negative) resist becomes soluble (insoluble) in the developing solution, allowing selective removal of the exposed (unexposed) area. The LSM, although not designed or intended for lithographical use, has software designed to allow 'photobleaching' experiments. These require selective exposure of areas of a substrate at one laser frequency, and then the observation of the effect at another. The areas to be 'bleached' are defined on screen via the software, and patterns can be saved and used repeatedly. Hence, not only does the LSM allow lithographic definition of user defined patterns on the substrate, but also exact alignment, or 'registration', to existing features is possible by scanning at a laser frequency that the resist is insensitive to. The focussing system is roughly identical for both laser frequencies, hence focussing on the substrate can be done at the second laser frequency. Figure 2.10 shows an image from the LSM of gold electrodes under resist, the area to be exposed could subsequently be drawn onto the image with submicron registration.

The theoretical resolution of lithography with the LSM is diffraction limited

and given by

$$l_m \cong \frac{\lambda}{NA} \tag{2.1}$$

Where λ is the wavelength of the laser used, and NA is the numerical aperture of the lens system used. In practise proximity effects, resist thickness and sensitivity to depth of focus meant that the resolution obtained with a 458 nm laser, and a lens with NA of 0.8, was 1 - 2 μm. This could be reduced, however, by using a higher NA lens, or a UV laser. The UV laser was unavailable on the LSM at Warwick, a Zeiss LSM 510. Although higher NA lens' were available they were higher magnification, resulting in smaller scan sizes and hence smaller patterns. With the 20 $\times$ objective used, the lowest magnification lens that was available, the maximum scan size was 650 μm square.

The major disadvantage of the LSM for lithography was the time taken. The positive resist used, Shipley Microposit 1805, was designed for use with UV optical lithography. It was still sensitive to the 458 nm laser line of the HeNe laser, however the required dose rate was much higher. The time taken to expose one pattern of 650 μm square was $\sim$ 5 min. Each pattern must be exposed sequentially, rather than simultaneously as with a mask aligner. Since the resist was almost insensitive to the 543 nm laser line of the Ar laser, this was used for imaging prior to 'bleaching' of the resist. Shipley Microposit MF®-319 developer was used to remove the exposed areas of resist.

Recently a mask aligner was purchased. Unfortunately there was insufficient time to optimise its use for the fabrication of SWNT devices, although it was used to fabricate the calibration samples used in Chapter 5. The same resist and developer were used, however a resist residue was left after developing which was not present when using LSM lithography. A conventional 'ashing step'[7] to remove the photoresist residue and enable the formation of contaminant free contacts was not

[7]oxygen plasma etch

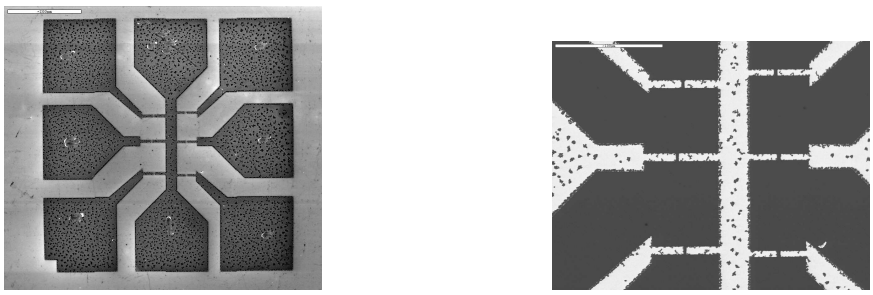

(a) (b)

Figure 2.11: (a) SEM image of an electrode pattern, and (b) back-scattered SEM image of the electrodes. Scale bars are (a) 200 μm, and (b) 100 μm.

possible as this would also destroy the SWNT.

Device Fabrication

Figure 2.11 shows SEM images of the pattern used. The large contact pads are 150 μm wide. The scratches on the pads are the marks left by the use of probers. Figure 3.2 in Chapter 3 shows an SEM image of a pattern after bonding. The lengths of the gaps (width of the electrodes), and widths of the gaps (separation of electrodes) were varied according to the concentration of SWNTs on the substrate. Typically gap lengths of 5 - 10 μm, and widths of 2 - 5 μm were used.

cCVD was used to grow SWNT at a low density (< 1 μm^{-2}), and with low catalyst concentration. High catalyst particle concentration on the surface after growth may effect electrical transport through the SWNT, and complicates AFM imaging[8]. Resist was then spun on the substrate and the electrode pattern defined by LSM lithography as described above. After developing the resist, thermal evaporation was used to deposit a layer of Au (45 - 70 nm) with an adhesive underlayer of Cr (5 - 10 nm)[9]. The metal on the resist was then removed by dissolving the resist

[8]Large catalyst particles increase the probability of damaging the AFM tip, as well as increasing the minimum lift height that can be used

[9]The evaporator used was an Edwards 306 thermal evaporator. Thanks to Frank Courtney of the Engineering Department.

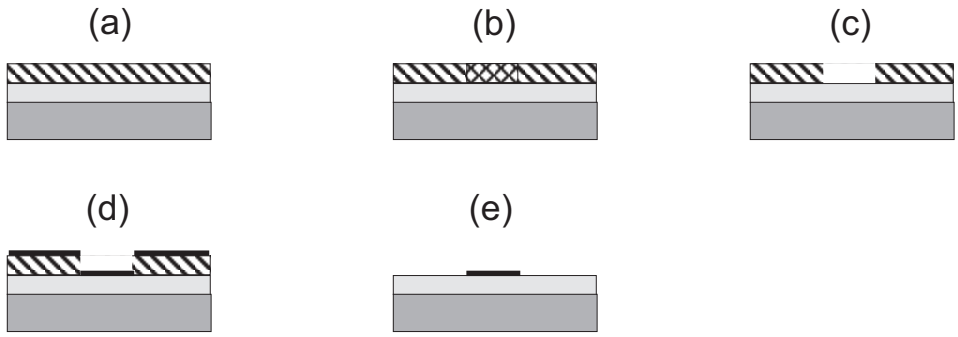

Figure 2.12: Schematic of the process used for the fabrication of electrodes. (a) Resist is spun onto a substrate giving a uniform thickness layer. (b) areas of the resist are exposed, and then (c) removed using the developer. (d) Metal is evaporated on top forming a uniform layer, discontinuous where the resist has been removed. (e) subsequent dissolving of the remaining resist 'lifts-off' the metal everywhere except where the resist was exposed.

in warm acetone and agitating. This 'lift-off' procedure is illustrated schematically in Figure 2.12. A short burst of ultrasound aids in the 'lift-off' process, however this could not be employed when fabricating the SWNT devices since ultrasound is known to damage the SWNT.

Following [RYP+02, YPR+04], the devices were then annealed by placing in an oven under a flow of Ar at 600 °C for 30 - 40 min. This has been found to considerably improve the contact resistances. A side product of the annealing process is the formation of insulating regions within the electrodes. These are clearly visible in optical, SEM, and SCM images as shown in Figures 2.11 and 2.13. The SCM image demonstrates that the areas are insulating, and the back-scattered SEM image, sensitive to atomic number, clearly shows that there is a reduced Au content. It is possible, therefore, that they correspond to regions of greater concentration of Cr, this would be consistent with the observation of improved contacts since Au with no sticking layer is known to make a good contact to SWNTs, e.g. [NCL00, YPR+04]. Following annealing the metal was also found to be more easily scratched, and less easily bonded, again consistent with a decrease in the Cr adhesive layer.

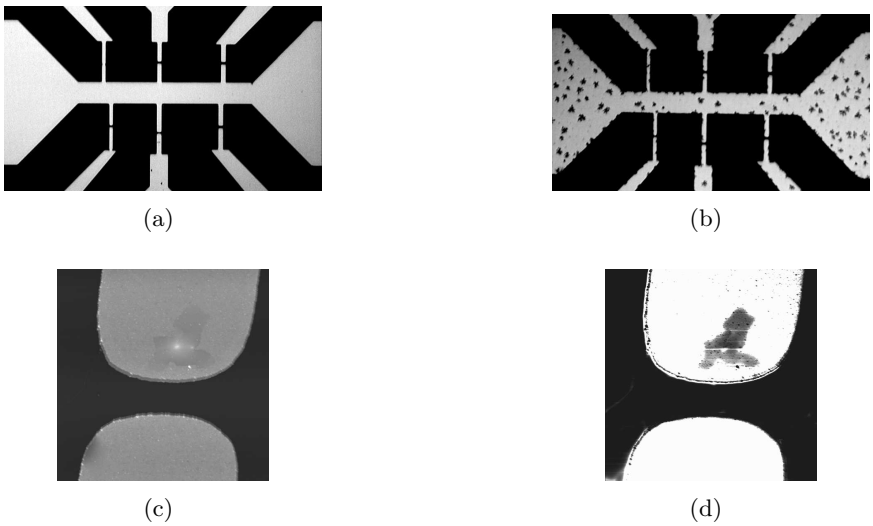

Figure 2.13: Optical images of electrode patterns before, (a), and after, (b), annealling. 10 μm square height image, (c), and SCM image, (d), of an electrode pattern after annealling.

2.2.1 Room Temperature Electronic Transport Characteristics

Characterisation of the electronic transport properties were performed at room temperature using a probe station. Back contact was made to the highly doped Si substrate, which was used as the gate electrode.[10] A schematic of the device is given in Figure 2.14. Voltages were applied using a Data Translation USB DAQ card, DT9804, controlled by Labview, which was also used to measure the current, after conversion to a voltage by an Ithaco 1211 current preamplifier. The current flowing through the device, i, was measured either as a function of the applied bias, V_{sd}, at constant gate voltage, V_G, the '$i - V_{sd}$ response', or as a function of V_G at constant V_{sd}, the 'gate response'.

Electrical transport through a three terminal device, such as described above, is effectively through three resistances in series: (i) the contact resistance between

[10]There was often a large leakage current between the source or drain contact on the surface and the gate electrode. Various wafers were used, all with oxide thicknesses of at least 300 nm. It is possible that the growth process induced defects in the oxide layer, making it more prone to breakthrough. The leakage currents were usually increased by the bonding process.

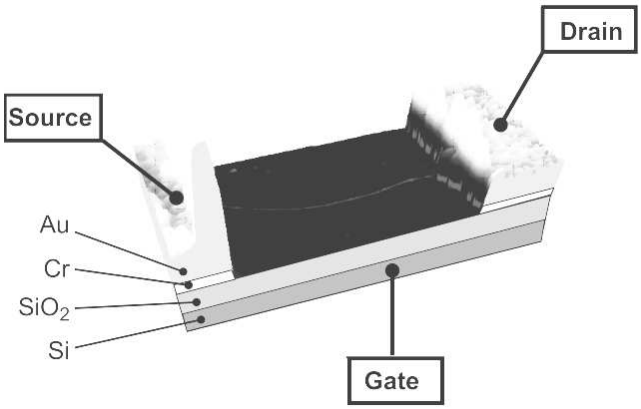

Figure 2.14: AFM topography image / schematic of a SWNT device.

the source electrode and the SWNT; (ii) the resistance of the SWNT itself; and (iii) the contact resistance between the SWNT and the drain electrode.

The resistance of the SWNT is composed of two parts: (i) the intrinsic resistance of the SWNT molecule, R_{int}, due to e.g. interaction effects such as electron-phonon scattering in the SWNT, or the absence of carriers in undoped sSWNT; (ii) defects in the SWNT will act as localised scattering centres with an associated resistance, R_{def}, probably both V_{sd} and V_G dependent.

The total contact resistance, R_c, is also composed of two parts. If tunnel barriers are created at the contacts, by e.g. Schottky barriers to sSWNT or contamination on the SWNT, there will be reflection of electronic states from the barriers, and an associated resistance, R_c'. However, even in the absence of scattering points at the contact, there is a 'quantised conductance' due to the crossover from the bulk contacts, with many modes for electron transport, to the SWNT, which has only four modes at low bias[11]. The quantised conductance is given by $G = Me^2/h$ [Dat95], where $M = 4$ is the number of modes for a SWNT. Hence, a SWNT device will have a quantised contribution to the resistance of $R_Q \sim 6.5$ kΩ.

[11] A two fold degeneracy in the K points, as discussed in Chapter 1, and a two fold spin degeneracy

The total resistance of a SWNT device is thus given by

$$R_{tot} = R'_c + R_Q + R_{int} + R_{def} \tag{2.2}$$

Standard transport experiments probe only R_{tot}. R'_c, R_{int} and R_{def} could all be both V_{sd} and V_G dependent, hence standard transport experiments using a three terminal device geometry cannot isolate the components of R_{tot}. [12]

Figure 2.15 shows the gate response from a SWNT device fabricated by the techniques described above. Of the devices whose conductance was due to an individual SWNT, the majority gave gate responses similar to this and can be identified as sSWNT devices. As the gate voltage is made more negative the SWNT is positively electrostatically doped, i.e. electrons are drawn out. The gate response shows that the device acts as a field effect transistor (FET), showing a low conductance state for $V_G > 0$, and a high conductance state for $V_G < 0$. For a typical device the ratio of high to low conductances is $\sim 10^5$. The low bias $i - V_{sd}$ response as a function of V_G is shown in the middle figure.

This behaviour is characteristic of a sSWNT device. The schematic at the bottom of Figure 2.15 explains the FET behaviour at the most basic level. The band structure near the Fermi level, E_F, is schematically represented by two parabolic bands with an energy gap between them, E_g, which is diameter dependent Eq. 1.13. At $V_G = 0$ the Fermi level lies in the gap, just above the top of the conduction band. Hence, there is only limited conduction through the sSWNT, and the dominant carriers are holes. Setting $V_G > 0$ raises the Fermi level further into the band gap, reducing the number of carriers and decreasing the conductance. Setting $V_G < 0$ lowers E_F into the conduction band, increasing the carrier density and hence increasing the conductance. The gate response thus implies that the sSWNT are 'p-doped'. This has been attributed to both chemical doping from gas and water

[12] A conventional four point probe approach cannot be used to remove the effect of contact resistances since the contacts are intrusive and influence the device under study.

vapour adsorption [CBIZ00, JLC00, KFZ$^+$00], electrical doping by the metal contacts [TVD98, RFTJ02], and doping by the SiO_2 substrate [MYSM04]. The most common metals used for forming the contacts, Au and Pd, are both found to produce 'p-type' behaviour, e.g. [RYP$^+$02, JGW$^+$03], whilst Co has been reported to produce 'n-type' sSWNT devices [RFTJ02]. Application of large positive V_G can electrostatically dope the sSWNT sufficiently to push E_F into the valence band, producing an ambipolar FET, e.g. [MDL$^+$01, RFTJ02, RYP$^+$02]. However, the observed mobility of electrons is lower than that of holes in p-type sSWNT devices.

Clearly the picture described above is a vast over simplification. For example, the source and drain electrodes screen the gate effect so that different areas of the SWNT will be gated to different extents, complicating the simple band structure explanation outlined above. R'_C is also likely to make a significant contribution to R_{tot}. A contact between a metal and semi-conductor is likely to form a Schottky barrier [Sze85]. Conduction through sSWNT FETs can be dominated by transport through these Schottky barriers, e.g. [HTD$^+$02, HRTA03], and the gate response is then due to changing the heights of the Schottky barriers. This effect has been studied using separate, independently addressable, gate electrodes on top of the device [WRAA03, BMM04], enabling the effect of gating the contacts or the bulk of the sSWNT to be studied independently. An AFM tip can also be used as a local gate, and the conductance of the device studied as the tip is scanned over it, e.g. [BFP$^+$00, TZKD00, WM02]. This is called Scanning Gate Microscopy (SGM), and is discussed in more detail in Chapter 3. Recently, the use of Pd contacts to large diameter ($\sim 2-3$ nm) sSWNT has been shown to result in ohmic contacts [JGW$^+$03].

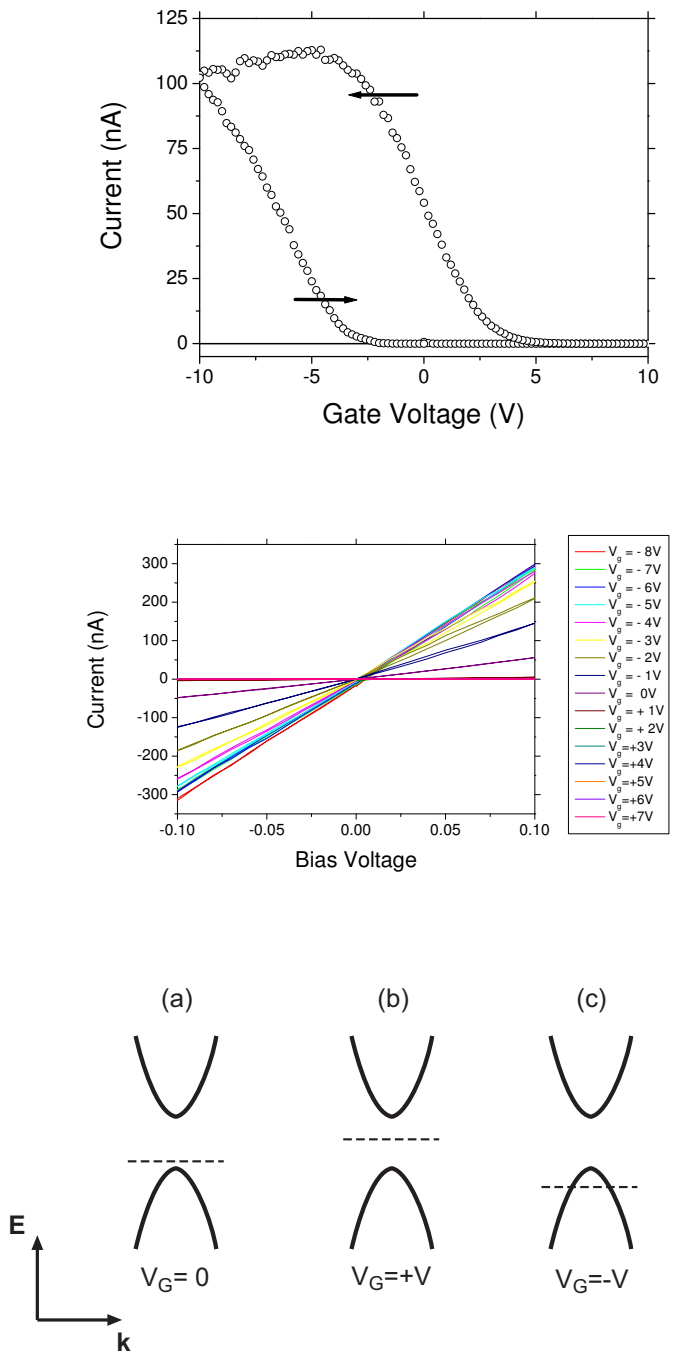

Figure 2.15: *top*, gate response of a sSWNT device, $V_{sd} = 25\ mV$. *centre* $i - V_{sd}$ response of a sSWNT at low bias voltages for different V_G. *bottom*, schematic explaining the gate dependence of the conductance. The dashed line represents the position of the Fermi level in the sSWNT at different gate voltages.

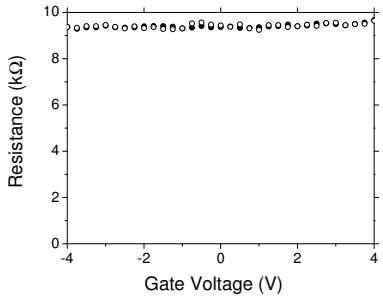

Figure 2.16: Gate response of a metallic SWNT device.

The transconductance of a device is defined to be

$$g_m = \frac{\partial i}{\partial V_G} \tag{2.3}$$

measured at constant V_{sd}. The transition from low conductance to high conductance in the gate response corresponds to a large transconductance. The upper figure in Figure 2.15 shows two curves, marked by arrows. The data was taken by starting at $V_G = 0\ V$, increasing to $V_G = 10\ V$, decreasing to $V_G = -10\ V$, and then returning to $V_G = 0\ V$. The arrows mark the direction of scanning. Clearly there is a large hysteresis in the transconductance of the device. This is always present, although seldom reported in the literature. The cause of this hysteresis has been attributed to moisture on the oxide surface, or charge traps in the oxide, and its use as a memory device has been suggested, see e.g. [RFTJ02]. This effect is studied in more detail in Chapter 3, however we note here that it has major implications for the application of SWNT devices. The dopant level of the SWNT is history dependent.

Figure 2.16 shows the gate response of a SWNT device made with EBL at the Niels Bohr Institute in Copenhagen with Dr Jesper Nygård. The gap width on this device was submicron. The absence of V_G dependence on the conduction implies that the density of states is constant, and hence it is a mSWNT device. However, this was the only device found which exhibited these characteristics. In general all devices showed gate dependence, although a significant fraction showed only a weak

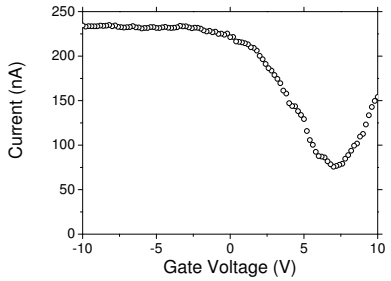

Figure 2.17: Gate response of a mSWNT device displaying weak V_G dependence, $V_{sd} = 25\ mV$.

dependence.

Individual SWNT devices which did not demonstrate true FET behaviour, characterised by complete suppression of the current at $V_G \gg 0$, usually exhibited a dip in the conductance at positive V_G. An example of this is given in Figure 2.17. This behaviour is consistent with small band gaps induced by curvature as explained in Chapter 1.1, however it has also been attributed to resonant defects, and gas molecule adsorption. These are sometimes referred to as small band gap sSWNT, however, we will still refer to them as mSWNT. These devices also show hysteresis in their transconductance, as with the sSWNT devices, however only one scan direction ($V_G = +10 \rightarrow -10\ V$) is shown in Figure 2.17 for clarity.

mSWNT devices with relatively high conductances ($R_{tot} < 100$ kΩ) exhibit

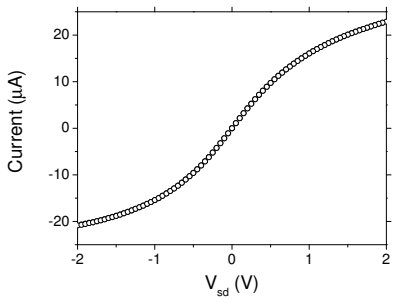

Figure 2.18: $i - V_{sd}$ response of a mSWNT device at $V_G = 0$ V.

an ohmic $i-V_{sd}$ response at low bias, but at high bias the current saturates [YKD00]. The $i - V_{sd}$ response of a typical mSWNT device is shown in Figure 2.18. The saturation current is 20 - 25 μA, independent of the low bias resistance of the device, and was proposed in [YKD00] to be due to the onset of electron-phonon scattering. Hence, it is similar to the well known velocity saturation in semiconductor devices [Sze85]. This effect is studied in more detail in Chapter 3. The $i - V_{sd}$ response of sSWNT devices gated to be highly conductive has also been found to exhibit current saturation, e.g. [JGW$^+$03]. This allows a simple method for characterising the number of SWNT connecting the electrodes in a device. The saturation current observed at large positive V_G, when the sSWNTs are also conducting, should be a multiple of $20 - 25$ μA.

2.3 Conclusions and future work

SWNTs have been grown by cCVD using different catalysts and different substrates. SWNT growth has been characterised by AFM, SCM, TEM, FESEM, micro-Raman spectroscopy, and the fabrication of electronic devices. In particular AFM reveals diameters in the range 0.8 - 3 nm implying that the carbon nanotubes grown are indeed SWNT. micro-Raman analysis confirmed the presence of individual SWNT, and was consistent with the diameter range observed by AFM. TEM demonstrated that little or no amorphous carbon was present, and again gave SWNT diameters consistent with AFM analysis. FESEM and SCM analysis showed the SWNT density to vary over the substrate after growth, and indicated the presence of long, apparently gas flow aligned, SWNT. Electronic device fabrication confirmed the presence of sSWNT and mSWNT. Further analysis of the SWNT devices will be presented in Chapter 3, and, to preempt, shows a low defect concentration in the cCVD grown SWNT.

Future work on cCVD growth will focus on the use of patterned catalyst for the formation of SWNT devices. In addition, as understanding of the growth process improves, control over the length of the SWNT grown will be striven for. In particular, we will focus on the growth of the long, flow aligned, SWNT for device applications, and samples of short ($\lesssim 5$ μm) SWNT suitable for the fabrication of SWNT-AFM tips as discussed in Chaper 4.

Improvements in SWNT device fabrication will initially focus on the optimisation of the use of the mask-aligner for the fabrication of large numbers of SWNT devices using patterned catalyst. Work will also focus on the easier task of fabricating multiple SWNT devices, and their application as sensor devices.

Chapter 3

EFM and SGM of carbon nanotube devices

Early in SWNT device research it was realised that AFM based techniques could make a significant contribution to the study of electronic transport through the devices. The use of scanned probe techniques, in combination with standard transport measurements, made it possible to bypass the limitations of standard device geometries outlined in the previous chapter. In particular, the use of a scanned probe enables individual sections of the SWNT in the device to be studied, allowing separate analysis of the different components of R_{tot}, Eq. 2.2. SGM was used to highlight the presence of defects [TD00], and Schottky barriers [FRZJ01], in sSWNT and their effect on transport. Resonant, spatially localised, defects in mSWNT were also identified by SGM [BLB$^+$01]. More recently variations on c-AFM have been used to characterise transport[1].The AFM tip was used as an electrical probe, enabling a third mobile contact to be made with a SWNT device [PRY$^+$04, YPR$^+$04, dPGNM$^+$02, FRCJ00].

[1]Standard c-AFM cannot be used due to the large lateral forces. Instead the SWNT is located in tapping mode AFM , or non-contact AFM, and then the tip is gently placed on the SWNT

AFM has also been used for manipulation of SWNT devices. The use of scanned probe techniques to manipulate as well as measure was made famous by the formation of the letters 'IBM' from Xenon atoms on Nickel by Don Eigler in 1990 [ES90]. AFM tips have been used mechanically to push SWNT around substrates. Due to the large Van der Waals attraction between SWNTs and the substrate, as discussed in Chapter 1, the SWNT will stay in the configuration into which it is pushed. This technique has been used to form tunneling barriers in mSWNT by creating regions of high local curvature, e.g. [BBH$^+$01]. Placing two such barriers close to each other ($<$ 100 nm apart) resulted in a quantum dot exhibiting room temperature Coulomb Blockade, [PTY$^+$01]. This was also achieved by using the AFM tip as an electrical probe, and applying a high bias between the tip and SWNT to electrically 'nick' the SWNT [PYB$^+$02]. Both of these techniques can be used to cut the SWNT completely. [TMD$^+$01] used an electrical pulse to cut a SWNT and then repositioned the ends to create contacts to a gold nanoparticle. This enabled transport measurements on an isolated 7 nm diameter gold nanoparticle to be made. EFM has also been used to study electrical transport through SWNT devices. It was this technique that originally confirmed that transport through mSWNT devices was ballistic, in contrast to transport through metallic MWNT which was shown to be diffusive [BFP$^+$00].

In this Chapter we illustrate the usefulness of EFM by applying it to study current saturation in mSWNT devices, and hysteresis effects due to surface charging. We demonstrate the use of AFM tips for manipulation of SWNT devices, and SGM for studying transport through SWNT devices, and the effects of defects in particular.

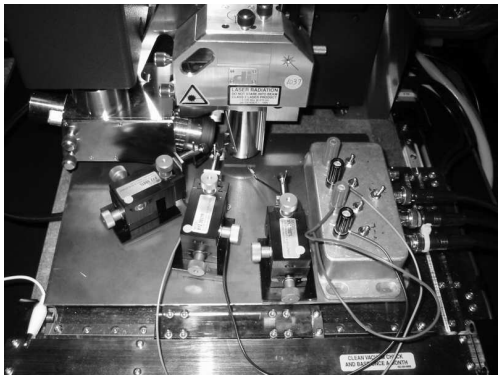

Figure 3.1: Experimental setup for multiple contact experiments on the Dimension AFM. The three probers shown enabled contact to source, drain, and gate electrodes. The tip voltage could be specified through the control software.

3.1 Experimental setup for EFM and SGM

The AFM's used were not designed to be compatible with the multiple contact electrical measurements required for EFM and SGM measurements. Experimental setups were thus designed to facilitate these measurements on both the Dimension and Multimode AFMs.

The Dimension is the easier of the two to configure for multiple contact transport experiments. The stage has a large sample area, and it is the tip that scans over the sample, so the stage is stationary during scanning. Hence, it is possible to simply use probers to contact the electrodes on the sample. Photographs of the setup are shown in Figure 3.1. The optical microscope incorporated into the Dimension is sufficient for aligning and placing the probes on the contact pads, and the vibration isolation table and acoustic hood provide a good, simple, Faraday cage.

The Multimode, by contrast, has very limited sample access once the tip is in place, and the sample moves relative to the rest of the AFM. Hence, it is not possible to simply use probers as in the Dimension. A printed circuit board (PCB) sample mount was designed to allow thin wires to be attached, which then extend from the front of the AFM sample area. The wires were required to be thin to minimimise

resistive forces on the movement of the sample during scanning, but were kept as short as possible, whilst still allowing free movement of the sample, to minimise electrical noise. Contact between the contact pads on the PCB ($\sim$ 1 mm square) and those on the sample (150 μm square) were made by bonding. Unfortunately the bonding process is irreversible, and occasionally punched through the oxide layer rendering the device useless. Once the sample was bonded and wired up the setup was easy to use, and did not noticeably effect the image quality. Electrical noise was dramatically reduced by the use of the Faraday cage constructed by the mechanical workshops in the Physics Department, University of Warwick. Figures 3.2, 3.3, and 3.4 demonstrate a sample bonded to a PCB, and the whole experimental setup for multiple connection measurements on the Multimode AFM.

Electrical connection to the tip was made through the Multimode itself, as was electrical connection to the piezo stack on which the sample sits. As a result two terminal measurements, involving the tip as one contact and the sample as the other, could be made simply, and without the need for cables extruding from the sample area. Measurements of this kind, such as c-AFM, were used extensively in the work presented in Chapter 4[2].

For both microscopes, external signals could be recorded by the AFM software, simultaneously to the conventional AFM signals, using the Signal Access Module. [3]

The results presented in this Chapter were performed on the Dimension AFM, however the preliminary results taken were on the Multimode, as were the majority of the results in Chapter 5.

[2]This was also the setup used for SCM, the electrical connection between the silicon substrate (which only had its top face oxidised) and metal puck on the grounded piezo stack proved to be sufficient.

[3]The Nanoscope IV controller also had four 16 bit inputs which could be used as well as / instead of the Signal Access Module.

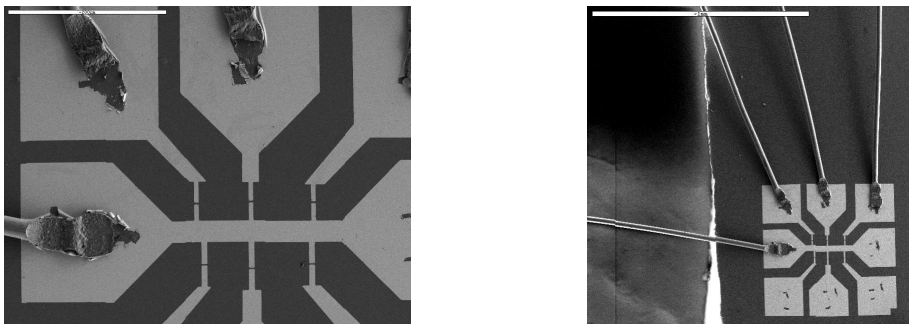

(a) (b)

Figure 3.2: The scale bars are (a) 200 μm, and (b) 1 mm. Taken with Steve York.

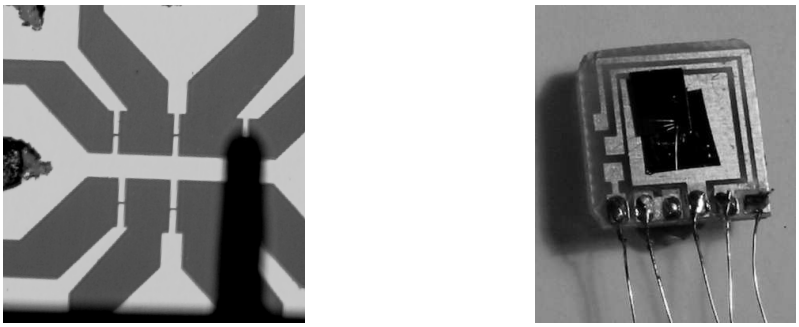

(a) (b)

Figure 3.3: (a) optical image from the Multimode optical microscope showing the cantilever over the bonded device. (b) photograph of a bonded sample on the PCB with wires attached. The PCB is $\sim$ 1 cm square.

Figure 3.4: Experimental setup for multiple contact experiments on the Multimode AFM.

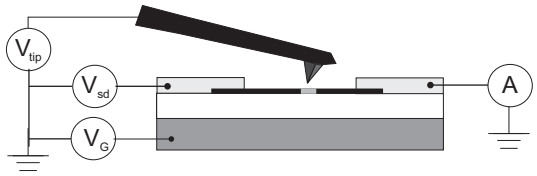

Figure 3.5: Schematic of the setup for SGM.

3.2 Manipulation of SWNT devices, and characterisation by SGM

In most cases the AFM is used as a non-invasive probe, and significant effort is made to minimise the perturbation of the sample by the probe. In this section we discuss the use of the AFM probe to perturb the sample, either mechanically or electrostatically. SGM was originally used to investigate electron transport through a point contact in a two dimensional electron gas (2DEG) [EBT$^+$96, TLaEJH$^+$00], and since then has been used to study 1D states in 2DEG's [CSSR00b, WVM$^+$01], and 2D transport through 2DEG's [CSSR00a]. SGM has also been applied to study carbon nanotube devices, e.g. [TD00, BFP$^+$00, BLB$^+$01, FRZJ01, WM02].

In SGM a conductive tip is scanned over the device whilst the current flowing through the device is recorded. The tip acts as a local gate electrode, locally shifting the Fermi level. The current image produced thus maps out the local sensitivity of conductance to the fermi level. Using lift-mode, the topography can be simultaneously recorded, allowing features in the height and SGM images to be correlated. A schematic of the setup is shown in Figure 3.5.

A SWNT device is ideally suited to study by SGM. Transport through SWNT is effectively through a 1D system. If we consider the SWNT to be divided into sections, classically the total resistance through the SWNT device is the sum of the resistances of the sections. Since most SWNT devices show fairly strong gate

(a) (b) (c)

Figure 3.6: 5 μm wide (a) topography, and (b) SGM image of a sSWNT device. (c) Linescan shown in the SGM image (11 line average). Sample courtesy of I. Radu, University of Washington. $V_{sd} = 0.1$ V, $V_G = 0$ V, $V_{tip} = 10$ V, $l_h = 20$ nm. The area shown is the gap between the source and drain electrodes (above and below the image).

dependence[4], the resistance of each section of the device can be strongly modulated by the tip voltage. As Figure 3.5 shows, there are 3 voltages which are specified in an SGM experiment; V_{sd}, V_G, and V_{tip}. Figure 3.6 shows an SGM image of a sSWNT device. V_G and V_{sd} were chosen so that the sSWNT device was in between its high conductance and low conductance state, i.e. at its most sensitive to the gate potential. A large tip potential, $V_{tip} = +10$ V, was applied. As the tip passes over the sSWNT it totally depletes the carriers from the sSWNT, suppressing conductance completely.

Figure 3.7 demonstrates another application of SGM. In the device shown 4 SWNT appear to cross the gap, however only one reveals any SGM response. Transport through the device is dominated by that SWNT. Note that the simultaneously recorded dc-EFM image cannot distinguish between the SWNTs.

Figure 3.8 demonstrates a more extreme perturbation possible with the AFM

[4]sSWNT device conductances are modulated by about 5 orders of magnitude by the back gate voltage, and most 'mSWNT' devices by a factor of at least 2

(a) (b) (c)

Figure 3.7: 5.5 μm wide (a) topography, (b) SGM, and (c) simultaneous dc-EFM image. The area shown is the gap between the source and drain electrodes (above and below the image).

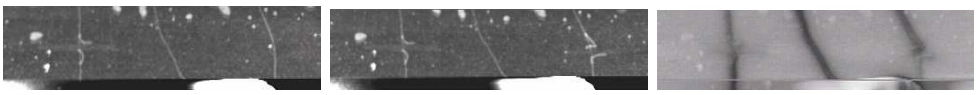

(a) (b) (c)

Figure 3.8: 4 μm wide (a) topography image showing one cut SWNT, (b) after cutting a second SWNT, (c) dc-EFM image taken simultaneously with (b). The area shown is the gap between the source and drain electrodes (above and below the image).

tip. Two SWNT are deliberately cut, leaving one remaining SWNT crossing the gap. When imaging in tapping mode it is possible to 'interleave' contact mode linescans. In this case, the area of the SWNT which was required to be cut was imaged at small scan size. The tip was then interleave scanned in contact mode with $V_{tip} = \pm 10$ V, mechanically cutting the SWNT.

Although in Figure 3.8 the SWNTs are obviously and deliberately cut, transport through SWNT can also be stopped without any topographically obvious cause. Figure 3.9 shows a topography and SSPM image of multiple SWNT crossing a gap. The SSPM image demonstrates that 2 of the 3 SWNT crossing the gap do not conduct all the way across, although there are no obvious topographic features to indicate this. The fact that both stop at the same horizontal line is indicative that the cause of the cut was the AFM tip. In this case the tip was scanning in SSPM mode at insufficient lift height. As a result the tip contacted the SWNTs, and cut them due to the large ac potentials applied to the tip in SSPM mode. Caution must be exercised when imaging the SWNT devices not to unintentionally mechanically

(a) (b)

Figure 3.9: 3 μm wide (a) topography image, and (b) SSPM image.

or electrically damage the SWNT.

The rest of the section presents an example of the use of SGM for studying transport through defects in SWNT devices. In this case the defect is artificially induced into the SWNT by mechanical pushing of the SWNT by the AFM tip. However, most SWNT devices have defects (or scattering points) on them at some gate voltages. Further examples of scattering from defects in SWNT devices will be given in Chapter 5.

Figure 3.10 shows topography images of a mSWNT device before and after the mechanical insertion of a kink. The position of the SWNT prior to insertion of the kink is still observable in (b). This is possibly indicative that a small amount of resist residue is left on the SWNT after device fabrication, this then stuck to the surface rather than the SWNT when it was moved. The measured height of the SWNT, and hence inferred diameter, is 1.6 - 1.7 nm.

A comparison of the gate response before and after insertion of the kink shows that the conductance has been greatly suppressed. The large dip in the conductance signifies a gap in the density of states[5]. This is confirmed by the $i - V_{sd}$ response, Figure 3.11. The formation of a curvature induced gap has been predicted theoretically, e.g. [CBC02, YH00], and used previously for the formation of short quantum dots in SWNT devices [PTY$^+$01, BBH$^+$01]. Here we study the effect of the kink using SGM, and directly associate a feature in the gate response of a SWNT device with a spatially localised feature in the device.

[5]The position of the dip in the gate response scan is chiefly determined by the hysteresis. The SGM images show that the Fermi level is at the lower edge of the gap.

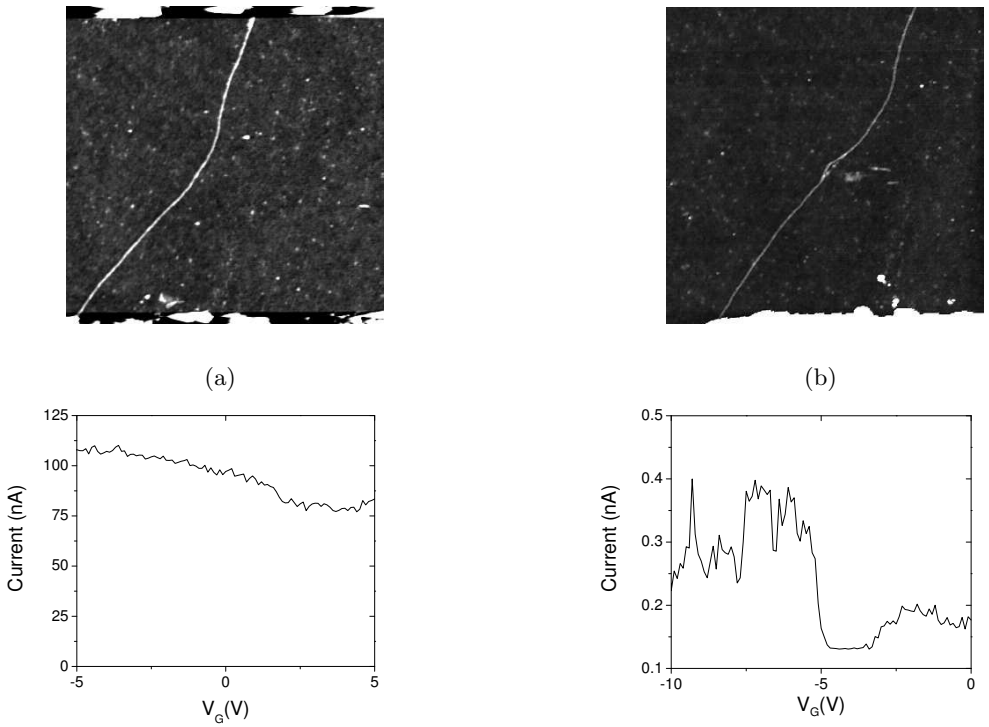

Figure 3.10: Topography images, and gate responses, of the device before (a), and after (b), insertion of a kink in the SWNT device. The topography image in (a) and (b) are 2.4 and 2.5 μm wide respectively.

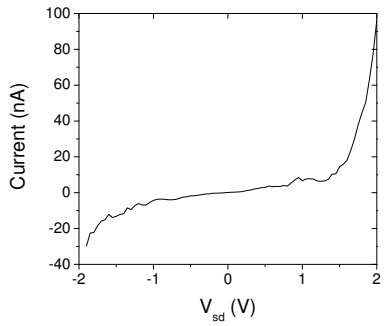

Figure 3.11: $i - V_{sd}$ response of the device after insertion of kink.

(a) height (b) SGM (c) dc-EFM

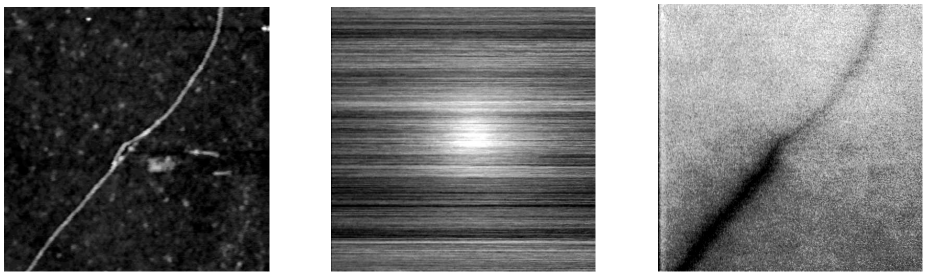

(d) height (e) SGM (f) dc-EFM

Figure 3.12: (a)-(c) 3 μm, and (d)-(f) 1.3 μm square images of the mSWNT device after insertion of the kink. (b) and (c) taken with $V_{sd} = -1$ V, $V_G = 0$ V, $V_{tip} = +1$ V and $l_h = 20$ nm. (e) and (f) taken with $V_{sd} = -1$ V, $V_G = 0$ V, $V_{tip} = -3$ V and $l_h = 20$ nm. The source electrode is above the image, and the drain electrode is at the lower edge.

Figure 3.12 shows SGM and dc-EFM images of the device at positive and negative V_{tip}. The source electrode is above the image and the drain electrode below. Hence when $V_{sd} = -1$ V, and $V_{tip} = +1$ V, greater contrast in the dc-EFM image is observed above the mSWNT closer to the upper source electrode. Whereas, for $V_{sd} = -1$ V, and $V_{tip} = -3$ V, the SWNT closer to the drain electrode gives greatest dc-EFM contrast. From the dc-EFM image it is clear that the majority of the potential is dropped at the kink, and hence the device resistance is dominated by the kink. At positive V_{tip} a dark spot is evident in the SGM image, corresponding to decreased conductance. The position of this spot correlates with the position of the kink. At negative V_{tip} the spot becomes light, indicating increased conductance.

Figure 3.13 shows a wider range of V_{tip}. As V_{tip} is made more negative the conductance increases further. However, at increasingly positive gate voltages the

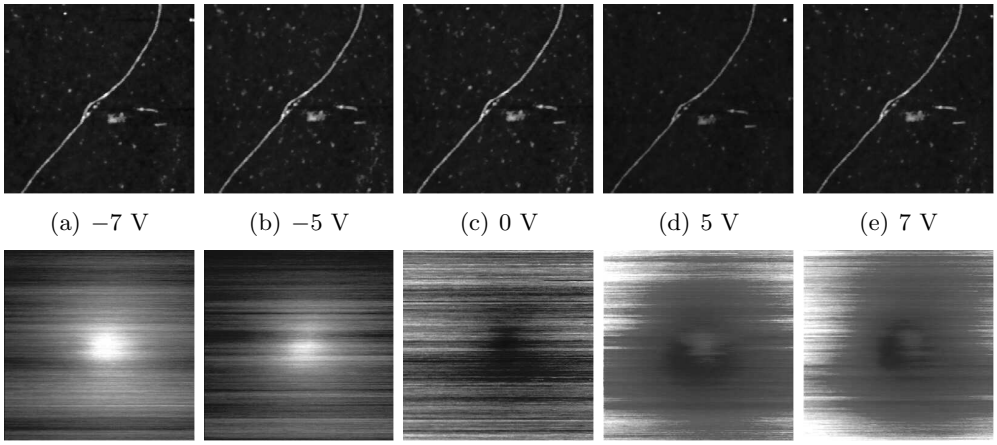

Figure 3.13: 1.3 μm topography and SGM images at different V_{tip}, $V_{sd} = -1$ V.

presence of a lighter spot within the dark spot becomes apparent. This indicates that the conductance through the kink reaches a minimum at low positive V_{tip} and then increases again, i.e. consistent with the dip in conductance seen in the gate response. Figure 3.14 shows the current through the device, as a function of V_{tip}, when the tip is over the kink. There is a distinct minimum in the conductance, and it correlates well with the gate response of the device, Figure 3.10. The current as a function of distance of the tip, $V_{tip} = 5$ V, from the kink is also shown in Figure 3.14. Increasing the separation between the tip and the kink reduces the gating effect of the tip. Increasing the separation is thus equivalent to decreasing the V_{tip}

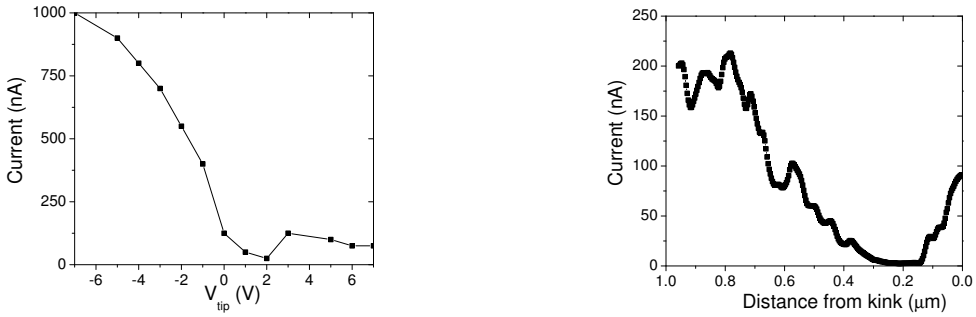

Figure 3.14: *left*; V_{tip} response of the device after insertion of kink. *right*; Current as a function of distance of the tip from the kink, $V_{tip} = 5$ V.

whilst the tip is above the kink. The similarity between the two effects is clear from the response.

SGM is a useful tool for the study of electronic transport through SWNT devices, and is particularly effective for the investigation of the contribution of defects to the device resistance. SGM also demonstrates the perturbative effect of a conducting tip on transport through SWNT devices.

3.3 SSPM of SWNT devices

The practical aspects of SSPM were setup according to [JKS99]. In particular an uncoated highly doped Si tip was used. As remarked in [JKS99], the use of uncoated tips improves the stability of the results relative to metal coated tips, which tend to wear rapidly. SSPM is an option within the AFM software and hence no extra hardware was required. In the software it is necessary to set not only l_h and V_{tip}^{ac}, but also the phase (Φ) between the reference signal used and the deflection signal. Additionally there are extra feedback parameters which are adjusted in the same way as normal. As suggested in [JKS99], the SSPM setup was calibrated before performing the experiments by imaging in SSPM above one of the electrodes away from the gap. A square wave potential was applied to the electrode, and the amplitude of oscillation of the tip observed as Φ was changed with the feedback loop turned off. The optimal value for Φ corresponds to the maximum amplitude, however it is easier to find the minimum response and then add 90°. The feedback parameters were then adjusted so that the observed potential matched the applied potential[6]. This could be achieved with a resolution $\lesssim$ 10 mV. The calibration procedure was repeated before each set of measurements.

[6]Both could be observed simultaneously on the screen by inputting the square wave potential through the Signal Access Module.

3.3.1 Current saturation in mSWNT devices

One of the first applications of EFM to the study of transport through SWNT devices proved that the conductance through mSWNT devices was ballistic, all the potential was dropped at the contacts [BFP$^+$00]. However, once the contacts were improved it was found that the conductance of mSWNT devices decreased with higher bias voltages. In fact, the current tends to a saturation value of ~ 25 μA [YKD00]. This value seemed to be independent of the length of the device, and was attributed to scattering of electrons from optical or zone boundary phonons. This would correspond to a change in transport through the device from ballistic transport at low bias, to diffusive at high bias. Yao et al., [YKD00], were using a standard three terminal device geometry and hence were unable to confirm this.

We applied SSPM to study transport through a mSWNT device demonstrating current saturation. The $i - V_{sd}$ response of the device is shown in Figure 3.15. Also shown is a plot of $R \equiv V_{sd}/i$ against V_{sd}. There is a simple linear dependence of R on V_{sd} for most of the applied voltage range, corresponding to

$$R = R_0 + V/I_0 \tag{3.1}$$

In this case $R_0 = 54$ kΩ, and the saturation current $I_0 = 24$ μA. As mentioned in Chapter 2.2, I_0 was consistently found to be around this value for all individual mSWNT devices showing current saturation.

A topography image of the device is shown in Figure 3.16, along with simultaneous SSPM and SGM measurements. The SGM image shows that the tip potential is not perturbing transport through the mSWNT device. This is one of the advantages of SSPM, and Kelvin probe methods in general, over other EFM techniques. The time average potential of the tip is equal to the local potential of the surface beneath the tip, hence its perturbing effect is minimised. In all the results that follow simultaneous SGM measurements were taken to confirm that the tip was

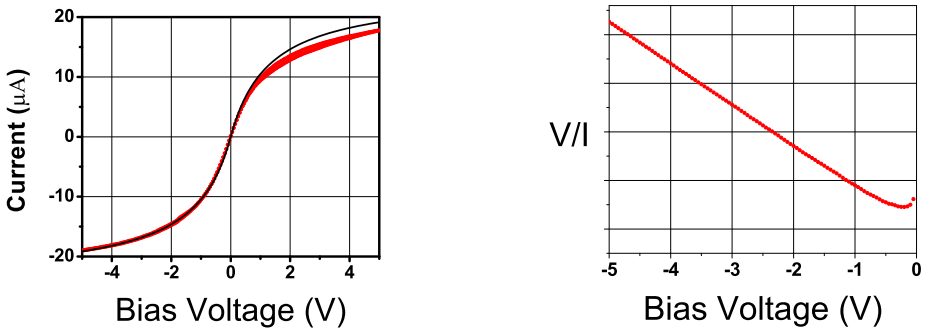

Figure 3.15: $i - V_{sd}$ response of a mSWNT device showing current saturation.

acting as a non-invasive probe, and hence an accurate representation of transport through the device was being given.

Although two SWNT can be seen in the image, only one crosses the gap. No other SWNT were found to cross the gap, hence transport through this device was due solely to the SWNT shown. The observed height of the SWNT is $\simeq 1.7$ nm. The second SWNT will always be at the potential of the upper electrode, since it is not connected to the lower one, thus providing a convenient reference.

Before presenting the results we consider how SSPM will differentiate between diffusive and ballistic transport in the SWNT. Figure 3.17 shows a simplified schematic of the potential along a SWNT device in both cases. In ballistic transport all the potential is dropped at the contacts, and the potential along the SWNT is

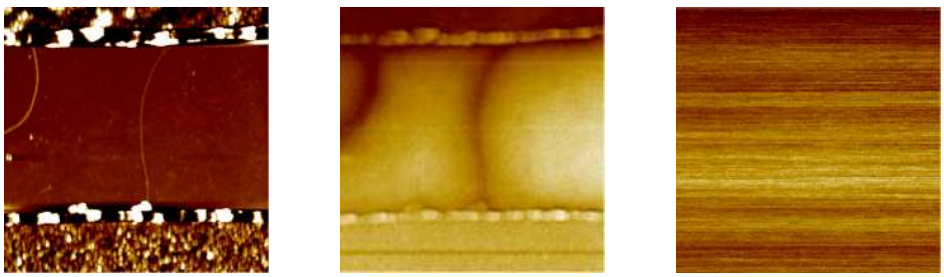

(a) height (b) SSPM (c) SGM

Figure 3.16: 4 μm square images of the mSWNT device, with $V_{sd} = -500$ mV. The lower electrode is the drain electrode.

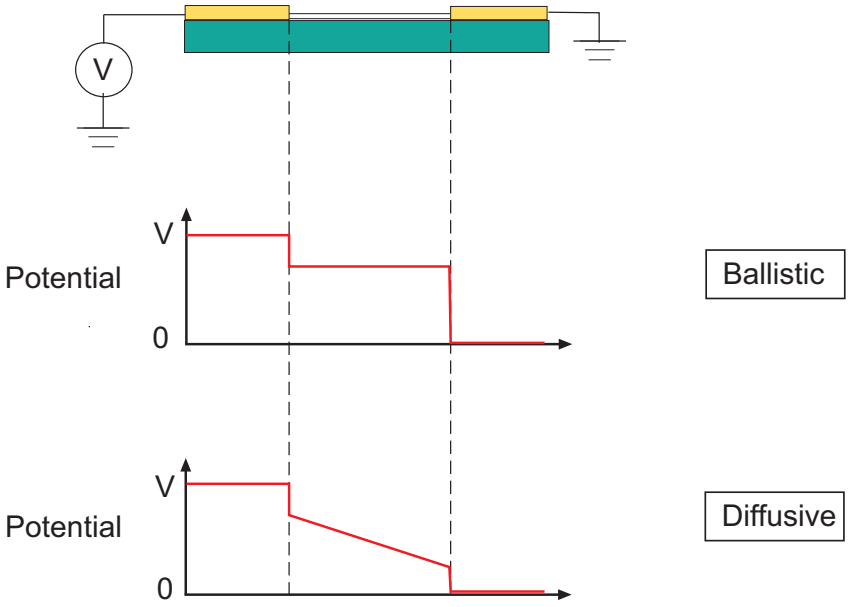

Figure 3.17: Simplified schematic demonstrating the variation in potential along the SWNT in a device for ballistic, and diffusive transport.

flat. I.e. the resistance of the device is completely dominated by the contacts (R_C), and the intrinsic resistance of the SWNT (R_{int}) is negligible. In the diffusive case there will still be potential drops at the contacts due to R_C. However, there is now also a significant contribution due to R_{int}, and hence the potential also drops linearly along the SWNT. The linear drop in potential is indicative of diffusive transport, rather than defect dominated transport. The presence of defects would result in steps in the potential along the SWNT.

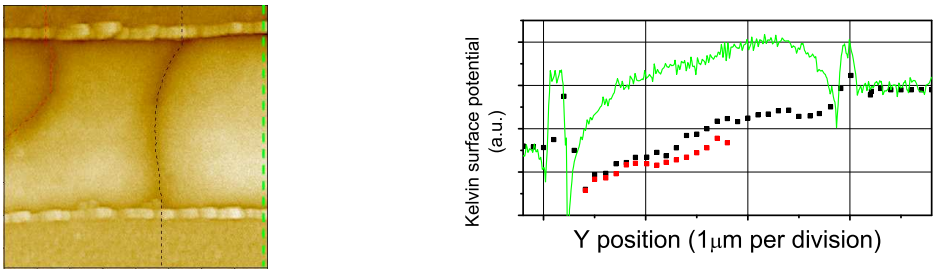

(a) $V_{sd} = -200$ mV

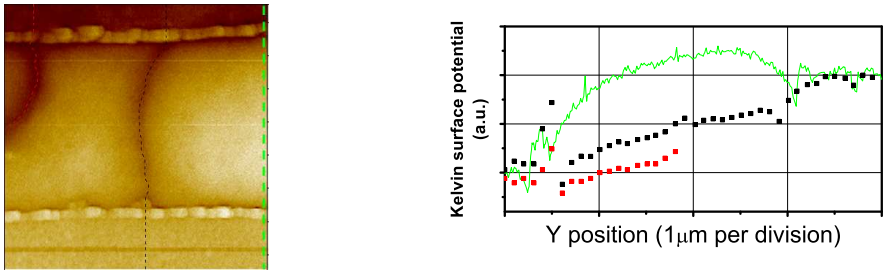

(b) $V_{sd} = -500$ mV

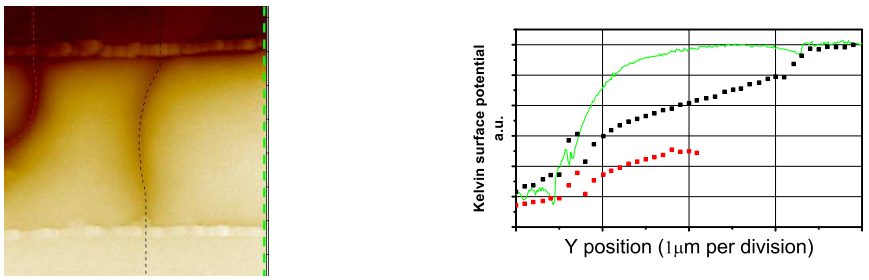

(c) $V_{sd} = -2$ V

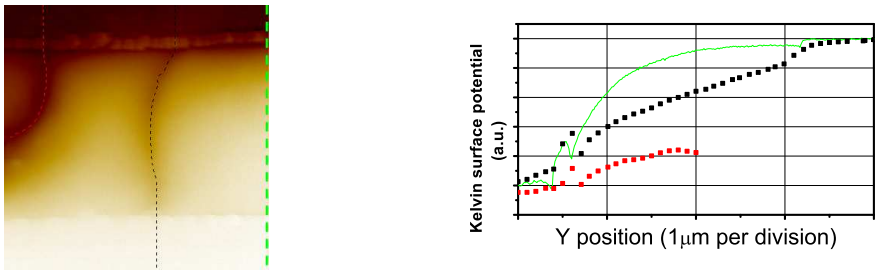

(d) $V_{sd} = -4$ V

Figure 3.18: 4 μm square SSPM images of the mSWNT device at low, (a) and (b), and high, (c) and (d), bias voltage.

Figure 3.18 shows SSPM images of the mSWNT device at low and high bias voltage. Also shown are linescans along the lines drawn on the images. The

term Kelvin surface potential (KSP) is used to explicitly make the point that it is not the actual local potential that is measured, but a weighted average. The KSP signal at each point is due to contributions from the tip-apex, tip-cone and cantilever as discussed in Chapter 1.2, and its relation to the actual local potential will be discussed in more detail in Chapter 5. Although the calibration procedure was followed, it would be misleading to have presented results in terms of potentials, hence the vertical axes of the linescans are in arbitrary units. A guide to the scales can be drawn from the fact that the potential difference between the source (upper) and drain (lower) electrodes is the bias voltage.

The red dotted line on the images corresponds to the topographic position of the unconnected SWNT, and the black dotted line to the SWNT crossing the gap. Each point in the KSP linescans along the SWNTs corresponds to an 11 line average of the KSP, at the position of the SWNT in the topography image (not shown). The green dashed line is a linescan through the gap, away from both SWNTs, to provide a second, 'background', reference. The long range dependence of the KSP signal is evident in this background signal, especially in (d) where the KSP signal clearly decays away from the source electrode at high bias.

Although this long range effect makes it difficult to interpret the KSP signal along the connected SWNT quantitatively, by comparing it with that of the unconnected SWNT, and the background, we can make some qualitative statements. In (a) the drop in KSP signal of both SWNT from the source electrode is evidence of the difference in workfunction between the Au electrode and the SWNT. We can estimate the difference in workfunction to be $\sim$ 100 mV by comparison with the bias voltage. The work function of Au is 5.1 eV, whilst that of SWNT is $\sim$ 5.0 eV [ZHL02], although it is thought to be diameter dependent. Also evident in (a) is that the KSP of the connected SWNT remains parallel to that of the unconnected SWNT, except for what appears to be a small step in the signal probably due to a

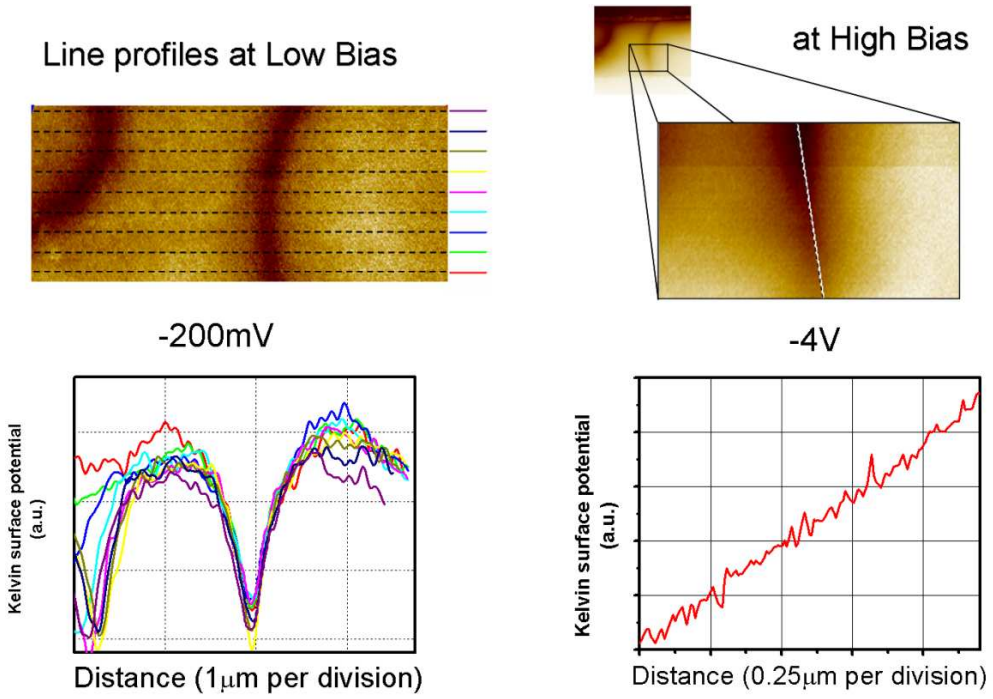

Figure 3.19: Fitted SSPM images comparing the behaviour at low and high bias

weak defect[7]. Hence, most of the potential is dropped at the contacts. This is even more evident in (b), where there is a clear drop in the KSP signal of the connected SWNT compared to the unconnected SWNT at the source electrode. After the drop the signals remain parallel.

By contrast the behaviour at high bias is markedly different. There is still an obvious KSP drop at the contacts, however the KSP signal along the connected SWNT also drops relative to both the unconnected SWNT and the background line.

Figure 3.19 shows the results from (a) and (d) after a plane-fitting procedure has been used to correct for the background signal. At low bias the KSP signal is constant along the SWNT, and hence transport through the SWNT is ballistic. Whereas at high bias there is a clear linear decrease in the KSP signal, indicating diffusive transport. We also note at this point that the SSPM linescans perpendicu-

[7]a weak scattering point was evident in SGM measurements taken separately.

lar to the SWNT, as shown in the low bias results of Figure 3.19, are Lorentzian in shape. This will be discussed in more detail in Chapter 5, and used as a calibration standard for the spatial resolution of tips for EFM.

In conclusion, we have used SSPM to directly image the transition from ballistic transport in mSWNT at low bias, to diffusive transport at high bias. This was complicated by the poor spatial resolution of SSPM, and the long range nature of the electrostatic forces, which result in significant contributions from objects several microns from the tip apex (in this case the source and drain electrodes). In order to study transport truly at the nanoscale, techniques with higher spatial resolution and fewer tip/cantilever artefacts are required. Chapter 5 addresses some of these issues, and demonstrates the increase in spatial resolution for EFM provided by the use of SWNT tips.

Since this work was orally presented at the March APS meeting 2003 in Austin Texas, two recent papers have been submitted by other authors addressing this topic. Paul McEuen's group from Cornell have studied high-field (i.e. high bias) transport in mSWNT devices using a SWNT tip as a mobile drain electrode, [PRY$^+$04]. Hongjie Dai's group in Stanford have studied current saturation in mSWNT devices with gap widths varying from ~ 10 μm - 10 nm [JGP$^+$04]. Both groups come to the conclusion that transport through mSWNT devices at high-bias is diffusive in devices $\gtrsim 50$ nm long, with inferred mean free paths of $l_{mfp} \sim 10$ - 15 nm. At low bias [JGP$^+$04] infer $l_{mfp} \sim 300$ - 600 nm, whilst [PRY$^+$04] find $l_{mfp} \sim 2$ μm (both at room temperature). These results are consistent with our results reported above, although the negligible potential drop along the SWNT at low bias over ~ 2.5 μm suggests a l_{mfp} closer to that of [PRY$^+$04]. Both groups found that higher currents could be achieved in shorter devices.

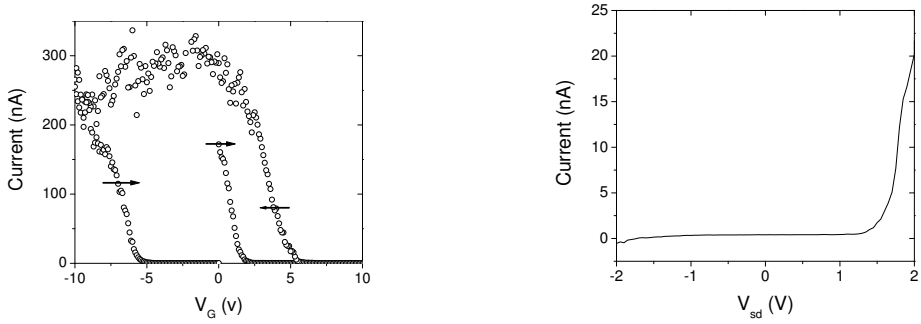

Figure 3.20: *left*; Gate response of the device taken at 1 V bias. *right*; $i - V_{sd}$ response at $V_G = 0$ V.

3.3.2 Hysteresis in the transconductance of SWNT devices

The hysteresis in the transconductance of SWNT devices mentioned in Chapter 2.2 is a generic feature of transport through SWNT devices (and possibly through any nanoscale device), although it is seldom reported. Its cause is the small diameter of the SWNT, as a result the electric field is concentrated at the SWNT surface. Approximating the SWNT and gate electrode as a cylindrical capacitor, the field at the SWNT is given by

$$E = \frac{V_G}{K r_{nt} \ln(R_G/r_{nt})} \approx \frac{V_G}{25 r_{nt}} \tag{3.2}$$

where $K = 3.9$ is the dielectric constant of SiO_2, $R_G \approx 500$ nm is the thickness of the oxide layer, and r_{nt} is the radius of the SWNT. Hence for a 2 nm diameter SWNT, with $V_G = 10$ V, the field is $E \approx 0.4$ V nm^{-1}, greater than the breakdown field of SiO_2 (~ 0.25 V nm^{-1}). The cause of the hysteresis has thus been proposed to be due to local charging around the SWNT as a result of the high electrical fields. The type of charging has been attributed to localised charge traps in the oxide [RFTJ02, FKDB02], or charging of adsorbed water molecules on the surface of the oxide and SWNT [KJV$^+$03]. Here we directly image injection of charge into the surroundings of the SWNT using SSPM, and correlate it with the observed change in conductance.

The gate response, and $i - V_{sd}$ response, of the device used are shown in

Figure 3.20[8]. The gate response was taken from $V_G = 0 \rightarrow +10 \rightarrow -10 \rightarrow 0$ V, and the hysteresis is obvious in the response. As noted in [RFTJ02] and [FKDB02], this can be used as a memory device. Figure 3.21 shows the current flowing through the device, $V_{sd} = 1$ V, after a series of alternating pulses of $V_G = \pm 10$ V. The change in conductance is over two orders of magnitude, reversible, and stable over relatively long time scales.

After a pulse of $V_G = +10$ V, during which the conductance through the device is greatly suppressed, the conductance is increased. From Figure 3.20, an increase in conductance is associated with negative V_G. Conversely, after a pulse of $V_G = -10$ V, during which the conductance through the device is greatly increased, the conductance is suppressed. Hence the negative pulse results in an effective positive V_G.

The effect of the V_G pulse is illustrated schematically in Figure 3.22. A positive V_G makes the SWNT in the device negative compared to its surroundings, increasing the Fermi level (and hence depleting p-type sSWNT of holes and decreas-

[8]In fact this was the same device as used for the SGM measurements at the start of this Chapter, a second kink increased the band gap further, making it behave as a semiconducting device. This had the advantage of moving the active area of the device away from the electrodes, where the Schottky barriers are situated in sSWNT devices, to areas where SSPM can image with less perturbation.

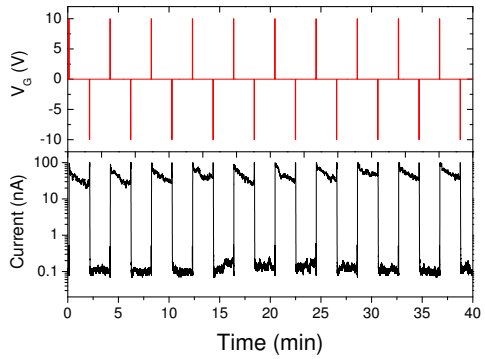

Figure 3.21: Current at 1 V bias through the device as a function of time, with pulses of $V_G = \pm 10$ V.

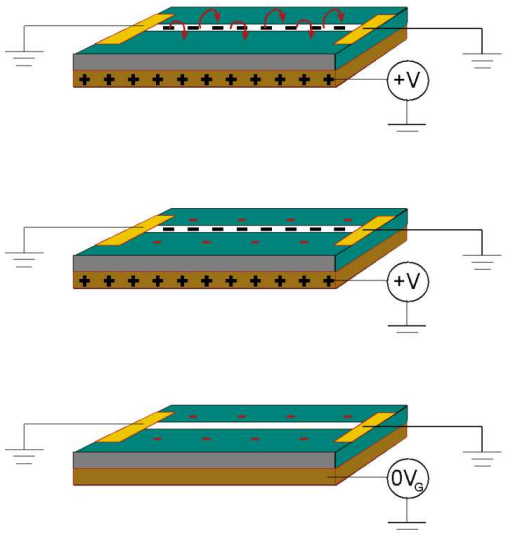

Figure 3.22: Schematic of the charge injection process

ing their conductance). The high local field results in injection of electrons into the region surrounding the SWNT, screening the effect of V_G on the SWNT. When V_G is set back to 0 V the injected charges remain. The SWNT is now positive relative to its surroundings, equivalent to a negative V_G.

The presence of charges on the sample can also be detected using SSPM. The force acting on the cantilever when an ac potential $V_{ac}(\omega)$ is applied to a system with applied dc potential V_{dc}, charge Q, and differences in work function $\Delta\Psi_{cpd}$ is, in analogy to Eq. 1.28 (see e.g. [DMJ+03]),

$$F(\omega) = \left(C'_{ts}(z) \left(V_{dc}^{appl.} + \Delta\Psi_{cpd} \right) + \frac{QC_{ts}}{4\pi\epsilon_0 z^2} \right) V_{ac} \tag{3.3}$$

Thus the injection of charge can also be visualised by SSPM, and positive charge will give the same sign response as a positive dc potential.

Figure 3.23 (a) shows a topography image of the device studied. (b)-(e) show SSPM images, and current flow through the device, and are in chronological order. (b) shows the device initially. The contrast between the metal electrodes is due to

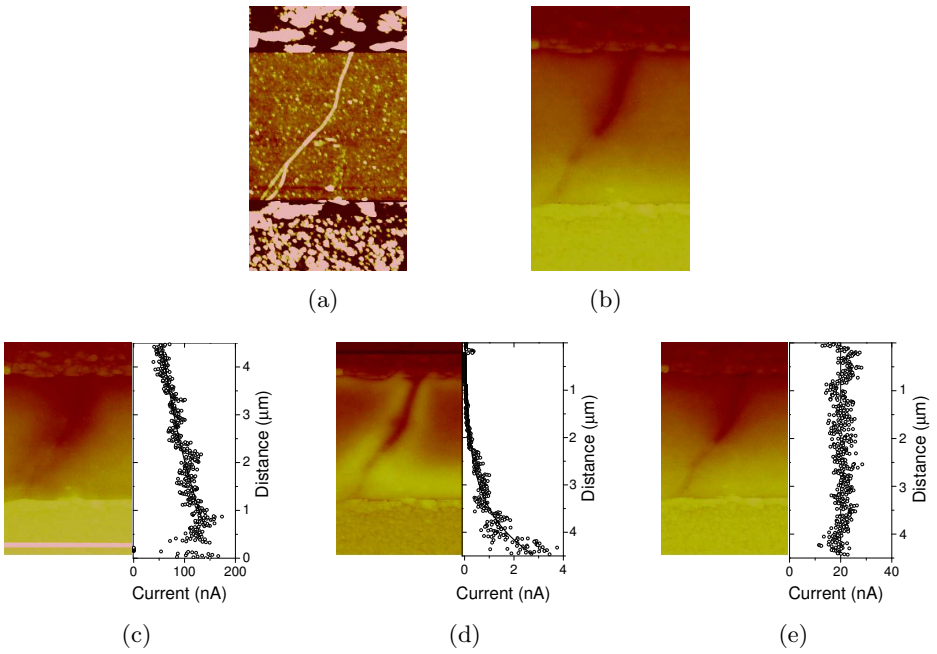

Figure 3.23: (a) topography and (b)-(e) SSPM images, with corresponding conductance through the devices. The applied bias is 1V, and except during pulses $V_G = 0$ V. (b) shows the initial state of the device, (c) after a $V_G = +10$ V pulse (scan direction upwards), and (d) after a $V_G = -10$ V pulse (scan direction upwards). Both pulses are visible in the images. (e) was taken half an hour after (d). The scan rate was 1 Hz, and each image took approximately 9 minutes.

the applied bias of 1 V, and the potential drops at the scattering sites along the SWNT are evident. In (c) the tip is scanning from the bottom upwards. A pulse of $V_G = 10$ V is applied at the start of the scan, evident by the white section of the lower electrode. The conductance is completely suppressed during the pulse, but is high after the pulse finishes. The time for each scan is ~ 9 minutes, so the y distance axis corresponds also to time (~ 2 minutes μm^{-1}). The conduction is gradually decreasing over time. Comparing the SSPM image with (b), darker areas surrounding the dark SWNT are evident, corresponding to induced negative charge. In the subsequent scan, (d), the tip is scanning downwards and a pulse of $V_G = -10$ V is applied at the start of the scan. The conductance is suppressed as a result of the pulse, and gradually increases over time. The line plotted is a fit of exponential

growth to the current data. The SSPM image shows lighter areas surrounding the SWNT, corresponding to positive charging of the substrate. The final image, (e), is taken half an hour later. The SSPM image has returned to its original appearance, and the current through the device is constant.

The SSPM results are thus consistent with the charge injection explanation of the hysteresis in the transconductance. The uniformity of the observed charge around the SWNT implies that the charge is not due to spatially localised charge traps[9]. The results are consistent with the charging being in an adsorbed water layer.

Control over this effect, and further understanding of it, is vital for the use of SWNT electronic devices. In particular SWNT sensor devices usually work by transducing the signal (for instance the presence of a chemical species) into a change in conductance of a sSWNT device. This works since sSWNT are very sensitive to their environment, however this sensitivity also results in a strong dependence on the injected charge. The use of passivation layers to reduce this effect has been reported, e.g. [MMA+03, KJV+03]. However, this obviously cannot be used in sensor applications. It is also important to note that the charge injection is a result only of the small diameter of the SWNT, and so could be evident in conduction experiments through other nanoscale devices. Due to the importance of this effect Professor Cobden's group in the Physics Department, University of Washington are continuing and extending the work presented above.

3.4 Conclusions and future work

We have demonstrated the use of scanned probe microscopy techniques as tools for the study of electronic transport through SWNT devices. The perturbative

[9] Unless the charge traps are distributed with separations less than the resolution of this technique, i.e. less than $\sim$ 100 nm

effect of the AFM tips can be capitalised upon in SGM to investigate the local gate dependence of transport through the device. The AFM tip can also be used to mechanically alter the device, either by cutting unwanted SWNTs, or creating kinks in a SWNT. Applied unperturbatively, the AFM tip was used in SSPM to demonstrate the transition from ballistic transport through a mSWNT device at low bias, to diffusive transport at high bias. The injection of charge into the substrate surrounding the SWNT at high gate voltages was also visualised using SSPM. Its presence was correlated with the conductance of the device, thus linking the charge injection to the hysteresis in the transconductance of SWNT devices.

Although we have shown both SGM and SSPM to give complementary information to standard transport measurements, the long range nature of the electric forces involved limits their spatial resolution. The non-local components of the SSPM signal complicate quantitative interpretation of the results, and the low (> 100 nm) spatial resolution does not allow investigation of transport truly at the nanoscale. SGM, although effective for studying the effect of defects in particular, also has a low spatial resolution. In addition, due to the SWNT devices being fairly noisy, SGM is only capable of distinguishing large changes in conductance, i.e. fairly strong scatterers.

In Chapter 5 we discuss the contributing factors to the spatial resolution of EFM in more detail, and ways in which to improve it. A novel form of SGM is also demonstrated, which shows not only increased spatial resolution, but also increased signal to noise performance, enabling it to discern weaker scatterers.

Chapter 4

SWNT as AFM probes

The remarkable physical properties of carbon nanotubes make them obvious candidates for AFM tips. The primary requirements of AFM tips for topographical imaging are that they are: (i) sharp, to maximise the spatial resolution; (ii) high aspect ratio, to enable probing of sharp or deep structures; and (iii) robust, to limit degradation of the tip during imaging. The small diameter of SWNTs clearly fulfils (i), their micrometer lengths combined with extreme stiffness provide a high aspect ratio probe (ii), and, crucially, their ability to bend and buckle under large strain rather than break [FCT+97], makes them extraordinarily robust (iii).

Conventional, commercially available AFM tips are fabricated from single crystal Si. This provides reproducible tips attached to well defined cantilevers. It is an exceptionally successful technology, creating tips which fulfil the requirements above, and incorporating them onto cantilevers whose dimensions can be varied to provide ranges of spring constants, resonance frequencies and Q factors. The tip used is usually chosen by compromise, since sharp high aspect ratio tips wear quickly. Tip wear is a significant problem, not only does it decrease the spatial resolution over time, but, more importantly, it also makes robust comparisons between different surfaces difficult.

The advent of MWNTs provided a material which could give sharp, high aspect ratio **and** robust tips. The discovery of SWNTs made a further increase in resolution possible. A SWNT is of similar diameter to biologically important molecules such as DNA. Hence, for example, the use of a SWNT with diameter < 1.2 nm should enable the double helix structure of DNA to be resolved.

Initial interest in carbon nanotube AFM tips has focussed primarily on high resolution imaging with SWNTs, e.g. [WWO$^+$98, CHL00, WSM$^+$04, BRM04], and high aspect ratio imaging with MWNTs, e.g. [CWCT03, PLC$^+$04]. The need for high aspect ratio probes increases as the size of the lithographically defined patterns used in the semiconductor industry decreases. 'Critical dimension metrology' requires high aspect ratio probes to accurately measure profiles of resist structures with sub-micron widths and micron scale height features. Conventional Si microfabricated probes typically have cone angles of $> 30°$, leading to strong convolution effects.

Carbon nanotubes can also be chemically functionalised, and have shown great promise for Chemical Force Microscopy (CFM) [WJW$^+$98, WWJL99, YZNL02]. CFM uses a tip with a specific chemical functionality to probe the surface chemistry of a sample. Using functionalised carbon nanotube AFM tips, CFM spatial resolution down to 3 nm has been demonstrated [WWJ$^+$98].

The high aspect ratio of the carbon nanotubes also makes them ideal for applications where long range forces are important, such as magnetic force microscopy (MFM) [KH03]. The use of longer carbon nanotubes removes the bulky tip cone further from the sample, increasing the relative contribution of the sharper tip apex to the magnetic force, and hence increasing the resolution. The electrical conductivity of SWNTs can also be exploited by using carbon nanotubes as high resolution EFM probes, the subject of Chapter 5. However, in general there has been little work capitalising upon the unique combination of exceptional electrical and mechanical

properties demonstrated by SWNTs. The possibility of using SWNT-AFM tips for c-AFM, and as conducting probes for electrochemical applications, will be briefly discussed later in this chapter.

We start by outlining the procedures used for the fabrication of SWNT-AFM tips, and the methods for characterising them. The advantages of SWNT-AFM tips for topographical imaging are then discussed. Electrical transport through the SWNT-AFM tips is investigated using liquid (Hg) and solid electrodes, and it is shown that reproducible electrical contacts can be made to the SWNT-AFM tips. Finally, a novel application of the SWNT-AFM tips as templates for the formation of metal nanowire-AFM tips is demonstrated.

4.1 Fabrication of SWNT-AFM tips

The primary complication to the widespread use of carbon nanotubes as AFM tips has been the difficulty in their fabrication. Initially MWNT sticking out from a mat of fibres were attached to the AFM tip using an optical microscope with nanomanipulators [DHR+96]. This had the unfortunate effect of selectively attaching the thicker MWNTs, which were visible optically. Modern versions of this technique use nanomanipulators in a FESEM, allowing thinner (down to $\sim$ 10 nm diameter) MWNTs to be attached, e.g. [LMF+02, PSMR04]. However this is a time consuming process, and it is not easy to envisage how this could be scaled up for mass production. MWNT tips made by this technique can be bought from various sources, for example Piezomax[1] sell a variety of MWNT-AFM probe tips at $ 450 - $ 750 per tip.

The advent of cCVD enabled a simpler solution, carbon nanotubes could be directly grown onto the tip. This was originally demonstrated by [HCL99] in 1999

[1] see www.piezomax.com

Figure 4.1: TEM image of a SWNT-AFM tip fabricated by cCVD growth directly onto the Si tip. Thanks to Steve York for help with the TEM

for fabricating MWNT-AFM tips, but SWNT-AFM tips soon followed in early 2000 [CHO$^+$00]. Since then there has been much interest in the use of cCVD for the fabrication of both MWNT-AFM tips, e.g. [PLC$^+$04], and SWNT-AFM tips, e.g. [CHL00, YWC$^+$02].

Initially we used cCVD for the fabrication of SWNT-AFM tips. Figure 4.1 shows a SWNT-AFM tip fabricated by direct growth of the SWNTs onto the Si tip. The catalyst used was ferric nitrate, with ethylene as the carbon feedstock. The catalyst particles, visible in the TEM image, were deposited everywhere on the tip, cantilever and tip body, and presumably SWNT growth occurred at all these places. However, imaging only occurs from the closest point on the tip to the sample, which will be the SWNTs protruding from the Si tip-apex, hence the presence of SWNTs elsewhere is unimportant.

It is clear from Figure 4.1 that the SWNT do not originate from the tip-apex but rather from further up the tip-cone. The Van der Waals attraction between the Si tip and the SWNTs is very large, as discussed in Chapter 1. The pyramidal tip thus acts as a funnel, directing all the SWNTs towards the tip-apex. This results in self-alignment of the SWNT-AFM tips so that, almost without exception, the

SWNTs are found to pass directly through the tip-apex. There are also large Van der Waals forces between the SWNTs themselves. As a result, if multiple SWNTs are present they will self-assemble into a bundle. We will subsequently refer to SWNT-AFM tips composed of bundles of SWNTs as 'nt tips'. The SWNTs are adhered to the tip by Van der Waals forces alone.

The main disadvantage of the cCVD technique for fabrication of SWNT-AFM tips was that it was time consuming. There was also a low yield due to the unpredictability of SWNT growth. The yield was especially low when trying to fabricate SWNT-AFM tips composed of an individual SWNT.

For the majority of the work in this Chapter, and Chapter 5, we used instead the 'pick-up' technique [HCOL01] to fabricate the SWNT-AFM tips.

The 'pick-up' technique

The pick-up technique relies on the occasional SWNT growth substrate containing a significant concentration of SWNTs which do not lie flat on the surface, but instead point away from it. The pick-up process is illustrated schematically in Figure 4.2. If a SWNT pointing away from the substrate surface is in the path of the scanning tip, the SWNT will become adhered to the tip due to the strong Van der Waals interaction. The Van der Waals interaction is strong enough that the SWNT will

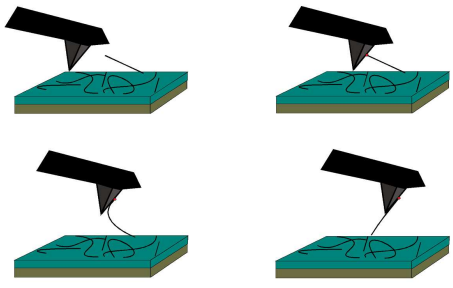

Figure 4.2: Schematic of the pick-up process.

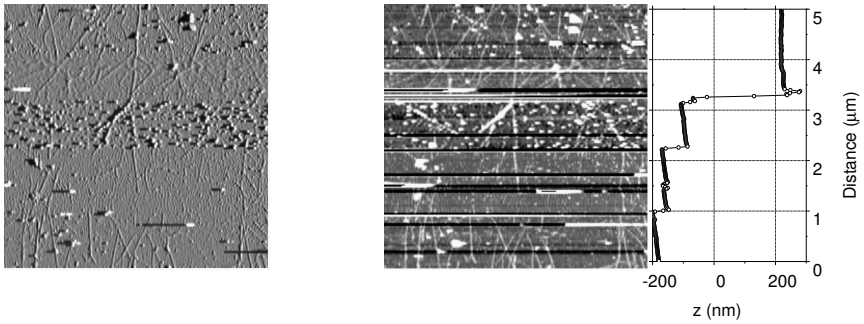

Figure 4.3: 5 μm square *left* amplitude and *right* flattened height images whilst scanning a pick-up sample. *far right* The corresponding z position of the tip.

maximise its length in contact with the tip by passing through the tip-apex. If the SWNT was pointing at an angle to the surface, then some of its length will extend beyond the tip-apex, creating a SWNT-AFM tip. If the scan is continued, and another SWNT pointing away from the surface is encountered, then multiple SWNTs can be attached, and an nt tip formed. As in the cCVD grown nt tips, the SWNTs tend to stick together, forming bundles.

Figure 4.3 shows height (a), and amplitude (b), images taken whilst scanning a SiO_2 substrate with cCVD grown SWNTs[2]. The fast scan axis is from left to right, and the start of the image is at the bottom. The z profile shows a series of jumps in the tip position. The SiO_2 surface is flat, hence a jump in the z position corresponds to the attachment of a SWNT to the tip-apex. The jumps also correlate with changes in the amplitude and height images. Picking up a SWNT usually results in not only a jump in the z position of the tip, but also a reduction in magnitude of the amplitude image, and a decrease in resolution of the height image. These effects can also be created by picking up contaminants from the surface, and so cannot by themselves be taken as proof of the attachment of a SWNT.

The pick-up technique for the formation of nt tips is a high yield (approaching 100%), and rapid process. In principle, the pick-up technique can be used for tips

[2]All AFM results presented in this Chapter were performed on the Multimode AFM at the University of Warwick.

with arbitrary coatings. This is of particular importance for the study of electrical transport through nt tips, as discussed later in this chapter. A major disadvantage of cCVD growth for the formation of nt tips is the limitations placed on the tip materials. For instance, the high growth temperatures, and sensitivity of SWNT growth to substrate interactions, precludes the use of metal coated tips[3].

An additional advantage of the pick-up technique is its versatility for the formation of nt tips of varying diameters. Increasing the area being scanned increases the probability of picking up SWNTs. When trying to attach only one, or a few, SWNTs an area of around 5 - 10 μm square is typically used, although this is obviously sample dependent. For the fabrication of larger nt tips, scan sizes of up to $\sim$ 50 μm square are used. This enables nt tips composed of from 1 to $\sim$ 500 SWNTs to be formed as desired.

There are two major practical limitations to the pick-up technique. The first is the difficulty of fabrication of suitable growth samples. This is an area we are still pursuing, and trying to understand. The second is the difficulty in scaling up the process to batch fabrication of SWNT-AFM tips. cCVD growth has been demonstrated for the formation of SWNT-AFM tips at the wafer scale, [YWC$^+$02], and the yield is likely to increase as the understanding of the growth process increases. The recent advances in dispersion of SWNT in aqueous solution, discussed previously, has also led to preliminary work on the fabrication of SWNT-AFM tips from solution, e.g. [HMS$^+$03]. Due to the negligible cost of both of these techniques, and obvious scalability to mass production, it is likely that in the future nt tips will become commercially available, and widely used.

[3]It is possible to use a supported catalyst on Mo, e.g. [ZCC$^+$01], however Mo does not make a good contact to the SWNTs, and is hence also unlikely to make a stable nt tip (see discussion later in the Chapter).

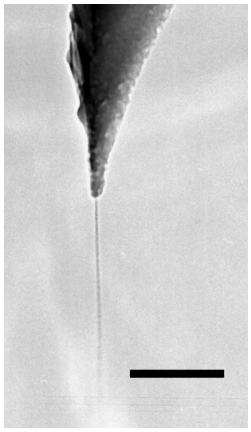

Figure 4.4: TEM image of an nt tip fabricated by the pick-up technique. The scale bar is 200 nm.

Electrical Pulse Shortening

After pick-up the length, l_{nt}, of the bundle protruding past the tip apex can be up to a few micrometers[4]. A TEM image of an nt tip after pick-up is shown in Figure 4.4. The blurring of the lower end of the nt tip is indicative of the thermally induced vibration of the SWNTs. The axial force the nt tip can sustain before buckling is also dependent on l_{nt}, so prior to use for imaging the nt tips must be shortened.

Appendix A derives the following formulae for the critical force required to buckle the nt tip, F_b, and its lateral spring constant[5], k_l:

$$F_b = \frac{\pi^2 \alpha_{nt}}{l_{nt}^2} \tag{4.1}$$

$$k_l = \frac{3\ \alpha_{nt}}{l_{nt}^3} \tag{4.2}$$

α_{nt} is the 'flexural rigidity', which for an nt tip is

$$\alpha_{nt} = \frac{Y_{nt} \pi r_{nt}^4}{4} \tag{4.3}$$

where r_{nt} is the radius of the nt tip. The lateral amplitude of thermal oscillation of

[4] this is also true after cCVD growth, and the following applies equally to cCVD grown nt tips

[5] i.e. relating the lateral displacement of the end of the nt tip to the magnitude of the force applied perpendicular to it

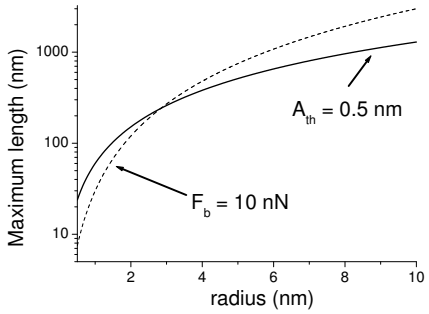

Figure 4.5: Length of nt tip giving $A_{th} = 0.5$ nm (solid line), and $F_b = 10$ nN (dashed line), plotted as a function of nt tip radius.

the end of the nt tip, A_{th}, is then given by the equipartition theorem

$$A_{th} = \sqrt{\frac{k_B T}{k_l}} \tag{4.4}$$

Using $Y_{nt} \approx 1$ TPa, and measuring r_{nt} and l_{nt} in nm, we find

$$F_b \approx \quad 1000 \left(\frac{\pi r_{nt}^2}{l_{nt}}\right)^2 \qquad nN \tag{4.5}$$

$$k_l \approx \quad 3 \times 10^3 \, \frac{r_{nt}^4}{l_{nt}^3} \qquad N\ m^{-1} \tag{4.6}$$

$$A_{th} \approx \quad 1 \times 10^{-3} \sqrt{\frac{l_{nt}^3}{r_{nt}^4}} \qquad nm \tag{4.7}$$

In order to enable imaging in tapping mode the nt tip must be sufficiently resistive to axial loading forces, a suitable limit is $F_b \gtrsim 10$ nN. A limit should also be placed on A_{th}, since the effective imaging diameter of the nt tip will be increased by thermal oscillations, typically $A_{th} \lesssim 0.5$ nm is sufficient. The nt tip should be shortened so that it satisfies both of these conditions. The maximum l_{nt}, for given r_{nt}, is plotted for each of these conditions in Figure 4.5. Given an nt tip of diameter 6 nm, it must be shortened to $l_{nt} \lesssim 200$ nm. This is achieved by electrical pulse etching, [HCOL01].

Applying short (~ 50 μs) voltage pulses whilst imaging a conductive surface removes sections from the end of the nt tip. The length removed is dependent on the magnitude of the voltage pulse. Typically voltages in the range 5 - 10 V were

used[6], each nt tip is slightly different and so the voltage required varied from tip to tip. The voltage pulses are repeated until the nt tip is short enough to image satisfactorily. Initially, Au and highly doped Si substrates were used, however, it was found that Pd is an ideal shortening substrate[7]. Pd is inert, forms a good electrical contact to SWNTs, and has a fine grain structure. The Pd grains are $\sim 10-20$ nm in diameter, providing an excellent test substrate for the spatial resolution of the nt tips whilst shortening.

Examples of images taken during the shortening process are shown in Figures 4.6 (a) and (b), and a high resolution image of the Pd surface taken with an nt tip after shortening in (c). The z profiles of the shortening images demonstrate that $\sim$ 50 nm can be removed sequentially from the end of the nt tip. With care this amount can be reduced, and it can trivially be increased by using larger voltage pulses. The increase in the image quality as l_{nt} is reduced is obvious.

The details of the shortening process are not well understood. After most voltage pulses there are no obvious remains on the surface, and so we can postulate that the end of the SWNT has been vapourised by the large pulse of current. However, occasionally a section of SWNT bundle is observed on the substrate after a pulse. For example, in Figure 4.6 (b) a short section is clearly observable in the upper portion of the image. The start of the section correlates with the position of a voltage pulse, and its length is equal to the step change in the z position[8]. The diameter of the section, $\sim$ 3 nm, provides a guide to the diameter of the nt tip.

[6] the pulses were applied using a Data Translation DT3016 DAQ card, controlled by Labview
[7] evaporated Pd (60 nm) on highly doped Si with an adhesive Ti (10 nm) underlayer
[8] i.e. its length is equal to the decrease in l_{nt}

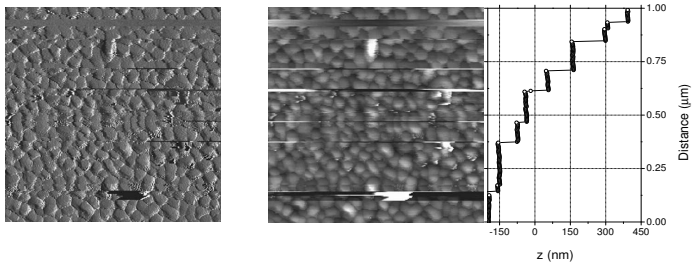

(a)

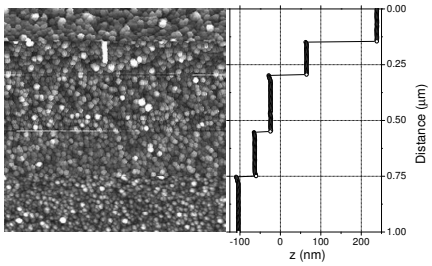

(b)

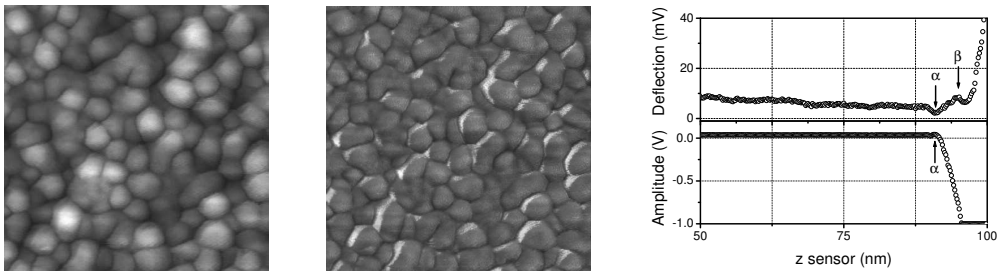

(c)

Figure 4.6: (a) *left* amplitude, *right* height, and *far right* average y - z profile of a Pd surface during shortening, similarly height and y - z profiles in (b). (c) 200 nm square *left* height and *centre* phase images of Pd surface taken with an nt tip after shortening, and *right* a force curve demonstrating the buckling response of the nt tip used.

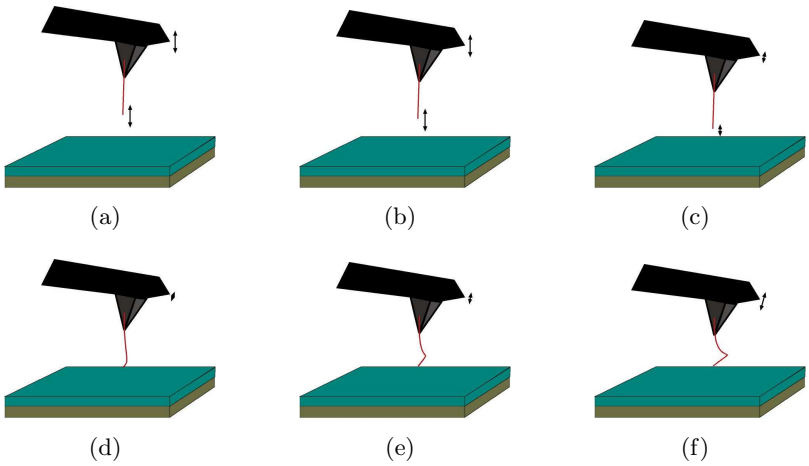

Figure 4.7: Schematic of the buckling of an nt tip.

4.1.1 Characterisation

Force curve analysis

The primary characterisation technique used for nt tips was force curve analysis. One of the fundamental characteristics of carbon nanotube tips is that they buckle, rather than break, when subjected to axial loads, [DHR+96]. This is almost unique, and so can be used to positively identify the presence of carbon nanotubes attached to the AFM tip. Force curves were performed in tapping mode, as described in Section 1.2. Figure 4.7 demonstrates schematically the behaviour of the oscillating SWNT-AFM tip as it is lowered towards the surface, and Figure 4.8 (a) shows a typical amplitude and deflection response of an nt tip.

Away from the surface the tip oscillates with free amplitude A_0. As the tip is lowered the SWNT(s) will start to contact the surface, point α, damping the oscillation as for a normal tip. As the tip is lowered further the axial force on the SWNT(s) will increase, damping the oscillation further. In contrast to a normal tip[9], once the axial force on the SWNT(s) exceeds F_b the SWNT(s) will buckle, point β. This process is reversible, hence the amplitude signal will start to gradually increase

[9]see page 28

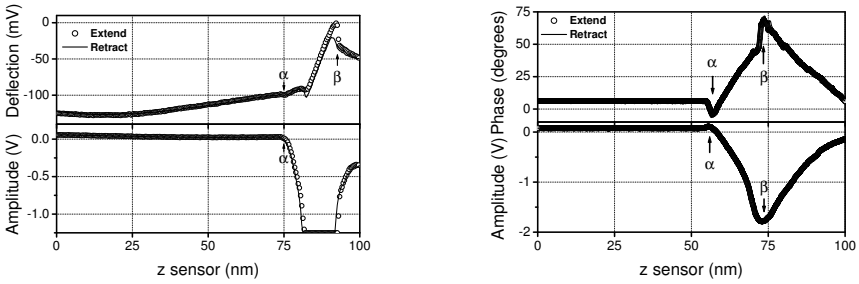

(a) (b)

Figure 4.8: (a) simultaneous deflection and amplitude, and (b) simultaneous phase and amplitude response of the buckling of different nt tips. Note that ∘ corresponds to the 'extend', and the solid line to the 'retract' response.

as the tip is lowered further. The resistance to flexion of the buckle in the SWNT(s) is small, so the amplitude returns to almost its free value as the tip is lowered further still.

The degree to which the amplitude is damped before the SWNT(s) buckle depends on F_b. For stiff nt tips the amplitude will be damped completely, as in Figure 4.7 (a), and the cantilever will start to deflect. The point of buckling will then also be evident in the deflection signal. For very short nt tips there will be no increase in the amplitude signal after buckling, since the Si tip itself will then be in contact with the surface. The presence of the SWNT(s) is then only apparent from the deflection signal. An example of this is shown in Figure 4.6 (c), from the deflection response we can see that $l_{nt} \lesssim 10$ nm.

Figure 4.8 (b) shows simultaneously recorded amplitude and phase response of an nt tip. The buckling of the SWNT(s) is clearly visible in the phase response, as is the subsequent decrease in repulsive, or damping, force. The buckling response of multiple SWNTs can often be seen in the amplitude response, for example in Figure 4.9, confirming the presence of at least 4 SWNTs.

Repeated force curve analysis on nt tips appears to have no damaging effect, not the case for conventional Si tips, even when lowering the tip significantly past

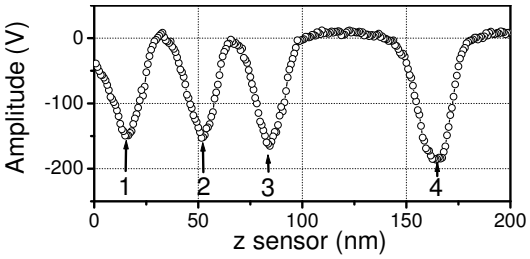

Figure 4.9: Amplitude response showing 4 buckling events, implying the presence of several SWNTs of different lengths.

the buckling point. This is another example of the robustness of nt tips, and their resistance to wear. Occasionally the SWNT(s) appear to slip, or be pushed, up the tip during force curve analysis. However, they usually stabilise with time, and indeed performing a force curve is a useful technique for checking, and improving, the stability of the SWNT(s) on the tip prior to shortening. During shortening force curves were used to monitor the increase in F_b as l_{nt} is decreased, visible in the extent to which the amplitude is damped before buckling.

Electron microscopy

FESEM and TEM were also used to characterise the nt tips. Figure 4.10 shows an FESEM image of an nt tip on an Au coated Si tip. The bundle of SWNTs is clearly visible although the SWNTs are not resolved. FESEM allows visualisation of the length of the nt tip, as well as its orientation relative to the tip cone. The main limitations of FESEM were its limited resolution (it was not possible to resolve the width of SWNTs or the presence, or absence, of small amounts of amorphous carbon on them), and its limited availability. Care must also be taken not to contaminate the nt tips.

TEM was extensively used to characterise the SWNT-AFM tips, this was made possible due to the easy access to the TEM in the Physics Department, at the

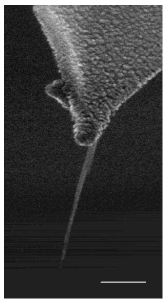

Figure 4.10: FESEM image of an nt tip, taken with Professor John Weaver, at the University of Glasgow. The scale bar is 100 nm, the Si tip was coated with Au prior to 'pick-up'.

University of Warwick.[10] TEM allowed confirmation that the nt tips were indeed composed of many SWNTs as opposed to one, or a few, larger diameter MWNT. It was also possible to confirm that very little, if any, amorphous carbon was present on the SWNTs from most of the 'pick-up samples'. This is of importance not only for their use as AFM tips, but also to confirm the quality of the SWNTs used for device fabrication. This information could not be obtained by any other means.

The tip was set at an angle of $\approx 60°$ in the TEM holder to enable the SWNTs at the tip-apex to be imaged. However, at this large tilt angle the TEM could not function at its optimum performance, as a result high-resolution images were difficult to obtain. In addition, as mentioned in Chapter 2, the SWNTs were found to be highly sensitive to damage by the electron beam. Hence, it was difficult to obtain high enough resolution images to accurately measure the diameter of the SWNTs on the tip, and care had to be taken not to damage the nt tips. However, the observed SWNT diameters were roughly consistent with those observed by AFM, and it was possible to routinely observe the length and relative angle of the SWNTs protruding from the tip apex, as well as gain an estimate of the diameters of the nt tips.

Figure 4.11 shows a selection of TEM images of nt tips of different lengths and widths, and Table 4.1 shows their properties. All the nt tips had been shortened

[10]Many thanks to Steve York for his continual help with its use.

prior to imaging, and have $F_b > 10$ nN, and $A_{th} < 5$ Å. By varying the number of SWNTs attached to the tip it is possible to create nt tips of varying properties, and hence suitable for different applications. The next section will discuss the advantages of nt tips for various imaging applications.

Other authors, [WSM$^+$04], have found that the diameter of the SWNTs attached to the tip using the pick-up technique (for them typically 4 - 6 nm) is significantly larger than those observed lying on the substrate (for them typically 2 - 3 nm). However, as Figures 4.11 (a), (c) and (d) demonstrate, this is not the case for our pick-up samples. Several SWNTs can be resolved in (a), with measured diameters of $\sim 2 \pm 0.5$ nm, only slightly larger than the average diameter of the SWNTs on the substrate (~ 1.5 nm).

In general the angle at which the nt tip protrudes is determined by the section of tip which the SWNT(s) lie on approaching the tip apex. As a result, the nt tips are typically aligned parallel to one of the faces of the Si pyramid, and are unlikely to be exactly perpendicular to the surface to be imaged. Interestingly, when nt tips are formed from large bundles of SWNTs the angle becomes an average over the faces of the pyramidal Si tip, as shown in Figure 4.11 (d)[11]. In principle, this could be capitalised upon to gain control over the orientation of the nt tips for high aspect ratio imaging, where length and orientation are more important than the radius of curvature of the tip.

[11]The dotted lines are a guide to the eye to demonstrate this effect.

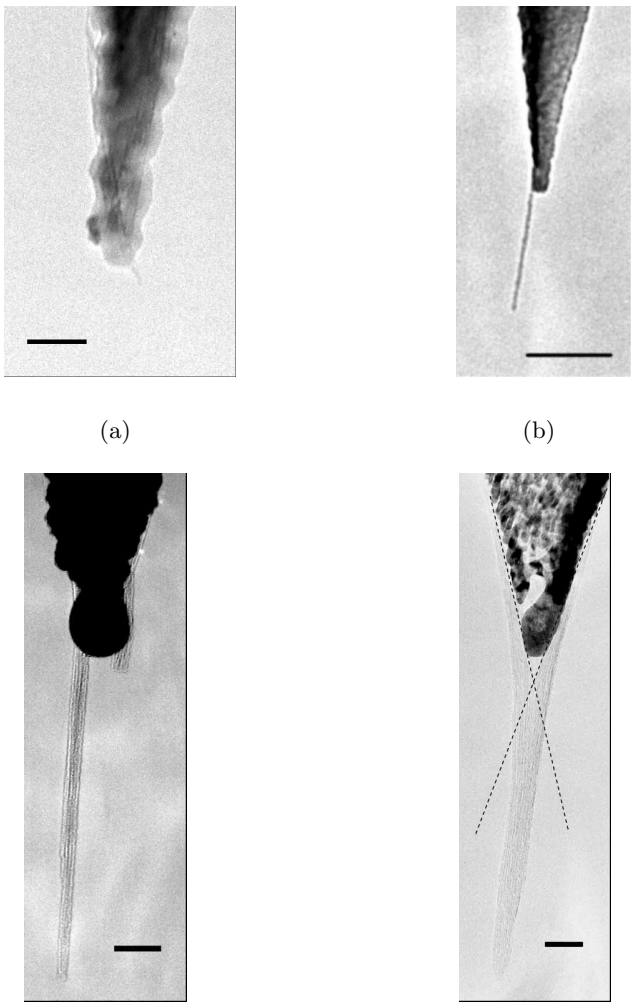

(a) (b)

(c) (d)

Figure 4.11: TEM images of nt tips. Scale bars (a) 25 nm, (b) 100 nm, (c) 50 nm, (d) 50 nm.

Tip	$l_{nt}(nm)$	$r_{nt}(nm)$	F_b (nN)	k_l (N m^{-1})	A_{th} (Å)	number of SWNTs
(a)	10	1	100	3	0.1	1
(b)	175	3	30	0.05	1	~ 10
(c)	300	8	500	0.1	0.3	~ 50
(d)	500	20	6000	4	0.1	~ 500

Table 4.1: Properties of the nt tips shown in Figure 4.11.

4.2 Imaging with SWNT-AFM tips

The most common use of SWNT-AFM probes in the literature is for high resolution topographic imaging. With a diameter of 1 - 2 nm the spatial resolution realisable with SWNT-AFM tips is an order of magnitude greater than for conventional Si tapping mode tips, whose nominal radii of curvature are typically $\gtrsim 10$ nm.

The highest possible resolution is achieved by using a SWNT-AFM tip with only one SWNT at its apex. This requires the attachment of an individual SWNT, a more difficult and lower yield process than attaching several SWNTs. After attachment, the SWNT must be shortened down to a length of $\sim 10 - 30$ nm, as shown by Figure 4.5. With care, the electrical pulse shortening process can be used with an accuracy of $\sim 20 - 50$ nm, although often larger lengths are removed. As a result, the shortening process for a tip composed of an individual SWNT tip has a comparatively low yield.

Combining the two low yields, fabrication of an individual SWNT-AFM tip can take a few days, and several Si tips. Once formed the tip is usually stable, and, importantly, its resolution does not degrade. Typically, the tip would eventually be damaged either by beam damage or contamination in the TEM, or by damage to the Si tip.

Figure 4.12 shows two examples of high resolution topographic images taken with the SWNT-AFM tip shown in Figure 4.11 (a). Figure 4.12 (a) is of silver nanoparticles on a quartz substrate, and an image of the same sample taken by a new Si TESP tip is given in (b) for comparison. The presence of the nanoparticles is evident in (b), however it is not possible to determine their height, or whether they are touching or are distinct. (a) demonstrates not only the presence of the nanoparticles, but also that they are distinct and have heights of 6 - 10 nm.

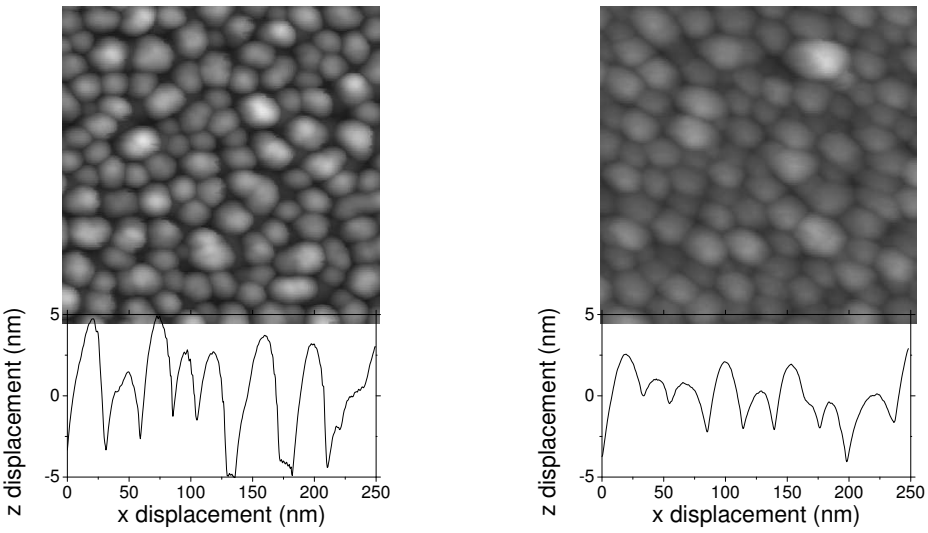

(a) (b)

(c) (d)

Figure 4.12: Examples of high resolution topographic imaging with a SWNT-AFM tip. (a) and (c) were taken with the SWNT-AFM tip shown in Figure 4.11 (a), $r_{nt} \approx 1$ nm, $l_{nt} \approx 10$ nm. (b) and (d) were taken with new Si TESP tips, nominal radius of curvature $R_c \sim 10$ nm. (a) and (b), 250 nm square height images, 15 nm full scale, of silver nanoparticles on quartz. Sample courtesy of Dr Frank Hübenthal, University of Kassel. Example cross sections of the images are shown underneath. (c) and (d), 250 nm square height images, 5 nm full scale, of a silica thin film. Sample courtesy of Carolyn Wilson, University of Warwick.

Figures 4.12 (c) and (d), taken with a SWNT-AFM tip and Si TESP tip respectively, are of a silica thin film. These also clearly demonstrate the higher spatial resolution obtained by the SWNT-AFM tip, which reveals surface structure not resolved by the conventional Si tip.

The benefits of using individual SWNT-AFM tips are thus apparent. However, their application is limited by the difficulty posed by their fabrication. It is unlikely that they will be available for routine imaging in the near future.

The fabrication process for nt tips composed of a few SWNTs or more has a much higher yield. The pick-up procedure is rapid and reliable for attaching several SWNTs to the tip. As discussed previously, the SWNTs adhere to one another forming a bundle. As for an individual SWNT-AFM tip, the SWNTs are attached to the Si tip only by Van der Waals forces. When several are attached, they are adhered both to the tip, and to each other. As a result, the bundle is attached by the sum of the adhesion of the individual SWNTs. i.e. we expect the stability of the nt tips to increase linearly with the number of SWNTs in the bundle. Note that the diameter of the bundle will only scale with the square root of the number of SWNTs. TEM and SEM analysis has shown that the SWNT(s) tend to have from 100 nm to a few micrometres in contact with the Si tip before protruding from its apex. The binding energy of a SWNT to Si is ~ 2 eV/nm, see page 8, which for 10 SWNTs with 500 nm in contact with the Si tip results in a binding energy of 10^4 eV. An nt tip composed of 10 SWNTs is likely to be ten times as stable as an individual SWNT-AFM tip, whilst only ~ 3 times the diameter. Assuming an average diameter of SWNTs of 2 nm, this implies a tip radius of curvature of ~ 3 nm, significantly smaller than even new Si tips.

Importantly, the shortening procedure is also more reliable for such an nt tip. From Figure 4.5, we see that for an nt tip with $r_{nt} = 3$ nm, it must be shortened to $l_{nt} \lesssim 200$ nm. Given that the shortening procedure is typically accurate to ~ 50

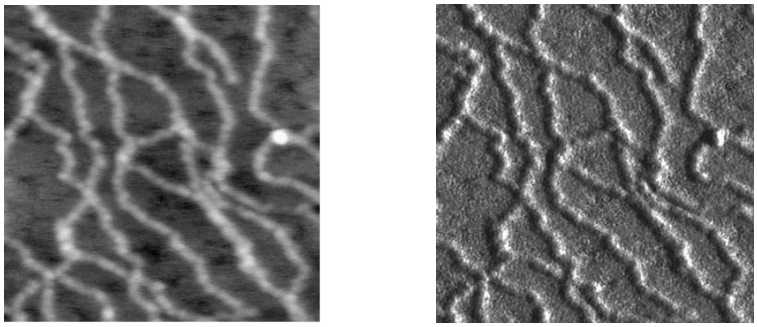

Figure 4.13: 200 nm square *left* height (2 nm full scale), and *right* amplitude (10 mV full scale) images of DNA on mica taken with an nt tip ($l_{nt} \approx 150$ nm) on a Si FESP tip. The imaging amplitude was 0.17 V. Sample courtesy of Dr Jaroslav Malina, University of Warwick.

nm, it is clear that this can be achieved with a high yield. As the diameter of the nt tip is increased, by 'picking-up' for longer, l_{nt} can be increased even further, and correspondingly the shortening yield increased as well.

The use of longer nt tips is also beneficial for imaging samples with sharper features, and for imaging techniques involving long range forces. The example of high resolution EFM with nt tips will be discussed in the next Chapter. Although longer nt tips are also required to be larger in diameter, as Figures 4.11 (c) and (d) show the nt tips often tend to taper so that they are sharper (composed of fewer SWNTs) at their apex.

Nt tips have other advantages over Si tips beyond higher spatial resolution. For example, due to their small tip apex area, and hydrophobicity [WJHK01], there are only small adhesion forces between the sample and tip. This allows the nt tips to be used at low oscillation amplitudes, and with low tip sample forces. Biological samples are particularly susceptible to deformation, and damage, by tip sample forces even in tapping mode. Figure 4.13 shows 200 nm square images of DNA on mica taken with an nt tip, $l_{nt} \approx 150$ nm. The apparent widths of the DNA are ≈ 6 nm, whilst their heights are only ≈ 0.5 nm. The nt tip was picked up on a Si FESP, and the setpoint amplitude used was 0.17 V (light tapping), corresponding to an

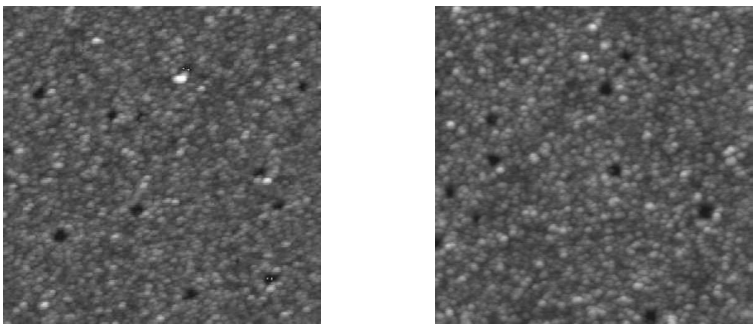

(a) (b)

Figure 4.14: 500 nm square height images (5 nm full scale) of a silica film, sample courtesy of Carolyn Wilson, University of Warwick. (a) was taken 8 hours hours of continuous imaging after (b).

rms amplitude of ≈ 3 nm. The theoretical diameter of a DNA molecule is ~ 2 nm, 4 times larger than the observed height. Using an nt tip we were able to confirm that this was not due to deformation of the sample by the tip. The discrepancy between observed and predicted heights is in fact caused by interaction of the DNA with the mica surface, and salts on the mica surface, see e.g. [MHCB03, KKR$^+$04].

Potentially the most significant advantage is the robustness of nt tips. Once fabricated they do not mechanically degrade, even when imaging hard, rough samples[12]. Si tips typically degrade in two ways: by gradual wearing of the tip-apex from normal imaging; and by catastrophic damage[13] from occasional collisions with large topographic features on the sample. The strength of the carbon-carbon bond, and the energy dissipated by the SWNTs' ability to bend, effectively eliminates the tip wearing issues. This is demonstrated by Figure 4.14, which shows two images of a silica thin film (the same sample as in Figures 4.12 (c) and (d)) taken with the nt tip shown in Figure 4.11 (b). The resolution is clearly better in both images than that demonstrated by the Si TESP tip. Figure 4.14 (b) was taken 8 hours after (a), during which time the tip was continuously scanning. There is no degradation in

[12]This is also true for MWNT-AFM tips, see [LMF$^+$02]
[13]i.e. a section from the end of the tip is removed

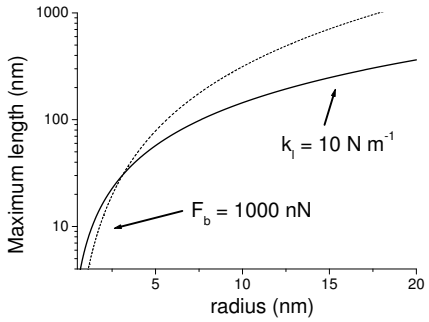

Figure 4.15: Length of nt tip giving $k_l = 10$ N m^{-1} (solid line), and $F_b = 1000$ nN (dashed line), plotted as a function of nt tip radius.

image quality, and there was no apparent change in the tip afterwards.

It is also not possible to catastrophically damage the nt tips as they buckle rather than break, and for longer nt tips the underlying Si tip is removed further from the sample, reducing the probability of damage to it. Figures 1.18 (d-f), in Chapter 1, demonstrate tapping mode imaging of polycrystalline, pressure densified alumina. This is one of the hardest known materials, and it had been thermally etched resulting in abrupt, deep, trenches at the grain boundaries. Imaging this sample in tapping mode with a normal Si tip proved to be challenging, the tip was clearly damaged through each image. Hence an nt tip was used instead, which enabled robust comparison of the grain boundaries[14].

A common problem when imaging with Si tips is tip convolution effects. In its most minor form this is just loss of spatial resolution due to the finite radius of curvature of the tip. However, other effects such as imaging from multiple points on the tip, and tip shape convolution, are also common. These effects are rare with nt tips since all the SWNTs adhere to one another forming a bundle, and the bundle is generally roughly spherical to maximise the total inter-SWNT Van der Waals forces.

Tip wear problems in contact mode are obviously more severe than in tapping mode, due to the larger tip sample forces involved. A natural question to ask is thus

[14]Figure 1.22 in Chapter 1 was also taken with an nt tip.

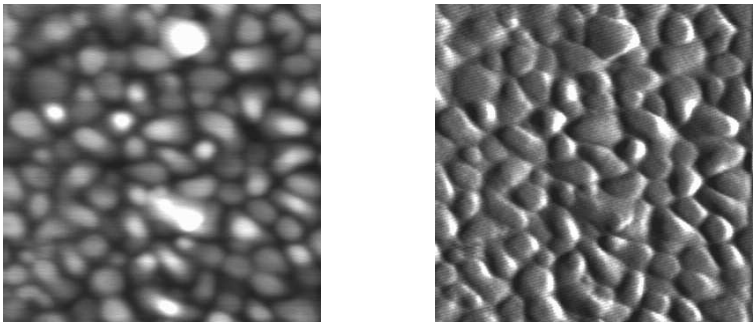

Figure 4.16: 500 nm square *left* height (10 nm full scale), and *right* deflection images of an evaporated Au film taken with an nt tip in contact mode.

whether nt tips can be used for contact mode imaging as well as tapping mode. For contact mode imaging the axial load on the tip is higher, as are the lateral forces. For imaging in contact mode we can estimate suitable nt tip properties of $F_b \gtrsim 1000$ nN (allowing imaging with setpoints $\lesssim 10$ V), and $k_l \gtrsim 10$ N m^{-1} (corresponding to lateral deflections of $\lesssim 1$ nm for typical imaging forces[15]). A plot of l_{nt} against r_{nt} is given for these conditions in Figure 4.15. It is clear that for contact mode imaging substantially shorter and thicker nt tips are required.

Contact mode imaging with nt tips is possible, as demonstrated by Figure 4.16. The nt tip used for this image had $r_{nt} \approx 6$ nm, and $l_{nt} \approx 60$ nm, giving $k_l \approx 20$ N m^{-1}, and $F_b \approx 4000$ nN. However, so far contact mode imaging with nt tips has not been achieved reliably, and work is continuing in this area.

[15] this is also comparable to the torsional spring constants of the Si contact tips [LOW97], hence allowing LFM, although at a lower frictional resolution.

4.3 Electrical transport through nt tips

Electrically connected SWNT-AFM tips hold considerable promise for conducting probe techniques such as STM, EFM, SGM and c-AFM. Also, an electrically contacted SWNT represents an ideal, geometrically well defined, nanometer-sized electrode for electrochemical applications. The high aspect ratio opens up the possibility of inserting a nanoscale electrode into small, deep, pore structures or through a membrane with little disruption.

There has, however, been little work capitalising upon the electrical properties of SWNT-AFM tips. EFM has been performed with MWNTs attached to Si tips using nonconductive adhesive [ARHH99], and with MWNTs manipulated onto Pt Ir coated Si tips [TWY$^+$02]. Electrochemical measurements have been made with MWNTs of diameter ca. 100 nm [CSC99]. There have also been limited reports of their use in STM, e.g. [STAN01, WMSS01, DHR$^+$96]. However, reproducible spectroscopy was not demonstrated, which was attributed to poor electrical contact between the carbon nanotube and the tip.

In order to reliably apply electrically connected SWNT-AFM tips it is vital to understand the nature and stability of the electrical contact between the SWNT and the tip.

Electrically connected nt tips also form a novel geometry for the study of electrical transport through SWNTs. One electrical contact is made to the SWNT(s) through the AFM tip, allowing a second contact in a two terminal configuration to be made by any metallic surface to which the nt tip may approach and make contact with. This geometry is complementary to the standard device geometries outlined in Chapter 2.2. In conventional devices both contacts are fixed, whereas for electrically contacted nt tips the second contact can be varied both in material and position.

This section presents some initial results on the characterisation of electrically

connected nt tips, and the study of electrical transport through them. Funding has been received from the Leverhulme Trust to continue the work presented in this and the following section.

4.3.1 Fabrication of electrically connected nt tips.

Direct cCVD growth onto metal coated AFM tips is limited to the few metals (such as Mo) which are unaffected by the growth conditions, and also do not contaminate the growth setup. As a result the pick-up technique was used exclusively for the formation of electrically connected nt tips. Although it was found that nt tips could be formed on tips with every coating tried, the ease with which they could be formed, and their stability, varied significantly with the coating.

Initially Pt coated tips were used. Picking up onto these was found to be difficult, and the resultant electrical connection poor (as discussed later). The Pt surface was very rough due to the large grain size, so Au coated tips with a smoother surface were used instead. These were easier to pick up on, and gave better electrical connection.

On the assumption that the adhesion was due mainly to smoothness of the coating on the tip, Pd and Au Pd were tried, as these are known to give smooth coatings even on Si AFM tips due to their small grain size. Picking up with both of these materials was substantially easier, and was in fact at least as successful as picking up on uncoated Si tips. This could also be attributed to the good adhesion of Pd to SWNTs, [ZD00], which also is now known to form ohmic, near ideal contacts to both mSWNT and sSWNT [JGW$^+$03, MJK$^+$03]. Although a systematic investigation of the contact resistance of nt tips on Pd or Au Pd coatings has not yet been done, preliminary results suggest that the contacts have lower resistances than those for nt tips on Au coatings.

4.3.2 Transport through nt tips and a liquid (Hg) electrode

Conductance through SWNTs is very sensitive to mechanical deformation of the SWNT, see for example [YH00, FYMK03, GZB03]. As a result, in order to characterise the electrical contact between the SWNTs and the metal coated tip a liquid (Hg) contact was used to minimise the forces on the SWNTs.

For the electrical transport measurements described here longer nt tips were used ($l_{nt} > 200$ nm) in order to record the current response as a function of immersion depth into the Hg drop. A hemisphere of Hg, formed by the electrochemical reduction of Hg_2^{2+} at a 50 μm diameter Pt disc ultramicroelectrode [WW85], functioned as the liquid metal contact. An optical microscope image of the setup is shown in Figure 4.17 (a).

The nt tip was first lowered towards the liquid metal using the z stepper motor, in increments less than l_{nt}. A sudden change in the deflection signal of the cantilever occurs when the SWNT first encounters the Hg surface. The z-piezo was then used to precisely control d, the z-piezo displacement (increasing away from the substrate). The voltage applied to the tip, V_{tip}, was controlled by an analog output from a data acquisition card (DAQ), allowing the current, i, to be recorded as a function of d and V_{tip}. Electrical measurements were carried out with both Pt (50 nm, sputter coated, with 5 nm Cr adhesion layer) and Au (50 nm, evaporated, with 10 nm Ti adhesion layer) nt tips. The current flowing through the nt tip was initially measured as a function of d, in the linear response region, for a fixed $V_{tip} = -25$ mV. Figures 4.17 (b) and (c) show typical traces of current and deflection against d for a Pt nt tip. As d is steadily decreased, the current suddenly rises from zero at the same point (P) as a small attractive force is observed. The current then rises in steps through a series of plateaus, while the force becomes repulsive and grows linearly.

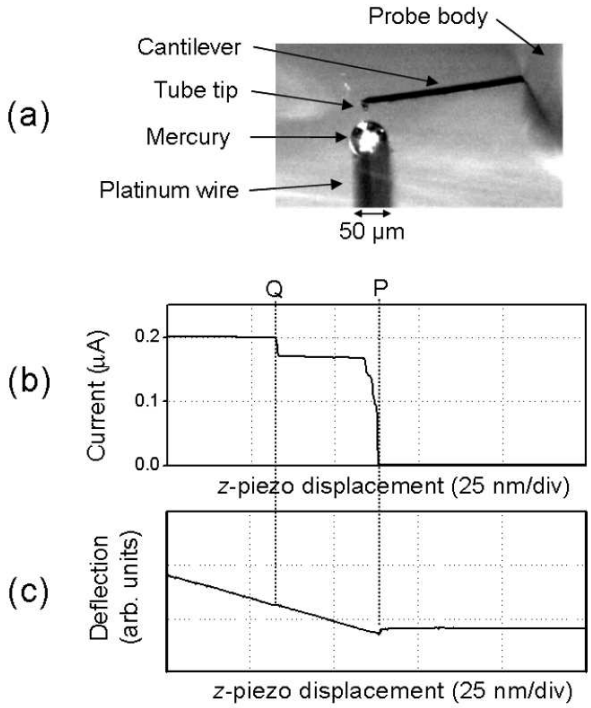

Figure 4.17: (a) Optical microscope image of the cantilever, nt tip, and Hg drop arrangement.(b) Current - and (c) deflection - distance characteristics for a Pt nt tip, as the tip was brought towards and into contact with the liquid Hg.

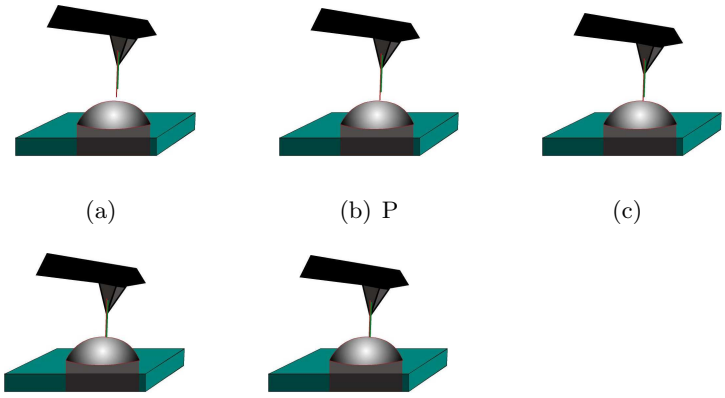

(a) (b) P (c)

(d) Q (e)

Figure 4.18: Schematic of immersion of an nt tip into a Hg microelectrode.

We often notice a small dip in the force at each current step, as for instance at point Q. For most nt tips the characteristics are highly reproducible. With only one SWNT on the tip, a single current plateau is observed, but the step is not well behaved, probably as a result of the lower rigidity of an individual SWNT.

While the force response is not yet fully understood, see Appendix B, the origin of the current steps and plateaus is clear. When using Au coated tips, if the Au coating touches the Hg it quickly dissolves (as confirmed by subsequent TEM imaging) and the current drops to zero. For Pt tips, if the Pt touches the Hg, a stable very-high conductance metal-metal contact is established. The movement of Hg along the SWNT to short to the tip is highly unlikely, as Hg does not wet carbon nanotubes [DEHT94]. Therefore, the current must flow through the SWNTs. Each current step is produced when a conducting SWNT penetrates the Hg. The existence of plateaus between the steps implies that the SWNT resistivity is small, as discussed later. The multiple features at the first current step in Figure 4.17 (b), P, may be due to several SWNTs in a bundle penetrating the Hg in close succession.

We could not determine conclusively whether the Fe catalyst particle remains attached to the free end of the SWNT after pick-up[16]. However, this is unlikely to influence the transport measurements as the SWNT end is always fully immersed in the Hg during current measurements.

To further characterize the nt tips, $i - V_{tip}$ curves were recorded at fixed d, on a stable plateau. Figure 4.19 (a) is a TEM image of an Au nt tip with a single protruding SWNT. The deformity of the apex is probably as a result of abrasion of the soft Au coating during scanning and has no consequence for the performance of the nt tip. Figure 4.19 (b) displays the $i - V_{tip}$ response of this nt tip with ca. 50 nm of the SWNT immersed in the Hg. The corresponding $i-$d response showed

[16]No catalyst particle has been observed at the end of the SWNT after pick-up, however the SWNTs are usually too long to see the ends at high resolution, and presumably the catalyst particle would be removed by the shortening process

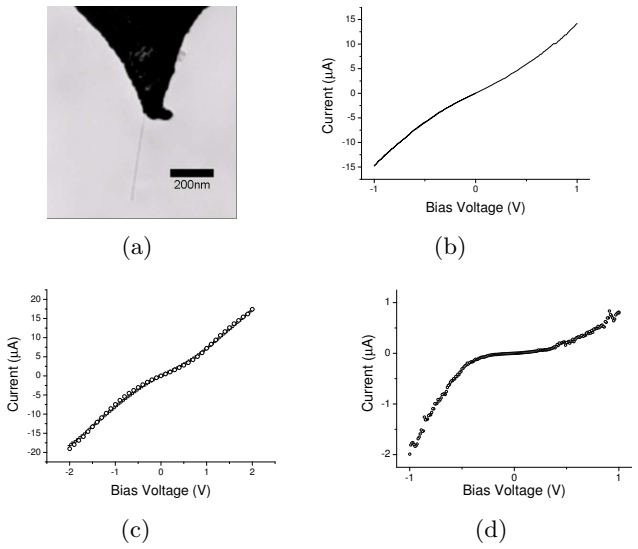

Figure 4.19: (a) TEM image of an Au nt tip. (b) $i-V_{tip}$ response of the nt tip shown in (a), indicative of a mSWNT. (c) $i - V_{tip}$ traces for another Au nt tip, recorded under identical conditions 3 hours apart, illustrating the stability of the system. (d) $i - V_{tip}$ response of an Au nt tip showing behaviour indicative of a sSWNT.

a very stable, single plateau. The $i - V_{tip}$ trace is highly symmetric with a low-bias ohmic resistance of ca. 170 kΩ. The observed characteristics are consistent with a mSWNT. Importantly, for all such mSWNT-AFM tips, the $i-$d and $i - V_{tip}$ responses are very stable, even for V_{tip} up to 4 V and currents up to 50 μA[17]. For example, Figure 4.19 (c) shows two almost identical $i - V_{tip}$ traces, which were recorded three hours apart, for an Au nt tip.

Figure 4.19 (d) shows the $i - V_{tip}$ trace recorded with another Au nt tip on an $i-$ d plateau. In this case, the trace is asymmetric and highly nonlinear, with a much higher resistance at low bias of $\sim$ 10 MΩ. This is the behaviour expected of a sSWNT, where Schottky barriers exist at both the metal contacts, which suppress the low-bias conductance, see for example [AKD$^+$02] and the discussion in Chapter 2. The asymmetry can be attributed to the difference between the Hg and the Au contacts. As discussed before, sSWNT are normally p-doped, the current should

[17]these were presumed to consist of bundles containing more than one mSWNT

thus be largest when holes are injected into the sSWNT from the contact with the lowest Schottky barrier, i.e. when that contact is positively biased. Because the current is found to be larger for a positive bias on the Hg, the implication is that the Schottky barrier to the Hg is smaller than that to the Au. This is consistent with the work function of Au (5.1 eV) being greater than that of Hg (4.5 ev).

In general, plateau resistances, from $i-$d curves, in the range 100 - 200 kΩ were obtained for mSWNTs. Note, for each nt tip we are able to accurately determine a value for this resistance. As in the conventional device geometry, see page 70, the measured plateau resistance, R_{tot}, corresponds to the sum of a series of resistances: the metal tip-SWNT contact (R_{met-nt}); the quantised resistance (R_Q); the resistance of the SWNT itself; and the resistance of the SWNT - Hg contact (R_{Hg-nt}). Since the plateaus are approximately flat, either one or both of the SWNT contacts must dominate the recorded resistance values. However, given that it has previously been demonstrated that Hg makes excellent electrical contact to carbon nanotubes [FPWdH98], it is highly likely that the measured resistance is dominated by R_{met-nt}. In fact resistances in the same range, 100 - 200 kΩ, are also obtained when SWNTs are laid flat on top of pre-fabricated gold electrodes [YKD00]. We found that it was easier to obtain reproducible lower resistance plateaus with Au than Pt. This was attributed primarily to the smoother Au tip coating, as observed in the TEM, which should result in a greater contact area between the SWNT and the metal. However, it may also be dependent on how well the metal wets the SWNT [ZD00].

Length dependence of resistance

The flat plateaus in current between successive SWNTs entering the Hg imply that the intrinsic resistance of the SWNTs is significantly less than the contact resistances. Closer inspection of the $i-$d plateaus for mSWNTs reveal that they are not exactly flat but appear to have a small slope, as shown in Figure 4.20, indicating a slight decrease in resistance as the gap between the electrodes is reduced. This demonstrates one of the advantages of this configuration. By varying d we can vary the length, L, of SWNT(s) between the two contacts.

Although R_{met-nt} is likely to dominate the overall resistance, it is independent of L. Previous investigations on the contacts between MWNTs and Hg found that the contact resistances were only very weakly dependent on immersion depth [PBY$^+$02][18]. R_Q is also independent of length, so, as defects are also spatially localised, the only length dependent contribution to the resistance is R_{int}. By varying L and monitoring the change in resistance we can thus isolate the length dependence of R_{int}.

Figure 4.21 shows a histogram of the average slope of an individual plateau. These results were made possible by the combination of the Picoforce module, and a DAQ card (controlled by specifically written Labview software[19]). The Picoforce

[18]The dependence is so as to decrease the resistance with increasing immersion depth, and so acts to make the subsequent estimate of SWNT resistivity an upper bound.

[19]the use of Labview was an enabling technique for most of the work in this thesis, and also occupied a substantial portion of the time taken

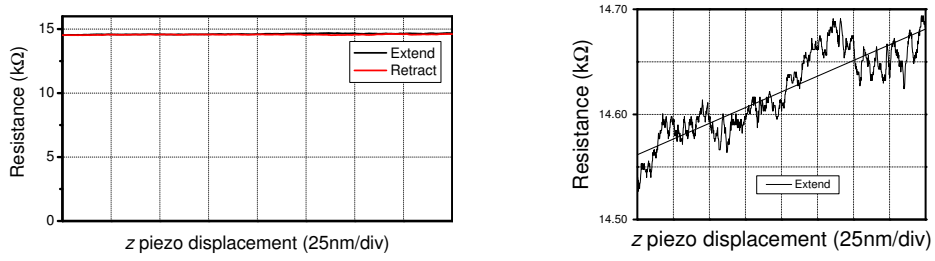

Figure 4.20: $i-$d response of an electrically connected nt tip on a plateau.

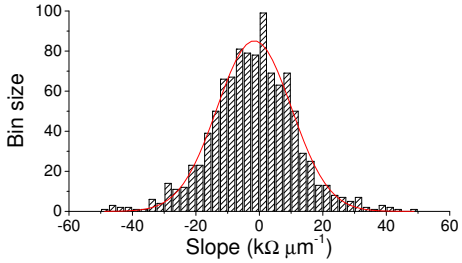

Figure 4.21: Average slope of an $i - d$ plateau. The red line is a Gaussian fit with mean value 1.6 kΩ μm^{-1}.

module enabled the same section of the same plateau to be investigated over long periods of time, removing the problems of piezo drift. The DAQ card was used to measure simultaneously the current, deflection, and z position. For each cycle of the tip (extend and retract) the current against z position was linearly fitted, and the value recorded. Hence, although the changes in resistance were in the noise level of an individual measurement, we can establish a resistivity for this plateau of 1.6 kΩ μm^{-1}.

The low resistance of the plateau suggests the presence of multiple mSWNTs. To estimate the resistivity of an individual mSWNT we conservatively estimate the number of mSWNT present to be ~ 6. This implies a resistivity of ~ 10 kΩ μm^{-1}, and hence a mean free path of ~ 500 nm. The upper limit on the mean free path, from assuming only one mSWNT is present, is ~ 4 μm. This demonstrates that mSWNT are ballistic conductors at room temperature, with mean free paths on the micrometer length scale. The mean free paths calculated above are consistent with the EFM results presented in Section 3.3.1 as well as with the other results quoted there.

Future work will use this geometry to probe the mean free path as a function of applied voltage, and will focus on improved techniques for isolating the length dependence of the resistance, and lowering R_{met-nt}.

4.3.3 Transport through nt tips and a solid electrode

The liquid Hg electrode was used to minimise the tip surface forces present, and hence allow the contact between the metal coated tip and SWNTs to be measured. Having characterised this contact, and its voltage dependence, we can consider transport through nt tips and a solid electrode. This allows investigation of the effect of an axial loading force on electronic transport through SWNTs.

The link between mechanical and electrical properties of SWNTs is of considerable importance in understanding the electronic properties of SWNTs and electrically connected nt tips, especially given the potential applications of SWNTs in nanoscale-electromechanical (NEM) devices, see for example [SBGv03, FYMK03]. There has been much recent interest in the NEM properties of SWNT, e.g. [MYS$^+$03, CWD03] which used suspended SWNTs in conventional device geometries. The experiments involved stretching the SWNTs, and clearly demonstrated the sensitivity of the conductance of SWNTs to axial forces.

By simply pressing an electrically connected nt tip against a metallic surface we are able to study the effect of compression on electronic transport. Importantly this also enables us to study an effect not visible when the SWNT is under tension - the buckling of the SWNT.

Figure 4.22 shows the current through an nt tip whilst performing a standard force - distance measurement. The nt tip is on a Pd coated contact Si tip, and is being pressed against a Au surface. Again, these measurements were only possible using the combination of the Picoforce module and a DAQ card. The Picoforce accurately measures the z position of the tip and outputs it linearly scaled to ± 10 V. The AFM would only record 2 data channels at once, e.g. z position and deflection. A DAQ card was thus used instead to enable simultaneous measurement of the current, amplitude, deflection and z position, and Labview was used to record

consecutive 'extend' and 'retract' responses.

The observed response of the nt tip indicates that the nt tip starts to conduct as it is pressed against the surface. However, when the SWNT(s) buckle, as observed from the deflection response, the current immediately drops. The drop in current and deflection are simultaneous (to the accuracy with which the DAQ card could sample, i.e. $< 10\ \mu$s). The process is reversible as indicated by the 'retract' response, and repeatable. This directly demonstrates the effect of mechanical deformation on the conductance through SWNTs, and is consistent with the theoretical prediction that a gap should open in the band structure of a mSWNT when it is subjected to a lateral strain, see for example [YH00, MSA02].

The magnitude of the current response also demonstrates that 'end contacting'[20] SWNTs results in a high resistance contact. The applied voltage was $V_{tip} = 100$ mV, giving a minimum resistance of 5 MΩ. Of the electrically connected nt tips studied using this technique most exhibited no current response, or too small to measure, whilst the remainder gave resistances of $\sim$ MΩ or higher. We can tentatively attribute the former responses to nt tips where the nt at the tip apex is a sSWNT, and the latter to mSWNT.

The electrical connection of the nt tip used for the results in Figure 4.22 was subsequently tested using a Hg electrode. Although the results were inconclusive since the nt tip was too short to rule out the possibility of Hg contacting the underlying Pd, they implied that $R_{met-nt} < 100$ kΩ.

[20] i.e. electrical contact is made with the end of the SWNT rather than the side. The SWNT probe end contacts a metal surface when it is lowered into contact with it.

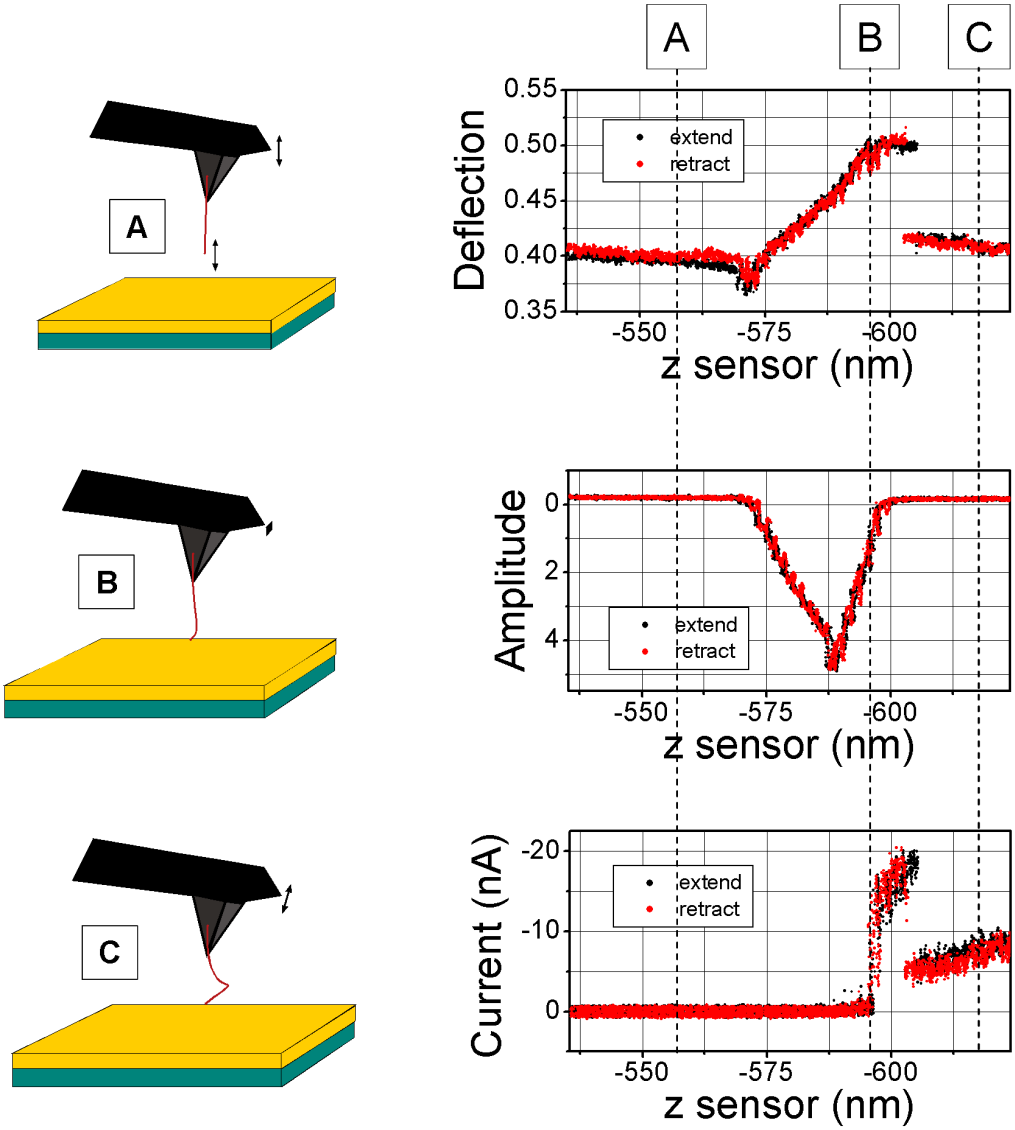

Figure 4.22: *left*, schematic of an nt tip approaching a surface and buckling. *right*, simultaneously measured current, amplitude and deflection response of the nt tip as it approaches a Au surface and buckles. The positions illustrated by the schematic are marked by points A, B and C. The deflection and amplitude signals are in arbitrary units.

These preliminary results demonstrate the possibilities presented by this novel geometry for the study of electronic transport through SWNTs. By using shorter nt tips, with larger buckling forces, we will be able to study the effect of compression on electronic transport in more detail. In addition, we will study the effect of substrate material on the current response, providing us with a simple technique for investigating the effect of a wide range of contact materials.

4.4 SWNTs as templates for nanowire conducting probes

The results presented above demonstrate the interesting electrical properties of electrically connected nt tips. However they also illustrate that nt tips are not ideally suited to c-AFM applications; contact mode imaging is difficult and their current response is highly force dependent. Previous work has shown that suspended SWNTs can act as templates for the formation of continuous nanowires of metals such as Ti, Au, and Fe with widths less than 10 nm [ZD00], as well as a superconducting Mo - Ge alloy [BLT00]. Thus for applications where robustness, reproducible low resistance electrical properties, or specific electrode materials are important we have developed metallic nanowire probes.

Here we demonstrate the use of nt tips as templates for the formation of high aspect ratio metallic nanowire tips, and show that they not only have excellent conducting properties but are also robust and durable for AFM imaging applications. The nanowires are formed by sputter coating a thin film of metal onto the nt tip. Thus, in principle, any material compatible with the sputter coating process could be used to form the nanowire. In this way nanowire probes are complementary to nt tips in the same way that conventional metal coated Si tips are complementary to Si tips. The resulting nanowire has a high aspect ratio, which is not only the optimal geometry for both electric and magnetic force microscopy, but also allows

the tip to probe small, deep pore structures. Additionally, there is the potential to form nanowires with a smaller tip apex than conventional metal coated probes, i.e. capable of higher resolution imaging. The core of SWNTs inside the nanowire anchors it firmly to the tip and confers increased mechanical and electrical stability. Moreover, in theory, the ability to produce a variety of different metallic nanowires, extends the capabilities of the probe to conductivity (Au Pd, Pt Ir), magnetic (Fe), and electrochemical imaging (e.g. Pt, Au, or Ir for pH sensing).

Coatings on carbon nanotube SPM probes have previously been utilised either for adhesive purposes to secure the nanotube for imaging under solution [WJW+98, LCD99, HCOL01] or for electrical insulation of the carbon nanotube [PSMR04]. To the best of our knowledge, we believe this is the first reported use of SWNT-AFM tips as templates for the formation of conducting metallic nanowires.

The nanowires are formed by sputter coating the nt tips. The sputtering process involves an isotropic deposition of material onto the sample due to the diffusive path of the material from source to sample. Despite the high aspect ratio of the probe this results in a uniform coating on both the tip and the SWNTs, which is not possible when depositing the material using an evaporator. Nt tips were deliberately used as the templates due to their increased rigidity compared to that of an individual SWNT. The greater rigidity of the SWNT bundle makes the nt tip more resistive to the mechanical and thermal stresses induced by sputtering, enabling the formation of longer and straighter nanowires.

Once deposited the nanowire is significantly stiffer and more robust than the original bundle. Not only is each SWNT in the bundle securely attached to the tip by the coating of metal on top of it, but also the metal adds to the rigidity of the bundle despite its comparatively low Young's modulus. For a nanowire formed from a metal of Young's modulus Y_{met}, outer radius R, and with inner SWNT bundle

radius r_{nt}, the resultant flexural rigidity is, from Appendix A,

$$\alpha_{nw} = \frac{\pi \left(Y_{nt} r_{nt}^4 + Y_{met}(R^4 - r_{nt}^4) \right)}{4} \tag{4.8}$$

Thus, recalling Equations 4.1, for a 500 nm long bundle 10 nm in diameter, a 25 nm thick coating of Au Pd (taking $Y_{AuPd} \approx 100$ Gpa) results in an increase of k_l from $\sim 1.5 \times 10^{-2}$ N m^{-1} to ~ 2 N m^{-1} and, although it will no longer buckle reversibly, an increase of F_b from ~ 25 nN to ~ 2500 nN. The resultant nanowire probe could be used for contact mode imaging if mounted on a contact Si tip.

A standard Emscope SC500 sputter coater was used, and typically metal films of thickness in the range 20 - 30 nm were deposited on the SWNT bundles. This initial study focused on Au Pd due to its well known small grain size and hence ability to form continuous films at low film thicknesses. By using shorter nanowires on contact tips, nanowire probes capable of imaging in contact mode were fabricated. For tapping mode applications nanowire probes with lengths up to a few micrometers on FESP tips could be employed.

Electrical transport through the nanowires was investigated by imaging an Au substrate (evaporated Au on a Si substrate with Ti adhesion layer) in c-AFM. Simultaneous force - distance, F_{ts} - d, and current - distance, i - d, measurements were performed using the Nanoscope IIIa controller and Picoforce module to control the distance between the Au surface and the probe, whilst externally recording the current, z position, and deflection. The current as a function of applied bias voltage, $i-V_{ts}$ response, was also measured whilst the nanowire was held stationary in contact with the Au surface.

Figure 4.23 (a) shows a TEM image of an nt tip on an Au Pd coated contact tip. [21] The bundle, ca. 10 nm in diameter, consists of many SWNT and protudes

[21] Coating the tips prior to picking-up was found to make the electrical shortening procedure more controllable and, in general, occur at slightly lower voltages. However, picking up on uncoated tips gives a greater likelihood of the SWNTs passing directly through the apex of the tip rather than to one side, as in Figure 4.23 (a).

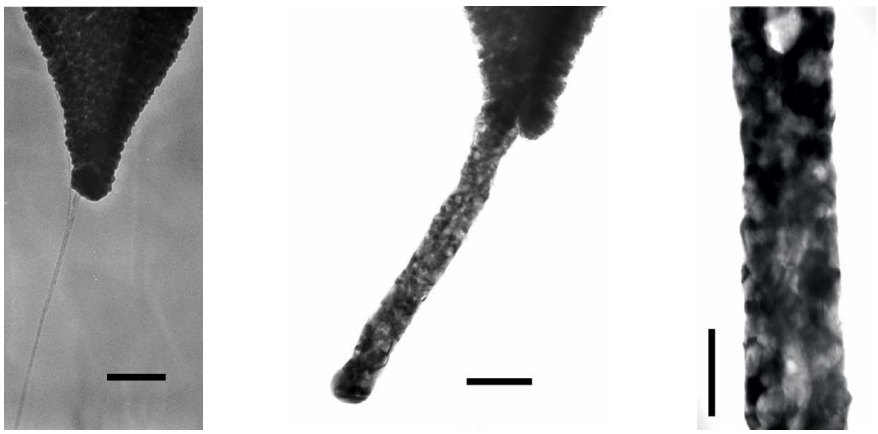

(a) (b) (c)

Figure 4.23: TEM image of (a) a bundle of SWNTs on a Au Pd coated tip, (b) the same tip after sputter coating with Au Pd and annealling, and (c) an enlarged view of the nanowire. The scale bars are (a), (b) 100 nm, and (c) 50 nm.

(a) (b)

Figure 4.24: TEM images of the same part of the same Au Pd nanowire (a) before and (b) after annealling. The images are 150 nm wide.

ca. 600 nm from the end of the tip (taking account of the 60° tilt angle of the TEM). Figure 4.23 (b) shows the apex of the same tip after sputter coating with 20 - 25 nm Au Pd and subsequent annealing, see below. The diameter of the nanowire is measured to be 50 nm whilst the length is 600 nm corresponding to the length of the original nt tip.

An enlarged view of the nanowire is shown in Figure 4.23 (c), its polycrystalline nature is evident as is the uniformity in diameter. By sputter coating with less Au Pd we have formed continuous nanowires with diameters as small as 30 nm, and are pursuing ways of reducing this further.

Figure 4.24 (a) shows a TEM image of part of an nt tip after sputter coating with Au Pd. The nanowire formed has an obvious grain structure, though the grain size is small, as expected for Au Pd, and the coating is uniform and continuous. Interestingly, we found that for Au Pd a structural change was induced by passing a large current through the nanowire. Figure 4.24 (b) shows the same area on the same nanowire after applying a 3 V bias (with a 100 kΩ resistor in series) with the nanowire in contact with a Au surface. The structure of the Au Pd alloy has clearly changed from granular to polycrystalline. We attribute this change to an annealing process due to the energy dissipated in the nanowire at the grain boundaries. This effect was consistently observed in all Au Pd nanowire tips produced, and could be induced by either applying the bias during F_{ts} - d measurements, or whilst scanning in contact or tapping mode.

The resultant nanowires have low resistance and high current carrying capacity. Figure 4.25 shows simultaneous F_{ts} - d and i - d measurements for an annealed Au Pd nanowire, roughly 50 nm in diameter and 250 nm in length, on a contact tip. A 3 V bias was applied through a 1.1 MΩ resistor in series. The cantilever spring constant here was 0.2 N m^{-1}, as measured by the thermal noise method. The black line shows the response as the probe is lowered towards the surface from right to left, 'extend', and the red line as it is brought away from left to right, 'retract'. 'A' marks the point on the 'extend' curve at which the nanowire first touches the surface, the current immediately jumps to its maximum value and remains there. The observed maximum current of 2.714 μA when in contact with the surface implies a resistance through the nanowire, cantilever and probe of 5 kΩ.

'B' marks the point on the 'retract' curve at which the nanowire loses contact with the surface. The hysteresis between the point at which the nanowire touches the surface on the 'extend' and leaves the surface on 'retract' is indicative of the adhesive forces between the nanowire and Au surface. Note that the current remains constant

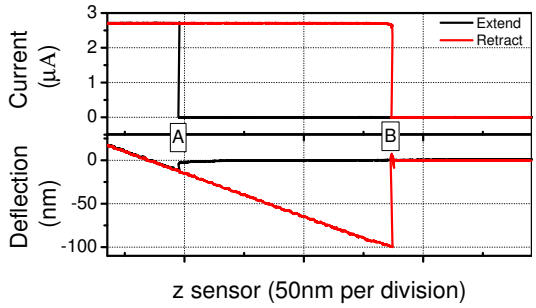

Figure 4.25: Current through the nanowire and deflection of the tip as the cantilever is brought down toward, extend (black line), and away from, retract (red line), a Au surface. "A" marks where the probe touches the surface on extend, and "B" where it leaves the surface on retract.

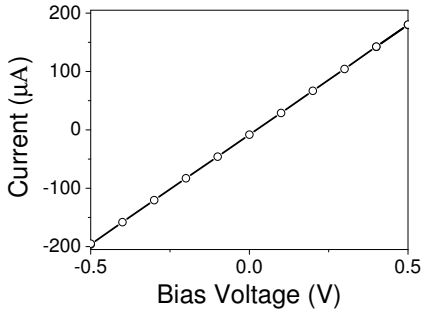

Figure 4.26: Current-voltage response of a Au Pd nanowire probe.

at its maximum value up until the moment at which the tip leaves the surface, i.e. the current response is independent of the applied force.

Although we could not measure a buckling force for the nanowire tips we did find that they were robust and capable of contact mode imaging as expected. Figure 4.26 shows the $i - V_{ts}$ response of the nanowire tip, shown in Figures 4.24 (b) and (c), the resistance in series was removed for these measurements. The response is ohmic, with a resistance of only 2.5 kΩ even though the wire is 600 nm long. This puts an upper bound on the resistivity of the nanowire of 30 $\mu\Omega$ cm, although it is likely that some of the 2.5 kΩ resistance is not due to the nanowire itself, but due also to the conducting path to the nanowire through the thin metal film on the tip.

Also of interest is the current density through the nanowire. At 0.5 V bias

the current through the nanowire is 200 μA corresponding to a current density of 25×10^5 A cm^{-2}. It is probable that much of the current will be flowing through the bundle of SWNTs at the core of the nanowire. SWNTs are known to be able to sustain current densities in excess of 10^9 A cm^{-2} [YKD00]. The SWNTs may also provide a thermal sink for heat dissipated in the nanowire due to their high thermal conductivity, greater than 200 W mK^{-1} [HLN$^+$00].

These results demonstrate the nanowire tips are near ideal conducting probes [OAW95] with low, ohmic, load independent resistance up to the point of contact. To test the robustness and longevity of the nanowire tips an Au surface was imaged continuously in conducting mode, with a 2 V bias applied across a 1.1 MΩ resistance in series. The same annealed Au Pd nanowire tip was used as for the i - d response shown in Figure 4.25. Figure 4.27 shows topography, (a) and (c), and current, (b) and (d), images taken after 4 hrs, (a) and (b), and 5 hrs, (c) and (d), of continuous scanning. The robustness of the nanowire tip is shown by both the clarity of the topography image after 4 hrs continuous imaging (a), and the current image, (b). The latter demonstrating there is still a good conducting contact between nanowire and surface. The small variations in the current signal reflect differences in the contact interaction between the apex of the nanowire and the substrate. Both the topography and current images recorded after 4 hrs are similar to those when imaging commenced.

After 5 hrs of imaging it is clear from the artifacts in the topography that the nanowire has been damaged in some way although, interestingly the current image still demonstrates a good electrical contact between nanowire and surface. Subsequent TEM imaging showed that the nanowire had reduced in length, as shown schematically by the insets in Figures 4.27 (b) and (d). However, given that the nanowire is conducting along its entire length, despite being worn down it still remains a good conducting tip. This is in marked contrast to a metal coated tip

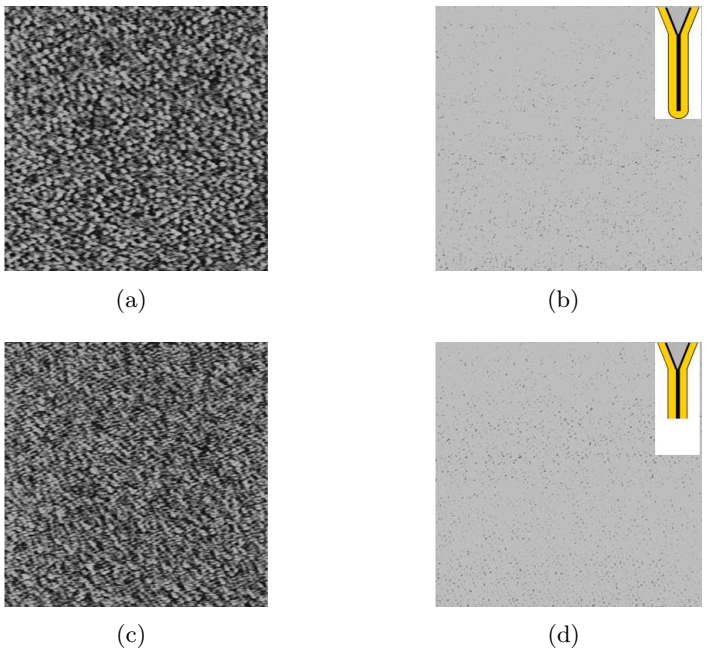

Figure 4.27: (a and c) topography, and (b and d) conductivity images of a Au surface taken with a Au Pd nanowire tip after scanning continuously for (a and b) 4 hr, and (c and d) 5 hr. The images are 3 μm square. Insets in (b) and (d) are schematics of the nanowire before and after damage respectively.

where, when the thin metal coating wears away at the tip, the insulating Si (or Si_3N_4) underneath becomes the point of contact. Clearly to improve the longevity for conductivity imaging tougher metals, such as Pt Ir, could be used to form the nanowire.

To demonstrate the generality of this nanowire tip fabrication method we have also formed Au nanowires. Au is particularly useful as an electrode material, and as such a well defined Au nanowire would be an invaluable tool for studying electrochemistry at the nanometre level. Figure 4.28 shows TEM images of an Au nanowire on a tapping mode tip. The nanowire is 1 μm in length, 80 nm wide at its base, and 50 nm at its end, the difference corresponding to the change in diameter of the SWNT bundle at its core. Although Au has a larger grain size than Au Pd, and although there appears to be only a weak interaction between Au and

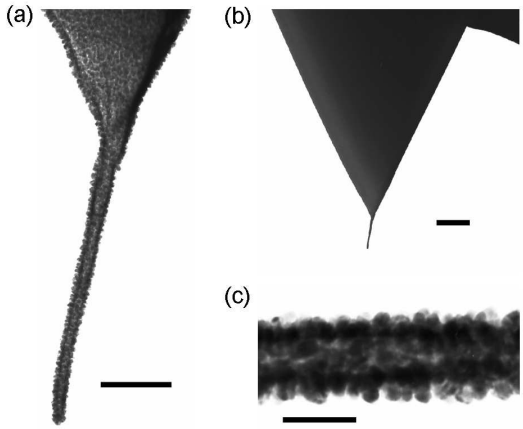

Figure 4.28: TEM images of (a) a Au nanowire tip and (b and c) an enlarged view of the nanowire. The scale bars are (a) 250 nm, (b) 1 μm, and (c) 50 nm.

SWNT's [ZD00], the nanowire formed is still continuous although not as uniform as the Au Pd nanowires.

In conclusion, we have demonstrated the use of SWNTs as templates for the formation of metal nanowire SPM tips. The high aspect ratio probes formed are robust, conducting, of a well defined geometry and can be used for imaging in either contact or tapping mode. The generality and simplicity of the method described presents an easy route to the formation of nanowires. The core of SWNTs inside the nanowire gives it mechanical and electrical stability, and the variety of different metallic nanowires which could be formed extends the capabilities of the probe to conductivity, magnetic, and electrochemical imaging.

4.5 Conclusions and future work

We have fabricated SWNT-AFM tips and demonstrated their use for high resolution topographic imaging. In addition we have shown the benefits of the use of tips composed of several SWNTs which stick together to form a bundle, 'nt tips', which can be fabricated more easily and are more stable than individual SWNT-AFM tips. We have demonstrated that nt tips possess many of the advantages of individual SWNT-AFM tips (e.g. high resolution, low tip-sample forces, ability to buckle rather than break) whilst having the additional advantages of greater robustness and enabling imaging at longer protruding lengths. Their use for EFM will be discussed in the next chapter.

Attachment of SWNTs to metal-coated AFM tips by Van der Waals forces produces mechanically and electrically stable, conducting nt tips, capable of high-resolution topographical imaging, with contact resistances to metallic tubes as low as 100 kΩ . These are key requirements for the application of nt tips as electrical or electrochemical scanned probes, research areas that we are currently exploring. Dipping the end of the SWNT(s) into liquid Hg and measuring the electrical characteristics as a function of immersion depth allows the electrical nature of the SWNT and its contact to the tip to be assessed effectively. Furthermore, this procedure opens up new possibilities for investigating the length dependence of the electrical transport properties of individual SWNTs. The use of a solid electrode allows the force dependence of SWNT conduction to be studied. Study of both these areas will be continued after these preliminary results, with the aim of investigating the unique possibilities opened up by this novel SWNT device, geometry.

We have demonstrated that nt tips also act as ideal templates for the formation of nanowire probes. Future work in this area will focus on a variety of multi-layer nanowires. In particular, we will form insulated 'nanoelectrode' probes

by coating the metallic nanowire in insulator, selectively removed at the end of the nanowire, with the aim of forming reproducible and geometrically well defined probes for combined scanning electrochemical microscopy and AFM [GM02]. To improve the uniformity of coating a multiple layer process will be employed; previous work proved that Ti coats SWNT uniformly at low film thickness, as low as 2 nm, and can act as an adhesive layer for the formation of uniform metal nanowires of diameter $\lesssim$ 10 nm [ZD00].

Chapter 5

Increased Resolution EFM and SGM

As electrical components continue to shrink in size the need for higher resolution electrical characterization techniques increases. Electric force microscopy (EFM) has proven its ability to probe the electrical properties of nanoscopic systems such as DNA [BMS+02], single wall carbon nanotubes [BMS+02] (SWNTs), and semiconductor nanocrystals [KB99, KOB01, DMJ+03]. However, EFM has suffered from two significant drawbacks which have limited its applicability: (i) it has lacked the spatial resolution associated with other scanned probe techniques; (ii) the difficulty of deconvoluting tip effects has complicated quantitative analysis of results.

The underlying principle in all EFM techniques is that an electrostatic force is experienced by a conducting tip due to capacitive coupling with a substrate. The many variants on this basic principle can be roughly separated into two categories: force sensitive techniques such as SSPM and scanned impedance microscopy (SIM); and force gradient sensitive techniques. In this work we focus on force gradient sensitive techniques which are well known to provide increased spatial resolution relative to force sensitive EFM, e.g. [CGB01, GRS02, GCGHB03]. This has two

corollaries: (i) it is possible to distinguish features at higher resolution; (ii) the image is dominated by local effects. In force sensitive EFM a significant proportion of the electrostatic force can come from the tip cone and even the cantilever [BL97, CGB01, GCGHB03]. The presence of large conducting objects within a few microns of the tip apex will thus make a significant contribution to the force, complicating the deconvolution of tip effects from an image. By comparison, when the tip is close (10 - 100 nm) to the surface, force gradient techniques are dominated by the tip apex-surface interaction [CGB01, GCGHB03] and hence probe, or conversely are determined by, the tip apex geometry and features local to it on the surface.

We demonstrate here that the use of SWNTs as tips for EFM increase the spatial resolution of the technique. In addition, we show that nt tips have a well defined tip-sample electrostatic force gradient, which should facilitate quantitative interpretation of EFM data.

5.1 Increased Resolution EFM

5.1.1 Theoretical background to force gradient EFM

Although a simple introduction to EFM was given in Section 1.2, in order to appreciate how the spatial resolution of EFM can be increased we must understand more fully how the technique works. To do this we start with the basics of idealized EFM, and then introduce the effects of standard tip cantilever geometries and realistic oscillation amplitudes.

The motion of the cantilever, when not in contact with the surface, can be described as an harmonic oscillator. The presence of long range forces adds a weak perturbation, $U_{ts}(z)$, to this. In dynamic mode AFM the damping of the cantilever oscillation is compensated by the driving force, hence it is usually sufficient to use the conservative equations of motion to consider the path of the tip. The unperturbed

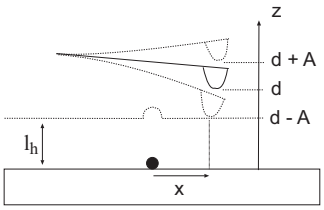

Figure 5.1: Schematic illustrating the oscillation of a tip with amplitude A, a height d above the surface.

motion of the tip is then determined by

$$m^* \ddot{z} + kz' = 0 \tag{5.1}$$

which is trivially solved to give

$$z'(t) = Acos(2\pi\nu_0 t) \tag{5.2}$$

where the resonance frequency

$$\nu_0 = \frac{1}{2\pi}\sqrt{\frac{k}{m^*}} \tag{5.3}$$

Adding a weak perturbing potential results in an additional force between the tip and sample $F_{ts}(z) = -\partial U_{ts}/\partial z$. Eq. 5.1 becomes

$$m^* \ddot{z} + kz' - F_{ts}(z) = 0 \tag{5.4}$$

We can expand the tip surface force into a Taylor series about the cantilever's equilibrium position d,[1]

$$F_{ts}(z) = F_{ts}(d) + \frac{\partial F_{ts}(d)}{\partial z}(z - d) + ... \tag{5.5}$$

In the simplest approximation the force gradient, $f'_{ts}(z) = \frac{\partial F_{ts}(z)}{\partial z}$, is assumed to be constant throughout the oscillation cycle, then (5.4) becomes

$$m^* \ddot{z} + \left(k - f'_{ts}(d)\right) z' - F_{ts}(d) = 0 \tag{5.6}$$

[1] the perturbing force will also deflect the cantilever a small amount from its unperturbed equilibrium position d_0

The solution of this equation of motion is $z' = Acos(2\pi(\nu_0 + \Delta\nu)t)$, where the frequency shift

$$\Delta\nu = \nu_0 \left(\sqrt{1 - \frac{1}{k} f'_{ts}(d)} - 1 \right) \tag{5.7}$$

Since the resonance frequency will always be much greater than the frequency shift this is well approximated by the relation

$$\Delta\nu = -\frac{\nu_0}{2k} f'_{ts}(d) \tag{5.8}$$

Eq. (5.8) is the often quoted statement that the frequency shift is a measure of the gradient of the tip sample force. This result primarily relies on the simplification that $f'_{ts}(z)$ is constant over the entire amplitude of oscillation, generally true only when the amplitude of oscillation is much smaller than the tip sample separation, $A \ll d$.

Figure 5.2 illustrates the effect of adding a perturbing potential to the unperturbed cantilever system. Figure 5.2 (a) and (d) show the potential energy and the force on the tip in the unperturbed case, whilst Figure 5.2 (b) and (e) are the perturbing potential and force. Figure 5.2 (c) and (f) show the total potential and force. The perturbing force illustrated corresponds to an attractive force decreasing away from the surface, such as would be expected from capacitive electrostatic interactions, and has been chosen so as to have a uniform force gradient. The effect of the uniform force gradient is to maintain the harmonic oscillator form of the potential, but, as shown in Figure 5.2 (c), shift the equilibrium position to $d < d_0$ closer to the sample, and reduce the energy minimum. The effective spring constant is also reduced, as shown by the slope of the lines in Figure 5.2 (f). In general, forces experienced by the tip decay away from the surface so that a positive force gradient corresponds to a negative (attractive) force.

In practise what is usually measured directly is the phase lag, ϕ, between the oscillation of the cantilever and the driving signal. We recall from Section 1.2 that

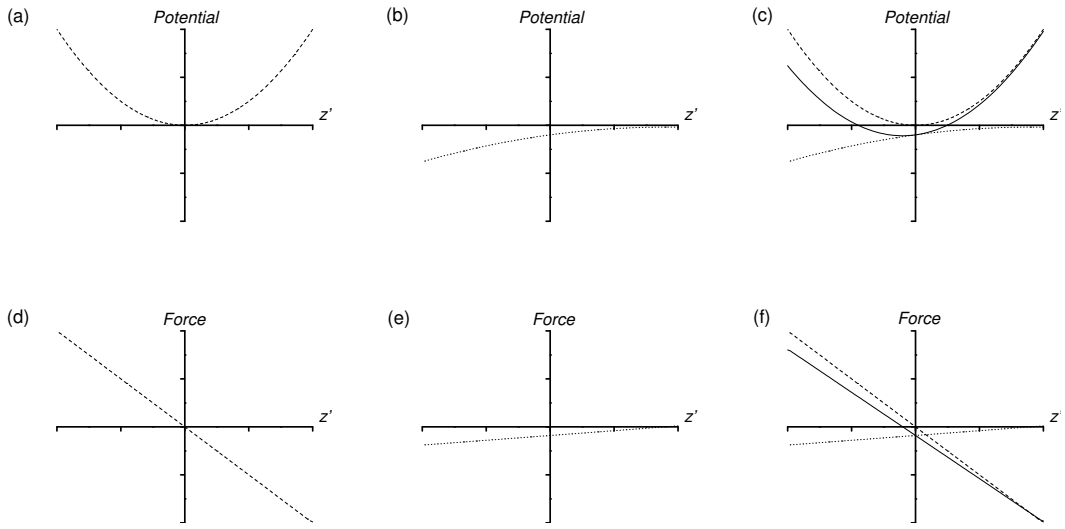

Figure 5.2: Total potential and force (solid lines) due to adding a perturbing potential (dotted lines) to the cantilever harmonic oscillator potential (dashed lines).

for small phase changes $\phi \propto \Delta\nu$, or explicitly

$$\phi \cong 2Q\frac{\Delta\nu}{\nu_0} = -\frac{Q}{k}\, f'_{ts}(d_0) \tag{5.9}$$

where the phase shift is measured in radians. Hence negative phase changes correspond to positive force gradients, and so attractive forces.

As described previously, see page 33, an electrostatic force is experienced by a conducting tip due to capacitive coupling with a substrate. Given a dc potential difference, V_{dc}, between the tip and substrate[2] the electrostatic potential energy is $U_{ts}(z) = -C_{ts}(z)V_{dc}^2/2$. The tip surface capacitance, $C_{ts}(z)$, is the total capacitance between the entire tip and the entire surface[3]. The resultant force on the tip is given, as before, by

$$F_{ts}(z) = -\frac{\partial}{\partial z}U_{ts}(z) = \frac{1}{2}\frac{\partial}{\partial z}C_{ts}(z)V_{dc}^2 = \frac{1}{2}C'_{ts}(z)V_{dc}^2 \tag{5.10}$$

and the electrostatic force gradient

$$f'_{ts}(z) = \frac{\partial}{\partial z}F_{ts}(z) = -\frac{1}{2}\frac{\partial^2}{\partial z^2}C_{ts}(z)V_{dc}^2 = \frac{1}{2}C''_{ts}(z)V_{dc}^2 \tag{5.11}$$

[2] included in this, as before, is the difference in work function between the tip and substrate

[3] i.e. this expression is really an integral over the local potential and capacitance of all the tip and surface

It is useful at this point to consider the electrostatic force gradient due to different geometrical configurations. In general, a conducting tip above a uniform conducting plane follows a power law behavior ${f'_{ts}}^n(z) = C_n/z^n$. The power law due to several idealised tip geometries is discussed in [BL97], for example a spherical tip gives $n = 2$ for small z, whilst both a conical tip and a uniform line charge (they are in effect equivalent) give $n = 1$.

Tip cone and cantilever contributions to the electrostatic force

Following [GCGHB03, CGB01] we separate C_{ts} into three parallel components; the tip apex to surface capacitance C_{tas}, the tip cone to surface capacitance C_{tcs}, and the cantilever to surface capacitance C_{cs}.

$$C_{ts}(z) = C_{tas}(z) + C_{tcs}(z) + C_{cs}(z) \tag{5.12}$$

The total force, or force gradient, experienced by the tip is thus the sum of the contributions from the tip apex, tip cone, and cantilever. Although the tip cone and cantilever are further away from the surface than the tip apex they contribute significantly to the electrostatic forces involved [BL97, JLHS98, CGB01, GCGHB03]. Figure 5.3, taken from [GCGHB03], demonstrates that for usual tip geometries the cantilever contribution to the force dominates until the tip apex is less than a few nm from the surface .

It is important to realize that the three different components also have different characteristic areas, or effective spatial resolutions [GCGHB03]. Clearly the cantilever, at about 10 μm from the surface and of similar width, will have an effective spatial resolution on the order of several micrometres. The tip cone is also, on average, a few micrometres away from the surface and micrometre scale in diameter, resulting in a resolution also on the micrometre length scale. The tip apex, with radius of curvature $r \sim 20$ nm and < 100 nm from the surface, is by contrast likely

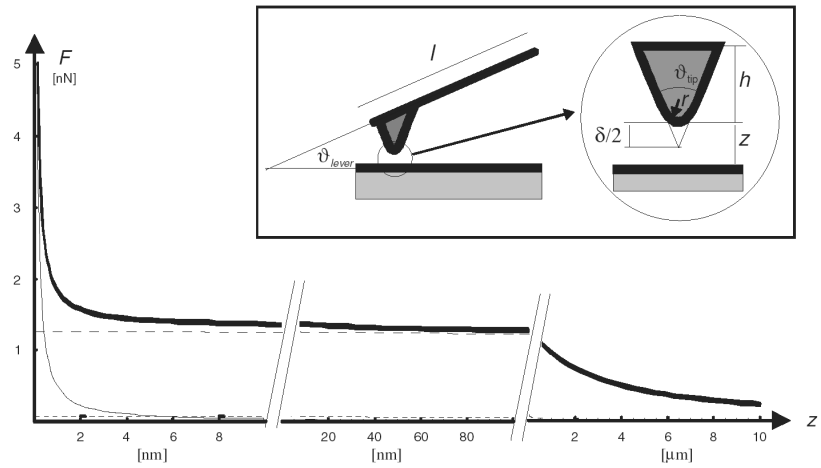

Figure 5.3: *Calculated electrostatic force versus tip sample distance. The thick solid curve corresponds to the total electrostatic force, while the other three represent each of the contributions from the cantilever (dashed line), the tip cone (short dash) and the tip apex (thin solid). These curves have been calculated for $U = 1$ V, and a probe with a cantilever of 100 μm length and 40 μm width, a tip cone of 3 μm length and a radius of 20 nm for the tip apex. The opening angle for the tip is $\vartheta_{tip} = 45°$ and an angle of $\vartheta_{lever} = 20°$ was assumed between the cantilever and the sample. Inset: probe proposed for modelling an EFM set-up. This probe is composed of three basic units: a cantilever of length l, width w and tilting angle ϑ_{lever} with respect to the sample, a mesoscopic tip cone of height h and (full) opening angle ϑ_{tip}, as well as a parabolic tip apex of radius r.* Taken from [GCGHB03].

to have a resolution closer to 100 nm.

Figure 5.3 demonstrates that for typical lift heights, $l_h \gtrsim 10$ nm, the force is dominated by contributions from the cantilever and tip cone. However, the low spatial resolution of these contributions implies that small features in the EFM image are still due to the tip apex to sample interaction. Quantitative analysis of these features is complicated by the longer range forces due to the cantilever and tip cone. For example, the asymmetric sample geometry under investigation in Section 3.3.1, consisting of two electrodes of width $5 - 10$ μm and separation $1 - 5$ μm with a bias voltage dropped between the two, resulted in spatially varying components of the force due to the cantilever and cone. This complicated analysis of the image, making only qualitative statements possible. The Kelvin method, as

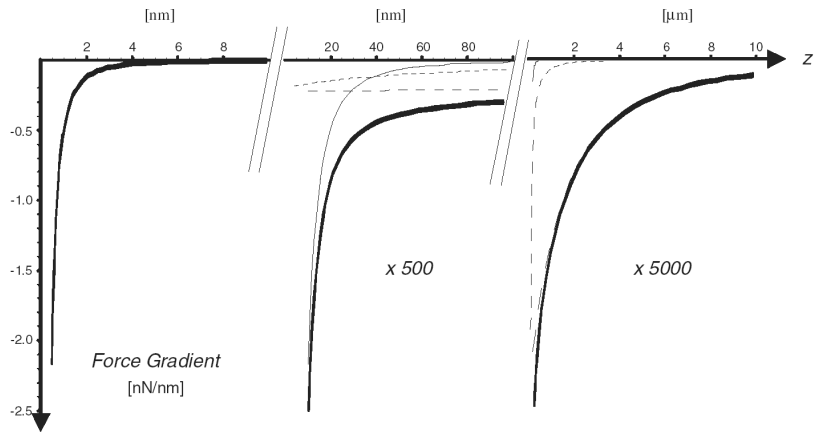

Figure 5.4: *Electrostatic force gradient versus tipsample distance calculated from the model proposed in the main text. The thick solid curve corresponds to the total electrostatic force gradient, while the other three represent separately each of the contributions from the cantilever (dashed line), the tip cone (short dash) and the tip apex (thin solid). These curves have been calculated for the same parameters as those used in Figure 5.3.* Taken from [GCGHB03].

explained in Chapter 1, finds the average potential of the surface below. This average potential consists of an average over each section of the surface weighted by its total capacitance to the whole tip [GCGHB03], i.e. including components due to the tip apex, tip cone, and cantilever. The Kelvin potential measured in this way is thus not the local potential at the tip-apex as is often claimed; quantitative interpretation must include consideration of tip convolution effects, including objects up to a few micrometres away from the tip-apex.

Figure 5.4 shows the force gradient contributions of each part of the tip as a function of distance from the surface. There is still a substantial, though much reduced, component due to the cantilever. However, under normal experimental conditions, i.e. $l_h \simeq 20$ nm, the tip apex to surface interaction is the dominant contribution. So, force gradient based EFM probes, or conversely is determined by, the tip apex geometry and features local to it on the surface. In addition, the force gradient due to a specific feature on the surface decays spatially more rapidly than

the force (a spherical tip above a surface has an electrostatic force $\propto z^{-1}$, whilst the force gradient is $\propto z^{-2}$). Thus the tip apex contribution itself will demonstrate higher spatial resolution in force gradient techniques.

Real oscillation amplitudes

The relation quoted in (5.8) is only true when the force gradient is constant over the entire oscillation of the cantilever. In typical experimental conditions, where $A \simeq 50$ nm and $l_h \simeq 20$ nm, this is clearly not the case. The force gradient varies significantly over the oscillation of the cantilever. So, it is necessary to include higher order terms in the Taylor expansion, eqn. 5.5.

The energy associated with the oscillation of the tip in the simple harmonic oscillator approximation is given by $E = kA^2/2$; for $k \sim 10$ Nm^{-1}, and $A \sim 10$ nm, we find $E \sim 10\ keV$. By comparison, the typical interaction forces between the tip and the surface are small $\sim 10\ eV$ [Gie03]. As a result of the large ratio of the oscillation energy to the interaction potential, first order perturbation theory works well in describing the effect of the interaction forces. Using the Hamilton-Jacobi approach the frequency shift to first order has been calculated to be [Gie03]

$$\Delta\nu(z)_{z=d} = -\frac{\nu_0}{kA^2}\langle F_{ts}(z)z'\rangle_{z=d} \tag{5.13}$$

where the brackets indicate averaging over one oscillation cycle. Integrating by parts gives, in analogy to Eq. (5.8),

$$\Delta\nu(d) = -\frac{\nu_0}{kA^2}\langle f'_{ts}(d)\rangle \tag{5.14}$$

where the force gradient is replaced by a weighted force gradient

$$\langle f'_{ts}(d)\rangle = \frac{1}{\pi A^2/2}\int_{-A}^{A} f'_{ts}(d-z')\sqrt{A^2-z'^2}\ dz' \tag{5.15}$$

We see that the effect of a non-uniform force gradient can be accounted for by using an effective force gradient, which is a weighted average of the force gradient over the

amplitude of oscillation.[4] With a power law force of the form $F_{ts}^{m}(z) = -\alpha_m z^{-m}$ Eq. 5.15 is equivalent to [Gie97, HSW99]

$$\Delta\nu_m(d) = \frac{\nu_0\alpha_m}{kA}\int_0^{2\pi}\frac{\cos(x)}{(d+A\cos(x))^m} \tag{5.16}$$

which can be solved analytically for small values of m. For example, for $m = 1$[5] this becomes [HSW99]

$$\Delta\nu_1(d) = \frac{\nu_0\alpha_1}{kA^2}\left(1 - \frac{d}{\sqrt{d^2-A^2}}\right) \tag{5.17}$$

In the limit $d \gg A$

$$\Delta\nu_1(d) = \frac{\nu_0\alpha_1}{2kd^2} = \frac{\nu_0}{2k}\frac{\partial}{\partial z}(-\alpha_1 z^{-1})_{z=d} \tag{5.18}$$

we recover the original approximation Eq. (5.8) as expected. In the opposite limit where $d = A + \delta$ and $\delta \ll A$, i.e. the tip at the bottom of its oscillation is almost hitting the surface, we find

$$\Delta\nu_1(\delta) = -\frac{\nu_0 C_1}{2kA^{3/2}}\delta^{-1/2} \tag{5.19}$$

Although this is for the specific case of a force with a $1/z$ dependence, it illustrates the following trends that are true for all inverse power law forces, and even for exponential forces [Gie97]: (i) for $d \gg A$ the simple approximation from Eq. (5.8) is true and $\Delta\nu \propto f'_{ts}$; (ii) for $d = A + \delta$ and $\delta \ll A$ (i.e. $l_h \ll A$) the magnitude in frequency shift $\Delta\nu \propto A^{-3/2}$, and (iii) $\Delta\nu \propto \delta^{m-1/2}$ for a force law $F \propto z^{-m}$.

Figure 5.5 (b) shows that the observed frequency shift is always less than that predicted by Eq. 5.8, but tends towards it for $d \gg A$. At a given lift height the frequency shift will increase as the amplitude is reduced [6], asymptotically approaching the value predicted by Eq. 5.8, Figure 5.5 (a). The tip-cone and cantilever are both

[4] This approach assumes that the perturbation is small enough that the oscillation can still be taken to be symmetric. For small oscillation amplitudes and large potential differences this may not be valid.

[5] i.e. $n = 2$ for the force gradient discussed previously, and the relevant force law for a sphere

[6] assuming the same amplitude is used for topographical imaging as well as in lift-mode

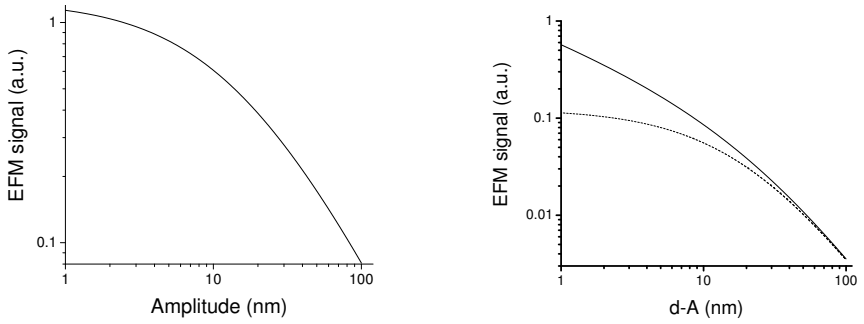

(a) (b)

Figure 5.5: Electrostatic force gradient versus (a) amplitude ($l_h = 20$ nm) and (b) tip sample distance (A = 20 nm). The dashed line in (b) corresponds to the constant force gradient approximation, and the solid line to the amplitude corrected model. The frequency shifts plotted are for a tip with a $1/z$ electrostatic force dependence

far from the surface and so amplitude independent, thus by operating at reduced amplitude the relative contribution of the tip apex is maximised. Although the minimum lift height is usually set by the sample topography, this analysis shows that the relative tip apex contribution is also maximised by minimising the lift height.

Conclusions

In force sensitive EFM a significant proportion of the electrostatic force can come from the tip cone and even the cantilever. The presence of large conducting objects within a few microns of the tip apex will thus make a significant contribution to the force, complicating the deconvolution of tip effects from an image. By comparison, force gradient techniques, when the tip is close to the surface, are dominated by the tip apex-surface interaction and hence probe, or conversely are determined by, the tip apex geometry and features local to it on the surface.

Jacobs et al.[JLHS98] show that the electrostatic force contribution of the tip apex is maximised using *'a long and slender but slightly blunt tip, supported by a cantilever of minimal width and surface area'*. Although we have little control over the cantilever dimensions, the ideal *'long and slender but slightly blunt tip'* is surely

the nanowire tips demonstrated in Section 4.4.

However, it is clear from the above analysis that the greatest increase in spatial resolution can be achieved by using force gradient EFM. In particular, using an nt tip for force gradient EFM would have several advantages. The increased spatial topographic resolution allows more accurate comparison of EFM features with topographic features. The decreased tip sample adhesive forces allows smaller oscillation amplitudes to be used, and the high aspect ratio of the SWNT enables the rest of the tip cone to be far enough from the surface so that it has only minimal contribution to the signal.

5.1.2 Force gradient EFM with nt tips

Following the previous discussion we aim to maximise the spatial resolution of EFM by using nt tips for force gradient microscopy at low lift heights and low amplitudes. First, we show that the nt tips provide increased spatial resolution over conventional Si tips. Metal coated tips, although they have a higher capacitance to the surface and hence higher resolution to the applied bias, also have substantially large tip radii than the uncoated Si tips, and so lower spatial resolution.

In this chapter we will investigate three forms of force gradient microscopy. As discussed in the previous section, the application of a dc potential difference, V_{dc}, between the tip and sample results in a change of resonance frequency $\Delta\nu$, and hence a change in phase $\Delta\phi$. It is $\Delta\phi$ that is measured directly by the lock-in in the AFM, and this can be recorded (dc-EFM) to give a measure of the force gradient as discussed previously. Alternatively, the AFM can use an additional feedback loop to maintain the phase lag between the cantilever oscillation and driving force at $\pi/2$, and hence on resonance, by changing the driving frequency. This change in frequency can be recorded, allowing direct measurement of $\Delta\nu$. This technique is called frequency modulation EFM (fm-EFM).

dc-EFM is limited in its application due to its low voltage resolution. In addition, the large potentials required result in a strong perturbing field on the sample, making the technique very invasive. This can effect conduction through the device being studied, for example in SGM, as well as inducing surface charge injection. In analogy to surface potential microscopy we can apply an additional ac potential at frequency ω, such that the total potential difference between the tip and sample is $V = V_{dc} + V_{ac}(\omega)$. The resultant force gradient has three components,

$$\begin{aligned} f'_{ts} &= f'_{ts}(dc) + f'_{ts}(\omega) + f'_{ts}(2\omega) \\ f'_{ts}(\omega) &= V_{dc} V_{ac} C''_{ts} \sin(\omega t) \end{aligned} \tag{5.20}$$

This results in a component of $\Delta\phi$ at ω. $\Delta\phi_{rms}(\omega)$ is measured using a lock-in (Stanford Research Systems SR810 digital dual phase lock-in amplifier) and the output fed back into the AFM through the Signal Access Module. $V_{ac}(\omega)$ must be at a low enough frequency for the cantilever to react to it, and its phase response adjust. Although the phase response of the cantilever oscillation is very fast, as discussed in Chapter 1, the AFM controller has a 1.5 kHz low pass filter see e.g. [CCW$^+$03]. However, ω must be high enough to allow sensible imaging speeds since the time per pixel in an image should be greater than the period of the applied voltage. In this work, V_{ac} frequencies in the range 500 Hz to 1.5 kHz were used, with V_{ac} rms amplitudes of 2 - 4 V. Advantages of this ac technique, here called ac-EFGM, over dc-EFM and fm-EFM include: the increased signal to noise ratio due to the lock-in, and hence increased voltage sensitivity; the selective measurement of the electrostatic component of the force gradient, even in the presence of other long range forces such as magnetic or Van der Waals forces; and the reduction of induced charging on the surface which can be caused by large dc potentials.

SWNT arrays for EFM spatial resolution calibration

The spatial resolution of electric force microscopy is difficult to quantify since there is no hard surface to image. In the past 'potential step' standards have been used composed of well defined interfaces between different materials, e.g. [GRS02, KBFJ02, SGS+03]. As shown by Kalinin et al. [KBFJ02] SWNTs are near ideal line sources for the characterization of EFM tips, due to their small diameter, significantly smaller than the typical tip radius of curvature, and high aspect ratio. An EFM linescan perpendicular to a SWNT on, and biased relative to, an insulator was shown to have a Lorentzian response. The Lorentzian dependence of an EFM linescan perpendicular to a SWNT was commented on in Chapter 3, and in [KBFJ02] was suggested as a means of calibrating the EFM transfer function of a tip (i.e. the convolution effect). The well defined functional form of the Lorentzian allows an easily quantifiable measure of the resolution of a tip. The standard definition of a Lorentzian is

$$y = \frac{2A_L}{\pi} \frac{w}{4(x - x_c)^2 + w^2} \tag{5.21}$$

A_L is the area under the peak, x_c the centre of the peak, and w the peak width. The peak height $h_L = 2A_L/\pi w$. The peak width can be used as a quantitative measure of the spatial resolution of the tip, and the peak height as a measure of the amplitude of the response. It is worth noting at this point that the EFM technique used in [KBFJ02] was in fact a force gradient based technique, SIM, as was the technique used in Chapter 3, SSPM. However, as we shall shortly see, the force gradient EFM linescan perpendicular to a SWNT is also well fit by a Lorentzian.

The calibration samples used here consist of SWNTs grown by cCVD on highly doped Si, with 300 nm thick insulating SiO_2 layer. An array of linear electrodes (5 nm Cr, 45 nm Au), of width and spacing 5 μm, were patterned ontop by photolithography and lift-off. The underlying Si was grounded, and electrical con-

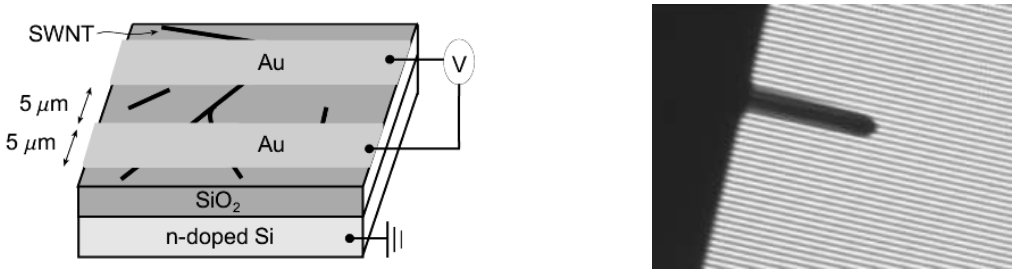

Figure 5.6: *left* schematic of calibration grid, *right* optical micrograph of cantilever and calibration sample

nection was made to the electrodes. A mask aligner was used for photolithography, with SU1805 photoresist. A schematic of the device geometry is shown in Figure 5.6. The sample consists of a large array of electrodes ($\sim$ 5 mm square), minimising the asymmetry in the cantilever contribution to the EFM signal. The optical microscope image also shown in Figure 5.6 shows the scale of the cantilever relative to the electrodes. The large array also removed the need for careful positioning of the tip on the sample, simplifying the experiment. The consistency of the width and height of the Lorentzian response for a given tip under the same conditions is illustrated by Figure 5.7, and is clearly independent of the individual SWNT or small bundle across which it is scanned.

In ac-EFGM, V_{dc} was applied to the tip and V_{ac} to the SWNT calibration

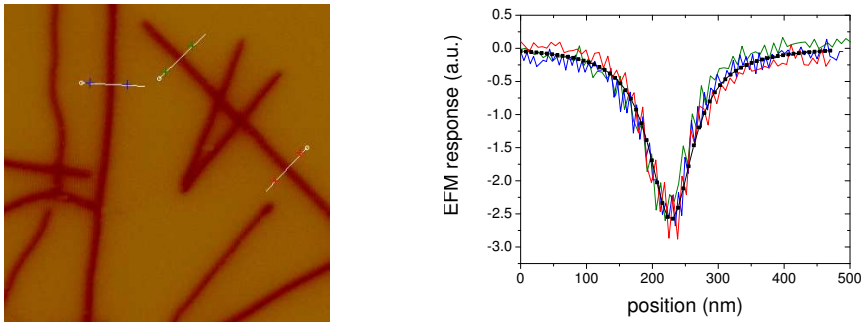

Figure 5.7: *left* 2.5 μm square dc-EFM image of SWNTs biased relative to the SiO_2 substrate, *right* the linescans illustrated in image, the solid line is a Lorentzian fit to the data.

substrate, whereas in fm-EFM V_{dc} was applied to the SWNT calibration substrate. These configurations ensured contrast only came from SWNT attached to electrodes and not from other features on the surface. For each measurement the tip was repeatedly scanned perpendicular to an isolated SWNT, connected to at least one electrode on the calibration sample, with the 'y-axis' motion disabled. Each measurement corresponds to an average over at least 32 lines. EFM measurements were taken in 'lift-mode' and the topography linescan was taken under light tapping conditions. All potentials were only applied during imaging in lift mode, where the tip is not in contact with the surface. This was achieved by applying V_{dc} through the Nanoscope software, which enables different potentials to be set on the 'Main' and 'Interleave' line, and Signal Access Module. $V_{ac}(\omega)$ was taken from the output of the lock-in, via a transistor relay switch, which was switched on and off by a dc potential from the Nanoscope software and Signal Access Module.

Typically nt tips used for this work had l_{nt} from 150 to 300 nm, and r_{nt} from $\sim$ 3 to 6 nm, substantially smaller than the nominal radius of curvature of the Si tips used ($\approx$ 15 nm as new). Figure 5.8 (c) shows a TEM image of a SWNT bundle ($l_{nt} \approx 150$ nm, $r_{nt} \approx 3$ nm), on an uncoated Si tip, after shortening. In addition, nt tips were formed on Au Pd ($\sim$ 30 nm thick) coated Si tips. These tips gave similar results to the uncoated nt tips, provided the length of the bundle was sufficient to make the contribution of the metal coated tip insignificant. The optimum length of SWNT bundle will be discussed later.

Standard oscillation amplitudes of 1.5 - 2 V (corresponding to 40 - 70 nm[7]) were used for Si tips. Due to decreased adhesive forces the nt tips imaged stably at low oscillation amplitudes, typically $A \simeq 0.4$ V (10 - 15 nm) was used here. The work presented in this section was all performed with the Multimode AFM,

[7]For comparison with the theory discussed in the previous section, real amplitudes here are quoted in terms of $z = A\cos(\omega t)$, not as rms values.

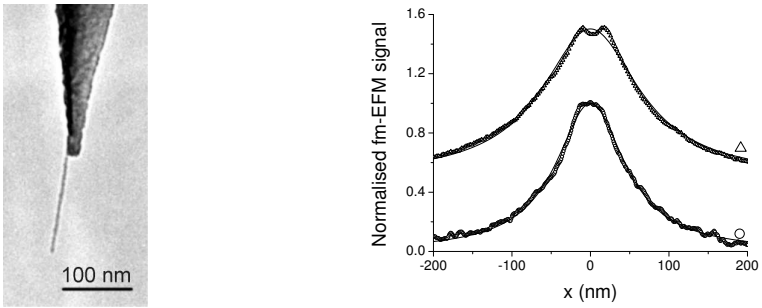

(a) (b)

Figure 5.8: (a) TEM image of an nt tip, (b) EFM response of SWNT calibration substrate taken with a Si tip (△), and an nt tip (○). The solid lines are Lorentzian fits to the data. The Si tip response is offset for clarity.

Nanoscope IIIa Controller, and Quadrex module. Electrical connection was made to the uncoated Si tips using silver dag as recommended in [JKS99].

Both Si and nt tips, for both ac-EFGM and fm-EFM, gave EFM line-scans that could be fitted by Lorentzians. fm-EFM line-scans taken with $l_h = 20$ nm and $V_{dc} = -4$ V by an nt tip, and a Si tip are shown in Figure 5.8 (b), as are the Lorentzian fits to the data. The Lorentzian shape of the observed response is clear, although it is not obvious why force sensitive and force gradient sensitive EFM should both give Lorentzian responses, see Appendix C.

In order to use the SWNT calibration sample it is important first to check that the Lorentzian peak heights and widths respond to voltage changes as expected. Figure 5.9 shows the voltage response of the Lorentzian peak heights and widths for a Si tip. As expected, the peak heights were proportional to ${V_{dc}}^2$ for fm-EFM, and to both V_{dc} and V_{ac} (not shown) for ac-EFGM. The peak widths were roughly independent of the voltage applied, although for large voltages at low lift heights the peak widths were increased by 20 - 30 nm in fm-EFM due to charge injection[8].

[8]When large potentials are applied to SWNT on SiO_2 charge is injected into the oxide due to the high local field, see Section 3.3.2, this charge is visible in EFM images and increases the apparent width of the EFM linescan across the SWNT. This effect was minimized by applying the potentials only during lift mode, and should not be present in ac-EFGM due to the relatively long timescales involved in the charge injection and diffusion.

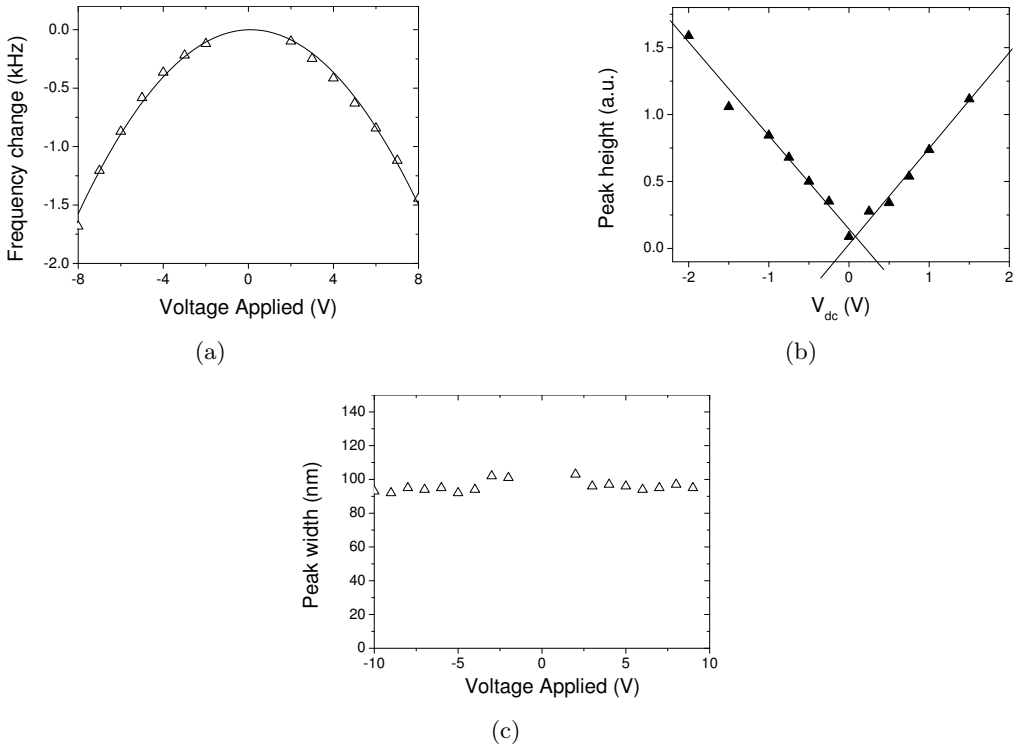

Figure 5.9: Dependence of Lorentzian peak heights on (a) the applied voltage in fm-EFM, and (b) the applied V_{dc} in ac-EFGM. (c) dependence of Lorentzian peak widths on applied V_{dc} in ac-EFGM.

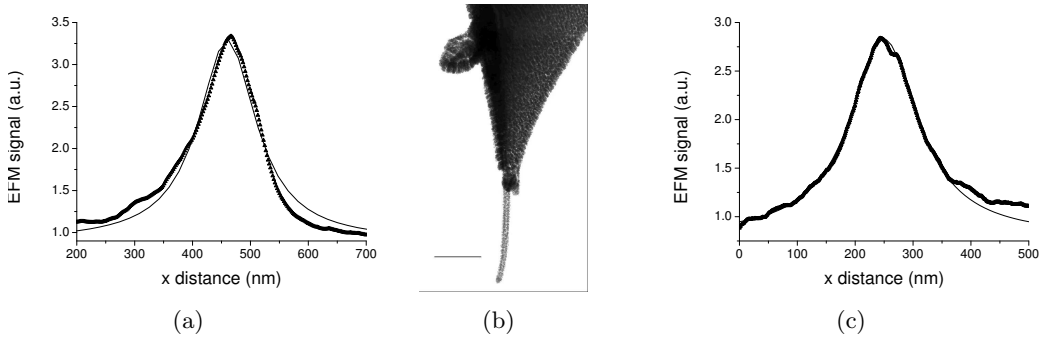

Figure 5.10: (a) ac-EFGM linescan prior to attachment of Au Pd nanowire and (c) after attachment of nanowire. (b) TEM image of the nanowire tip used, the scale bar is 200 nm. Note the presence of a contaminant on the side of the tip.

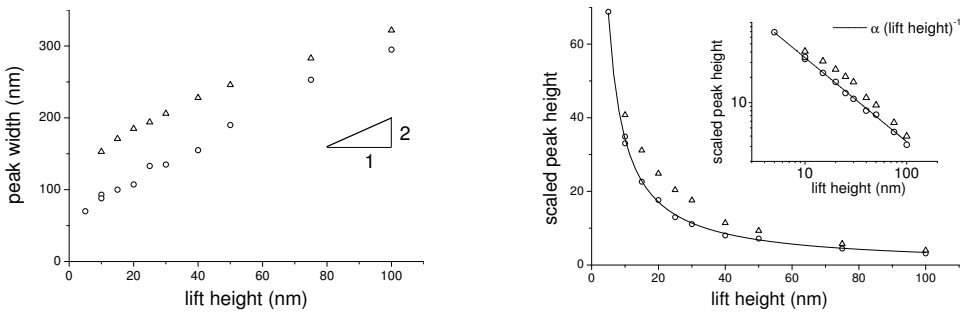

(a) (b)

Figure 5.11: Lorentzian peak widths (a) and heights (b) as a function of lift height for an nt (o) and normal ($\triangle$) tip. Inset in (b) log-log plot of peak heights, the line is a fit of α(lift height)$^{-1}$ to the nt tip peak heights.

The calibration sample can also be used to test for tip asymmetry convolution effects. These are not just defined by the tip-apex geometry as in topographical imaging, but due to the long range forces are also determined by objects away from the tip-apex. An example of this is given in Figure 5.10. The linescan response of an Au Pd coated tip is shown in (a), it is clearly asymmetric. TEM analysis of the tip revealed a contaminant particle situated away from the tip-apex. An nt tip was then picked up onto the tip, and a further layer of Au Pd sputtered on top to form the nanowire, as described in Section 4.4, and the resultant tip is shown in Figure 5.10 (b). The Lorentzian response of the nanowire tip, shown in (c), is symmetric.

Comparison of the resolution of Si tips and nt tips.

Figure 5.11 (a) shows the peak widths of the Lorentzian fits to fm-EFM linescans for normal ($\triangle$) and nt (o) tips as a function of l_h. The narrower widths of the line-scans from the nt tip demonstrates the higher spatial resolution achieved, especially at low l_h. The peak widths shown here for the Si tip are significantly smaller than those found in [KBFJ02] (> 250 nm at $l_h = 20$ nm), demonstrating the increased spatial resolution of force gradient sensitive techniques as compared to the force sensitive

technique used therein. The scaled peak heights, h, plotted in Figure 5.11 (b) are obtained from dividing the peak height of the Lorentzian fit to the linescans by ${V_{dc}}^2$. Empirically it was found in [KBFJ02] that $h \propto {l_h}^{-1}$ for a Si tip at $l_h > 100$ nm[9], however, for nt tips the inverse power law holds at lower l_h.

High resolution EFM imaging with nt tips

When imaging at small l_h ($\leq$ 15 nm) with the nt tips, the difference between the topographical width of the SWNT linescan and the EFM response width is small, especially for ac-EFGM where charging effects were minimized. Unfortunately, the lithographic process used to define the electrodes for the SWNT calibration substrate left a residue. This is evident in the topography image Figure 5.12 (a), taken with the nt tip shown in Figure 5.8 (a). Figure 5.12 (b) shows the simultaneously acquired ac-EFGM image ($l_h = 10$ nm, $V_{ac} = 2$ V, and $V_{dc} = -2$ V). The topographical width of the SWNTs in the image is $\sim$ 20 nm, much bigger than the observed width of the tip ($r_{nt} \approx 3$ nm), and the observed height of the SWNT bundle of 3 nm, and so probably due to a surface contamination layer.

Figure 5.13 was taken with a different nt tip at a lift height of 5 nm and shows 250 nm square (a) topography, and (b) fm-EFM images. The sample had not had electrodes defined on it, hence there is no evidence of resist residue in the topographic image. $V_{dc} = -4$ V was applied to the tip whilst the underlying Si on the sample was grounded. The contrast in the fm-EFM image is due to capacitive charging of the SWNT [BMS$^+$02], i.e. it is a frequency modulation version of SCM.

[9]See Appendix C for a possible explanation

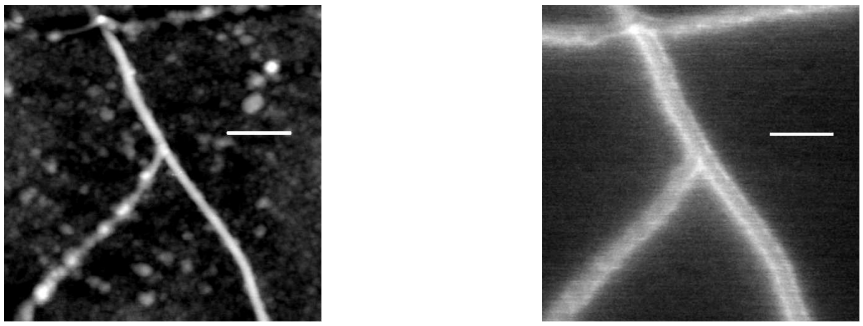

(a) (b)

Figure 5.12: (a) topography and (b) ac-EFGM image taken with the nt tip shown in Figure 5.8 (a); $l_h = 10$ nm, $V_{ac} = 2$ V, $V_{dc} = -2$ V. Scale bars 100 nm.

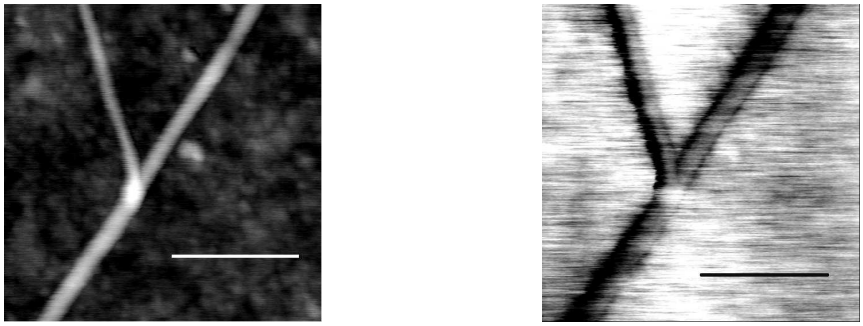

(a) (b)

Figure 5.13: (a) topography and (b) fm-EFM images taken with a different nt tip; $l_h = 5$ nm, $V_{dc} = -4$ V. Scale bars 100 nm.

Figure 5.13 demonstrates the utility of higher resolution imaging. The topography image reveals a 'y-junction' shape whereby two SWNT (or bundles of SWNTs) come from the top of the image, and merge to form one small bundle in the lower part of the image. The minimum separation at which the two SWNTs (or bundles) can be distinguished in the fm-EFM image is $\approx$ 15 nm, i.e. better resolution than topographical imaging with the Si tip.

The white spot in the fm-EFM image over the joining of the y-junction is due to the large curvature of the SWNTs at that point making it non-conductive, a similar effect to that observed in Section 3.2, although here observed directly. This effect has not been observed using Si tips, presumably due to the small size of the non-conductive area (here observed to be $\sim 10 - 20$ nm) making it below the resolution of the Si tips.

Interestingly, the high resolution topographic image also has important ramifications. The lower part of the y junction is $\sim$ 15 nm at full width half maximum (FWHM), but only $\sim$ 1.7 nm high. The upper left section has a FWHM of $\sim$ 8 nm and a height of $\sim$ 1.3 nm, consistent with the observed tip diameter of $\sim$ 6 nm. The upper right section has a FWHM of $\sim$ 12 nm with a height of $\sim$ 1.5 nm. At the junction the height is $\sim$ 2.7 nm, consistent with the sum of the heights of the two upper sections, i.e. the left appears to cross the right. This information, combined with the fact that the upper right section does not bend at the joint whilst the upper left section bends dramatically, implies that the upper right section is probably already a small bundle of SWNTs lying next to each other. This is of fundamental significance to the study of SWNT devices. Frequently devices are identified as being composed of individual SWNT by topographically verifying the presence of only one SWNT (or bundle of SWNTs), and then taking a height of $\lesssim 2$ nm as indicating an individual SWNT. These relatively small changes in widths are difficult to reliably measure using Si tips as they are less than the size of the tips.

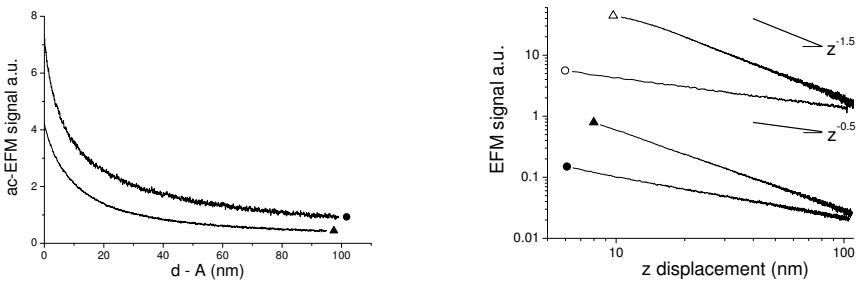

(a) (b)

Figure 5.14: (a) ac-EFGM response of an nt (•) and a Si tip (▲). (b) Power law fitted data of dc-EFM (open symbols) and ac-EFGM (closed symbols) for normal (▲) and nt (•) tips, for reference $z^{-0.5}$ and $z^{-1.5}$ are shown.

z dependence of the frequency shift

The z dependence of the frequency shift was also studied for Si and nt tips by recording the EFM signal as a function of distance from a uniform metal surface (evaporated Pd with a Ti underlayer on Si).

Figure 5.14 (a) shows representative ac-EFGM response ($\Delta\phi_{rms}(\omega)$) plotted with respect to $d - A$, see Figure 5.1. $d - A = 0$ corresponds to the position of first contact of the tip with the surface, and is marked by the onset of hard surface damping in the simultaneously acquired amplitude signal. Figure 5.14 (b) shows a fit to the power law relation $\phi_{rms}(\omega) = \phi_0 + \alpha|z - z_0|^{-p}$ with the four fitting parameters ϕ_0, α, z_0, p, for dc-EFM (open symbols) and ac-EFGM (closed symbols) with a Si (△) and an nt (○) tip. These provide good fits for both dc-EFM and ac-EFGM force gradient curves. In particular the power law exponent was found to be roughly independent of the voltage applied and consistent between dc-EFM and ac-EFGM. The exponent was, however, different between normal tips, $p \sim 1.4$, and nt tips, $p \sim 0.5$. But, although the parameter y_0 has a physical origin in the small near constant contribution of the rest of the tip and cantilever to the force gradient, the parameter z_0 corresponded neither to the bottom point of oscillation of the tip hitting the surface, i.e. $d - A = 0$, nor to the center of oscillation of the

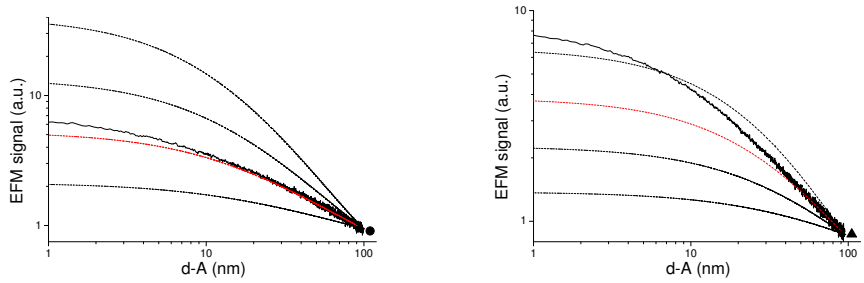

(a) (b)

Figure 5.15: ac-EFGM response above a metal surface for (a) an nt, and (b) a Si tip. The lines plotted are $\alpha_p d^{-p} + \gamma$, for $p = 2, 1.5, 1, 0.5$ from top to bottom.

tip coinciding with the surface (i.e. $d = 0$) but somewhere in between. In order to make sensible comparisons with the theoretically predicted power law dependencies (e.g. $p = 1$ for a cone or $p = 2$ for a sphere etc.) we must take account of the amplitude of oscillation[10]

Figures 5.15 (a) and (b) show $\Delta\phi_{rms}(\omega)$ plotted with respect to $d - A$ with logarithmic scales. The lines plotted in addition to the experimental results correspond to $\alpha_p\ d^{-p} + \gamma$ for $p = 0.5, 1, 1.5, 2$ from top to bottom, where α_p and γ were chosen to fit the experimental data as $d - A \to 100$ nm. As discussed earlier, the assumption that $\Delta\phi_{rms}(\omega) \propto \partial^2 C_{ts}/\partial z^2{}_{z=d}$ is reliant on $A \ll l_h$ so that the force gradient, f'_{ts}, is constant over the amplitude of oscillation. When this is the case the EFM signal is proportional to $\partial^2 C/\partial z^2{}_{z=d}$. In typical experimental conditions, where $A \simeq 50$ nm and $l_h \simeq 20$ nm, this is clearly not true. However, for $d - A > l_h$ we expect this relation to become asymptotically true [HSW99]. The amplitude of oscillation of the nt tip in Figure 5.15 (a) was $A = 15$ nm, and the experimental results correlate well to the $p = 1$ line (marked in red) for $d - A \geq 20$ nm. The amplitude of oscillation of the Si tip in 5.15 (b) was $A = 45$ nm and the correlation to the $p = 1.5$ line (marked in red) for $d - A \geq 50$ nm is reasonable. Previous

[10]This does not seem to be recognised in other studies of tip response in EFM, e.g. [KOB01, CCW+03], but has been studied extensively for non-contact applications, e.g. [HSW99].

authors have also found $p \sim 1.5$ for a conventional Si tip [KOB01].

γ corresponds to the components of the frequency shift which do not decay over length scales of the order 100 nm, i.e. it can be associated with the cantilever and tip cone contributions. For the fits shown in both Figures 5.15 (a) and (b) $\gamma < 10\%$ of the signal at $l_h = 20$ nm. This implies firstly that the force gradient response at $l_h = 20$ nm is dominated by the tip-apex, and secondly that the nt tip used was long enough to sufficiently reduce the Si tip contribution. From the response of the Si tip, the decaying component is three times the magnitude of γ at $d - A = 100$ nm. At $d - A = 200$ nm it would be equal in magnitude, and at $d - A = 300$ nm it would be half the magnitude of γ. Hence using nt tips with lengths in the range $150 - 300$ nm is sufficient to maintain the contribution of the Si tip apex to the EFM signal at $\lesssim 10\%$.

These results reveal two further advantages for nt tips over Si tips beyond their enhanced resolution: firstly, $f'_{ts}(d)$ above a uniform metallic surface seems to be well fit by an inverse power law for an nt tip, which should facilitate modelling of the tip convolution effect; secondly, they can be used to image with stably at lower amplitudes of oscillation and so in conditions where the simple approximation that $\Delta\phi_{rms}(\omega) \propto \partial^2 C_{ts}/\partial z^2{}_{z=d}$ is valid.

Conclusions

We have demonstrated that nt tips enhance the resolution of EFM relative to standard Si tips, and are capable of distinguishing similar features at separations as small as 15 nm. In addition we have shown that the response of an nt tip is consistent with a uniform line charge model, which, combined with their ability to image stably at low oscillation amplitudes, should facilitate quantitative interpretation of EFM data. These results demonstrate the great promise nt tips show for quantitative, high resolution EFM imaging.

5.2 Torsional Resonance Mode EFM

The preceding discussion revealed that optimal conditions for EFM are small oscillation amplitudes and low lift heights. Tapping mode AFM is not the ideal imaging mode for these conditions, the relatively large vertical oscillation of the tip requires it to be on average $\gtrsim 10$ nm away from the surface. Torsional resonance (TR) mode imaging by contrast has small oscillation amplitudes, and since the oscillation is perpendicular to the surface the tip can be approached close to it.

TR mode is sensitive to forces and force gradients parallel to the sample, rather than perpendicular to the sample as is the case for tapping mode AFM. However, the same techniques can be used in TR mode as in tapping mode, and hence we can consider EFM in TR mode, TREFM. Although the electric field above a conducting surface will be perpendicular to it, and hence have no effect on the TR oscillation, at inhomogeneities on the surface there will be a component of the electric field parallel to the surface. Figure 5.16 shows the equipotentials for a uniform line charge tip (a) above, and (b) to one side of, a uniform line charge (i.e. SWNT) lying on a dielectric surface. When the tip is directly over the SWNT there is no electric field parallel to the surface, but when the tip is to one side there is a parallel component of the field.

Figure 5.17 shows a comparison between dc-EFM and dc-TREFM images of the same area on one of the calibration samples used in the previous section. The

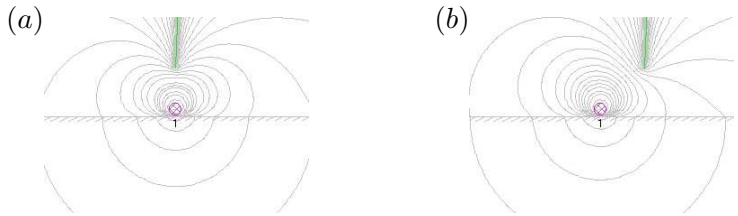

Figure 5.16: Simulations of uniform line charge tip above a uniform line charge on a dielectric, created using 'Equipotential Surfaces', available from http://www.electrostatics.20m.com/

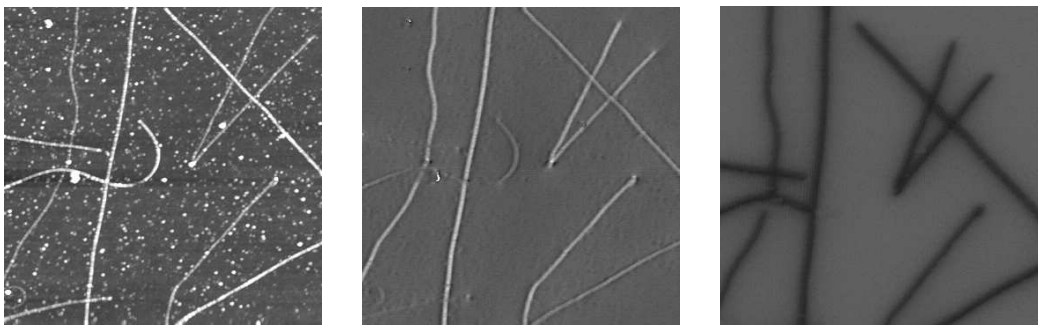

(a) (b) (c)

Figure 5.17: 2.5 μm square (a) height, and (b) dc-TREFM images. $V_{tip} = -12$ V. (c) dc-EFM of the same area (slightly offset).

dc-TREFM image was taken by imaging in tapping mode and interleaving a lift mode scan in TR mode. The tip used was a Si FESP, and the imaging amplitude was 1.46 V, i.e. $\sim$ 25 nm (rms). The lift height used was $l_h = -10$ nm, which is thus roughly equivalent to $l_h = 20$ nm for normal tapping mode AFM. A line scan response across a SWNT from Figure 5.17 (b) is shown in Figure 5.18. When the tip is directly over the SWNT, as it oscillates the attractive electrostatic force effectively increases the spring constant, increasing the resonance frequency, and so resulting in a positive change in phase. However, when the tip is to one side of the SWNT, the attractive electrostatic force will result in an asymmetric effective decrease in spring constant, decreasing the resonance frequency, and so resulting in

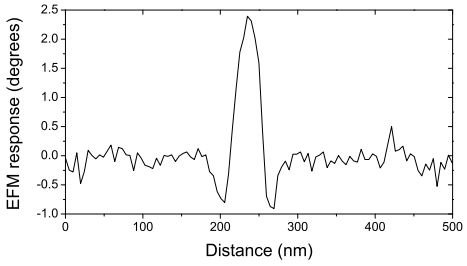

Figure 5.18: dc-TREFM linescan across a SWNT, taken from Figure 5.17(b).

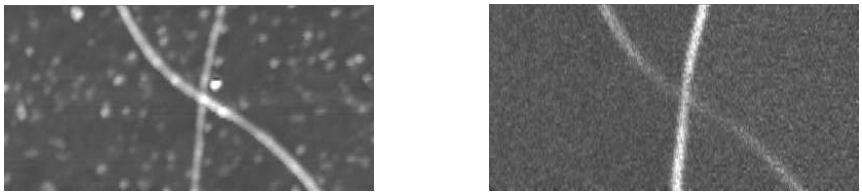

Figure 5.19: 1 μm wide *left* height, and *right* ac-TREFGM images .

a negative change in phase. This response is evident in Figure 5.18, as is the high spatial resolution of the response.

As discussed above, in TR mode the oscillation is sensitive only to forces parallel to the plane of the sample. However the criterion is more strict than that, the response is sensitive only to forces in the direction of oscillation of the tip, i.e. parallel to the sample surface, **and** perpendicular to the cantilever. This is visible in Figure 5.17, where two sections of SWNT are visible in (c) but not (b). It is more evident in Figure 5.19, where the ac-TREFGM[11] response is clearly dependent on the orientation of the SWNT.

To the best of my knowledge this is the first demonstration of TREFM, and it shows both the promise of the technique (high spatial resolution and complementary information to tapping mode EFM), and the drawbacks (low voltage resolution and orientation dependent). As TR mode imaging matures, and in particular tips designed specifically for TR mode are made, TREFM will probably be developed into a useful technique. Its main advantages are likely to be its low oscillation amplitudes, and small and constant tip sample separation, which combined should make quantitative interpretation of TREFM images a relatively easy procedure.

[11] this is an equivalent technique to ac-EFGM as discussed in the previous section, and was implemented in a similar fashion.

5.3 Increased Resolution SGM

Section 3.2 showed the efficacy of SGM for probing the conductance through SWNT devices. SGM highlights the presence of energy dependent scattering sites by locally changing the Fermi energy. Its main advantage over EFM is that it reveals changes. As a result it is more sensitive than EFM, since a weak defect will only cause a small proportion of the total voltage to be dropped across it. However, there are two limitations on the applicability of SGM for studying conduction through SWNT devices at the nanoscale

1. SWNT devices tend to be noisy (due in part to the generally poor contacts, and high sensitivity to their environment). Since the change due to the tip gating effect must be greater than the background noise in order to be visible, SGM is only effective at probing relatively strong scattering centres.

2. There is a low spatial resolution associated with SGM, lower than EFM since it is dependent on the tip sample capacitance (C_{ts}) rather than C'_{ts} as in EFM, or C''_{ts} as in EFGM.

The obvious solution to the first problem is to use an ac-based technique, a standard procedure for reducing noise levels. The easiest method is to use an ac bias voltage across the SWNT device, see for example [FJKB02], and measure the conductance using a lock-in amplifier. The lock-in amplifier rejects all signals not at the frequency of the applied bias, reducing the noise level and hence increasing the SGM sensitivity. An alternative approach would be to apply an ac potential to the tip, $V_{tip}(\omega')$, whilst applying a dc bias voltage (V_{sd}), and use a lock-in amplifier to measure the resultant change in conductance at ω'. This would have the advantage of selectively measuring the tip gating effect, and rejecting all other electrical noise, and hence would increase the sensitivity further. However, this would not increase

the spatial resolution of the technique.

In order to address both problems we return to the discussion at the start of this Chapter which concluded that EFGM resulted in higher spatial resolution than EFM since it relied on C''_{ts} as opposed to C'_{ts}. Hence, to increase the spatial resolution of SGM we should use a technique based on C'_{ts} as opposed to C_{ts}. Figure 3.14 demonstrated that decreasing the distance of the tip from the defect gave an equivalent SGM response to increasing the potential on the tip. The conductance of a SWNT device showing gate dependence can be written as a function of the back gate potential (V_G), the capacitance of the device to the back gate (C_G), the tip potential (V_{tip}), and the tip-device capacitance (C_{td}), i.e.

$$G(V_G, C_G, V_{tip}, C_{td}) \tag{5.22}$$

For a conventional device C_G is fixed, however C_{td} is not and will depend on the distance separating the tip from the device. If the tip is situated vertically above the device displacing it a small vertical distance (δz) will change the device conductance

$$\begin{aligned} \delta G &= \tfrac{\partial G}{\partial C_{td}} \, \tfrac{\partial C_{td}}{\partial z} \, \delta z \\ &= \tfrac{\partial G}{\partial C_{td}} \, C'_{td} \, \delta z \end{aligned} \tag{5.23}$$

If δG can be isolated then the longer range contributions to the SGM signal from the cantilever and tip-cone will be reduced, and the spatial resolution of the technique increased.

Figure 5.20 illustrates the above discussion for a device which shows p-type transistor behaviour. A positive voltage on the tip reduces conductance through the device, and reducing the separation of the tip from the device decreases G even further by increasing C_{td}. The change in separation between the tip and surface during tapping mode is significant, for typical imaging conditions in lift mode[12] the

[12] $l_h = 20$ nm, imaging amplitude $A \approx 1.5$ V, FESP tip

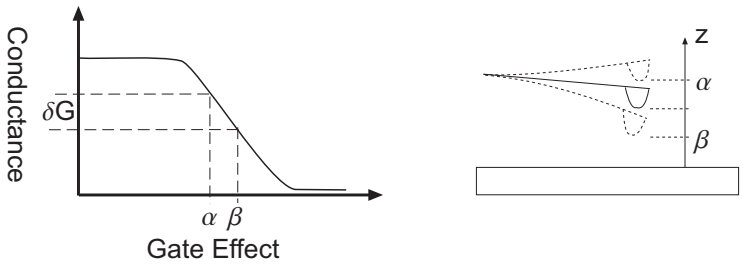

Figure 5.20: Schematic of the effect of tip oscillation on conductance through a p-type FET device.

tip moves from a minimum tip surface separation of $\sim$ 20 nm, point β in Figure 5.20, to a maximum tip surface separation of $\sim$ 100 nm, point α. This results in a large change in C_{td} and so a significant δG. In conventional SGM the response is usually independent of the tip oscillation during the lift mode scan because the current recorded for each pixel is an average over many oscillations of the tip.

Applying a constant dc V_{sd}, as well as a constant dc V_{tip}, whilst operating the tip in tapping mode on the lift scan, and measuring the change in conductance at the cantilever oscillation frequency (ω) would thus isolate the component of δG due to the changing tip device separation. Assuming small changes and a linear response the change in conductance is given by

$$\delta G_{rms}(\omega) \simeq \frac{\partial G}{\partial C_{td}} \, C'_{td} \, A_{rms} \tag{5.24}$$

where A_{rms} is the rms oscillation amplitude in lift mode. This ac based technique, which shall be referred to as 'ac-SGM', is thus dependent on C'_{td} rather than C_{td} and hence increases both the sensitivity and the spatial resolution of SGM.

5.3.1 ac-SGM of SWNT device

Figure 5.21 schematically illustrates the experimental setup for ac-SGM of a SWNT device.[13] V_{sd} was applied externally using a DAQ card (DT9804). V_{tip} was applied

[13]All experimental results reported in this section were taken with the Dimension AFM and Nanoscope IV controller at the University of Seattle.

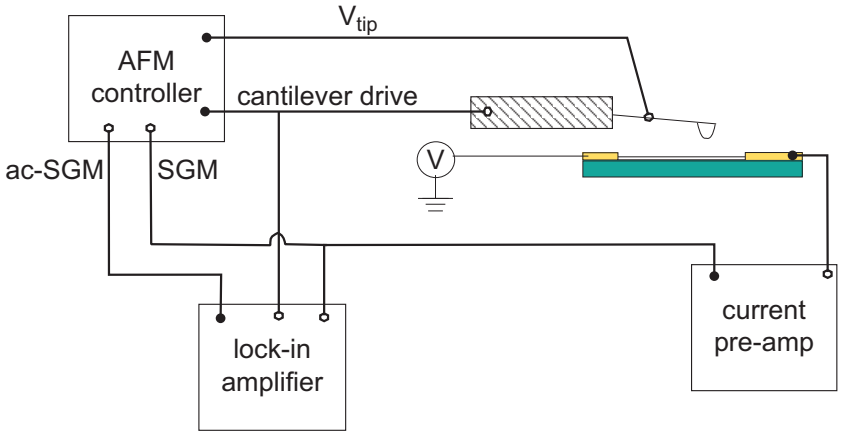

Figure 5.21: Schematic of the experimental setup for ac-SGM of a SWNT device.

through the AFM software, and was only applied during lift mode. The cantilever drive signal was inputted into the lock-in amplifier (EG&G Princeton Applied Research Model 5209 lock-in amplifier) as the reference signal. The current through the SWNT device was converted to a voltage using a current pre-amp (Ithaco 1211), the output of which was inputted both to the Nanoscope IV controller (the SGM response) and to the lock-in amplifier[14]. The lock-in amplifier was used to measure $\delta G_{rms}(\omega)$, which was then inputted back into the Nanoscope IV controller. The Si tips used had typical resonance frequencies of $\sim$ 75 kHz[15]. This enabled lock-in time constants suitable for imaging purposes (typically $\sim$ 1 ms) to be used, without exceeding the upper frequency limit of the lock-in used (100 kHz).

The cantilever drive signal gives a stable, clean, reference signal, however the phase of the cantilever oscillation relative to the cantilever drive is not constant, especially when voltages are applied to the tip, c.f. dc-EFM p. 33. The change in conductance should be in phase with the cantilever oscillation, not the cantilever drive signal. Measuring the conductance change phase-locked to the cantilever drive

[14]For the results shown below a voltage preamplifier (Stanford Research Systems Model SR560 low-noise preamplifier) was used to filter out the dc component of the current and amplify the remainder of the signal before inputting into the lock-in amplifier, however this could have been done by the lock-in as well.

[15]spring constants of $\sim$ 0.5 Nm^{-1}, and lengths of $\sim$ 130 μm, fabricated by μMasch

signal will not give a valid response. There are two ways of circumventing this complication: (i) a dual phase lock-in can be used; (ii) the tip can be operated in fm-EFM mode during the lift-scan. By operating the tip in fm-EFM mode, the phase between the cantilever oscillation and the drive signal is maintained constant at 90°. Both approaches were tried and gave good results, however the second is the more robust approach[16] and has the added advantage of maintaining a more constant amplitude of oscillation.

Figures 5.22, 5.23 and 5.24 show simultaneously recorded height, SGM, and ac-SGM images of two different sSWNT devices, which exhibited standard p-type FET behaviour as discussed in Chapter 2, taken at different V_{tip}.[17] Figures 5.22 and 5.23 demonstrate the massively increased sensitivity of ac-SGM. There is no SGM response evident in either case, but the ac-SGM response clearly reveals a signal which correlates exactly with the position of the SWNT in the height image. Figure 5.23 was taken with $V_{tip} = -10$ V, i.e. the tip is acting to locally increase the conductance of the sSWNT. This is particularly difficult to observe in SGM measurements as it results only in small changes in the device conductance (the resistance of the device will be dominated by the rest of the sSWNT), however it is clear from this image that the tip gating acts almost uniformly along the sSWNT.

[16]The dual phase approach is only strictly valid when the conductance change is in the linear response regime.

[17]Device 1, shown in Figures 5.22 and 5.23, was fabricated at Warwick University using the mask aligner for photolithography. Device 2, shown in Figure 5.24, was fabricated at the University of Washington by Iuliana Radu, also using a mask aligner for photolithography but with a different photoresist which left a large amount of residue on the device. This was subsequently removed using a wet etch, which possibly caused the large number of weak defects observable in both the SGM and ac-SGM images. In both cases only one SWNT was observed to cross the gap.

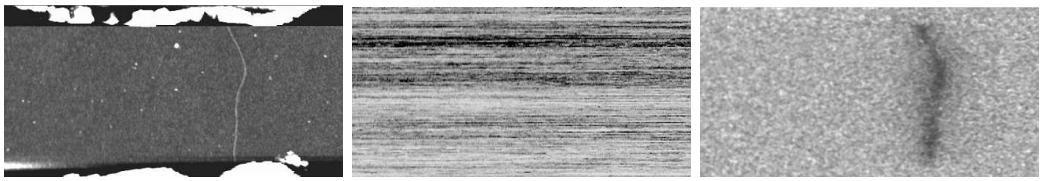

(a) height (b) SGM (c) ac-SGM

Figure 5.22: 4 μm wide images of a sSWNT device (device 1). $V_{tip} = 0$ V, $V_{sd} = 1$ V, $V_G = 0$ V, $l_h = 20$ nm, $A \approx 2$ V.

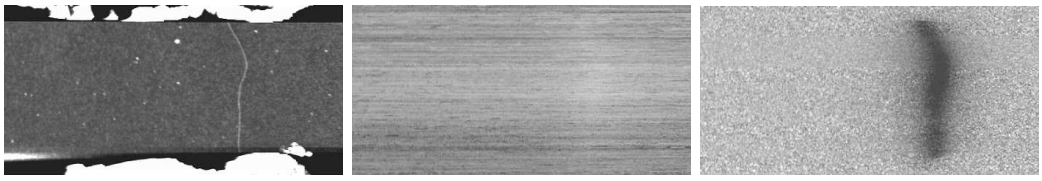

(a) height (b) SGM (c) ac-SGM

Figure 5.23: 4 μm wide images of a sSWNT device (device 1). $V_{tip} = -10$ V, $V_{sd} = 0.5$ V, $V_G = 0$ V, $l_h = 20$ nm, $A \approx 2$ V.

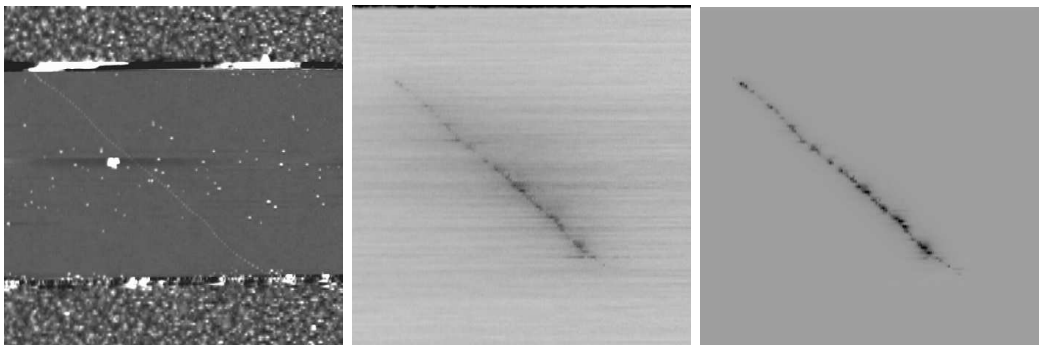

(a) height (b) SGM (c) ac-SGM

Figure 5.24: 5 μm square images of a sSWNT device (device 2). $V_{tip} = 2.5$ V, $V_{sd} = 0.1$ V, $V_G = 0$ V, $l_h = 20$ nm, $A \approx 1.8$ V. Sample courtesy of Iuliana Radu, University of Washington.

The uniformity of ac-SGM response implies that each section of the sSWNT is contributing equally to conduction through the device at this V_{sd} and V_G, and that every section is p-type semiconducting in nature. Note that there is no evidence of gating of a Schottky barrier at either contact. In this device the contact electrodes have flared up slightly after lift-off, it is possible that the section of sSWNT with the Schottky barrier is underneath the metal contacts and so shielded by them.

Figure 5.24 was taken with $V_{tip} = 2.5$ V, i.e. the tip acts to locally deplete the sSWNT. This is the more standard method for SGM, and the SGM response clearly shows the presence of many weak scattering sites. The features in the simultaneously recorded ac-SGM image correlate well with those in the SGM image, confirming that both techniques reveal similar information about the device being studied. However, the ac-SGM image demonstrates much lower background noise than the SGM image, and importantly only reveals features local to the position of the sSWNT in the height image. These results show the massively increased sensitivity of the ac-SGM technique over SGM. They also reveal that ac-SGM is a more localised probe than SGM, in a similar way that EFGM is more localised than EFM.

In the most simple approximation ac-SGM can be thought of as the z-derivative of the SGM signal. Figure 5.25 shows simultaneously recorded ac-SGM and SGM responses of device 1 taken with $V_{tip} = 10$ V. Strong SGM and ac-SGM responses are evident as conduction through the device is suppressed by the large positive tip voltage. The linescans shown below the image correspond to the identically positioned lines indicated in the images. Assuming the sSWNT device to be in a linear response regime[18] we would expect a linescan ac-SGM response, $\delta i_{rms}(x)$, across the sSWNT to fit a Lorentzian dependence, by analogy to the SSPM response

[18] i.e. Equation 5.24 is valid and $\frac{\partial G}{\partial C_{td}}$ is constant

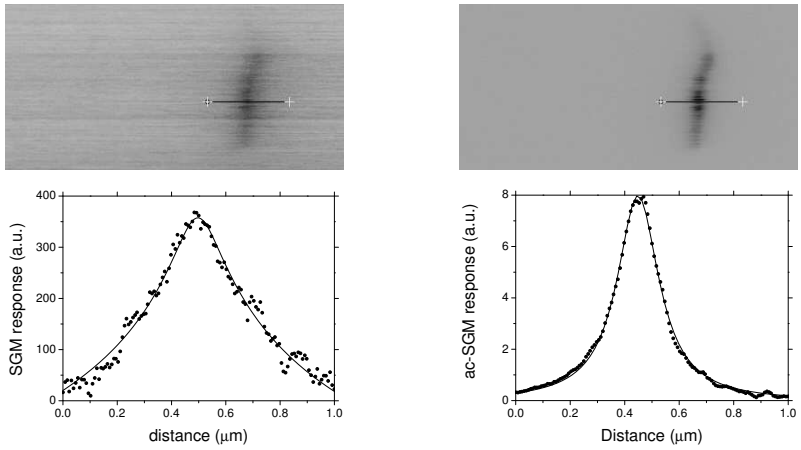

(a) SGM (b) ac-SGM

Figure 5.25: 4 μm wide images of device 1. The linescans shown below correspond to the identically positioned lines indicated in the images. $V_{tip} = 10$ V, $V_{sd} = 0.5$ V, $V_G = 0$ V, $l_h = 20$ nm, $A \approx 2$ V.

in Section 3.3.1. Explicitly

$$\delta i_{rms}(x) = \frac{2A_L}{\pi} \frac{w}{4(x - x_c)^2 + w^2} \tag{5.25}$$

This would imply the following dependency of the SGM response, $i(x)$, see Appendix C[19],

$$i(x) = i_0 + \frac{A'_L}{\pi} \ln(4(x - x_c)^2 + w^2) \tag{5.26}$$

The solid lines also shown in the linescans in Figure 5.25 correspond to the fits of the SGM data to Eqn. 5.26, and the ac-SGM data to Eqn. 5.25. The closeness of the fit indicates the validity of this approach, and supports the approximation that ac-SGM can be thought of as simply the z-derivative of the SGM response. The FWHM of the ac-SGM response is $\sim$ 200 nm, compared to $\sim$ 400 nm for the SGM response, demonstrating once again the increase in spatial resolution. Note that although the data is shown as a peak it corresponds to a suppression of the sSWNT conductance.

[19] Effectively these equations correspond to a ln dependence of C_{td} on the separation between tip and sSWNT

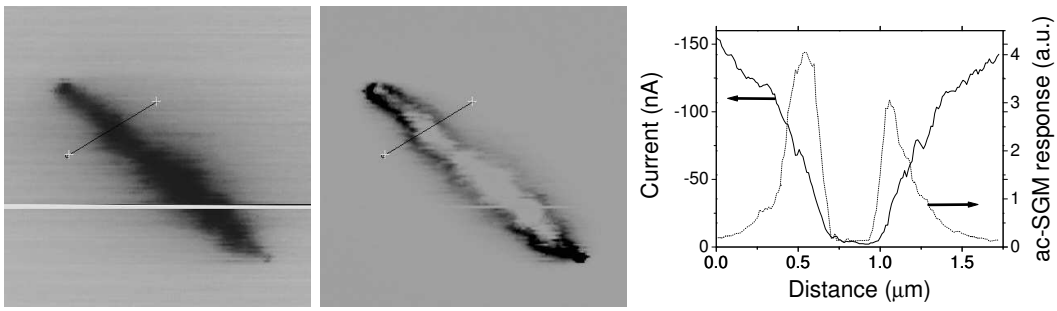

(a) SGM (b) ac-SGM (c) linescans

Figure 5.26: 5 μm square images of device 2. The linescans correspond to the identically positioned lines indicated in the images. $V_{tip} = 10$ V, $V_{sd} = 0.1$ V, $V_G = 0$ V, $l_h = 20$ nm, $A \approx 1.8$ V.

A final example is given in Figure 5.26, illustrating that care must be taken in interpreting the ac-SGM response. Simultaneous SGM and ac-SGM images of device 2 taken with $V_{tip} = 10$ V are shown. The SGM response demonstrates that the tip suppresses conduction all along the sSWNT. The ac-SGM image shows a large response to either side of the sSWNT, but zero response over the SWNT. The linescans, taken at identical places on the two images, show the cause of this behaviour. In the SGM linescan conduction through the sSWNT is totally suppressed when the tip is within ~ 100 nm of the SWNT, as a result the ac-SGM response in this area is zero. The ac-SGM linescan response also shown in Figure 5.26 (c) is as expected for the derivative of the SGM response.

5.3.2 Conclusions

An enhanced form of scanned gate microscopy has been demonstrated which not only increases the sensitivity but also increases the spatial resolution of the technique. By isolating the effect of tip oscillation on conductance through the device an SGM based technique dependent on $\partial C_{td}/\partial z$ rather than C_{td} is created. A lock-in amplifier is used to measure the change in conductance at the frequency of the tip oscillation, which is caused by the variation in C_{td} as the separation between the

tip and device changes. To the best of my knowledge this is the first discussion, or implementation, of such a technique (here called ac-SGM). The efficacy of the technique has been investigated through its application to the study of transport through SWNT devices. This confirmed that the spatial resolution and sensitivity is increased relative to conventional SGM, and that ac-SGM probes a more localised response than SGM. As a simple approximation the ac-SGM response can be considered to be the z derivative of the SGM response.

The increase in sensitivity is great enough to consider application of the technique to 2D geometries, such as electrical devices made from thin polymer films. For electrode dimensions similar to those used for the SWNT devices in this thesis the expected change in conductance of a 2D polymer film based FET due to tip gating can be estimated to be $\sim 1\%$[20]. This would be challenging for conventional SGM, but within the sensitivity of ac-SGM. Future goals would be to address such a 2D geometry, as well as investigating conduction through SWNT devices in more detail.

[20]For a very simplified estimate we can consider a gap of width and length 5 μm. Splitting this into a grid of 500 nm squares and considering each square in a line parallel to the gap as resistors in parallel, and then adding each line as resistors in series, the effect of turning off one square would be to change the conductance by $\approx 1\%$. Although this is a very simplified picture it gives an order of magnitude estimate.

Chapter 6

Conclusions and future work

This thesis presents developmental work on the growth, understanding and application of single-walled carbon nanotubes. In Chapter 2 the direct growth of SWNTs by catalysed chemical vapour deposition was demonstrated and used for the fabrication of electronic devices consisting of individual SWNTs. These devices were investigated in Chapter 3 using various scanning probe techniques such as scanning gate microscopy and electric force microscopy. In Chapter 4 the application of SWNTs as AFM tips was presented, and by forming electrical connection to SWNT-AFM tips a novel geometry for investigating electronic transport through SWNTs was demonstrated. Chapter 5 addressed the need for higher resolution electrical characterisation techniques through the application of SWNT-AFM tips for EFM, and the development of a new form of SGM.

We have shown that the application of scanning probe techniques to the study of electrical transport through SWNT devices gives insight into the mechanism of electrical transport through individual SWNTs. In particular, the use of SGM highlighted the role of defects in transport through semiconducting SWNT. The ballistic nature of transport through metallic SWNTs was demonstrated both by EFM, and by using electrically connected SWNT-AFM tips and a Hg contact. The

transition from ballistic to diffusive transport in mSWNT at high bias voltages was also demonstrated using EFM.

The fabrication of SWNT-AFM tips, especially electrically connected SWNT-AFM tips, was investigated. The 'pick-up' technique was shown to produce the most reliable results. The nt tips formed have many advantages over conventional Si AFM tips, including greater spatial resolution and higher aspect ratios. Following the results presented in this thesis funding was sought, and awarded, to continue research in this area:

1. 'Development of Single-Walled Carbon Nanotube Scanned Probes for High Resolution Electrical and Electrochemical Measurements' Principle Investigator Dr Julie V. Macpherson. Recognised Researcher Neil R. Wilson. Funded by the EPSRC - GR/S24138/01(P)

2. 'Properties and Application of Nanotube and Nanowire Scanned Probe Sensors'. Principle Applicant: Dr Julie V. Macpherson. Nominated Researcher Neil R. Wilson. Funded by the Leverhulme Trust - F/00215/S

These grants will enable continued research into (1) the development and application of SWNT-AFM tips in general, and (2) electrical transport studies using electrically connected SWNT-AFM tips. (2) also supports the further development and application of the nanowire tips discussed in Chapter 4.

The advances in electrical characterisation techniques described in Chapter 5 demonstrated increased resolution EFM and SGM. These techniques will be applied to studying electrical transport in SWNT devices truly at the nanoscale, with the aim of furthering understanding of the devices and thus enabling applications. The high resolution EFM and SGM techniques we have developed here are applicable to studying electrical transport in a wide range of devices at the nanoscale, and as such we hope to apply them to a variety of systems.

"We are at the very beginning of time for the human race. It is not unreasonable that we grapple with problems. But there are tens of thousands of years in the future. Our responsibility is to do what we can, learn what we can, improve the solutions, and pass them on." - Richard Feynman

Appendix A

Mechanical properties of SWNT and nanowire AFM tips

The SWNT and nanowire AFM tips are effectively rods with one end clamped, see Figure A. As such we can estimate their mechanical properties using simple continuum mechanics. The bending moment applied to a rod is balanced by the axial stress in the rod. The local radius of curvature, ρ, of a rod is dependent on the bending moment applied, $M(x)$, and the 'flexural rigidity', α (see later) of the rod

$$\frac{1}{\rho} = \frac{M(x)}{\alpha} \tag{A.1}$$

In a linear, or small deflection approximation, this becomes

$$\frac{\partial^2 y}{\partial z^2} = \frac{M(x)}{\alpha} \tag{A.2}$$

First we consider the stiffness of the rod, and calculate the lateral spring constant, i.e. the resistance of the rod to a load at its end as illustrated in Figure A. For this situation the bending moment is $M(x) = -Px$, and Eqn. A.2 can trivially be integrated to give

$$\alpha\, y = -\frac{1}{6}Px^3 + c_1 x + c_2 \tag{A.3}$$

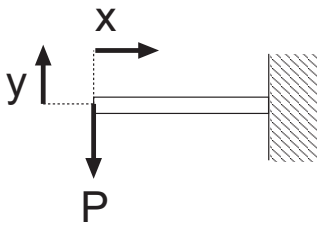

Figure A.1: Schematic of a clamped rod.

where c_1 and c_2 are constants of integration. Application of the boundary conditions that both the position and gradient are fixed at zero at the clamped end (i.e. at $x = L$) gives $c_1 = PL^2/2$, and $c_2 = -PL^3/3$. Using these values we can calculate the deflection of the free end of the rod

$$y(x = 0) = -\frac{PL^3}{3\alpha} \tag{A.4}$$

From this we can calculate the lateral spring constant

$$k_L = -\frac{\partial P}{\partial y} = \frac{3\alpha}{L^3} \tag{A.5}$$

The thermal oscillations resulting from this are given by the equipartition theory to be

$$\sqrt{\langle y^2 \rangle} = \sqrt{k_B T k_L} \tag{A.6}$$

For a 5 μm long SWNT, 1.4 nm in diameter, this would imply an average radius of curvature of around 10 μm at the growth temperature. However as the AFM and SEM images presented in Chapter 2 show the typical radii of curvature are significantly lower than this implying strong substrate interactions.

Considering an axial force along the rod the bending moment becomes $M = -P\,y$. This gives

$$\frac{\partial^2 y}{\partial z^2} = -\frac{P\,y}{\alpha} \tag{A.7}$$

Given boundary conditions of $y = 0$ at either end we find

$$y = A \sin\left(\sqrt{\frac{P}{\alpha}}\, x\right) \tag{A.8}$$

where $A = 0$ or

$$P = \frac{n^2\pi^2\alpha}{L^2}$$

for integer n. This implies a minimum force, i.e. $n = 1$ to buckle the rod of

$$F_B = \frac{\pi^2\alpha}{L^2} \tag{A.9}$$

Depending on the boundary conditions there will be a different numerical prefactor. However, it is difficult to say what the boundary conditions of the SWNT or nanowire on the surface would be so we will use Eqn. A.9 as an approximation. The orientation of the SWNT or nanowire relative to the surface will also have a significant impact.

A.1 Flexural rigidity

The flexural rigidity, α, of a material is defined by the Youngs modulus, Y, of the material integrated over its moment of inertia and gives the materials resistance to flexion.

$$\alpha = YI = Y\int_A y^2 dA \tag{A.10}$$

where I, is the moment of inertia of the beam about its neutral axis. Due to the high degree of symmetry of the nanowire (i.e. completely axially symmetric) the moment of inertia is trivial to calculate

$$\begin{aligned} I &= Y\int_A y^2 dA \\ &= Y_{nt}\int_0^r 2y^2 2\sqrt{r^2-y^2}dy + Y_{nw}\int_r^R 2y^2 2\sqrt{r^2-y^2}dy \qquad \text{(A.11)} \\ &= Y_{nt}\frac{\pi r^4}{4} + Y_{nw}\frac{\pi(R^4-r^4)}{4} \qquad \text{(A.12)} \end{aligned}$$

The flexural rigidity of a SWNT bundle is just the first term in the above.

Appendix B

Force exerted by a Hg surface

Although we do not fully understand the force exerted by the Hg surface on the SWNTs we can make the following observations. Hg does not wet carbon nanotubes [DEHT94], as a result there will be a repulsive force on the SWNTs as they enter the Hg. However to first approximation this force will be constant irrespective of the length of SWNT immersed in the Hg. We can estimate the force using the surface tension of Hg (0.5 Nm^{-1}) and for a SWNT with $r_{nt} = 1$ nm it will result in a force of $\approx \pi$ nN. This is a reasonable order of magnitude, however it does not explain the linearly increasing force. The electrostatic component of the force is also unlikely to produce a force which starts when the SWNT touches the Hg, and then increases

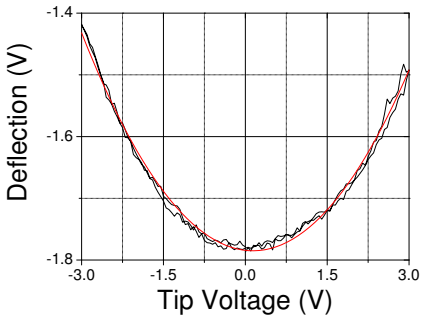

Figure B.1: Dependence of the deflection of the tip on the applied tip voltage, the red line is a quadratic fit to the data.

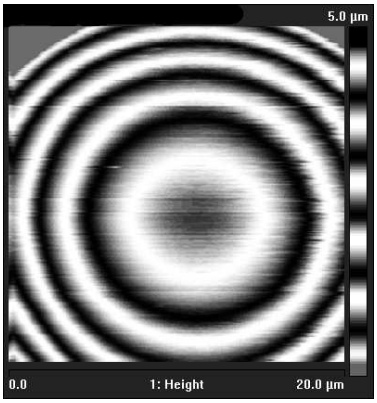

Figure B.2: Contact mode image of a 50 μm diameter Hg hemisphere taken with a Si_3N_4 tip.

linearly. We measured the dependence of the deflection of the tip on the voltage applied, Figure B. As expected it shows a quadratic dependence with a slight offset due to differences in work function. However it is only a small contribution to the total force.

In order to rule out electrical forces we used an insulating Si_3N_4 tip, a linear force was found similar to before. In addition, due to the low spring constant of the Si_3N_4 tip it was possible to image the surface of the Hg hemisphere in contact mode, Figure B.

The greatest puzzle posed by the observed force dependence is that it greatly exceeds the critical buckling force of the SWNT-AFM tips, without apparently causing them to buckle.

Appendix C

Toy model for the lorentzian dependence of the EFM linescan

In the simplest approximation respecting the symmetry of the SWNT we can approximate the tip-SWNT as a coaxial cylindrical capacitor. The tip-SWNT capacitance will then be $C \sim \ln r$. Calculating the derivative of this with respect to vertical distance z at a horizontal distance x away gives

$$C' = \frac{\partial C}{\partial z} \sim \frac{\partial}{\partial z}(\ln(\sqrt{(x^2 + z^2)}) \sim \frac{z}{x^2 + z^2} \tag{C.1}$$

This gives a Lorentzian dependence on C' when scanning in the x direction at a constant z. The width of the Lorentzian peak is predicted to be twice the lift height, and the height when $x = 0$ inversely proportional to z.

Interestingly the experimental data shown in Chapter 5 demonstrated Lorentzian peak heights inversely proportional to the lift height, and peak widths with a linear component of roughly twice the lift height. However, it is important to note that $l_h \neq z$, and that the force gradient technique used is proportional to C'' not C'. It is not clear why the force gradient response follows the same dependence as the force response, both in terms of functional form and the dependence of the heights and

widths. One possibility is that it is due to the convolution effect of a broad tip, and integration over the entire amplitude of oscillation. However, the application of the Lorentzian response of the EFGM linescan does not require an understanding of its origin.

Figure 5.25 demonstrated that for SGM and ac-SGM the responses were surprisingly consistent with the simple picture described above, indicating a logarithmic dependence on distance for the capacitance between tip and SWNT.

Bibliography

[AKD+02] J. Appenzelller, J. Knoch, V. Derycke, R. Martel, S. Wind, and Ph. Avouris. Field-modulated carrier transport in carbon nanotube transistors. *Phys. Rev. Lett.*, 89(12):126801(4), September 2002.

[AM76] Ashcroft and Mermin. *Solid State Physics*. Saunders College Publishing, 1976.

[AOML02] Lei An, Jessica M. Owens, Laurie E. McNeil, and Jie Liu. Synthesis of nearly uniform single-walled carbon nanotubes using identical metal-containing nanoclusters as catalysts. *J. Am. Chem. Soc.*, 124(46):13688–13689, 2002.

[ARHH99] S. B. Arnason, A. G. Rinzler, Q. Hudspeth, and A. F. Hebard. Carbon nanotube-modified cantilevers for improved spatial resolution electrostatic force microscopy. *Appl. Phys. Lett.*, 75(18):2842–2844, November 1999.

[Avo02] Phaedon Avouris. Molecular electronics with carbon nanotubes. *Acc. Chem. Res.*, 35:1026–1034, 2002.

[BBH+01] Dolores Bozovic, M. Bockrath, Jason H. Hafner, Charles M. Lieber, Hongkun Park, and M. Tinkham. Electronic properties of mechanically induced kinks in single-walled carbon nanotubes. *Appl. Phys. Lett.*, 78(23):3693, June 2001.

[BBSG04] K. Bradley, M. Briman, A. Star, and G. Gruner. Charge transfer from adsorbed proteins. *Nano Lett.*, ASAP article, 2004.

[BCD+02] T. Brintlinger, Y. F. Chen, T. Durkop, E. Cobas, M. S. Fuhrer, and J. D. Barry amd J. Melngailis. Rapid imaging of nanotubes on insulating substrates. *Appl. Phys. Lett.*, 81(13):2454–2456, September 2002.

[BCH+03] N. A. Burnham, X. Chen, C. S. Hodges, G. A. Matei, E. J. Thoreson, C. J. Roberts, M. C. Davies, and S. J. B. Tendler. Comparison of calibration methods for atomic-force microscopy cantilevers. *Nanotechnology*, 14:1–6, 2003.

[BCL+97] Marc Bockrath, David H. Cobden, Paul L.McEuen, Nasreen G. Chopra, A. Zettl., Andreas Thess, and R. E. Smalley. Single-electron transport in ropes of carbon nanotubes. *Science*, 275:1922, March 1997.

[BCL+99] Marc Bockrath, David H. Cobden, Jia Liu, Andrew G. Rinzler, Richard E. Smalley, Leon Balents, and Paul L. McEuen. Luttinger-liquid behaviour in carbon nanotubes. *Nature*, 397:598–561, February 1999.

[BFP+00] A. Bachtold, M.S. Fuhrer, S. Plyasunov, M. Forero, Erik H. Anderson, A. Zettl., and Paul L. McEuen. Scanned probe microscopy of electronic transport in carbon nanotubes. *Phys. Rev. Lett.*, 84(26):6082(4), June 2000.

[BHND01] A. Bachtold, P. Hadley, T. Nakanishi, and C. Dekker. Logic circuits with carbon nanotube transistors. *Nature*, 294:1317–1320, November 2001.

[BKD+93] D. S. Bethune, C. H. Kiang, M. DeVries, G. Gorman, R. Savoy, J. Vazquez, and R. Beyers. Cobalt-catalysed growth of carbon nanotubes with single-atomic-layer walls. *Nature*, 363:605–607, 1993.

[BL97] S. Belaidi and P. Girard G. Leveque. Electrostatic forces acting on the tip in atomic force microscopy: Modelization and comparison with analytical expressions. *J. Appl. Phys.*, 3:1023–1030, February 1997.

[BLB+01] Marc Bockrath, Weinjie Liang, Dolores Bozovic, Jason H. Hafner, Charles M. Lieber, M. Tinkham, and Hongkun Park. Resonant electron scattering by defects in single-walled carbon nanotubes. *Science*, 291:283–285, January 2001.

[BLT00] A. Bezryadin, C. N. Lau, and M. Tinkham. Quantum suppression of superconductivity in ultrathin nanowires. *Nature*, 404:971–974, April 2000.

[BLW+03] Koen Besteman, Jeong-O Lee, Frank G. M. Wiertz, Hendrik A. Heering, and Cees Dekker. Enzyme-coated carbon nanotubes as single-molecule biosensors. *Nano Lett.*, 3(6):727–730, 2003.

[BMM04] M. J. Biercuk, N. Mason, and C. M. Marcus. Local gating of carbon nanotubes. *Nano Lett.*, 4(1):1–4, 2004.

[BMS+02] Marc Bockrath, Nina Markovic, Adam Shephard, M. Tinkham, Leonid Gurevich, Leo P. Kouwenhoven, Mingshaw W. Wu, and L.L. Sohn. Scanned conductance microscopy of carbon nanotubes and λ DNA. *Nano Lett.*, 2(3):187–190, 2002.

[BQG86] G. Binnig, C. F. Quate, and C. Gerber. Atomic force microscope. *Phys. Rev. Lett.*, 56:930–933, March 1986.

[BR87] Gerd Binnig and Heinrich Rohrer. Nobel lecture: Scanning tunneling microscopy - from birth to adolescence. *Nobel Lecture*, 59:615–625, 1987.

[BR99] G. Binning and H. Rohrer. In touch with atoms. *Rev. Mod. Phys.*, 71(2):S324–330, 1999.

[BRM04] J. S. Bunch, T. N. Rhodin, and P. L. McEuen. Noncontact-AFM imaging of molecular surfaces using single-wall carbon nanotube technology. *Nanotechnology*, 15:S76–S78, 2004.

[BSK+02] Sergei M. Bachilo, Michael S. Strano, Carter Kittrell, Robert H. Hauge, Richard E. Smalley, and R. Bruce Weisman. Structure-assigned optical spectra of single-walled carbon nanotubes. *Science*, 298:2361–6, December 2002.

[BZd02] Ray H. Baughman, Anvar A. Zakhidov, and Walt A. de Heer. Carbon nanotubes - the route toward applications. *Science*, 297:787–792, August 2002.

[CBC02] L. F. Chibotaru, S. A. Bovin, and A. Ceulemans. Bend-induced insulating gap in carbon nanotubes. *Phys. Rev. B*, 66:R161401–R161404, 2002.

[CBIZ00] Philip G. Collins, Keith Bradley, Masa Ishigama, and A. Zettl. Extreme oxygen sensitivity of electronic properties of carbon nanotubes. *Science*, 287:1801–1804, March 2000.

[CBM+98] David H. Cobden, Marc Bockrath, Paul L. McEuen, Andrew G. Rinzler, and Richard E. Smalley. Spin splitting and even-odd effects in carbon nanotubes. *Phys. Rev. Lett.*, 81(3):681–684, July 1998.

[CCB+04] R. J. Chen, H. C. Choi, S. Bangsaruntip, E. Yenilmez, X. Tang, Q. Wang, Y.-L. Chang, and H. Dai. An investigation of the mechanisms of electronic sensing of protein adsorption on carbon nanotube devices. *J. Am. Chem. Soc.*, 126(5):1563–1568, 2004.

[CCW+03] Oksana Cherniavskaya, Liwei Chen, Vivian Weng, Leonid Yuditsky, and Louis E. Brus. Quantitative noncontact electrostatic force imaging of nanocrystal polarizability. *J. Phys. Chem. B*, 107:1525–1531, 2003.

[CFM+03] Xiaodong Cui, Marcus Freitag, Richard Martel, Louis Brus, and Phaedon Avouris. Controlling energy-level alignment at carbon nanotube/Au contacts. *Nano Lett.*, 3(6):783–787, 2003.

[CGB01] J. Colchero, A. Gil, and A. M. Baró. Resolution enhancement and improved data interpretation in electrostatic force microscopy. *Phys. Rev. B*, 64:245403, 2001.

[CHL00] Chin Li Cheung, Jason H. Hafner, and Charles M. Lieber. Carbon nanotube atomic force microscopy tips: Direct growth by chemical vapour deposition and application to high-resolution imaging. *Proc. Nat. Ac. USA*, 97(8):3809–3813, 2000.

[CHO+00] Chin Li Cheung, Jason H. Hafner, Teri W. Odom, Kyoungha Kim, and Charles M. Lieber. Growth and fabrication with single-walled carbon nanotube probe microscopy tips. *Appl. Phys. Lett.*, 76(21):3136–3138, May 2000.

[CKPL02] Chin Li Cheung, Andrea Kurtz, Hongkun Park, and Charles M. Lieber. Diameter-controlled synthesis of carbon nanotubes. *J. Phys. Chem. B*, 106:2429–2433, 2002.

[CKW+03] H. C. Choi, S. Kundaria, D. Wang, A. Javey, Q. Wang, M. Rolandi, and H. Dai. Efficient formation of iron nanoparticle catalysts on silicon dioxide by hydroxylamine for carbon nanotube synthesis and electronics. *Nano Lett.*, 3(2):157–161, 2003.

[CMGR03] S. Chopra, K. McGuire, N. Gothard, and A. M. Rao. Selective gas detection using a carbon nanotube sensor. *Appl. Phys. Lett.*, 83(11):2280–2282, September 2003.

[CN02] David H. Cobden and Jesper Nygård. Shell filling in closed single-wall carbon nanotube quantum dots. *Phys. Rev. Lett.*, 89(4):046803(4), July 2002.

[CS02] Daniel T. Colbert and Richard E. Smalley. *Perspectives of Fullerene Nanotechnology*, chapter Past, Present and Future of Fullerene Nantubes: Buckytubes, pages 3–10. Kluwer Academic Publishers, 2002.

[CSC99] J. K. Campbell, L. Sun, and R. M. Crooks. Electrochemistry with single carbon nanotubes. *J. Am. Chem. Soc.*, 121:3779–3780, 1999.

[CSSR00a] R. Crook, C. G. Smith, M. Y. Simmons, and D. A. Ritchie. Imaging cyclotron orbits and scattering sites in a high-mobility two-dimensional electron gas. *Phys. Rev. B*, 62(8):5174–5178, 2000.

[CSSR00b] R. Crook, C. G. Smith, M. Y. Simmons, and D. A. Ritchie. One-dimensional probability density observed using scanned gate microscopy. *J. Phys. Condens. Matter*, 12:L735–L740, 2000.

[CWCT03] Y. C. Chang, D. C. Wang, C. S. Chang, and Tien Y. Tsong. Easy method to adjust the angle of the carbon nanotube probe of an atomic force microscope. *Appl. Phys. Lett.*, 82(20):3541, May 2003.

[CWD03] Jien Cao, Qian Wang, and Hongjie Dai. Electromechanical properties of metallic, quasimetallic, and semiconducting carbon nanotubes under stretching. *Phys. Rev. Lett.*, 90(15):157601(4), April 2003.

[Dai00] Hongjie Dai. Controlling nanotube growth. *Physics World*, June 2000.

[Dai02a] Hongjie Dai. Carbon nanotubes: opportunities and challenges. *Surf. Sci.*, 500:218–241, 2002.

[Dai02b] Hongjie Dai. Carbon nanotubes: Synthesis integration and properties. *Acc. Chem. Res.*, 35:1035–1044, 2002.

[Dat95] Supriyo Datta. *Electronic Transport in Mesoscopic Systems*. Cambridge University Press, 1995.

[DDC02] J. W. Ding, X. H. Dan, and J. X. Cao. Analytical relation of band gaps to both chirality and diameter of single-wall carbon nanotubes. *Phys. Rev. B*, 66:073401–073404, 2002.

[DDJ+02a] M. S. Dresselhaus, G. Dresselhaus, A. Jorio, a. G. Souza Filho, and R. Saito. Review: Raman spectroscopy on isolated single wall carbon nanotubes. *Carbon*, 40:2043–2061, 2002.

[DDJ+02b] M. S. Dresselhaus, G. S. Dresselhaus, G. Jorio, A.G. Souza Filho, M. A. Pimenta, and R. Saito. Single nanotube raman spectroscopy. *Acc. Chem. Res.*, 35:1070–1078, 2002.

[de 00] Walt de Heer. Industry sizes up nanotubes. *Physics World*, June 2000.

[DEHT94] E. Dujardin, T. W. Ebbesen, H. Hiura, and K. Tanigaki. Capillarity and wetting of carbon nanotubes. *Science*, 265:1850–1852, September 1994.

[DGCF04] T. Durkop, S. A. Getty, E. Cobas, and M. S. Fuhrer. Extraordinary mobility in semiconducting carbon nanotubes. *Nano Lett.*, 2(7):35–39, 2004.

[DHR+96] Hongjie Dai, Jason H. Hafner, Andrew G. Rinzler, Daniel T. Colbert, and Richard E. Smalley. Nanotubes as nanoprobes in scanning probe microscopy. *Nature*, 384:147–150, November 1996.

[DMJ+03] M. Drndić, R. Markov, M. V. Jarosv, M. G. Bawendi, M. A. Kastner, N. Markovic, and M. Tinkham. Imaging the charge transport in arrays of CdSe nanocrystals. *Appl. Phys. Lett.*, 83(19):4008 – 4010, November 2003.

[dPGNM+02] P.J. de Pablo, C. Gómez-Navarro, M. T. Martínez, A. M. Benito, W. K. Maser, J. Colchero, J. Gómez-Herrero, and A. M. Baró. Performing current versus voltage measurements of single-walled carbon nanotubes using scanning force microscopy. *Appl. Phys. Lett.*, 2002.

[EBT+96] M. A. Eriksson, R. G. Beck, M. Topinka, J. A. Katine, R. M. Westervelt, K. L. Campman, and A. C. Gossard. Cryogenic scanning probe characterisation of semiconductor nanostructures. *Appl. Phys. Lett.*, 69(5):671–673, July 1996.

[EHJ95] P. C. Ecklund, J. M. Holden, and R. A. Jishi. Vibrational modes of carbon nanotubes; spectroscopy and theory. *Carbon*, 33(2):959–972, 1995.

[ES90] D. M. Eigler and E. K. Schweizer. Positioning single atoms with a scanning tunneling microscope. *Nature*, 344:524–526, 1990.

[FBP+03] X. Fan, R. Buczko, A. A. Puretzky, D. B. Geohegan, J. Y. Howe, S. T. Pantelides, and S. J. Pennycook. Nucleation of single-walled carbon nanotubes. *Phys. Rev. Lett.*, 90(14):145501(4), April 2003.

[FCT+97] M. R. Falvo, G. J. Clary, R. M. Taylor, V. Chi, F. P. Brooks, S. Washburn, and R. Superfine. Bending and buckling of carbon nanotubes under large strain. *Nature*, 389:582–584, October 1997.

[FD00] Nathan R. Franklin and Hongjie Dai. An enhanced CVD approach to extensive nanotube networks with directionality. *Adv. Mater.*, 12(12):890–894, 2000.

[FJKB02] Marcus Freitag, A. T. Johnson, Sergei V. Kalinin, and Dawn A. Bonnell. Role of single defects in electronic transport through carbon nanotube field-effect transistors. *Phys. Rev. Lett.*, 89:216081(4), 2002.

[FKDB02] M. S. Fuhrer, B. M. Kim, T. Durkop, and T. Brintlinger. High mobility nanotube transistor memory. *Nano Lett.*, 2(7):755–759, July 2002.

[FLC+01] Nathan R. Franklin, Yiming Li, Robert J. Chen, Ali Javey, and Hongjie Dai. Patterened growth of single-walled carbon nanotubes on full 4-inch wafers. *Appl. Phys. Lett.*, 79(27):4571–4573, December 2001.

[FPWdH98] Stefan Frank, Phillipe Poncharal, Z. L. Wang, and Walt A. de Heer. Carbon nanotube quantum resistors. *Science*, 280:1744–1746, June 1998.

[FRCJ00] M. Freitag, M. Radosavljevic, W. Clauss, and A.T. Johnson. Local electronic properties of single-wall nanotube circuits measured by

conducting-tip AFM. *Phys. Rev. B*, 62(4):R2307–R2310, February 2000.

[FRZJ01] Marcus Freitag, Marko Radosavljevic, Yangxin Zhou, and A. T. Johnson. Controlled creation of a carbon nanotube diode by a scanned gate. *Appl. Phys. Lett.*, 79(20):3326–3328, November 2001.

[FYMK03] Amir A. Farajian, Boris I. Yakobson, Hiroshi Mizuseki, and Yoshiyuki Kawazoe. Electronic transport through bent carbon nanotubes: nanoelectromechanical sensors and switches. *Phys. Rev. B*, 67:205423, 2003.

[GCGHB03] A. Gil, J. Colchero, J. Gómez-Herrero, and A. M. Baro. Electrostatic force gradient signal: resolution enhancement in electrostatic force microscopy and improved Kelvin probe microscopy. *Nanotechnology*, 14:332–340, 2003 2003.

[GG03] Wanlin Guo and Yufeng Guo. Giant axial electrostrictive deformation in carbon nanotubes. *Phys. Rev. Lett.*, 91(11):115501, September 2003.

[GHL00] L. A. Girifalco, M. Hodak, and R. S. Lee. Carbon nanotubes, buckyballs, ropes, and a universal graphitic potential. *Phys. Rev. B*, 62(19):13104–13110, November 2000.

[Gie97] Franz J. Giessibl. Forces and frequency shifts in atomic-resolution dynamic-force microscopy. *Phys. Rev. B*, 56(24):16010–16015, December 1997.

[Gie03] Franz J. Giessibl. Advances in atomic force microscopy. *Rev. Mod. Phys.*, 75:949–983, July 2003.

[GM02] C. E. Gardner and J. V. Macpherson. Atomic force microscopy probes go electrochemical. *Anal. Chem.*, 74(21):576A–584A, November 2002.

[GRS02] P. Girard, M. Ramonda, and D. Saluel. Electrical contrast observations and voltage measurements by kelvin probe force gradient microscopy. *J. Vac. Sci. Technolo. B*, 20(4):1348–1355, 2002.

[GZB03] Yu N. Gartstein, A.A. Zakhidov, and R. H. Baughman. Mechanical and electromechanical coupling in carbon nanotube distortions. *Phys. Rev. B*, 68:115414, 2003.

[HB93] Jeffrey L. Hutter and John Bechhoefer. Calibration of atomic-force microscope tips. *Rev. Sci. Instrum.*, 64(7):1868–1873, July 1993.

[HCDL03] Shaoming Huang, Xianyu Cai, Chunsheng Du, and Jie Liu. Oriented long single-walled carbon nanotubes on substrates from floating catalysts. *J. Phys. Chem. B*, 107(48):13251–13254, December 2003.

[HCL99] Jason H. Hafner, Chin Li Cheung, and Charles M. Lieber. Growth of nanotubes for probe microscopy tips. *Nature*, 398:761–761, April 1999.

[HCL03] S. Huang, X. Cai, and J. Liu. Growth of millimeter-long and horizontally aligned single-walled carbon nanotubes on flat substrates. *J. Am. Chem. Soc.*, 125(19):5636–5637, 2003.

[HCOL01] Jason H. Hafner, Chin-Li Cheung, Tjerk H. Oosterkamp, and Charles M. Lieber. High-yield assembly of individual single-walled carbon nanotube tips for scanning probe microscopies. *J. Phys. Chem. B*, 105(4):743–746, February 2001.

[HKO+03] Yoshikazu Homma, Yoshiro Kobayashi, Toshio Ogino, Daisuke Takagi, Roichi Ito, Yung Joon Jung, and Pulickel M. Ajayan. Role of transition metal catalysts in single-walled carbon nanotube growth in chemical vapour deposition. *J. Phys. Chem. B*, 107:12161–12164, 2003.

[HL02] Min Ouyang Jin-Lin Huang and Charles M. Lieber. One-dimensional energy dispersion of single-walled carbon nanotubes by resonant electron scattering. *Phys. Rev. Lett.*, 88(6):0668041–4, February 2002.

[HLN+00] J. Hone, M. C. Llaguno, N. M. Nemes, Johnson A. T, J. E. Fischer, D. A. Walters, M. J. Casavant, J. Schmidt, and R. E. Smalley. Electrical and thermal transport properties of magnetically aligned single wall carbon nanotube films. *Appl. Phys. Lett.*, 77(5):666–668, July 2000.

[HMS+03] A. Hall, W. G. Matthews, R. Superfine, M. R. Falvo, and S. Washburn. Simple and efficient method for carbon nanotube attachment to scanning probes and other substrates. *Appl. Phys. Lett.*, 82(15):2506–2508, April 2003.

[HRTA03] S. Heinze, M. Radosavljević, J. Tersoff, and Ph. Avouris. Unexpected scaling of the performance of carbon nanotube schottky-barrier transistors. *Phys. Rev. B*, 68:235418(5), 2003.

[HSW99] H. Hōlscher, U. D. Schwarz, and R. Wiesendanger. Calculation of the frequency shift in dynamic force microscopy. *Appl. Surf. Sci.*, 140:344–351, 1999.

[HTD+02] S. Heinze, J. Tersoff, R. Martel V. Derycke, J. Appenzeller, and P. Avouris. Carbon nanotubes as Schottky barrier transistors. *Phys. Rev. Lett.*, 89(10):106801(4), September 2002.

[HWA98] Tobias Hertel, Robert E. Walkup, and Phaedon Avouris. Deformation of carbon nanotubes by surface Van der Waals forces. *Phys. Rev. B*, 58(20):13870–3, November 1998.

[II93] S. Iijima and T. Ichihashi. Single-shell carbon nanotubes of 1-nm in diameter. *Nature*, 363:603–605, 1993.

[Iij91] S. Iijima. Helical microtubules of graphitic carbon. *Nature*, 354:56–58, 1991.

[IKS+03] Hiroyoshi Ishii, Hiromichi Kataura, Hidetsugu Shiozawa, Hideo Yoshioka, Hideo Otsubo, Yasuhiro Takayama, Tsuneaki Miyahara, Shinzo Suzuki, Yohji Achiba, Masashi Nakatake, Takamasa Narimura, Mitsuhara Higashiguchi, Kenya Shimada, Hirofumi Namatame, and Masaki Taniguchi. Direct observation of Tomanaga-Luttinger-liquid state in carbon nanotubes at low temperature. *Nature*, 426:540–544, December 2003.

[JGP+04] Ali Javey, Jing Guo, Magnus Paulsson, Qian Wang, David Mann, Mark Lundstrom, and Hongjie Dai. High-field, quasi-ballistic transport in short carbon nanotubes. *Phys. Rev. Lett.*, 92(10):10684(4), March 2004.

[JGW+03] Ali Javey, Jing Guo, Qian Wang, Mark Lundstrom, and Hongjie Dai. Ballistic carbon nanotube field-effect transistors. *Nature*, 424:654–657, August 2003.

[JHaMH+01] A. Jorio, J. H. Hafner, C. M. Lieber abd M. Hunter, T. McClure, G. Dresselhaus, and M. S. Dresselhaus. Structural (n,m) determination of isolated single-wall carbon nanotubes by resonant Raman scattering. *Phys. Rev. Lett.*, 86(6):1118(4), February 2001.

[JHN+04] Ane Jensen, Jonas Rahlf Hauptmann, Jesper Nygård, Janusz Sadowski, and Poul Erik Lindelof. Hybrid devices from single wall carbon nanotubes epitaxially grown into a semiconductor nanostructure. *Nano Lett.*, ASAP article, 2004.

[JKS99] H. O. Jacobs, H. F. Knapp, and A. Stemmer. Practical aspects of Kelvin probe force microscopy. *Rev. Sci. Instrum.*, 70(3):1756–1760, March 1999.

[JL02] Ernesto Joselevich and Charles M. Lieber. Vectorial growth of metallic and semi-conducting single-wall carbon nanotubes. *Nano Lett.*, 2(10):1137–1141, 2002.

[JLC00] Seung-Hoon Jhi, Steven G. Louie, and Marvin L. Cohen. Electronic properties of oxidised carbon nanotubes. *Phys. Rev. Lett.*, 85:1710–1713, 2000.

[JLHS98] H.O. Jacobs, P. Leuchtmann, O. J. Homan, and A. Stemmer. Resolution and contrast in Kelvin probe force microscopy. *J. Appl. Phys.*, 84(3):1168–1173, 1998.

[JPF+03] A Jorio, M A Pimenta, A G Souza Filho, R Saito, G Dresselhaus, and M S Dresselahaus. Characterising carbon nanotube samples with resonance Raman scattering. *New Journal of Physics*, 5:139.1–139.17, 2003.

[JSD02] Ali Javey, Moonsub Shim, and Hongjie Dai. Electrical properties of large-diameter single-walled carbon nanotubes. *Appl. Phys. Lett.*, 80(6):1064–1066, February 2002.

[JWY+02] A. Javey, Q. Wang, A. Yral, Y. Li, and Dai H. Carbon nanotube transistor arrays for multistage complementary logic and ring oscillators. *Nano Lett.*, 2(9):929–932, 2002.

[KB99] Todd D. Krauss and Louis E. Brus. Charge, polarizability, and photoionization of single semiconductor nanocrystals. *Phys. Rev. Lett.*, 83(23):4840 – 4843, December 1999.

[KBB+03] Kinneret Keren, Rotem S. Berman, Evgeny Buchstab, Uri Sivan, and Erez Braun. DNA-templated carbon nanotube field-effect transistor. *Science*, 302:1380–2, November 2003.

[KBFJ02] Sergei V. Kalinin, Dawn A. Bonnell, Marcus Freitag, and A. T. Johnson. Carbon nanotubes as a tip calibration standard for electrostatic scanning probe microscopies. *Appl. Phys. Lett.*, 81(4):754 – 756, July 2002.

[KBM02] Valery N. Khabashesku, W. Edward Billups, and John L. Margrave. Fluorination of single-wall carbon nanotubes and subsequent derivatization reactions. *Acc. Chem. Res.*, 35:1087–1095, 2002.

[KCD98] Jing Kong, Alan M. Cassell, and Hongjie Dai. Chemical vapour deposition of methane for single-walled carbon nanotubes. *Chem. Phys. Lett.*, 292:567–574, August 1998.

[KCDA02] Jing Kong, Jien Cao, Hongjie Dai, and Erik Anderson. Chemical profiling of single nanotubes: Intramolecular p-n-p junctions and on tube single electron transistors. *Appl. Phys. Lett.*, 80:73, 2002.

[KCL+02] W. Kim, H. C Choi, Y. Li, D. Wang, and H. Dai. Synthesis of ultralong and high percentage of semiconducting single-walled carbon nanotubes. *Nano Lett.*, 2(7):703–8, 2002.

[KDE+98] A. Krishnan, E. Dujardin, T. W. Ebbesen, P. N. Yianilos, and M. M. J. Treacy. Young's modulus of single-walled nanotubes. *Phys. Rev. B*, 58(20):14013–141019, November 1998.

[KE01] Alex Kleiner and Sebastien Eggert. Band gaps of primary metallic carbon nanotubes. *Phys. Rev. B*, 63:073408, 2001.

[KFZ+00] Jing Kong, Nathan Franklin, Chongwu Zhou, Michael G. Chapline, Shu Peng, Kyeongjae Cho, and Hongjie Dai. Nanotube molecular wires as chemical sensors. *Science*, 287:622–625, January 2000.

[KH03] M. R. Koblischka and U. Hartmann. Recent advances in magnetic force microscopy. *Ultramicroscopy*, 97:103–112, 2003.

[KHO+85] H. W. Kroto, J. R. Heath, S. C. O'Brien, R. F. Curl, and R. E. Smalley. C_{60}: Buckminsterfullerene. *Nature*, 318:162–162, 1985.

[KHvK03] Ralph Krupke, Frank Hennrich, Hilbert v. Löhneysen, and Manfred M Kappes. Separation of metallic from semi-conducting single-walled carbon nanotubes. *Science*, 301:344–347, July 2003.

[KJV+03] W. Kim, A. Javey, O. Vermesh, Q. Wang, Y. Li, and H. Dai. Hysteresis caused by water molecules in carbon nanotube field-effect transistors. *Nano Lett.*, 3(2):193–198, 2003.

[KKR+04] A. Yu Kasumov, D. V. Klinov, P.-E. Roche, S. Gueron, and H. Bouchiat. Thickness and low-temperature conductivity of DNA molecules. *Appl. Phys. Lett.*, 84(6):1007–9, February 2004.

[KM97] C. L. Kane and E. J. Mele. Size shape, and low energy electronic structure of carbon nanotubes. *Phys. Rev. Lett.*, 78(10):1932, March 1997.

[KM03] C. L. Kane and E. J. Mele. Ratio problem in single carbon nanotube flourescence spectroscopy. *Phys. Rev. Lett.*, 90(20):207401, May 2003.

[KOB01] Todd D. Krauss, Stephen O'Brien, and Lousi E. Brus. Charge and photoionization properties of single semiconductor nanocrystals. *J. Phys. Chem. B*, 105:1725–1733, 2001.

[KOHL99] Philip Kim, Teri W. Odom, Jin-Lin Huang, and Charles M. Lieber. Electronic density of states of atomically resolved single-walled carbon nanotubes: Van Hove singularities and end states. *Phys. Rev. Lett.*, 82(6):1225–8, February 1999.

[KSC+98] Jing Kong, Hyongsok T. Soh, Alan M. Cassell, Calvin F. Quate, and Hongjie Dai. Synthesis of individual single-walled carbon nanotubes on patterned silicon wafers. *Nature*, 395:878–881, October 1998.

[LBB+01] Wenjie Liang, Marc Bockrath, Dolores Bozovic, Jason H. Hafner, M. Tinkham, and Hongkun Park. Fabry-perot interference in a nanotube electron waveguide. *Nature*, 411:665–669, June 2001.

[LBP02] Wenjie Liang, Marc Bockrath, and Hongkun Park. Shell filling and exchange coupling in metallic single-walled carbon nanotubes. *Phys. Rev. Lett.*, 88(12):126801(4), March 2002.

[LCD99] Jun Li, Alan M. Cassell, and Hongjie Dai. Carbon nanotubes as AFM tips: measuring DNA molecules at the liquid/solid interface. *Surf. Interface Anal.*, 28:8–11, 1999.

[LHF03] J Lefebvre, Y Homma, and P Finnie. Bright band gap photoluminescence from unprocessed single-walled carbon nanotubes. *Phys. Rev. Lett.*, 90(21):217401(4), May 2003.

[LKZ+01] Y. Li, W. Kim, Y. Zhang, M. Rolandi, D. Wang, and H. Dai. Growth of single-walled carbon nanotubes from discrete catalytic nanoparticles of various sizes. *J. Phys. Chem. B*, 105(46):11424–11431, 2001.

[LLTR04] Yuehe Lin, Fang Lu, Yi Tu, and Zhifeng Ren. Glucose biosensors based on carbon nanotube nanoelectrode ensembles. *Nano Lett.*, ASAP article, 2004.

[LLY+03] Jing Li, Yijang Lu, Qi Ye, Martin Cinke, and Jie Han M. Meyyappan. Carbon nanotube sensors for gas and organic vapor detection. *Nano Lett.*, 3(7):929–933, 2003.

[LM02] R. Levy and M. Maaloum. Measuring the spring constant of atomic force microscope cantilevers: thermal fluctuations and other methods. *Nanotechnology*, 13:33–37, 2002.

[LMF+02] T. Larsen, K. Moloni, F. Flack, M. A. Eriksson, M. G. Lagally, and C. T. Black. Comparison of wear characteristics of etched-silicon and carbon nanotube atomic-force microscopy probes. *Appl. Phys. Lett.*, 80(11):1996–1998, March 2002.

[LMR+04] Y. Li, D. Mann, M. Rolandi, W. Kim, A. Ural, S. Hung, A. Javey, J. Cao, D. Wang, E. Yenilmez, Q. Wang, J. F. Gibbons, Y. Nishi, and H. Dai. Preferential growth of semi-conducting single-walled carbon nanotubes by a plasma enhanced CVD method. *Nano Lett.*, asap article, 2004.

[LOW97] M. A. Lantz, S. J. O'Shea, and M. E. Welland. Lateral stiffness of the tip and tip-sample contact in frictional force microscopy. *Appl. Phys. Lett.*, 70(8):970–972, February 1997.

[LY04] M. Lucas and R. J. Young. Effect of uniaxial strain deformation upon the raman radial breathing modes of single-wall carbon nanotubes in composites. *Phys. Rev. B*, 69:085405–085413, 2004.

[MBC+99] Paul McEuen, Marc Bockrath, David H. Cobden, Young-Gui Yoon, and Steven G. Louie. Disorder, pseudospins and backscattering in carbon nanotubes. *Phys. Rev. Lett.*, 83(24):5098(4), December 1999.

[McE00] Paul L McEuen. Single-wall carbon nanotubes. *Physics World*, pages 31–36, June 2000.

[MDL+01] R. Martel, V. Derycke, C. Lavoie, J. Appenzeller, K. K. Chan, J. Tersoff, and P. Avouris. Ambipolar electrical transport in semiconducting single-wall carbon nanotubes. *Phys. Rev. Lett.*, 87(25):256805, December 2001.

[MFP02] Paul L. McEuen, Michael Fuhrer, and Hongkun Park. Single-walled carbon nanotube electronics. *IEEE Trans. on Nanotech.*, 1, 2002.

[MHCB03] F. Moreno-Herrero, J. Colchero, and A. M. Baro. DNA height in scanning force microscopy. *Ultramicroscopy*, 96:167–174, 2003.

[MJK+03] David Mann, Ali Javey, Jing Kong, Qian Wang, and Hongjie Dai. Ballistic transport in metallic carbon nanotubes with reliable Pd ohmic contacts. *Nano Lett.*, 3(11):1541–1544, 2003.

[MMA+03] J. A. Misewich, R. Martel, Ph. Avouris, J. C. Tang, S. Heinze, and J. Tersoff. Electrically induced optical emission from a carbon nanotube FET. *Science*, 300:783–786, May 2003.

[Mor01] Philip Moriarty. Nanostructured materials. *Rep. Prog. Phys.*, 64:297–381, 2001.

[MSA02] A. Maiti, A. Svizhenko, and M. P. Anantram. Electronic transport through carbon nanotubes: Effect of structural deformation and tube chirality. *Phys. Rev. Lett.*, 88(12):126805, March 2002.

[MYS+03] E. D. Minot, Yuval Yaish, Vera Sazonova, Ji-YOng Park, Markus Brink, and Paul L. McEuen. Tuning carbon nanotube band gaps with strain. *Phys. Rev. Lett.*, 90(15):156401(4), April 2003.

[MYSM04] E. D. Minot, Yuval Yaish, Vera Sazonova, and Paul L. McEuen. Determination of electron orbital magnetic moments in carbon nanotubes. *Nature*, 428:536–539, April 2004.

[NCK+03] Hou T. Ng, Bin Chen, Jessica E. Koehne, Alan M. Cassell, Jun Li, Jie Han, and M. Meyyappan. Growth of carbon nanotubes: a combinatorial method to study the effects of catalyst and underlayers. *J. Phys. Chem. B*, 107:8484–8489, 2003.

[NCL00] Jesper Nygård, David Henry Cobden, and Poul Erik Lindelof. Kondo physics in carbon nanotubes. *Nature*, 408:342–346, November 2000.

[NHH+03] S. Niyogi, M. A. Hamon, H. Hu, B. Zhao, P. Bhowmik, R. Sen, M. E. Itkis, and R. C. Haddon. Chemistry of single-walled carbon nanotubes. *Acc. Chem. Res.*, 35:1105–1113, 2003.

[NSH+03] J. P. Novak, E. S. Snow, E. J. Houser, D. Park, J. L. Stepnowski, and R. A. McGill. Nerve agent detection using networks of single-walled carbon nanotubes. *Appl. Phys. Lett.*, 83(19):4026–4028, November 2003.

[OAW95] S. J. O'Shea, R. M. Atta, and M. E. Welland. Characterization of tips for conducting atomic force microscopy. *Rev. Sci. Instrum.*, 66(3):2508–2512, 1995.

[OBH+02] Michael J. O'Connell, Sergei M. Bachilo, Chad B. Huffman, Valerie C. Moore, Michael S. Strano, Erik H. Haroz, Kristy L. Rialon, Peter J. Boul, William H. Noon, Carter Kittrell, Jianpeng Ma, Robert H. Hauge, R. Bruce Weisman, and Richard E. Smalley. Band gap flourescence from individual single-walled carbon nanotubes. *Science*, 297:593–596, July 2002.

[OHCL01] Min Ouyang, Jin-Lin Huang, Chin Li Cheung, and Charles M. Lieber. Energy gaps in 'metallic' single-walled carbon nanotubes. *Science*, 292:702–5, April 2001.

[OHKL98] Teri Wang Odom, Jin-Lin Huang, Philip Kim, and Charles M. Lieber. Atomic structure and electronic properties of single-walled carbon nanotubes. *Nature*, 391:62–64, January 1998.

[OHL02] Min Ouyang, Jin-Lin Huang, and Charles M. Lieber. Fundamental electronic properties and applications of single-walled carbon nanotubes. *Acc. Chem. Res.*, 35:1018–1025, 2002.

[PBY+02] Phillipe Poncharal, Claire Berger, Yan Yi, Z. L. Wang, and Walt A. de Heer. Room temperature ballistic conductance in carbon nanotubes. *J. Phys. Chem. B*, 106:12104–12118, 2002.

[PCS+98] S. R. Patel, S. M. Cronenwett, D. R. Stewart, A. G. Huibers, C. M. Marcus, C. I. Duruoz, J. S. Harris, K. Campman, and A. C. Gossard. Statistics of Coulomb Blockade peak spacings. *Phys. Rev. Lett.*, 80(20):4522–4525, May 1998.

[PLC+04] F. M. Pan, Y. B. Liu, Y. Chang, C. Y. Chen, T. G. Tsai, M. N. Chang, and J. T. Sheu. Selective growth of carbon nanotube on scanning probe tips by microwave plasma chemical vapor deposition. *J. Vac. Sci. Technol. B*, 22(1):90–93, 2004.

[PRY+04] Ji-Yong Park, Sami Rosenblatt, Yuval Yaish, Vera Sazonova, Hande Ustunel, Stephan Braig, T. A. Arias, Piet Brouwer, and Paul L. McEuen. Electron-phonon scattering in metallic single-walled carbon nanotubes. *Nano Lett.*, ASAP, 2004.

[PSMR04] Amol Patil, Jennifer Sippel, Gregory W. Martin, and Andrew G. Rinzler. Enhanced functionality of nanotube atomic force microscopy tips by polymer coating. *Nano Lett.*, 4(2):303–308, 2004.

[PTY+01] Henk W. Ch. Postma, Tijs Teepen, Zhen Yao, Milena Grifoni, and Cees Dekker. Carbon nanotube single-electron transitors at room temperature. *Science*, 293:76–79, July 2001.

[PYB+02] Ji-Yong Park, Yuval Yaish, Markus Brink, Sami Rosenblatt, and Paul L. McEuen. Electrical cutting and nicking of carbon nanotubes using an atomic force microscope. *Appl. Phys. Lett.*, 80(23):4446–4448, June 2002.

[QVG+03] Pengfei Qi, Ophir Vermesh, Mihai Grecu, Ali Javey, Qian Wang, and Hongjie Dai. Toward large arrays of multiplex functionalised carbon nanotube sensors for highly sensitive and selective molecular detection. *Nano Lett.*, 3(3):347–351, 2003.

[RFTJ02] M. Radosavlejvić, M. Freitag, K. V. Thadani, and A. T. Johnson. Nonvolatile molecular memory elements based on ambipolar nanotube field effect transistors. *Nano Lett.*, 2(7):761–764, July 2002.

[RG02] C. N. Rao and A. Govindaraj. Carbon nanotubes from organometallic precursors. *Acc. Chem. Res.*, 35:998–1007, 2002.

[RHC04] Iuliana Radu, Yael Hanein, and David H. Cobden. Oriented growth of single-wall carbon nanotubes using alumina patterns. *Nanotechnology*, 15:473–476, 2004.

[RHSH03] Saleem G. Rao, Ling Huang, Wahyu Setyawan, and Seunghun Hong. Large-scale assembly of carbon nanotubes. *Nature*, 425:36–37, September 2003.

[RYP+02] S. Rosenblatt, Y. Yaish, J. Park, J. Gore, V. Sazanova, and P. L. McEuen. High performance electrolyte gated carbon nanotube transistors. *Nano Lett.*, 2(8):869–872, 2002.

[SBGv03] S Sapmaz, Y M Blanter, L Gurevich, and H S J van der Zant. Carbon nanotubes as nanoelectromechanical systems. *Phys. Rev. B*, 67(23):235414, June 2003.

[SBL+97] M. V. Salapaka, H. S. Bergh, J. Lai, A. Majumdar, and E. McFarland. Multi-mode noise analysis of cantilevers for scanning probe microscopy. *J. Appl. Phys.*, 81(6):2480–2487, March 1997.

[SDD98] R. Saito, G. Dresselhaus, and M. S. Dresselhaus. *Physical Properties of Carbon Nanotubes.* Imperial College Press, 1998.

[SDU+03] Michael S. Strano, Christopher A. Dyke, Monica L. Usrey, Paul W. Barone, Matthew J. Allen, Hongwei Shan, Carter Kittrell, Robert H. Hauge, James M. Tour, and Richard E. Smalley. Electronic structure control of single-walled carbon nanotube functionalization. *Science*, 301:1519–22, September 2003.

[SF00] Christian Schönenberger and Laszlo Forró. Multiwall carbon nanotubes. *Physics World*, June 2000.

[SFLH02] Ya-Ping Sun, Kefu Fu, Yi Lin, and Weijie Huang. Functionalised carbon nanotubes: Properties and applications. *Acc. Chem. Res.*, 35:1096–1104, 2002.

[SGBG03] A. Star, J.-C. Gabriel, K. Bradley, and G. Gruner. Electronic detection of specific protein binding using nanotube fet devices. *Nano Lett.*, 3(4):459–463, 2003.

[SGS+03] S. Sadewasser, Th. Glatzel, R. Shikle, Y. Rosenwaks, and M.Ch. Lux-Steiner. Resolution of Kelvin probe force microscopy in ultrahigh vacuum: comparison of experiment and simulation. *Appl. Surf. Sci.*, 210:32–36, 2003.

[SSK+03] Takao Someya, Joshua Small, Philip Kim, Colin Nuckolls, and James T. Yardley. Alcohol vapor sensors based on single-walled carbon nanotube field effect transistors. *Nano Lett.*, 3(7):877–881, 2003.

[STAN01] Tetsuo Shimizu, Hiroshi Tokumoto, Seiji Akita, and Yoshikazu Nakayama. Stable atomic imaging of Si(1 1 1)-7×7 surface by scanning tunnelling microscope with carbon nanotube tip. *Surf. Sci.*, 486:L455–L460, 2001.

[Sze85] S. M. Sze. *Semiconductor Devices: Physics and Technology.* John Wiley and Sons, 1985.

[TD00] Sander J. Tans and Cees Dekker. Molecular transistors: Potential modulations along carbon nanotubes. *Nature*, 404:834–825, 2000.

[TDD+97] Sander J. Tans, Michael H. Devoret, Hongjie Dai, Andreas Thess, Richard E. Smalley, L. J. Geerligs, and Cees Dekker. Individual single-wall carbon nanotubes as quantum wires. *Nature*, 386:474–477, April 1997.

[TLaEJH+00] M. A. Topinka, B. J. LeRoy, S. E. J. Shaw aand E. J. Heller, R. M. Westervelt, K. D. Maranowski, and A. C. Gossard. Imaging coherent electron flow from a quantum point contact. *Science*, 289:2323–2326, September 2000.

[TLN+96] A. Thess, R. Lee, P. Nikolaev, H. Dai, P. Petit, J. Robert, C. Xu, Y. Lee, S. Kim, A. Rinzler, D. Colbert, G. Scuseria, D. Tomanek, J. Fischer, and R. Smalley. Crystalline ropes of metallic carbon nanotubes. *Science*, 273:483–487, 1996.

[TMD+01] Claes Thelabder, Martin H. Magnusson, Knut Deppert, Lars Samuelson, Per Rugaard Poulsen, Jesper Nygård, and Jørn Borggreen. Gold nanoparticle single-electron transistor with carbon nanotube leads. *Appl. Phys. Lett.*, 79(13):2106, September 2001.

[TVD98] Sander J. Tans, Alwin R. M. Verschueren, and Cees Dekker. Room-temperature transistor based on a single carbon nanotube. *Nature*, 393:49–52, May 1998.

[TWY+02] S.-D. Tzeng, C.-L. Wu, Y.-C. You, T. T. Chen, and S. Gwo. Charge imaging and manipulation using carbon nanotube probes. *Appl. Phys. Lett.*, 81(26):5042–5044, December 2002.

[TXJ+04] Y.-C. Tseng, P. Xuan, A. Javey, R. Malloy, Q. Wang, J. Bokor, and H. Dai. Monolithic integration of carbon nanotube devices with silicon MOS technology. *Nano Lett.*, 4(1):123–127, 2004.

[TZKD00] Thomas W. Tombler, Chongwu Zhou, Jing Kong, and Hongjie Dai. Gating individual nanotubes and crosses with scanning probes. *Appl. Phys. Lett.*, 76:2412, 2000.

[Vee] Veeco (Digital Instruments). *Multimode SPM instruction manual*, version 4.22ce edition.

[WE64] R. S. Wagner and W. C. Ellis. VLS. *Appl. Phys. Lett.*, 4:89–91, .. 1964.

[WJHK01] J. H. Walther, R. Jaffe, T. Halicioglu, and P. Koumoutsakos. Carbon nanotubes in water: structural characteristics and energetics. *J. Phys. Chem B*, 105:9980–9987, 2001.

[WJW+98] Stanislaus S. Wong, Ernesto Joselevich, Adam T. Woolley, Chin Li Cheung, and Charles M. Lieber. Covalently functionalized nanotubes as nanometre-sized probes in chemistry and biology. *Nature*, 394:52–55, July 1998.

[WM02] Michael T Woodside and Paul L McEuen. Scanned probe imaging of single-electron charge states in nanotube quantum dots. *Science*, 296:1098–1101, May 2002.

[WMSS01] Hiroyuki Watanabe, Chirake Manabe, Taishi Shigematsu, and Masaaki Shimizu. Dual-probe scanning tunnelling microscope: measuring a carbon nanotube ring transistor. *Appl. Phys. Lett.*, 78(19):2928–2930, May 2001.

[WRAA03] S. J. Wind, M. Radosavljević, J. Appenzeller, and Ph. Avouris. Transistor structures for the study of scaling in carbon nanotubes. *J. Vac. Sci. Techno. B*, 21(6):2856, 2003.

[WSL97] Eric W. Wong, Paul E. Sheehan, and Charles M. Lieber. Nanobeam mechanics: eleasticity, strength, and toughness of nanorods and nanotubes. *Science*, 277:1971–1975, September 1997.

[WSM+04] Lawrence A. Wade, Ian R. Shapiro, Ziyang Ma, Stephen R. Quake, and C. Patrick Collier. Correlating AFM probe morphology to image resolution for single-wall carbon nanotube tips. *Nano Lett.*, 4(4):725–731, 2004.

[WVM+01] Michael T. Woodside, Chris Vale, Paul L. McEuen, C. Kadow, K. D. Maranowski, and A. C. Gossard. Imaging inter-edge state scattering centers in the quantum Hall regime. *Phys. Rev. B Rapid Comm.*, 64:041310, 2001.

[WVR+98] Jeroen W. G. Wildöer, Liesbeth C. Venema, Andrew G. Rinzler, Richard E. Smalley, and Cees Dekker. Electronic structure of atomically resolved carbon nanotubes. *Nature*, 391:59–62, January 1998.

[WW85] Kenneth R. Wehmeyer and R. Mark Wightman. Cyclic voltammetry and anodic stripping voltammetry with mercury ultramicroelectrodes. *Anal. Chem.*, 57(9):1989–1993, 1985.

[WWJ+98] Stanislaus S. Wong, Adam T. Woolley, Ernesto Joselevich, Chin Li Cheung, and Charles M. Lieber. Covalently functionalised single-walled carbon nanotube probe tips for chemical force microscopy. *J. Am. Chem. Soc.*, 120:8557–8558, 1998.

[WWJL99] Stanislaus S. Wong, Adam T. Woolley, Ernesto Joselevich, and Charles M. Lieber. Functionalization of carbon nanotube afm probes using tip-activated gases. *Chem. Phys. Lett.*, 306(5):219–225, June 1999.

[WWO+98] Stanislaus S. Wong, Adam T. Woolley, Teri Wang Odom, Jin-Lin huang, Philip Kim, Dimitri V. Vezenov, and Charles M. Lieber. Single-walled carbon nanotube probes for high resolution nanostructure imaging. *Appl. Phys. Lett.*, 73(23):3465–3467, December 1998.

[YH00] Liu Yang and Jie Han. Electronic structure of deformed carbon nanotubes. *Phys. Rev. Lett.*, 85(1):154–157, July 2000.

[YKD00] Zhen Yao, Charles L. Kane, and Cees Dekker. High-field electrical transport in single-wall carbon nanotubes. *Phys. Rev. Lett.*, 84(13):2941–2944, March 2000.

[YPR+04] Yuval Yaish, Ji-Yong Park, S. Rosenblatt, Vera Sazonova, Markus Brink, and Paul L. McEuen. Electrical nanoprobing of semiconducting carbon nanotubes using an atomic force microscope. *Phys. R3ev. Lett.*, 92(4):046401(4), January 2004.

[YWC+02] Erhan Yanilmez, Qian Wang, Robert J. Chen, Dunwei Wang, and Hongjie Dai. Wafer scale production of carbon nanotube scanning probe tips for atomic force microscopy. *Appl. Phys. Lett.*, 80(12):2225–2227, March 2002.

[YZNL02] Yanlian Yang, Jin Zhang, Xiaolin Nan, and Zhongfan Liu. Toward the chemistry of carboxylic single-walled carbon nanotubes by chemical force microscopy. *J. Phys. Chem B*, 106:4139–4144, 2002.

[ZCC+01] Yuegang Zhang, Aileen Chang, Jien Cao, Qian Wang, Woong Kim, Yiming Li, Nathan Morris, Erhan Yenilmez, Jing Kong, and Hongjie Dai. Electric-field-directed growth of aligned single-walled carbon nanotubes. *Appl. Phys. Lett.*, 79(19):3155–3157, November 2001.

[ZD00] Y. Zhang and Hongjie Dai. Formation of metal nanowires on suspended single-walled carbon nanotubes. *Appl. Phys. Lett.*, 77(19):3015–7, November 2000.

[ZHL02] Jijun Zhao, Jie Han, and Jian Ping Lu. Work functions of pristine and alkali-metal intercalated carbon nanotubes and bundles. *Phys. Rev. B*, 65:193401–193404, 2002.

[ZJS+03] Ming Zheng, Anand Jagota, Michaels S. Strano, Adelina P. Santos, Paul Barone, S. Grace Chou, Bruce A. Diner, Mildred S. Dresselhaus, Robert S. Mclean, G. Bibiana Onoa, Georgii G. Samsonidze, Ellen D. Semke, Monica Usrey, and Dennis J. Walls. Structure-based carbon nanotube sorting by sequence-dependent DNA assembly. *Science*, 302:1545–8, November 2003.